

DTIC FILE COPY.

①

AD-A217 461

AGARD-CP-461

AGARD-CP-461

AGARD

ADVISORY GROUP FOR AEROSPACE RESEARCH & DEVELOPMENT

7 RUE ANDRÉ LÉVY 92100 NEUILLY-EN-FRANCE

AGARD CONFERENCE PROCEEDINGS No.461

High Temperature Surface Interactions

DISTRIBUTION STATEMENT A

Approved for public release;
Distribution Unlimited

DTIC
ELECTE
JAN 24 1990
S E D

NORTH ATLANTIC TREATY ORGANIZATION



DISTRIBUTION AND AVAILABILITY
ON BACK COVER

90 01 23 2 46

AGARD-CP-461

NORTH ATLANTIC TREATY ORGANIZATION
ADVISORY GROUP FOR AEROSPACE RESEARCH AND DEVELOPMENT
(ORGANISATION DU TRAITE DE L'ATLANTIQUE NORD)

AGARD Conference Proceedings No.461
HIGH TEMPERATURE SURFACE INTERACTIONS

Accession For	
NTIS GRA&I	<input checked="" type="checkbox"/>
DTIC TAB	<input checked="" type="checkbox"/>
Unannounced	<input type="checkbox"/>
Justification	
By _____	
Distribution/	
Availability Codes	
Dist	Avail and/or Special
A-1	



Papers presented at the 68th Meeting of the Structures and Materials Panel of AGARD in Ottawa,
Canada, 23-28 April 1989.

THE MISSION OF AGARD

According to its Charter, the mission of AGARD is to bring together the leading personalities of the NATO nations in the fields of science and technology relating to aerospace for the following purposes:

- Recommending effective ways for the member nations to use their research and development capabilities for the common benefit of the NATO community;
- Providing scientific and technical advice and assistance to the Military Committee in the field of aerospace research and development (with particular regard to its military application);
- Continuously stimulating advances in the aerospace sciences relevant to strengthening the common defence posture;
- Improving the co-operation among member nations in aerospace research and development;
- Exchange of scientific and technical information;
- Providing assistance to member nations for the purpose of increasing their scientific and technical potential;
- Rendering scientific and technical assistance, as requested, to other NATO bodies and to member nations in connection with research and development problems in the aerospace field.

The highest authority within AGARD is the National Delegates Board consisting of officially appointed senior representatives from each member nation. The mission of AGARD is carried out through the Panels which are composed of experts appointed by the National Delegates, the Consultant and Exchange Programme and the Aerospace Applications Studies Programme. The results of AGARD work are reported to the member nations and the NATO Authorities through the AGARD series of publications of which this is one.

Participation in AGARD activities is by invitation only and is normally limited to citizens of the NATO nations.

The content of this publication has been reproduced directly from material supplied by AGARD or the authors.

Published November 1989

Copyright © AGARD 1989
All Rights Reserved

ISBN 92-835-0533-6



Printed by Specialised Printing Services Limited
40 Chigwell Lane, Loughton, Essex IG10 3TZ

PREFACE

In keeping with the mission of AGARD, the Structures and Materials Panel (SMP) has traditionally provided aircraft deterioration control information to member nations through its Corrosion Subcommittee. This Specialists' Meeting on High Temperature Surface Interactions continues that tradition. In today's climate of life extension for military aircraft, the topic of corrosion control assumes a role of greater importance. This specialists' meeting focused on controlling the deteriorative effects of the flight environments on aircraft engine materials.

It was noted that not all corrosion control techniques are tremendously expensive. The simple washing of aircraft and engines with fresh water and simple cleaners greatly helps to preclude corrosion failures. Considering engine corrosion, there are several surface degradation problems that are encountered. These include: high temperature oxidation; hot corrosion, sulfidation; fretting and wear. These topics and the state-of-the-art solutions including protective coatings, were addressed in five sessions in two and a half days. It is expected this information will prove useful to the maintenance community of NATO's aircraft.

The publication of the proceedings of this specialists' meeting brings to closure the existence of this subcommittee.

John J. de Luccia
Chairman, Subcommittee on Corrosion

* * *

Traditionnellement, et conformément à la mission de l'AGARD, le Panel AGARD des Structures et Matériaux (SMP) a fourni aux pays membres de l'OTAN des informations concernant le contrôle de la détérioration de structure d'aéronefs par le biais de son sous-comité pour la corrosion. Cette réunion de spécialistes sur les interactions haute température/surface perpétue cette tradition. Le vif intérêt manifesté aujourd'hui par la communauté aéronautique pour la prolongation du cycle de vie des avions militaires ne fait que souligner l'importance de la maîtrise de la corrosion. Cette réunion de spécialistes a porté sur la maîtrise des effets corrosifs de l'environnement opérationnel sur les matériaux constitutifs des moteurs d'avion.

Il a été noté que toutes les techniques de lutte contre la corrosion ne sont pas nécessairement très coûteuses; le simple fait de laver le fuselage et les moteurs des avions avec de l'eau douce et un détergent évite le plus souvent les défaillances provoquées par la corrosion. Dans le cas particulier de la corrosion des moteurs, les problèmes de dégradation de surface sont divers et comprennent l'oxydation à haute température (le calaminage), la corrosion à chaud, la sulfuration, le frottement et l'usure. L'ensemble de ces questions, ainsi que des solutions incorporant les dernières techniques, y compris les revêtements anticorrosion, ont été examinées en cinq séances au cours des deux jours et demi de la réunion. Il y a tout lieu de croire que ces informations seront d'une grande utilité pour les organismes de maintenance des avions de l'OTAN.

La publication du compte-rendu de cette réunion de spécialistes marque la fin des travaux de ce groupe.

John J. de Luccia
Chairman, Subcommittee on Corrosion

STRUCTURES AND MATERIALS PANEL

Chairman: Prof Dr.-Ing. Hans Försching
Direktor der DFVLR
Institut für Aeroelastik
Bunsenstrasse 10
D-3400 Göttingen
Germany

Deputy Chairman: Mr Samuel L. Venneri
Director, Materials & Structures
Division (Code RM)
Office of Aeronautics & Space Technology
NASA Hq
Washington DC 20546
United States

SUB-COMMITTEE MEMBERS

Chairman: Dr J.J.de Luccia
Manager, Aerospace Materials Division
Naval Air Development Center (Code 606)
Warminster, PA 18974-5000
United States

Members: J.Auvinet	FR
H.J.G.Carvalhinhos	PO
P.Costa	FR
A.Deruyttere	BE
M.Doruk	TU
W.Elber	US
V.Giavotto	IT
R.H.Jeal	UK
G.Kamoun	FR
J.S.L.Leach	UK
G.Oddone	IT
P.J.Perry	UK
S.Signoretti	IT
J.Waldman	US
W.Wallace	CA
H.Zocher	GE

PANEL EXECUTIVE

Mr Murray C. McConnell — UK

AGARD-OTAN
7, rue Ancelle
92200 Neuilly sur Seine
France
Tel: (1) 4738 5790 & 5792
Telex: 610176F

From USA and CANADA
AGARD-NATO
Attn: SMP Executive
APO New York 09777

CONTENTS

	Page Reference
PREFACE	iii
STRUCTURES AND MATERIALS PANEL	iv
<u>SESSION I – GENERAL TOPICAL REVIEW</u>	
HIGH TEMPERATURE SURFACE INTERACTIONS: OVERVIEW by R.A.Rapp	1
DEVELOPMENTS IN TEST PROCEDURES FOR HOT-SALT CORROSION OF SUPERALLOYS by S.R.J.Saunders and T.B.Gibbons	2
THE EFFECTS OF A COMPRESSOR REBUILD ON GAS TURBINE ENGINE PERFORMANCE: FINAL RESULTS by J.D.MacLeod and J.C.G.Laflamme	3
<u>SESSION II – CHEMICAL MECHANISMS</u>	
OXIDATION, SULFIDATION AND HOT CORROSION: MECHANISMS AND INTERRELATIONSHIPS by T.A.Kircher	4
SCALE ADHERENCE EFFECTS IN OXIDATION AND SULFIDATION by M.A.DeCrescente and N.S.Bornstein	5
MOLTEN SALT INDUCED HIGH TEMPERATURE DEGRADATION OF THERMAL BARRIER COATINGS by S.Alpérine	6
HIGH TEMPERATURE OXIDATION OF AL-LI ALLOYS by P.G.Partridge	7
<u>SESSION III – MECHANICAL MECHANISMS</u>	
FRETTING WEAR AND FRETTING FATIGUE AT TEMPERATURES UP TO 600°C by R.B.Waterhouse	8
EFFECT OF PROTECTIVE COATINGS ON MECHANICAL PROPERTIES OF SUPERALLOYS by R.Mevrel and J.M.Veys	9
MICRODAMAGE TO CERAMIC SURFACES UNDER SLIDING CONDITIONS by P.J.Kennedy and A.Conte	10
FRETTING FATIGUE STRENGTH OF Ti-6Al-4V AT ROOM AND ELEVATED TEMPERATURES AND WAYS OF IMPROVING IT by R.Schäfer and W.Schütz	11
<u>SESSION IV – STATE-OF-THE-ART SOLUTIONS</u>	
HIGH TEMPERATURE PROTECTIVE COATINGS: RECENT TRENDS by R.Mevrel	12
THERMAL SHOCK AND OXIDATION RESISTANCE OF CERAMIC COATINGS by J.A.M.Boogers, R.J.H.Wanhill and H.J.C.Hersbach	13
EVALUATION OF HIGH TEMPERATURE PROTECTIVE COATINGS FOR GAS TURBINE ENGINES UNDER SIMULATED SERVICE CONDITIONS by A.K.Gupta, T.Terada, P.C.Patnaik and J.P.Immarigeon	14
Paper 15 withdrawn	

Reference

**SURFACE PROPERTY IMPROVEMENT IN TITANIUM ALLOY GAS TURBINE COMPONENTS
THROUGH ION IMPLANTATION**

by J.E.Elder, M.R.Pishva, N.C.Bellinger, P.C.Patnaik and R.Thamburaj

16

OVERVIEW ON HOT GAS TEST AND MOLTEN SALT CORROSION EXPERIMENTS AT THE DLR

by H.-J.Rätzer-Scheibe

17

SESSION V – SUMMARY DISCUSSION SESSION

REPORT OF DISCUSSIONS

by J.J.de Luccia

R

HIGH TEMPERATURE SURFACE INTERACTIONS: OVERVIEW

by

Robert A. Rapp

Department of Materials Science and Engineering

The Ohio State University

Columbus, Ohio 43210 U.S.A.

SUMMARY

A novel mechanistic model is presented to explain and interrelate the means for vacancy annihilation, stress generation and scale adherence for cation/vacancy diffusion-limited scale growth on a pure metal. Specifically, the climb into the metal of a fraction of the intrinsic interfacial misfit edge dislocations accounts for vacancy annihilation, ultimately leading to cooperative dislocation glide in both the metal and the scale.

The hot corrosion of metals by thin fused salt films is treated in terms of oxide solubilities, electrochemical experimentation, and corrosion mechanisms. The chemistry of mixed sodium sulfate/vanadate melts, and the influence of vanadate on the solubilities of oxides, are presented.

Temperature limitations to the protection of carbon/carbon substrates by SiC conversion coatings are discussed. Specifically, the rate of vitreous silica film growth on SiC, the partial pressures of SiO and CO at the SiC/SiO₂ interface, and the conditions for active/passive volatilization of SiC are considered. The vapor pressures for volatile iridium oxides as a function of temperature and oxygen pressure are calculated.

Analyses and experimental verification of simultaneous chromizing/aluminizing coating of Ni-base alloys in a chloride-activated cementation pack are explained. These inwardly grown diffusion coatings promise improved resistance to thermal fatigue and to hot corrosion.

1. INTRODUCTION

An overview of the corrosion of materials at elevated temperatures including some mechanistic interpretation and methods for minimization of corrosion or coating of materials, represents an imposing task which obviously cannot be treated extensively in detail here. Therefore, I have chosen for consideration four different subtopics with which I have been involved, as an indication of the status, opportunities, and problems in high temperature corrosion. The areas discussed are:

1. Scale Growth on a Pure Metal by Cation/Vacancy Diffusion
2. Hot Corrosion of Materials
3. Protection of Carbon-Carbon Composites
4. Codeposition Diffusion Coatings by the Pack Cementation Method

2. SCALE GROWTH ON A PURE METAL BY CATION/VACANCY DIFFUSION

Ever since the earliest studies of oxidation, this subject has been one of interest and importance. To predict the parabolic scaling rate for a pure metal forming a dense, adherent one-phase scale, Wagner (1) needed only to assume that the scale interfaces were in local equilibrium with the contacting gas and metal phases. However a classic question for scale growth by cation/vacancy diffusion which has endured (until recently), is the exact mechanism for the annihilation of vacancies at the metal/scale interface. The relevant diffusional fluxes are indicated schematically in Fig. 1. Previously, the assertion has been made that vacancies arriving through the scale are annihilated by the climb of dislocations in the metal, or else by vacancy condensation at grain boundaries or at second phase boundaries (alloy) in the metal (2). Limited to these means, a perfect single crystal could not be oxidized unless it generated dislocations or other vacancy sinks. Likewise, a simple calculation shows that the dislocation density in an annealed metal is not adequate to support the vacancy annihilation required for scale growth.

Last year, Pieraggi and Rapp (3) suggested a novel mechanism for vacancy annihilation at the metal/scale interface which is consistent with the following known (TEM) characterization of the locality:

1. epitaxial metal/scale relations, leading to excellent contact/adherence, at the metal/scale interface,
2. local tensile stresses in the metal and compressive stresses in the scale at the interface
3. locally high dislocation densities in the metal and the scale near the interface.

Figure 2 shows a computer-drawn schematic illustration of the positions for metal atoms and cations in a dominant epitaxial arrangement for a particular (simple) orientation for the growth of NiO on Ni. Consistent with the 18% larger cation spacing in the oxide compared to the atom spacing in the metal, the equilibrium metal/scale interface is comprised of a two-dimensional grid of intrinsic, misfit edge dislocations of spacing s^0 in Fig. 3a corresponding to approximately two extra atomic planes in the metal for each 13 atom planes. As a means to annihilate vacancies while retaining epitaxy, Pieraggi and Rapp (3) proposed that a crossed pair of the interfacial misfit dislocations climb into the metal, while the residual misfit dislocation network increases its spacing to s' as shown in Fig. 3b. This readjustment introduces elastic tensile stresses in the metal and compression in the oxide at the interface. Continued oxidation and vacancy annihilation drives the dislocation loops deeper into the metal and activates the climb of other pairs of interface misfit dislocations, with an associated increase in interfacial stress. Upon reaching some critical stress, corresponding to a dislocation spacing of s' in Fig. 3c, one or both of two stress relaxation processes would be activated:

1. glide of edge dislocations in the oxide, or
2. dissociation of the dislocation loops in the metal to provide glissile partials which return by glide to the interface, and upon recombination, enter the misfit dislocation grid in the interface.

Figure 4 illustrates schematically in two dimensions the progressive operation of the interfacial misfit dislocations for the annihilation of vacancies. This proposed mechanism is consistent with the known characteristics of the metal/scale interface (listed earlier), and would provide the needed vacancy sinks even for the scaling of a perfect single crystal. Unfortunately, direct TEM evidence for the validity of this model would require interfacial lattice resolution in a heated stage, which is not yet practical.

3. HOT CORROSION OF MATERIALS

The corrosive degradation resulting from the condensation or impingement deposition of thin fused salt films on metallic hardware at elevated temperatures is known as "hot corrosion". Consistent with the early suggestions of Bornstein and DeCrescente (4,5) and Goebel et al. (6,7), high-temperature (Type 1) hot corrosion is thought to involve an acidic or basic fluxing of the protective oxide on a metal or alloy, and a reprecipitation of the oxide as non-protective particles in the salt film. As illustrated schematically in Fig. 5, Rapp and Goto (8) suggested a negative solubility gradient for the protective oxide in the fused salt film as a criterion for sustained hot corrosion. The development of solid-state reference electrodes permits the identification of local values for the oxygen activity and basicity (defined as $-\log a_{Na_2O}$) in fused Na_2SO_4 melts or related solutions, or even in fused salt films.

Recent measurements (9) have led to quantitative determinations of the solubilities of several oxides, and their dependencies on oxygen activity and melt basicity in fused Na_2SO_4 at 1200K, as shown in Fig. 6. The large separations in the solubility minima between the protective acidic oxides Cr_2O_3 and Al_2O_3 and the basic oxides for the metals Ni, Co and Fe point to a problem of synergistic dissolution for multiphase scales on high-temperature alloys. When the local salt basicity is found between the solubility minima for two oxides, the oxide ions released upon the acidic dissolution of the more basic oxide will serve as a reactant for the basic dissolution of the more acidic (protective) oxide. Thus, the rate of dissolution of each oxide is accelerated, as demonstrated recently by Hwang and Rapp (10). The threat of synergistic hot corrosion emphasizes the importance for the elimination of low stability oxides during the transient oxidation of alloys or coatings.

3.1 Reaction Trace During Hot Corrosion of Preoxidized Nickel

The two solid-state electrochemical probes have been attached to coupons of nickel which were then preoxidized and subsequently exposed to thin films of fused Na_2SO_4 or related (chromate or vanadate) solutions in a $SO_2/SO_3/O_2$ gas phase (11). The continuous indications of the average oxygen activity and basicity for the fused salt film can be plotted onto the Na-Ni-S-O phase stability at 1200K as shown in Fig. 7. For a 99% pure Ni coupon, after an initiation period of about 15 min., the oxygen activity of the salt film dropped suddenly into a regime of NiS (and Na_2S) stability, and the film basicity increased significantly. During a period of rapid hot corrosion, the local salt chemistry was found to remain on the basic side of the solubility minimum for NiO, as indicated by the dashed line in Fig. 7. After rapid corrosion for 10 hours had consumed the coupon, the reference electrodes showed that the salt film reached an equilibrium with the surrounding gaseous environment. Auxiliary SEM and EDAX measurements have shown that sulfides were indeed formed at the metal/scale interface when the salt film infiltrated the initial oxide scale to contact the metal. The observed shift in basicity upon substrate sulfidation is consistent with the model proposed by Goebel and Pettit (6).

The sustained basic dissolution/reprecipitation of NiO meets the negative solubility gradient criterion of Rapp and Goto (8). This first measurement of a "reaction trace" points to "cathodic overpolarization" as the primary problem in hot corrosion. In Fig. 8, the solubility plot for NiO (12) is embellished with schematic drawings of the solubility gradients expected for basic and acidic dissolution of NiO. Clearly, only basic dissolution of NiO provides the negative solubility gradient needed to sustain NiO precipitation in the salt film. Interestingly, the average salt film chemistry was dominated by the substrate interaction, and not a gas phase equilibration. When 99% pure Ni was provided with a much thicker initial oxide scale, exposure to the fused Na_2SO_4 salt film in the $\text{SO}_2/\text{SO}_3/\text{O}_2$ gas resulted in negligible corrosion, and as seen in Fig. 9, the salt film chemistry remained on the acidic side of the NiO solubility minimum. While the sulfidation of nickel was observed to initiate sustained hot corrosion by a basic salt film, a very basic salt composition was also found to support sustained hot corrosion of preoxidized nickel without the occurrence of Ni sulfidation. Thus, the negative solubility gradient is a more general criterion for sustained hot corrosion than is substrate sulfidation.

3.2 Sulfate/Vanadate Chemistry and Oxide Solubilities

Recently, Zhang and Rapp (13) measured and interpreted the solubilities of the oxides HfO_2 , CeO_2 , and Y_2O_3 in a sulfate/vanadate solution of $0.7\text{Na}_2\text{SO}_4/0.3\text{NaVO}_3$ at 1200K. These oxides may find application as components in thermal barrier oxide coatings for marine gas turbines exposed to the combustion products of vanadium-contaminated fuels. Figure 10 provides a comparison of the solubility of CeO_2 in pure Na_2SO_4 to that in the sulfate/vanadate solution. Obviously, the acidic solubility of CeO_2 in the mixed solution is much higher, leading to a shift in the solubility minimum to a higher value at a more basic condition. Because this increased acidic solubility is tied to the complexing of oxide ions by metavanadate ions to form orthovanadate ions, an equivalent increased solubility in metavanadate melts must be expected for all oxides. Hwang and Rapp (14) have analyzed the acid-base chemistry of sulfate/vanadate solutions in order to interpolate and extrapolate the limited solubility measurements. Figure 11 shows the calculated vanadate solute concentrations for an ideal sodium sulfate/vanadate solution as a function of basicity. By use of these values, the solubility of CeO_2 in any sulfate-rich, $\text{Na}_2\text{SO}_4\text{-Na}_x\text{VO}_y$ solution can be calculated, as plotted in Fig. 12, upon the assumption of a constant activity coefficient for the acidic $\text{Ce}(\text{VO}_3)_4$ solute. Thus, limited measurements of CeO_2 in the $0.7\text{Na}_2\text{SO}_4\text{-}0.3\text{NaVO}_3$ solution can be interpolated to predict the solubility for other sulfate/vanadate solutions. Likewise, upon the assumption of the same activity coefficient for the acidic solute of Cr_2O_3 in the sulfate/vanadate solution, as for the pure sulfate melt (where the only solubility measurements exist), the solubility of Cr_2O_3 in sulfate/vanadate solutions can be predicted, as shown in Fig. 13. Obviously, these assumptions about the solution thermodynamics should receive experimental testing. In any case, the presence of even a small amount of vanadate solute in sulfate salt films causes a significant increase in the acidic solubility of any oxide.

4. PROTECTION OF CARBON-CARBON COMPOSITES

4.1 Silicon Carbide Coatings

The exceptional strength of carbon-carbon composites at very high temperatures cannot satisfy potential applications unless coating systems are developed to prohibit the outward diffusion of carbon, the inward ingress of oxygen, and the rapid growth or excessive volatilization of the protective oxide scale (film). To date, Si-rich SiC conversion (diffusion) or CVD coatings have sufficed for the demonstration of coated C/C blades in dynamic tests for about 5 hrs. in a combustion product environment at about 1760 C (3200 F). Figure 14 shows an extrapolation of the parabolic rate constant data of Schlichting (15) for the growth of a protective vitreous silica film on SiC. For the stated conditions (5 hrs. at 1760 C), about 5 microns of SiC would be converted to SiO_2 . In the absence of other problems, including the doping of lower valent impurity cations which reduces the silica viscosity and increases oxygen permeability, Fig. 14 would present absolute minimal values for the thickness of an SiC coating to protect C/C.

However, another problem is likely to intercede before scale growth becomes excessive, namely, the generation of gases (bubbles) at the SiC/ SiO_2 interface, as is treated for 2000K (3141 F) by Fig. 15. The calculated isobars for the gases $\text{SiO}(\text{v})$ and $\text{CO}(\text{g})$ along the sloping line for SiC/ SiO_2 coexistence reveal several important facts (16). In equilibrium with carbon (three-phase equilibrium), the $\text{CO}(\text{g})$ partial pressure equals 34 atm, enough to percolate gas through, and damage, the vitreous SiO_2 layer. For the three-phase Si/SiC/ SiO_2 equilibrium, the vapor pressures for both $\text{SiO}(\text{v})$ and $\text{CO}(\text{g})$ approximate only one atmosphere. With the consideration that some overpressure

is required to initiate bubble formation, Fig. 15 is nominally consistent with the stated 3200 F limit for Si-rich SiC coatings on C/C composites. In fact, a boride compound is generally introduced into the carbon matrix to serve as a temporary "inhibitor" to reaction via oxygen penetration through minor flaws in the protective coating. The coated composite cannot withstand major flaws.

While the vaporization of silica at the outer interface in a highly oxidizing gas is not a limiting problem, SiC or SiO₂ can destructively volatilize in the absence of an adequate oxygen flux to maintain silica growth. Wagner (17) originally described the active/passive oxidation of liquid Si in He/O₂ gas mixtures, and Hinze and Graham (18) experimentally observed the active/passive oxidation of Si and SiC in Ar/O₂ gases. Because of slow diffusion-limited arrival of oxygen to a substrate in an inert gas containing only a small oxygen content, the loss of oxygen by SiO evaporation from SiO₂ may not be supplied by an adequate arriving oxygen flux, leading to a progressive reduction in the local oxygen activity at the silica/gas interface (see Fig. 15). In the absence of the protective silica film, the rate of oxidation of an active SiC substrate becomes equal to the rate of arrival of oxygen—a degradation rate which can be orders of magnitude faster than passive silica growth at higher local oxygen activities.

Recently, Narushima et al. (19) experimentally determined the critical oxygen pressures in Ar/O₂ gas mixtures to passivate pure dense CVD SiC at quite high temperatures (1841-1923K). Their results are presented in Fig. 16. (Oxygen pressures are expressed in Pascals = 10⁻⁵ atm). The measured values for the critical transition oxygen pressure are somewhat lower than previous measurements for less pure, less dense, hot-pressed SiC, and the magnitudes and activation energy correspond best to a condition of forming SiO₂ on Si-saturated SiC, again the condition for minimum total vapor pressure of Fig. 15. According to the results of Narushima et al. (19), only a serious interruption in the fuel combustion process would lead to active SiC volatilization at the highest service temperatures.

4.2 Iridium Barrier Coating

As an alternative, future coating for carbon/carbon composites, one that avoids the vitreous silica protective film and its associated problems, a coating based on metallic iridium or an iridium alloy has been suggested. In that case, a refractory metal carbide bond coat would separate the C/C substrate from the iridium, which is an excellent barrier to both carbon and oxygen. On the other hand, the problem with Ir is the relatively high partial pressures of its volatile oxides, particularly IrO₂ (v).

Figure 17 is a plot of the maximum possible Ir recession rate resulting from the volatilization for the sum of Ir (v), IrO (v) and IrO₂ (v) as a function of temperature and oxygen partial pressure (20). To exceed (or even approach) the 3200 F temperature, clearly a thermal-shock resistant oxide overlay coating must be used to protect the Ir both from erosion and from oxidation/evaporation. Such an oxide overlay coating will need to possess a controlled, directional porosity to withstand thermal shock, so its function as a barrier to volatilization is only realized by the maintenance of partial pressure gradients for oxygen and for IrO₂ (v) in the continuous pores of the PVD overcoat oxide. Such a layered composite coating for the carbon/carbon substrate has not yet been demonstrated.

5. CODEPOSITION OF CHROMIUM AND ALUMINUM BY THE PACK CEMENTATION METHOD

The coatings for turbine components deposited by physical vapor deposition (evaporation, sputtering, plasma spray) are both expensive and subject to mechanical damage by thermal fatigue. On the other hand, diffusion coatings deposited by a halide-activated cementation pack method are less expensive, exhibit good adherence, but suffer from limited control of composition. In particular, generally only aluminizing is practiced for Ni-base alloys, but chromium is known as a necessary coating component, especially for hot corrosion resistance. Therefore, the simultaneous chromizing/aluminizing diffusion coating of Ni-base substrates is required to provide improved inexpensive coatings. The composition range for Ni-Cr-Al alloys which results in slow growing alumina scales is well known (21-23).

Thermodynamic calculations (24,25) show that the volatile halides (fluorides, chlorides) of aluminum are much more stable than the corresponding chromium halide vapors. Therefore, a halide-activated pack containing pure Cr and pure Al can only aluminize. Likewise, any fluoride-activated pack can only aluminize. However, because Cr-rich Cr-Al solid solutions exhibit significant negative deviations from ideal thermodynamic behavior (26) packs comprised of specific combinations of Cr-Al masteralloy powder and certain chloride activator salts provide comparable partial pressures for the volatile chlorides of Cr and Al in the pack. Figure 18 presents a computer-assisted evaluation of the equilibrium partial pressures of volatile species in a pack activated by NaCl salt at 1273K. A Cr-Al masteralloy composition of about 10

wt% Al provides the proper ratio of P_{CrCl_2} to P_{AlCl} such that both Cr and Al can be codeposited into a Ni-base (or Fe-base) alloy. Similar, more complex, results have been calculated for less stable chloride salts, including $CrCl_2$, $FeCl_2$, NH_4Cl , etc. (25). For a less stable chloride salt, the proper masteralloy composition for Cr/Al codeposition is moved to higher Al contents. As is obvious from Fig. 18, the proper pack conditions are quite sensitive to masteralloy composition and cannot be deduced by trial and error.

In experimental tests of the theory, very good success has been achieved in chromizing/aluminizing low-alloy steels (27), ferritic Fe-Cr steels, and austenitic steels (28). In certain packs, a small content of a reactive element (Y, Ti, Zr) can be introduced at the same time. For a few Ni-base superalloys, chromizing/aluminizing has resulted in inwardly grown diffusion coatings with promising microstructures and compositions. However, further detailed characterization and testing for hot corrosion and cyclic oxidation resistance is required. This research is continuing.

6. ACKNOWLEDGEMENTS

The research on hot corrosion is sponsored by the Metallurgy Program of the Division of Materials Research, National Science Foundation under Grant DMR 8620311. The coating research is sponsored by The Office of Naval Research (Contract N00014-87-K-0030) and by Martin-Marietta, ORNL, contract 19X-SB154C.

REFERENCES

1. C. Wagner, Z. Phys. Chem., B21, (1933) 25.
2. R.A. Rapp, Metall. Trans., 15A, (1984) 765.
3. B. Pieraggi and R.A. Rapp, Acta Met., 36, (1988) 1281.
4. N.S. Bornstein and M.A. DeCrescente, Trans. AIME, 245, (1969) 1947.
5. N.S. Bornstein and M.A. DeCrescente, Met. Trans., 2, (1971) 2875.
6. J.A. Goebel and F.S. Pettit, Metall. Trans., 1, (1970) 1943.
7. J.A. Goebel, F.S. Pettit, and G.W. Goward, Metall. Trans., 4, (1973) 261.
8. R.A. Rapp and K.S. Goto, "The Hot Corrosion of Metals by Molten Salts", in Molten Salts, J. Braunstein and J.R. Selman Eds., Electrochem. Soc., Pennington, N.J., (1981) 81.
9. R.A. Rapp, Corrosion, 42, (1986) 568.
10. Y.S. Hwang and R.A. Rapp, "Synergistic Dissolution of Oxides in Molten Salts", Proceedings of ASM-TMS workshop on Oxidation and High-Temperature Intermetallics, Eds. T. Grobstein, J. Doychak, and G.M. Michel, TMS-AIME Warrendale, PA (1988).
11. N. Otsuka and R.A. Rapp, submitted for publication to J. Electrochem. Soc.
12. D. Gupta and R.A. Rapp, J. Electrochem. Soc., 127 (1980) 2194 and 2656.
13. Y.S. Zhang and R.A. Rapp, Corrosion, 42, (1986) 348.
14. Y.S. Hwang and R.A. Rapp, "Thermochemistry and Solubilities of Oxides in Sodium Sulfate-Vanadate Solutions," accepted for publication in Corrosion.
15. J. Schlichting, Ber. Dt. Keram. Ges., 56, (1979) 196 and 256.
16. R.A. Rapp and G.R. St.Pierre, "New Options for the Protection of Carbon-Carbon Composites," Proceedings of High Temperature Composites Symposium, Dayton, OH, Oct. (1985).
17. C. Wagner, J. Appl. Phys., 29, (1958) 1295.
18. J.W. Hinze and H.C. Graham, J. Electrochem. Soc., 127, (1976) 1066.
19. T. Narushima, T. Goto and T. Hirai, "Active to Passive Transition in the Oxidation of CVD-SiC," Proceedings of MRS Intern. Sympos. on Adv. Materials, Tokyo, June 1988.
20. G.R. Holcomb, R.A. Rapp, and G.R. St.Pierre, unpublished research, The Ohio State University.
21. C.S. Giggins and F.S. Pettit, J. Electrochem. Soc., 118, (1971) 1782.
22. G.R. Wallwork and A.Z. Hed, Oxid. Metals, 3, (1971) 171.

23. C.A. Barrett and C.E. Lowell, *Oxid. Metals*, 11, (1977) 199.
24. S.C. Kung and R.A. Rapp, "Analyses of the Gaseous Species in Halide-Activated Cementation Coating Packs", accepted for publication in *Oxid. Metals*.
25. V.A. Ravi, P. Choquet, and R.A. Rapp, "Thermodynamics of Chromizing-Aluminizing in Halide-Activated Cementation Packs", *Proceedings of MRS Symposium on Advanced Materials*, Tokyo, 1988.
26. W. Johnson, K. Komarek and E. Miller, *Trans. Met. Soc. AIME*, 242 (1968) 1685.
27. R.A. Rapp, D. Wang, and T. Weisert, "Simultaneous Chromizing-Aluminizing of Iron and Iron-Base Alloys by Pack Cementation", *High Temperature Coatings*, M. Khobaib and R.C. Krutenat, Eds., TMS, Warrendale, PA (1987) 131.
28. D.M. Miller, S.C. Kung, S.C. Scarberry, and R.A. Rapp, *Oxid. Metals* 29, (1988) 239.

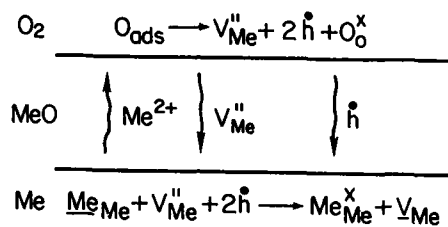


Fig. 1: General schematic illustration for growth of scale on pure metal by cation-vacancy diffusion.

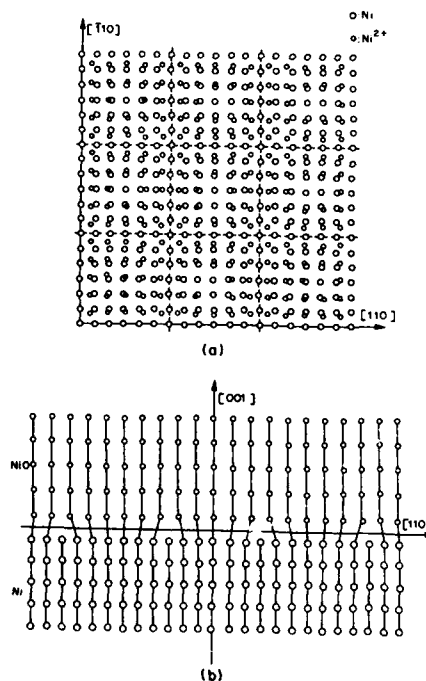


Fig. 2: In-plane (a) and frontal (b) views of cation and metal atom positions for parallel epitaxial interfacial arrangement of NiO scale on $\{100\}$ Ni.

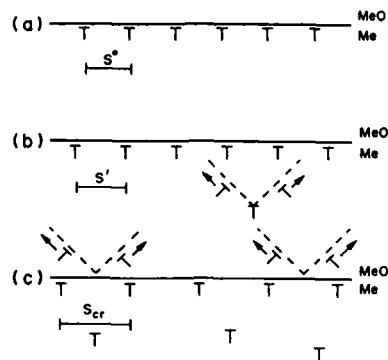


Fig. 3: Schematic illustration of interfacial dislocation dynamics in vacancy annihilation.

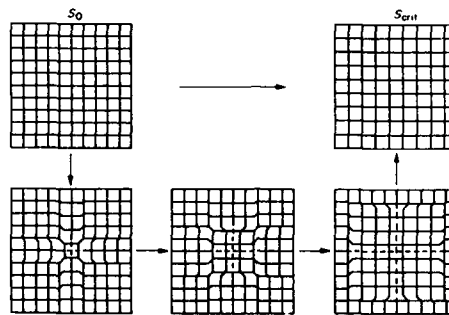


Fig. 4: Schematic illustration of interfacial dislocation dynamics in vacancy annihilation. Dashed lines represent dislocation loops in the metal beneath the interface.

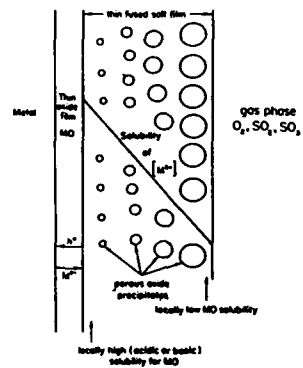


Fig. 5: Dissolution-precipitation of MO oxide driven by a negative solubility gradient in a fused salt film.

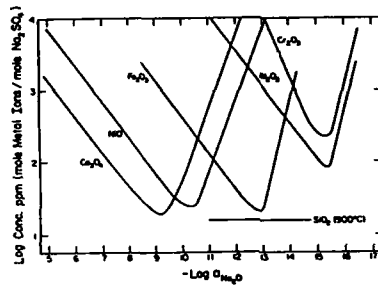


Fig. 6: Experimentally established oxide solubilities in fused Na_2SO_4 at 1200K and 1 atm O_2 .

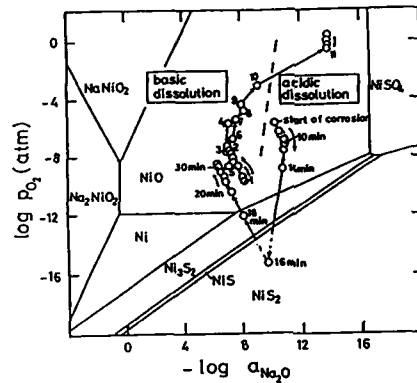


Fig. 7: Trace of basicity and oxygen activity measured for preoxidized 99% Ni covered with a Na_2SO_4 film at 900C in 0.1% SO_2 - O_2 gas atmosphere (preoxidized at 900C for 4 hours in O_2). Numbers designate reaction time in hours except as indicated, severe corrosion.

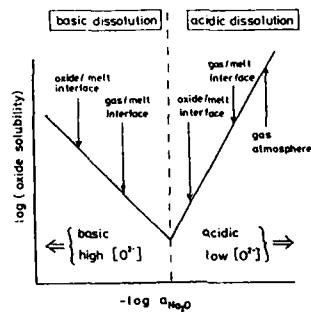


Fig. 8: Cases of self-sustaining hot corrosion for a pure Ni with a thin Na_2SO_4 film in a SO_2 - O_2 gas atmosphere (11).

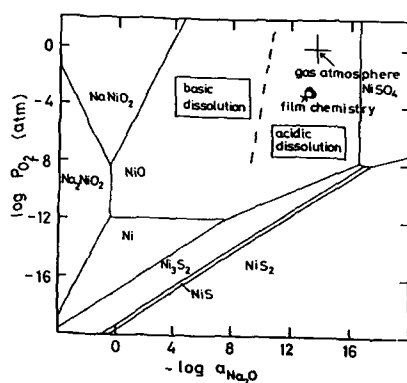


Fig. 9: Trace of basicity and oxygen activity measured for a preoxidized 99% Ni covered with a Na_2SO_4 film at 900C in 0.1% SO_2 - O_2 gas atmosphere (preoxidized at 1000C for 5 hours in air). Slight corrosion. Coupon thickness: 2mm (11).

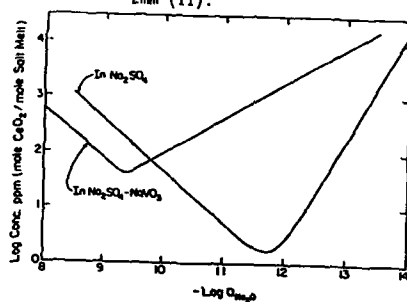


Fig. 10: Comparison of solubilities for CeO_2 in pure fused Na_2SO_4 and in 0.7 Na_2SO_4 -0.3 NaVO_3 at 900C in 1 atm O_2 .

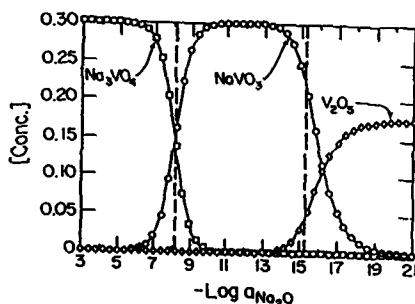


Fig. 11: Equilibrium concentrations of Na_3VO_4 , NaVO_3 , and V_2O_5 in 0.7 Na_2SO_4 -0.3 NaVO_3 in 1 atm O_2 at 900C.

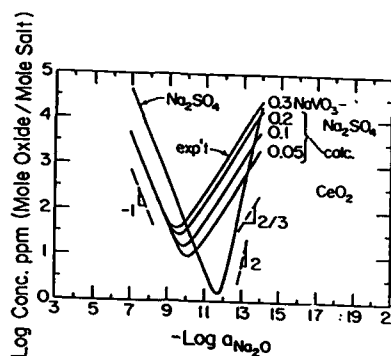


Fig. 12: Solubilities of CeO_2 in Na_2SO_4 - $x\text{NaVO}_3$ solutions at 900C in 1 atm O_2 ($x=0.3, 0.2, 0.1$ and 0.05).

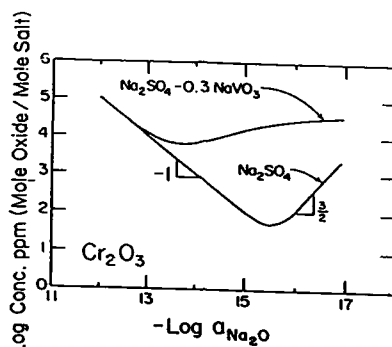


Fig. 13: Measured solubility of Cr_2O_3 in pure Na_2SO_4 and calculated solubility for $0.7\text{Na}_2\text{SO}_4$ - 0.3NaVO_3 solution at 900C in 1 atm O_2 .

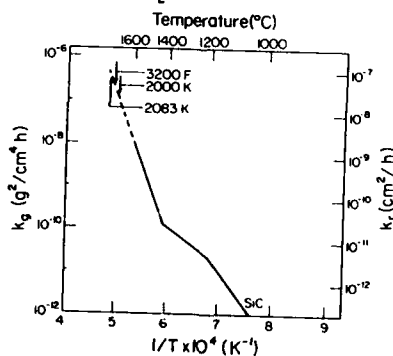


Fig. 14: Temperature dependence of the oxidation rate of "pure SiC" in air (from compilation of data by Schlichting⁶). For $T < 1400^\circ\text{C}$, partial cristobalite formation; $T > 1400^\circ\text{C}$, decreased viscosity for vitreous SiO_2 .

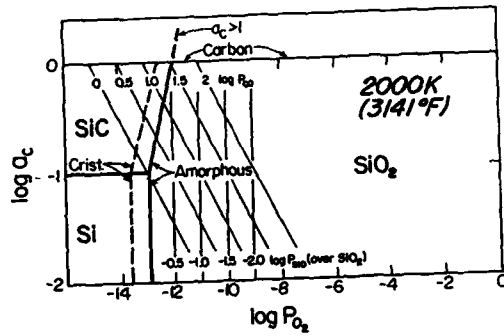


Fig. 15: Silicon-Carbon-Oxygen Phase stability diagram with superimposed isobars for 2000K (3141 F) (16).

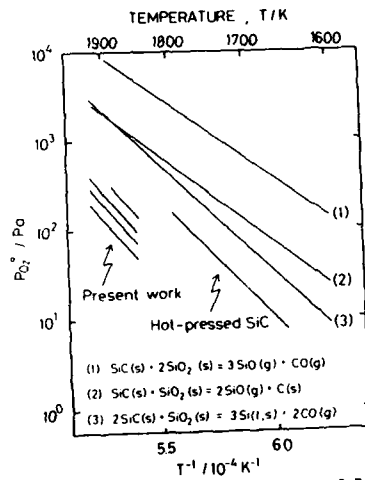


Fig. 16: Temperature dependence of $P_{O_2}^*$ for CVD-SiC active oxidation compared with that for hot-pressed SiC and thermodynamic predictions (19).

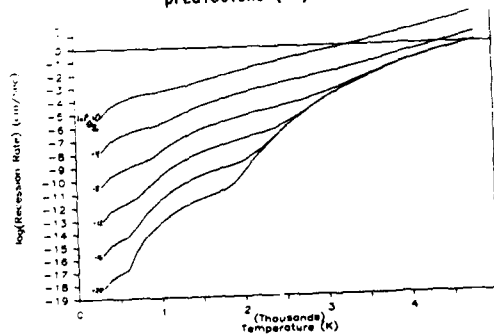


Fig. 17: Maximum possible recession rate for pure Iridium resulting from reactive vaporization (20).

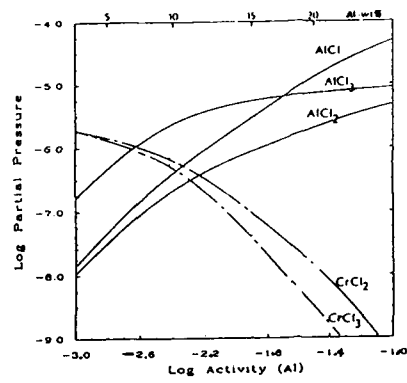


Fig. 18: Equilibrium partial pressures of gaseous species in a NaCl-activated pack as a function of Al activity in the masteralloy (Ar, 1273K), (25).

DEVELOPMENTS IN TEST PROCEDURES FOR HOT-SALT CORROSION OF SUPERALLOYS

S R J SAUNDERS AND T B GIBBONS

DIVISION OF MATERIALS APPLICATIONS

NATIONAL PHYSICAL LABORATORY
Teddington, TW11 0LW, UK

SUMMARY

It is important that the test procedures used to assess the resistance of superalloys to hot salt corrosion should reliably simulate conditions expected in service and the results should be capable of interpretation to provide a prediction of likely long-term behaviour. Past experience has shown that the many test methods available have frequently given conflicting measures of alloy performance and intercomparability between test procedures has frequently been poor. As a result of extensive research in Europe, much of which has been carried out within the COST Project, there is now a better understanding of the critical factors that must be controlled to provide a reliable and reproducible procedure and which gives corrosive attack similar to that encountered in service. In particular, contaminant flux rate has been identified as a key parameter. These activities are briefly reviewed and progress towards the definition of a unified test procedure is outlined. Plans for a new international intercomparison, organised under the auspices of VAMAS, to probe the validity of the procedure are described.

INTRODUCTION

In assessing materials performance it is important to measure appropriate properties in conditions relevant to the expected service environment. Considerable progress has been made in many areas of materials science and engineering in moving away from simple ranking tests to more sophisticated measurement procedures which give data of value to engineers concerned with design, maintenance etc.

There are many test procedures available for assessing the hot-salt corrosion resistance of superalloys for service in aero, marine, or industrial applications and in the main these are simple ranking tests. However, past experience has shown that when various test methods are used to rank alloys in terms of resistance to hot-salt corrosion resistance there is frequently some conflict between the results obtained. Tests that are available have generally been developed on an empirical basis and may have been recommended by a material supplier with the performance of a particular alloy in mind or by a user for a specific industrial application. On this basis therefore consistency of ranking would not necessarily be expected when individual test methods are used.

Recently there have been some significant developments in the general approach to materials testing for corrosion resistance and as a result the need for better and more harmonised procedures for evaluating hot salt corrosion in gas turbine materials has become evident. In the first place there is a greater tendency, certainly within Europe, for research on high temperature materials to be carried out in a collaborative fashion. Clearly agreed test procedures which are known to give reliable results are essential to allow test programmes to be shared and data exchanged. Also designers are becoming more aware of the need to allow for corrosion effects in component design and particularly in situations where interactions between stress and the corrosion medium can be expected to limit life in service.

In view of these requirements some effort has been made to develop an improved understanding of the mechanisms involved in hot-salt corrosion attack, so that test procedures can be defined and critical parameters controlled in the context of the corrosion mechanism. In this paper the main features of the various test procedures are briefly reviewed, the results of previous intercomparisons are considered and the status of a new intercomparison to test a draft test procedure developed within the VAMAS programme is outlined.

LABORATORY TESTING PROCEDURES

The techniques available for evaluating resistance to hot-salt corrosion in the laboratory can be grouped in three main categories viz

- (i) crucible tests
- (ii) furnace tests
- (iii) combustion rig tests

The main features of each and the typical corrosion morphologies obtained will be

described in this section.

(i) Crucible tests

This type of procedure involves immersion of specimens at an appropriate temperature in a molten salt based on sodium sulphate, but with additions of other alkali metal sulphates to form a low melting point eutectic mixture. The additions are necessary because test temperatures are usually lower than the melting point of sodium sulphate. In order to control the sulphidising potential (pS_2) in the environment to that characteristic of the combustion gas generated in service it is desirable to bubble air or oxygen containing SO_2/SO_3 through the melt. The choice of the correct pS_2 ensures the stability of the sulphate produced during the corrosion process and is particularly important for Type II corrosion which depends on the formation of, for example, a $CoSO_4 \cdot Na_2SO_4$ eutectic which is stabilised by a relatively high $p(SO_2)$. Fig.1 shows an example of the type of attack observed on IN738LC after exposure at 900 °C to a $(K_{0.1}Na_{0.9})_2SO_4$ salt mixture.

A major advantage of this type of test is that the rate of corrosion can be monitored continuously by measuring the corrosion current and no other test technique has this capability. Also, the use of imposed potentials will accelerate the corrosion reaction^{1,2} and it is claimed that in these conditions, alloy rankings correlate well with service experience.

Frequently however corrosion product morphologies are different from those observed on components in service suggesting that the crucible test involves corrosion processes which do not occur in practice. Factors which would be expected to influence the corrosion mechanism include initial salt composition and also the changes which occur as a result of dissolution of corrosion products, eg chromia. Thus the extent to which saturation and renewal of salt takes place is crucially important in the corrosion process. The move to higher test temperatures consistent with the application of advanced materials such as ceramics or intermetallics would eliminate the need for additives in the initial melt but reduced levels of condensation may limit the degree of corrosion attack.

(ii) Furnace tests

The Dean test³ which involves both evaporation and subsequent deposition of sodium sulphate is probably the most appropriate furnace test and the atmosphere can be controlled to give a pS_2 typical of the engine environment. Other types of furnace test involve pre-deposition of sodium sulphate and periodic renewal, the salt-shower test⁴, or the use of a synthetic ash simulating that found on components in industrial engines⁵. Fig.2 shows the corrosion morphology produced on IN738 after exposure in a Dean test at 850 °C.

Furnace tests do not require complex equipment and if the deposition conditions and sulphidising potential of the environment are carefully controlled realistic assessment of materials performance can be obtained. The major disadvantage is that it is difficult to obtain deposition rates that simulate real engine conditions.

(iii) Burner Rigs

Most of the limitations of the crucible and furnace tests can be overcome with burner rigs and, in particular, salt chemistry and deposition rate can be specified to simulate most engine operating conditions. Also, it is relatively easy to impose an erosion component on the degradation process and erosion is believed to be a significant factor in some modes of engine operation. The simplest form of burner rig is shown schematically in Fig.3 and equipment of this type can be readily operated in the laboratory. However the ultimate burner rig is the gas turbine engine itself and the more complex systems involving high velocity gases and high pressures approach this ultimate configuration. The high velocity rigs are, of course, most suited to corrosion-erosion testing. In general rigs are expensive to operate, are suited, in the main, to short term exposures only and corrosion information cannot readily be obtained during the test run.

INTERCOMPARISON OF TEST PROCEDURES

The various methods available for assessment of hot-salt corrosion resistance frequently give conflicting results and there have been several attempts to compare test procedures to provide a basis for comparison of data from different sources.

In 1970 the results of burner rig testing were compared for six different alloys in a programme carried out by ASTM. The findings are summarised in Fig.4 for U500 and IN738 and although the average rates of attack were similar for both alloys there was a considerable amount of variability especially for U500. Also the laboratories showing the greatest rates of attack for U500 did not show a similar result for IN738. A similar exercise was carried out in 1978 as part of the COST50 programme, the European Collaborative activity on gas turbine materials, and the results, for various burner rig tests are shown in Table 1. Here it is evident that rankings can be vastly different, depending on test conditions and the results for IN597 (Nimonic 101) clearly illustrated the problem.

DEPOSITION

In view of the variability in data obtained from test facilities for hot-salt corrosion resistance some effort has been devoted at various centres in Europe to developing a more detailed understanding of the mechanisms involved in order to provide an improved basis for test-method development. A key issue was the rate at which Na_2SO_4 deposited on specimens in rig environments and deposition rates have been measured for typical operating conditions.

The results of work at NPL and at SNECMA are summarised in Figs.5 and 6 and it can be seen that deposition rate increased with decreasing temperature and with increasing sodium contamination consistent with simple dew point considerations. A high velocity burner rig at CERL was used specifically to study deposition and a linear rate of deposition of Na_2SO_4 was observed over a 25 h period at 690-890 °C which was independent of the form in which Na was added and of the target temperature between 790 °C and 890 °C but was 30% greater at 690 °C. Deposition was directly proportional to Na content of the fuel up to ~ 20 ppm by weight and was not affected by the presence of 3 wt ppm of Mg nor by an order of magnitude increase in carbon burden due to incomplete combustion.

It was evident from this work that the rate of deposition was affected by the mass flux of sodium in the combustion gas and to a lesser extent by the temperature but the nature of the contaminant had little effect. This information along with other data on the performance of burner rigs⁶ suggests that deposition rates were probably controlled by mass flux of Na_2SO_4 through the burner rig and by the adhesive qualities of the deposit. Deposition rate is shown as a function of total mass flux in Fig.7 for several burner rig facilities and it is evident that for the range of mass flux considered, there was a close to linear relationship.

Thus it appears that mass flux of contaminant is a crucial factor in controlling deposition and hence corrosion behaviour and this parameter may provide a unifying basis for intercomparison of corrosion data. Hancock⁷ reached a similar conclusion and also pointed out that control of contaminant flux was one of the key parameters in achieving realistic simulations of engine service in laboratory tests, although the final link to deposition rates was not considered in his analysis. Values of contaminant flux rate for various engines were quoted, in the range 0.27 to 13 mg $\text{cm}^{-2}\text{h}^{-1}$, which were broadly consistent with those obtained for typical burner rigs thereby confirming the relevance of rig testing.

SPECIMEN EVALUATION

The nature of corrosion processes is such that it is not uncommon to find a large variation in the behaviour of samples and indeed from area to area on the same sample, and it is clear that this difficulty has confused the attempts to compare the behaviour of materials on the basis of test results. Thus, in recommending improved test procedures an equally important consideration must be to include in that recommendation some guidance on the method of evaluating the results.

Nicholls and Hancock⁸ have proposed a statistical approach which is designed to deal with variability in metal or coating loss typically encountered in corrosion testing. The approach has been illustrated, for the case of coated materials, by Saunders and Nicholls⁹ who showed that by using a cumulative distribution plot the probability of a given coating loss could be calculated. Figure 8 shows the results of that analysis. This procedure can be taken one step further by the use of extreme value statistics in which only the maximum values of coating loss are considered. This will give a distribution skewed to the right and if represented on probability paper a curve will result. This model has a cumulative distribution F_{imax} given by:

$$F_{\text{imax}} = (x_e, \mu_e, \sigma_e) \\ = \exp - \exp \left(- \frac{x_e - \mu_e}{\sigma_e} \right)$$

where μ_e and σ_e are the extreme value location parameter and standard deviation, respectively. Figure 9 represents the probability of maximum corrosion found on a coated sample where the deepest penetration actually observed was 99 μm but a value of 114 μm is calculated using the extreme value approach outlined above. This method of data analysis is particularly appropriate since a component lifetime is usually controlled by a worst-case scenario.

NEW INTERNATIONAL INTERCOMPARISON

Underlying Principles

It is generally accepted that dynamic burner rigs represent the best available test procedure for assessing hot-salt corrosion resistance in superalloys but comparison of results from different sources is difficult due to variations in rig design and to a lack of a standard procedure. A further difficulty arises through inconsistencies in measuring and reporting corrosion data. Accordingly an intercomparison programme, involving burner rig facilities in the USA, Europe and Japan has been initiated as part of the VAMAS (Versailles Agreement on Advanced Materials and Standards), Project.

In the first phase of this exercise the major operators of burner rigs have been surveyed to determine the details of the operating conditions being used and the dimensions of the working chamber. On this basis a set of recommended test parameters has been derived and guidelines for operation of burner rigs have been produced. The purpose of the intercomparison which forms the second phase of the programme is to probe the validity of the recommended test procedure and to assess the extent to which a similar degree of corrosion attack will be achieved for a harmonised set of test conditions. The concept of the contaminant flux rate is seen as the critical unifying parameter providing a basis for the intercomparison of data.

Test conditions and participants

The materials to be used will be IN738LC and Rene 80 and each will be assessed in the uncoated and coated condition. For IN738LC the coating will be the platinum aluminide RT22 and ATD2B (Co, 21Cr, 10Al, 0.3V) will be used on Rene 80. Tests will be carried out at 700 and 900 °C to examine both Type II and Type I corrosion attack and durations of 500 h with temperature cycling to room temperature at ten-hourly intervals are recommended. Continuous additions of Na_2SO_4 salt will be made to the combustion environment to give a flux of $13 \text{ mg cm}^{-2} \text{ h}^{-1}$ equivalent to a sodium flux of $4 \text{ mg cm}^{-2} \text{ h}^{-1}$ in the combustion gas, assuming no deposition within the combustor.

An important feature of the procedure is an assessment of deposition rate and deposit chemistry and platinum or alumina pins will be exposed in the test environment to enable the deposit chemistry to be determined.

Full details of the test conditions are given in the Guideline Document⁹.

Assessment of corrosion attack

A key feature of the intercomparison will be the statistical analysis of the degree of corrosion attack along the lines discussed earlier. Specimens will be examined and weighed at each shut-down period and, on completion of the exposure, one sample will be used to obtain a full analysis of corrosion product chemistry. The remaining samples will be sectioned and examined for section loss at three points along the length with twenty-four radial measurements being made on each section. The measurements will indicate:

- loss of section
- general internal attack
- grain boundary attack
- position and depth of maximum attack
- thickness of coating remaining (coated samples)

It is considered that an accuracy of $\pm 5 \text{ } \mu\text{m}$ will be required bearing in mind the errors involved in measurement systems and in preparation but modern measuring equipment can achieve repeatability of $\pm 2 \text{ } \mu\text{m}$.

These measurements will then be used in a full statistical analysis to give comparable assessments for each burner rig system.

Output

The VAMAS Guideline Document will be modified as necessary in the light of the results of the intercomparison and the revised document will serve as a basis for a Code of Practice for hot-salt corrosion testing. Also testpins remaining after the programme is complete will be available as reference specimens for calibration of test conditions in burner rigs and other test facilities.

CONCLUSION

The correlation between contaminant flux rate and deposition has provided the basis for rationalising test procedures for assessing the hot-salt corrosion resistance of superalloys. This advance along with improvements in the methods of evaluation of corrosion attack will result in a more quantitative approach to the assessment of alloy behaviour and more valid design data.

REFERENCES

1. D A Shores, Corrosion, 12(1975) 434.
2. A Rahmel, Werkstoff Korros, 28 (1979) 299.
3. A V Dean, NGTE Rep, January 1964, Royal Aircraft Establishment, Pyestock, Hants, UK.
4. S W K Shaw, M S Starkey and M T Cunningham, COST50 project, Final Report, Inco Europe Ltd, March 1979.

5. C H Just, P Huber and R Bauer, Proc. 13th Int. Congr. on Combustion (CIMAC), Paris, 1979 GT 34.
6. S R J Saunders and J R Nicholls, Thin Solid Films, 119, (1984) 247.
7. P Hancock, Corros, Sci 22 (1982) 51 and 4th US-UK Navy Conf. Gas Turbine Materials in Marine Environments, Annapolis 1979, Naval Sea Systems Command, Washington.
8. J R Nicholls and P Hancock, in R. A. Rapp (ed) High Temperature Corrosion, NACE 6, National Association of Corrosion Engineers, Houston, Tx, 1983, p 198.
9. Guidelines for Hot-Salt Corrosion Burner Rig Tests: VAMAS, NPL 1988.

**TABLE 1 Comparison of Relative Corrosion Resistance
of Four Alloys in Various Burner Rigs**

Alloy	Corrosion Resistance*				
	NPL Low-velocity rig 850 °C 0.16% S + 500ppm seawater		SNECMA Low-velocity rig 850 °C		SULZER High-velocity rig 850 °C 0.4% S 5ppm Na 5ppm V
	200 h data	1400 h data	0.25% S only	0.25% S + 5ppm NaCl	
IN597	2	4	3	1	1
IN738LC	1	2	2	2	2
IN713LC	3	1	4	3	3
IN100	4	3	1	4	ND

*1 = best
ND = not determined

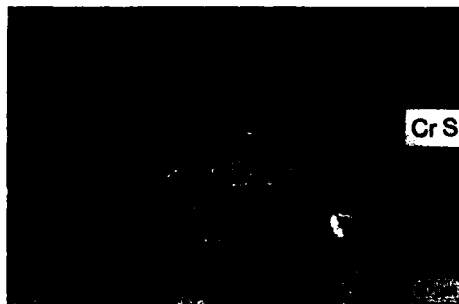


Fig 1: Type I corrosion morphology
IN738LC after 450h in
(Na_{0.9}K_{0.1})₂SO₄ melt;
electrolytic etch.



Fig 2: Type I corrosion morphology
in IN738LC after 800h at
900°C in CERL Dean Test;
etched.

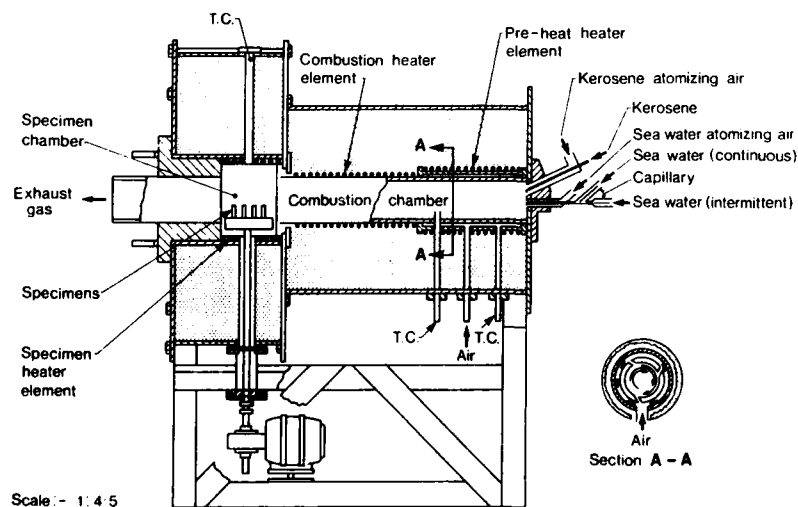


Fig 3: Schematic cross-section of simple burner rig.

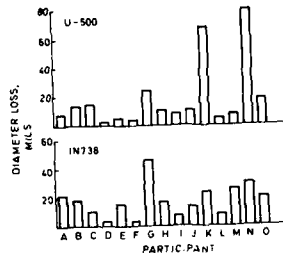


Fig 4: Metal loss results from ASTM intercomparison (a) U500; (b) IN738.

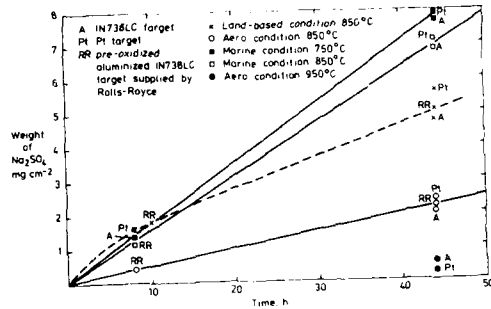


Fig 5: Na_2SO_4 deposition as a function of time for various conditions of operation of NPL burner rig.

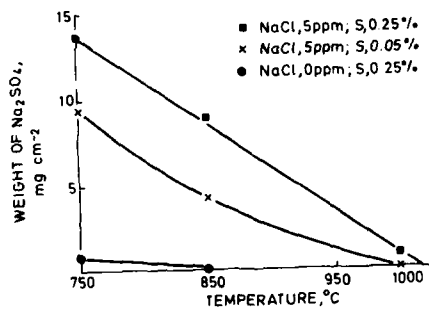


Fig 6: Na_2SO_4 deposition after 500h in SNECMA burner rig as function of temperature for various contaminant conditions.

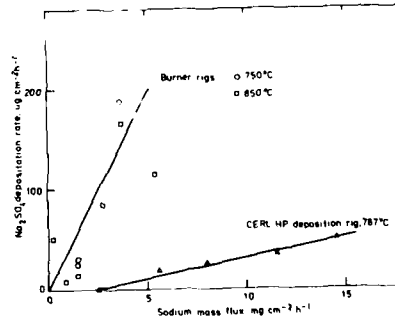


Fig 7: Na_2SO_4 deposition rate as a function of sodium mass flux for various burner rigs.

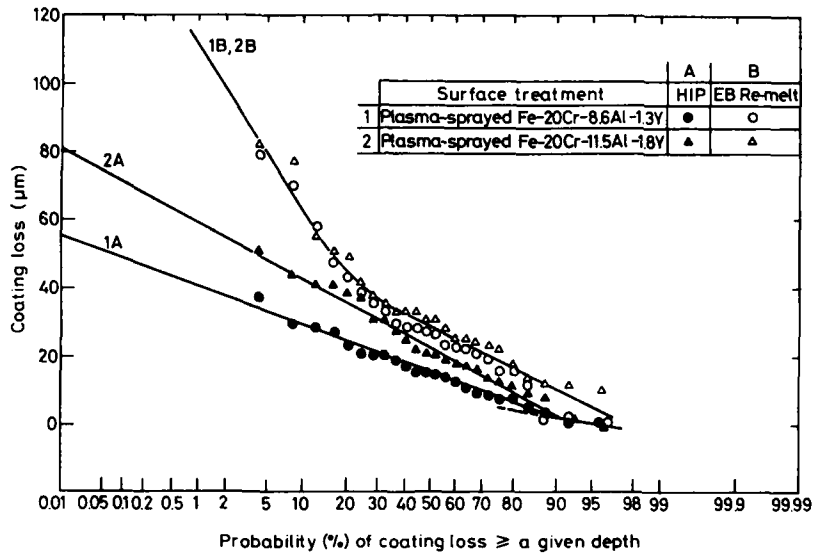


Fig 8: A cumulative distribution plot of the effect of surface processing on the corrosion of two Fe-Cr-Al-Y coatings; 308h at 900°C.

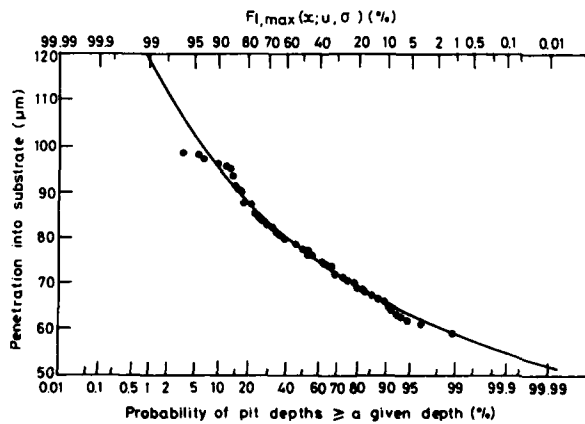


Fig 9: Probability plot of corrosion on an area of maximum attack from a coated MAR M509 component after 4804h in service: - extreme value statistics ($\mu_c = 73.3 \mu\text{m}$, $\sigma_c = 8.9 \mu\text{m}$, type 1 model of maxima): . data from a low magnification micrograph.

THE EFFECTS OF A COMPRESSOR REBUILD ON GAS TURBINE ENGINE PERFORMANCE: FINAL RESULTS

J.D. MacLeod
Research Officer
National Research Council
Montreal Rd, Building M-7
Ottawa, Canada, K1A 0R6

Major J.C.G. Laflamme
421 Tactical Fighter Squadron
Canadian Forces Base
Baden-Soellingen
Federal Republic Germany

SUMMARY

The Canadian Department of National Defence, in conjunction with the Engine Laboratory of the National Research Council Canada (NRCC), initiated a project for the evaluation of gas path coatings on the Allison T56 engine. The objective of this work was to evaluate blade coatings in terms of engine performance effects and material durability. The project included a study of the influence of rebuilding the compressor on performance, since dismantling and rebuilding was required for the coating process.

This paper describes the compressor rebuild study, including the overall objectives, the test set-up, the performance effects, and the uncertainty of the measured results. The impact of this work on the coatings project is also documented. This paper is an updated version of a paper (Reference 1) presented at the 71st AGARD Propulsion and Energetics Panel Symposium on Engine Condition Monitoring - Technology and Experience.

1.0 BACKGROUND

In 1983, the Canadian Department of National Defence expressed serious concerns over the rapidly escalating cost of operation and maintenance of aircraft gas turbine engines. The components of major concern were compressor and turbine blades and vanes. The increasing rate of rejection of these items during overhaul prompted a reassessment of the time between overhaul periods for certain engine types.

The blades and vanes of gas turbine engines are susceptible to deterioration as a result of erosion and corrosion. The deterioration (increased surface roughness, loss of material, and alteration of aerodynamic profile) manifests itself in terms of reduced stall margin and lower performance, characterized by poorer fuel economy and increased operating temperatures. The T56 engines used in the C130 Hercules and the CP140 Aurora aircraft have proven susceptible to this type of deterioration.

Recently, advances have been made in the state of the art in blade coating technologies. In addition to offering erosion and corrosion protection, these new "super smooth" coatings are claimed, by their manufacturers, to offer significant aerodynamic performance improvements. Modern blade coatings have not previously been qualified on T56 engines. Since smoothness effects are a function of blade Reynolds number, which is dependent on engine size and speed, claims based on evaluations on other engines were not satisfactory. Thus, there was a requirement to undertake an analytical and experimental engine testing program to identify and quantify the effects of coating a compressor.

As the program involved considerable, high-accuracy engine testing, the Canadian Forces requested the support of the National Research Council of Canada to undertake this evaluation and qualification. While the engineering documentation (blade frequency response, durability testing, surface finish, etc.) and the material characteristics study were assigned to the Materials Laboratory, the Engine Laboratory was requested to perform a performance evaluation on a coated engine. The Engine Laboratory has actively supported the development of military aero engine performance monitoring and fault isolation procedures. Current projects are aimed at correlating changes in gas turbine component and overall engine performance to physical degradation in the engine.

The Engine Laboratory was requested to evaluate the effect of coatings on engine performance and efficiency, and make recommendations for subsequent widespread use of coatings for operational application on the T56 and other gas turbine engines.

Since the compressor must be disassembled in order to be coated, it was deemed necessary to isolate the effect on performance of the rebuild from that of the coating. To achieve this, a program comprising three consecutive rebuilds was established which would quantify the portion of any performance shift which was not attributable to the coating itself. The assessment of the results from this rebuild program forms the basis of this paper; the specific objective is to establish the magnitude of the change in compressor and overall engine performance which was caused by the disassembly/reassembly of the compressor during overhaul.

2.0 EXPERIMENTAL INSTALLATION

To properly assess the various effects of a compressor rebuild on the performance of a gas turbine engine, a sophisticated test set-up, with specialized instrumentation was required. A description of the engine, instrumentation and test facility used for this assessment is included to illustrate the complexity of this project.

2.1 ENGINE DESCRIPTION

The test vehicle for this rebuild study is an Allison T56-A14LFE single spool turboprop engine from a CP-140 Aurora patrol aircraft. This engine is an excellent candidate for this study because it has no variable geometry or transient bleed valve operation that might vary the back-to-back performance of the engine. The T56 engine has a fourteen stage compressor, with bleed valves which are only open below the idle speed, a six can combustor, and a four stage turbine. The single shaft is coupled to a reduction gearbox mounted forward of the compressor. For the NRCC tests, power was transmitted through the gearbox to a flywheel and a Froude waterbrake dynamometer, which replaced the propeller used on the aircraft. A schematic diagram of the engine test set-up is shown in Figure 1. The figure illustrates how the engine, gearbox, dynamometer, and inlet duct were arranged in the test stand.

The engine control is one of a constant speed design using a governor to maintain a constant rotor speed of 13820 RPM. Power is controlled by setting the turbine inlet temperature with the power lever angle.

2.2 INSTRUMENTATION

Instrumentation used on the T56 was divided into two categories, external, and internal. The external instrumentation included a high Mach number airmeter in front of the engine, compressor inlet pressure and temperature rakes, a tailpipe airmeter mounted after the turbine, vibration sensors on the engine carcass, and turbine-type fuel flowmeters. The high velocity airmeter facilitated accurate flow measurement because of the large local difference between the total and static pressure. A diffuser mounted behind the airmeter reduced the airspeed to normal engine inlet conditions. The internal instrumentation consisted of total temperature and pressure probes in every stage of the compressor, as well as, compressor discharge and turbine inlet pressure and temperature rakes. With this degree of instrumentation, it was possible to monitor not only the condition of the overall engine, but also the performance of its major components, and the individual compressor stages. This report is limited in scope to an assessment of the data collected for the overall engine and its major components.

The data were recorded using a NEFF 620 data acquisition system controlled by a DEC PDP 11/34 computer. Measurement uncertainty estimates were available for the complete instrumentation package. Complete methodology for the fuel flow has been documented (Reference 2).

2.3 TEST FACILITY

The test cell used for the rebuild testing at the Engine Laboratory NRCC, at Ottawa, Canada, was Cell No. 2. Ambient air enters vertically from the roof through a retractable door. The planar dimension of the cell is a constant 4.6 x 4.6 metres throughout the test section. Engine exhaust and the entrained secondary airflow egress from the cell through a collector/augmentor tube to a vertical stack that discharges to the atmosphere. There is no acoustic attenuation in the inlet or outlet of the test cell. The entire cell is constructed of heavy reinforced concrete. The walls are covered with a 100 mm thick acoustic barrier to minimize noise propagation. The control, observation, and data acquisition room is located on the starboard side of the cell. An operator's window and a closed circuit television camera permit visual monitoring of the engine.

3.0 SUMMARY OF TESTING AND REBUILD PROCEDURES

In an attempt to isolate the effects of a compressor rebuild by monitoring small thermodynamic performance changes, a highly structured test plan was required. To achieve this goal, a test sequence was established which would best suit the requirements of the rebuild study, based on the knowledge of how the rebuilds were to be performed.

3.1 TEST SEQUENCE

To establish the effects of rebuilding the compressor on overall engine performance, a comparison of the results of three rebuilds was chosen. A larger sample would have been preferred, however, there were significant cost and time constraints on the project. The T56-A-14LFE engine chosen for the testing had no flight hours, in order to develop a legitimate "as-new" baseline. Baseline testing of the engine was performed to establish the "as-received" condition of the engine. Performance signatures of the overall engine and all its individual components were then quantified.

In the experimental program, the engine was run at a fixed, aerodynamically-corrected rotational speed to provide a common basis for comparison, ie. the mechanical speed of the engine was adjusted using the dynamometer, as a function of the ambient temperature.

The procedure used for each test run established a series of increasing power settings, for a given corrected rotor speed. At each power setting, the engine was allowed to stabilize for five minutes, then two sets of data were recorded. Typically, up to six power settings (12 data points) were recorded for each test. Several different corrected speeds, ranging from 13,000 to 14,500 RPM were run to assess the effects of corrected speed on any performance changes.

After the baseline testing was completed, the engine was sent to the overhaul contractor to be disassembled and rebuilt following normal procedures. On return to NRCC, the engine was retested using the same procedures utilized in the baseline tests. Following this testing, the engine was sent for the second rebuild, returned, and retested. This process was repeated for a third rebuild.

3.2 REBUILD PROCEDURE

The disassembly procedure entailed the removal of the turbine and combustor modules, leaving only the compressor. The compressor casing was then removed from the rotor, and the stator vanes were then detached from the casing. The rotor discs were unstacked and all the individual blades were removed. During removal, each blade was numbered, so that it could be returned to its original position upon reassembly. After disassembly, each piece underwent a petroleum solvent wash followed by an inspection to insure that no parts were damaged. Corrugated seals for stator vane segments were not replaced, nor were labyrinth seals reworked. Measurements of critical dimensions such as blade tip clearances, vane axial clearances, and rotor balance condition were recorded before disassembly and after reassembly. During the first rebuild, these measurements revealed that the axial clearance between the rotor and stator of several stages was out of tolerance. This may have occurred because of shifting during operation or improper assembly of the original build by the manufacturer. During reassembly, the clearances were set within the specified tolerances.

Upon reassembly of the compressor case, the stator vane axial clearances were set. The rotor blades were replaced in the same numbered order, and their balance checked. The entire compressor was then mated with the combustor and turbine modules, and a functional test was performed. The engine was then returned to NRCC for testing.

4.0 DATA PRESENTATION

Data recorded during a test were stored in basic engineering units so that observers could visually check the data quality as the test progressed. After a test was completed, the data were normalized, and used to calculate performance parameters such as, pressure and temperature ratios, corrected air and fuel flow, etc. These performance parameters were then curvefitted to quadratic equations, using a least squares method. The independent variable for curvefitting engine data was corrected turbine inlet temperature. Comparisons between various test runs were then made using the curvefitted values of each parameter. All data presented in this study were taken at 100 percent corrected rotor speed, or 13,820 RPM. For curvefit comparisons, the reference value used for the corrected turbine inlet temperature was 2200 degrees Rankine (1220 Kelvin). To facilitate comparisons with manufacturer's data, the performance parameters are presented in the U.S. Inconsistent system of units (Reference 4).

4.1 EFFECTS OF AMBIENT CONDITIONS

The NRCC test cell has no provision for controlling the ambient inlet air temperature. The engine was therefore operated over a wide range of temperatures experienced over the Canadian seasons. All performance data were corrected to standard day reference conditions for comparison. Previous experience at NRCC (Reference 5) and other test facilities (Reference 6), suggests that the normal standard day corrections do not ensure that the data will collapse to a single curve. Since temperature lapse rate data were not available for all of the parameters being considered in this study, test data presented here were all recorded at similar ambient temperature conditions.

The use of the long inlet duct on the T56 (Figure 1) causes a significant pressure loss and distortion at the compressor face. This pressure loss simulates an altitude of nearly 500 metres and a ram pressure ratio (compressor inlet total pressure divided by the static pressure at the exhaust exit plane) of approximately 0.97. The effect of ram pressure ratio on output power is accounted for using the manufacturer's procedures (References 7 and 8). However, there are no guidelines for any other parameters which may be affected by the ram conditions.

Since humidity affects the thermodynamic properties of the engine cycle, the following atmospheric limitations were observed to avoid condensation in the inlet air stream and minimize performance corrections (Reference 3):

maximum relative humidity: 75%

maximum absolute humidity: 14 g water per kg of air.

5.0 TEST RESULTS

For this study, fourteen performance parameters were chosen to describe the condition of the engine for each power setting. The selection of appropriate parameters was made to

analyze the performance of the overall engine and of its individual components, namely the compressor, combustor and turbine. To assess the compressor behavior, isentropic efficiency, corrected airflow, corrected speed, and compressor pressure and temperature ratios were examined. For combustor performance, combustor pressure and temperature ratios were analyzed. Isentropic efficiency was picked as a suitable parameter to describe the performance of the turbine. Corrected fuel flow, corrected output power, and specific fuel consumption were chosen to define overall engine behavior, as were engine temperature and pressure ratios. Corrected torque was added as a redundancy check on corrected output power.

Most of the performance parameters chosen for this study are commonly used in the existing literature (Reference 9). However, on the T56 engine, the presence of both turbine inlet temperature and pressure provided several additional parameters which are normally excluded from many engine test results. Combustor pressure and temperature ratios and turbine efficiency are notable examples of such additional parameters.

Since only the compressor was disassembled during the rebuild sequence, the strongest emphasis was in monitoring changes in the compressor performance and in turn, the effects on the overall engine performance. Combustor and turbine performance are included to see if a change in compressor operation affects any of the downstream components.

5.1 DATA QUALITY

There are many indicators of the data quality in any given set of engine test results. Influences of the test facility on engine operation are best typified by plotting the inlet and exhaust pressures, and temperatures as a function of power setting. Indications of engine thermal stability may be detected by observing the repeatability of the readings of engine spool speed and temperature and pressure ratios throughout the engine.

For this study, the quality of the data for each test was determined by the back-to-back repeatability of each of the performance parameters. This was done by comparing the deviations of the individual data points from the curvefitted quadratic equations derived from the data. A mean value of the deviation of the data from its curve was used to estimate the repeatability of each parameter within each test.

To establish the quality of the data recorded within each rebuild-test sequence, an analysis of the run-to-run repeatability was performed. This analysis consisted of comparing curvefitted test data recorded under the same ambient conditions during the same rebuild sequence. A mean deviation between the curvefits of each of the performance parameters was then used to define the repeatability within each rebuild.

An estimate of the overall repeatability of each of the parameters was accomplished by combining the back-to-back and run-to-run repeatabilities. With these estimated uncertainty values, a true comparison of the build-to-build effects would be carried out.

5.1.1 BACK-TO-BACK REPEATABILITY

For each power setting during a test, two complete scans were recorded by the data acquisition system. To assess the back-to-back repeatability, the values of these recorded points were compared to the values of the curvefit generated points at a specified corrected turbine inlet temperature. This procedure gave an indication of how close the repeated data points were to each other, and the "goodness" of the curvefit to the actual data points. These deviations are shown in Table 1 for the baseline tests and the first, second, and third rebuilds. A representative sample of the back-to-back repeatability of compressor efficiency and corrected output power are shown in Figures 2 and 3, respectively.

The compressor efficiency (Figure 2), corrected air and fuel flows (see Table 1) all show very tight repeatability ($\pm 0.02\%$ to $\pm 0.11\%$) for all four cases. The compressor pressure and temperature ratios also indicate very small deviations from the curve ($\pm 0.01\%$ to $\pm 0.09\%$), as do the combustor pressure and temperature ratios ($\pm 0.01\%$ to $\pm 0.07\%$), and the engine temperature ratio ($\pm 0.06\%$ to $\pm 0.18\%$). The corrected output power (Figure 3) and specific fuel consumption reveal a larger scatter ($\pm 0.28\%$ to $\pm 0.38\%$), especially during the second rebuild ($\pm 0.49\%$ for SFC). The turbine efficiency, engine pressure ratio and the corrected torque also display some noticeable data scatter ($\pm 0.14\%$ to $\pm 0.39\%$).

The deviation in the corrected output power and specific fuel consumption are to be expected because each of these parameters were calculated from two or three measured quantities. The scatter in the turbine efficiency is also expected because it is calculated using an approximate value for the specific heat ratio within the turbine. In addition, the turbine efficiency is an inverse parabolic function, which may not be conducive to a least squares quadratic curvefit.

5.1.2 RUN-TO-RUN REPEATABILITY

Within each rebuild test sequence, at least three complete runs were recorded for each corrected rotor speed condition. Having established the agreement of the test data

with the generated curvefits, the next step was to determine how well these curves collapsed within each rebuild. To evaluate the run-to-run repeatability of the data within each rebuild, the values of curvefitted data were compared from at least two runs taken at similar ambient conditions. These deviations within the rebuilds are shown in Table 2 for the baseline, and the three rebuilds. Unfortunately, during baseline testing, no two tests were performed at or near the same inlet temperature, so the repeatability figures for the baseline (Table 2), represent the average of the repeatabilities of the first and second rebuilds. For compressor efficiency and corrected output power, the repeatabilities from the second rebuild can also be seen in Figures 2 and 3.

Close examination of the run-to-run repeatability results (see Table 2) showed that compressor efficiency (Figure 2) and corrected airflow were reasonably close ($\pm 0.15\%$ to $\pm 0.24\%$). Corrected fuel flow displayed a slight aberration during the second rebuild ($\pm 0.41\%$), as did specific fuel consumption during the third rebuild ($\pm 0.54\%$). The corrected output power ($\pm 0.45\%$) and the corrected torque ($\pm 0.41\%$ to $\pm 0.52\%$) revealed significant scatter within each rebuild (see Figure 3). Compressor pressure and temperature ratios were extremely repeatable ($\pm 0.05\%$ to $\pm 0.08\%$), as were the combustor ($\pm 0.02\%$ to $\pm 0.07\%$), and engine pressure and temperature ratios ($\pm 0.07\%$ to $\pm 0.14\%$). The corrected speed ($\pm 0.02\%$ to $\pm 0.18\%$) and the turbine efficiency ($\pm 0.05\%$ to $\pm 0.16\%$) were in close agreement.

Certain parameters, such as turbine efficiency and engine pressure ratio had better run-to-run repeatability than back-to-back repeatability. In the case of turbine efficiency, this anomaly presumably results from difficulties in representing the uniquely shaped efficiency function with a quadratic equation.

5.1.3 COMBINED REPEATABILITY

Before a comparison of the rebuild data could be made, it was necessary to establish the overall or combined repeatability of the data from each rebuild. Since the same equipment, instrumentation suite, data system, and facility were used for each test, it is unlikely that the measurement bias errors would have changed. Thus the population of observed measurements taken at the same environmental conditions for a given engine build would be combined to form an overall datum with a defined data scatter. If when compared to the data taken under similar environmental conditions for an engine rebuild, there is a shift outside the scatter band, then a performance shift would be deemed to have occurred. A statistical approach using the methods described in Reference 10 was used to calculate expected bias and precision errors, and the measurement uncertainty for this experiment. These results are shown in Tables 1, 2 as expected random error. This information was compared to a more basic method using the observed repeatabilities. To accomplish this, a worst case scenario was assumed. In other words, it was assumed that both the back-to-back and run-to-run repeatabilities were acting in the same direction within each rebuild, and opposing each other across each rebuild. Therefore, the overall measured repeatability for each parameter would be the sum of all four observed repeatability figures (from Tables 1 and 2), between the baseline and its corresponding rebuild. For example, from Tables 1 and 2, the overall repeatability for compressor efficiency during the first rebuild would be,

$$(\pm 0.02\%) + (\pm 0.06\%) + (\pm 0.21\%) + (\pm 0.24\%) = \pm 0.53\%.$$

More probably, the data scatter would be calculated using the root-sum-square, which in this case, the observed repeatability in compressor efficiency would be only $\pm 0.33\%$. Thus, the method chosen to define the overall repeatabilities for this rebuild study always over-estimates the more appropriate statistical value.

Since the first rebuild becomes the new baseline for the second rebuild, and the second rebuild becomes the new baseline for the third, the overall repeatabilities will be slightly different for each cross-examination of rebuild data. A complete list of the overall repeatabilities for each of the parameters, for all three rebuilds are given in Table 3.

For the first rebuild, several parameters such as, compressor efficiency, corrected airflow and fuel flow, turbine efficiency, and engine pressure ratio, all exhibited overall repeatabilities of approximately $\pm 0.50\%$. Other parameters such as, corrected speed, compressor and combustor pressure and temperature ratios, and engine temperature ratio, had overall repeatabilities ranging from ± 0.16 percent to ± 0.32 percent. By far the largest overall data scatter appeared in the corrected output power ($\pm 1.44\%$), specific fuel consumption ($\pm 1.25\%$), and the corrected torque ($\pm 1.67\%$). The majority of the scatter in specific fuel consumption was attributed to the output power term. The corrected torque indicated some speed dependence which was accounted for in the output power measurements. The overall repeatabilities for the second and third rebuilds were very similar to those of the first rebuild.

In general, the quality of the test data for the baseline, and the three rebuilds appeared to be very good, with the possible exception of output power. Overall, the test data recorded for the rebuild study were considered to be of sufficiently good quality to be used for an accurate comparison.

5.2 COMPARISON OF REBUILD DATA

Having established the overall repeatabilities of the performance parameters selected for the rebuild evaluation, one representative test run from each rebuild was compared to its corresponding baseline. The observed shifts in the various performance parameters are given in Table 3. Several of these shifts are shown graphically in Figures 4 through 8. The results of each rebuild are discussed separately.

5.2.1 FIRST REBUILD RESULTS

To assess the various effects of the rebuild, the engine and its individual components were considered separately. The effects on compressor performance were noticed in the compressor efficiency (Figure 4), which showed an increase of 1.2% from the baseline value. This increase was double the pessimistic repeatability of the measured parameter. Corrected airflow (Figure 5) showed an increase of 0.77% from baseline to the first rebuild, which was also larger than the repeatability. The compressor pressure ratio (Figure 6) increased by 1.3%, which was nearly five times the estimated repeatability. The shift in the compressor temperature ratio was of the same magnitude as its uncertainty.

It was interesting to note that the performance of the combustor was also affected by the compressor rebuild. The combustor pressure ratio (Figure 7) decreased by 1.0%, which is significantly larger than its repeatability. This phenomenon is not entirely unexpected because earlier work (Reference 11) had suggested a direct relationship between the combustor pressure loss and the flow function at the compressor exit. In this case, the compressor exit pressure increased more than the airflow, thereby decreasing the flow function at the compressor exit. The effect on the combustor temperature ratio (-0.20%) was negligible, as was the effect on the turbine efficiency.

As far as overall engine performance was concerned, an increase of 0.73% was observed in the corrected fuel flow. Shifts in the corrected torque (+1.5%) and corrected output power (+0.79%), shown in Figure 8, were measured, but they were within the overall repeatability band. The specific fuel consumption, showed no shift because both fuel flow and output power shifted about the same amount and in the same direction.

5.2.2 SECOND REBUILD RESULTS

For the second rebuild, the first rebuild was used as the new baseline for comparison. The observed shifts in the performance of the engine and its components were very similar to the first rebuild. The compressor efficiency (Figure 4), showed a decrease of 0.84%, which was larger than the estimated repeatability. The corrected airflow (Figure 5) only decreased by 0.23%, which was less than the repeatability. The compressor pressure ratio (Figure 6) also decreased, this time by 1.3%, definitely beyond the measurement repeatability limits. The compressor temperature ratio remained unchanged.

As in the first rebuild, the combustor pressure ratio (Figure 7) was affected by the changes in compressor performance. An increase of 0.52% was observed in the combustor pressure ratio, which is well above its repeatability estimate. An increase in the compressor exit flow function, resulting from the compressor exit pressure decreasing more than the airflow, could be the cause of this behavior. The combustor temperature ratio was again unaffected by the rebuild, as was the turbine efficiency.

Concerning the overall engine performance, the corrected fuel flow, decreased by 1.4%, which is more than twice the established repeatability. Decreases in corrected output power (Figure 8), specific fuel consumption, and corrected torque (-0.76%) were observed, but these shifts were all within the projected repeatabilities for these parameters.

5.2.3 THIRD REBUILD RESULTS

For the third rebuild, the second rebuild was used as the new baseline for comparison. The observed shifts in the performance of the engine after the third rebuild are noticeably smaller from the first and second rebuilds. The compressor efficiency (Figure 4), showed an increase of only 0.31%, which is less than the estimated repeatability. The corrected airflow (Figure 5) increased only negligibly, while the compressor pressure ratio (Figure 6), and temperature ratio shifts were within the repeatability limits.

The only parameter that appeared to be affected by the third rebuild was the combustor pressure ratio (Figure 7), with a decrease of 0.40%. This shift is twice the estimated repeatability for that parameter. A change in combustor temperature ratio (+0.25) was noted, however, this shift was of similar magnitude to the overall repeatability. No change occurred in the turbine efficiency during the third rebuild.

Regarding the overall engine performance, the corrected fuel flow increased only 0.14%, while the corrected output power (Figure 8), decreased 0.52%. Changes in the corrected torque (-0.64%), and specific fuel consumption (+0.58%) were less than their predicted repeatabilities. The engine pressure and temperature ratios were similarly unaffected.

5.3 DISCUSSION OF THE REBUILD RESULTS

The results of the three rebuilds were compared assuming the overall repeatability was the worst combination of all of the back-to-back and run-to-run repeatabilities. A comparison (Table 1) of the back-to-back measured repeatability to the expected random error, which is twice the estimated precision error, shows very close agreement on most parameters, with the exception of torque. The run-to-run repeatability was shown (Table 2) to be slightly greater than the expected random error, indicating some portion of the bias error was included. On most parameters, the overall repeatability was found to be more pessimistic than the estimated uncertainties (Table 3) calculated using the methods described in Reference 10.

The actual cause for the observed shifts in the performance parameters is open for speculation. During the first rebuild, axial clearances were slightly altered between the rotor and stator of several of the compressor stages. In addition, inspections of critical internal gas path dimensions made before and after each rebuild (References 12, 13, and 14) suggest that the compressor internal geometry changed slightly, albeit within the manufacturers specified tolerances. These minor geometry changes include seal clearances, blade tip clearances, and stator position.

An investigation of the blade tip clearances measured during the rebuild processes provided some insight as to potential causes of the observed performance shifts. After the first rebuild, the measured tip clearances had decreased on 13 of the 14 stages within the compressor. The latter stages of the compressor were affected the most, where the flow area is smaller. This decrease in tip clearance would explain the increase in compressor efficiency observed after the first rebuild.

After the second rebuild, 9 of the 14 compressor stages showed an increase in tip clearances, which resulted in a decrease in compressor efficiency. The results of the third rebuild show that 50% of the compressor stages had an increase in tip clearance, while 50% experienced a decrease. These clearance changes were well mixed within the compressor, thus the change in compressor efficiency and all other engine parameters was small. Although these clearance changes are very small, the random combination of them may cause the compressor performance to shift sufficiently for laboratory instrumentation to detect it.

6.0 CONCLUSIONS

In setting up a project to quantify the effects rebuilding the compressor has on the performance of a gas turbine engine, there is always some difficulty in defining statistically measurable performance shift. The data presented here for the Allison T56 engine, illustrates that while some parameters have reasonably large repeatabilities associated with them, others have quite small limits, which makes them ideal for measuring important but small changes in performance.

The results of the rebuild study to date have indicated that performance shifts from simply disassembling and reassembling a compressor are measurable. The most significant shifts appear in parameters such as compressor efficiency, corrected airflow, compressor pressure ratio, corrected fuel flow, and combustor pressure ratio. The latter parameter is affected because of a change in the exit conditions of the compressor.

The effects of a compressor rebuild are, apparently, statistically random. After the first rebuild, the compressor performance improved, while following the second rebuild, the compressor performance deteriorated. The results of the third rebuild showed only minute changes in performance. These effects are consistent with variations in compressor tip clearance measured. Whether or not these three rebuilds have shown the full extent to which the performance may change is unknown. A much larger statistical sample would be required to completely determine the limits of the performance effects.

The impact of the rebuild study on the compressor blade coating is important. To the users of coated engine parts, the performance parameters of most concern are output power and specific fuel consumption. The repeatabilities associated with these parameters are larger than most other parameters and thus only gross shifts could be detected. The same may be said for engine health monitoring (EHM) testing, where faults are implanted in engine components to detect performance changes. Improved instrumentation, test techniques and correction methods (ambient temperature) are being pursued because of the importance of these applications.

7.0 RECOMMENDATIONS

It is recommended that more attention should be paid to the effects of temperature variation on the T56 engine. This would allow a larger supply of data from which a more confident set of repeatability estimates may be obtained. Until such time, data should only be compared when it has been recorded at the same ambient temperature conditions.

When analyzing data taken from the blade coating project and/or implanted fault studies, the effects of the rebuilding of the compressor should be considered. This implies increasing the uncertainty interval on certain parameters when comparing data taken across a compressor rebuild.

8.0 REFERENCES

- 1) MacLeod, J.D., Laflamme, Capt. J.C.G., The Effects of a Compressor Rebuild on Gas Turbine Engine Performance, AGARD CP-448-26, 1988.
- 2) Grabe, W., Humidity Effects on Gas Turbine Performance, National Research Council of Canada, TR-ENG-003, 1989.
- 3) Grabe, W., Fuel Flow Measurement in Gas Turbine Testing, National Research Council of Canada, TR-ENG-001, 1988.
- 4) Streeter, V.L., Wylie, E.B., Fluid Mechanics 7th Edition, 1979.
- 5) MacLeod, J.D., Effect of Inlet Temperature Variation on Gas Turbine Engine Performance, National Research Council of Canada, LM-ENG-007, 1987.
- 6) Greco, L., Gordon, S., Allison T56-A-14 Engine - Official Sea Level Low and High Temperature, and Altitude Performance Tests, NAEC-AEL-1836, 1966.
- 7) T56-A-14LFE Overhaul Manual, Volume I, C-14-33-000/MP-001, 1983.
- 8) Military Turboprop Engine Specification 670-D for Model T56-A-14, 1976.
- 9) Saravanamuttoo, H.I.H., et al, Gas Turbine Theory 3rd Edition, 1987.
- 10) Abernathy, R.B., Thompson, J.W., Handbook of Uncertainty in Gas Turbine Measurements, AEDC-TR-73-5, 1973.
- 11) Kirkhope, K.J., Computer Model of the T56 Turboprop Engine: Thermodynamic Analysis and System Design, GastOPS Report GTL-TR-19-22.1.1, 1984.
- 12) Dyke, L., NRC T56-A-14LFE Test Bed Engine: SAL Detailed Inspection Report, Standard Aero Report 54947, 1986.
- 13) Dyke, L., NRC T56-A-14LFE Test Bed Engine: SAL Compressor Inspection Data, Standard Aero Report J76796, 1987.
- 14) McLarty, V., NRC T56-A-14LFE Test Bed Engine: SAL Compressor Inspection Data for Third Rebuild, Standard Aero Report J17121, 1988.

TABLE 1: BACK-TO-BACK REPEATABILITY

PARAMETER	DEVIATION FROM CURVE (%)				EXPECTED RANDOM ERROR (%)
	BASELINE	FIRST REBUILD	SECOND REBUILD	THIRD REBUILD	
Compressor efficiency	±0.02	±0.06	±0.08	±0.06	±0.03
Corrected airflow	±0.06	±0.06	±0.11	±0.06	±0.10
Corrected fuel flow	±0.07	±0.10	±0.09	±0.12	±0.12
Corrected output power	±0.28	±0.38	±0.35	±0.16	±1.10
Specific fuel consumption	±0.28	±0.29	±0.49	±0.35	±1.10
Corrected speed	±0.01	±0.03	±0.04	±0.03	±0.01
Compressor pressure ratio	±0.05	±0.09	±0.08	±0.05	±0.06
Compressor temperature ratio	±0.01	±0.04	±0.05	±0.02	±0.00
Turbine efficiency	±0.20	±0.23	±0.23	±0.20	±0.02
Combustor temperature ratio	±0.01	±0.03	±0.04	±0.02	±0.00
Combustor pressure ratio	±0.07	±0.04	±0.05	±0.05	±0.08
Engine temperature ratio	±0.06	±0.07	±0.08	±0.18	±0.00
Engine pressure ratio	±0.15	±0.14	±0.15	±0.22	±0.03
Corrected torque	±0.30	±0.39	±0.35	±0.17	±1.10

Reference : Corrected speed = 13820 RPM
 Corrected Turbine Inlet Temperature = 2200 °R (1220 K)

TABLE 2: RUN-TO-RUN REPEATABILITY

PARAMETER	DEVIATION WITHIN REBUILD (%)				EXPECTED RANDOM ERROR (%)
	BASELINE	FIRST REBUILD	SECOND REBUILD	THIRD REBUILD	
Compressor efficiency	±0.21	±0.24	±0.18	±0.16	±0.03
Corrected airflow	±0.15	±0.16	±0.13	±0.17	±0.10
Corrected fuel flow	±0.28	±0.16	±0.41	±0.22	±0.12
Corrected output power	±0.39	±0.39	±0.39	±0.45	±1.10
Specific fuel consumption	±0.32	±0.36	±0.27	±0.54	±1.10
Corrected speed	±0.10	±0.18	±0.02	±0.11	±0.01
Compressor pressure ratio	±0.06	±0.07	±0.05	±0.05	±0.06
Compressor temperature ratio	±0.07	±0.07	±0.07	±0.08	±0.00
Turbine efficiency	±0.06	±0.05	±0.06	±0.16	±0.02
Combustor temperature ratio	±0.07	±0.07	±0.06	±0.06	±0.00
Combustor pressure ratio	±0.03	±0.02	±0.04	±0.05	±0.08
Engine temperature ratio	±0.08	±0.07	±0.08	±0.14	±0.00
Engine pressure ratio	±0.07	±0.08	±0.07	±0.07	±0.03
Corrected torque	±0.46	±0.52	±0.41	±0.45	±1.10

Reference : Corrected speed = 13820 RPM
 Corrected Turbine Inlet Temperature = 2200 °R (1220 K)

TABLE 3: REBUILD EFFECTS

PARAMETER	OVERALL REPEATABILITY (%)		UNCERTAINTY (ESTIMATED) (%)	DEVIATION BETWEEN REBUILD (%)		
	FIRST	SECOND		FIRST	SECOND	THIRD
Compressor efficiency	±0.53	±0.56	±0.48	±0.87	+1.16	-0.84
Corrected airflow	±0.43	±0.46	±0.47	±0.27	+0.77	-0.23
Corrected fuel flow	±0.61	±0.76	±0.84	±0.43	+0.73	-1.44
Corrected output power	±1.44	±1.51	±1.35	±1.42	+0.79	-0.70
Specific fuel consumption	±1.25	±1.41	±1.65	±1.52	-0.07	-0.80
Corrected speed	±0.32	±0.27	±0.20	±0.13	-0.11	-0.06
Compressor pressure ratio	±0.27	±0.29	±0.23	±0.25	+1.26	-1.31
Compressor temperature ratio	±0.19	±0.23	±0.22	±0.40	-0.20	+0.02
Turbine efficiency	±0.54	±0.57	±0.65	±0.90	+0.09	+0.18
Combustor temperature ratio	±0.18	±0.20	±0.18	±0.49	+0.20	-0.05
Combustor pressure ratio	±0.16	±0.15	±0.19	±0.35	-1.00	+0.52
Engine temperature ratio	±0.28	±0.30	±0.48	±0.40	+0.01	+0.01
Engine pressure ratio	±0.44	±0.44	±0.51	±0.12	-0.07	+0.23
Corrected torque	±1.67	±1.67	±1.38	±1.41	+1.50	-0.76

Reference : Corrected speed = 13820 RPM
 Corrected Turbine Inlet Temperature = 2200 °R (1220 K)

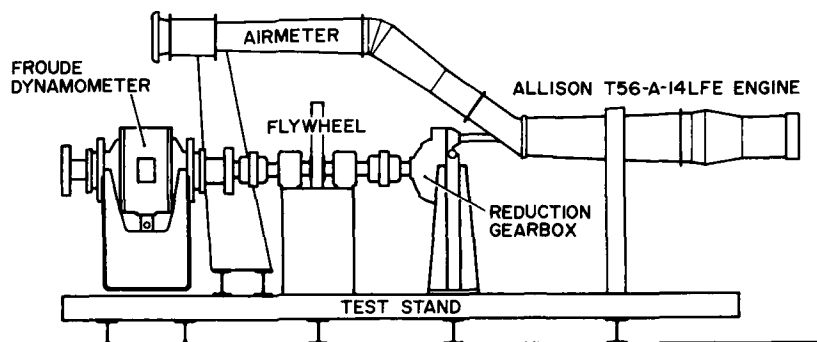


FIGURE 1: SCHEMATIC OF T56 TURBOPROP ENGINE ON TEST STAND

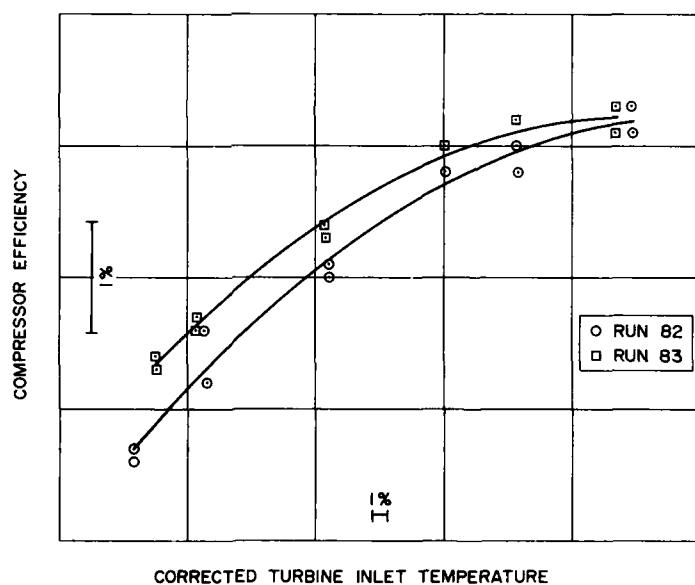


FIGURE 2: DATA QUALITY - COMPRESSOR EFFICIENCY

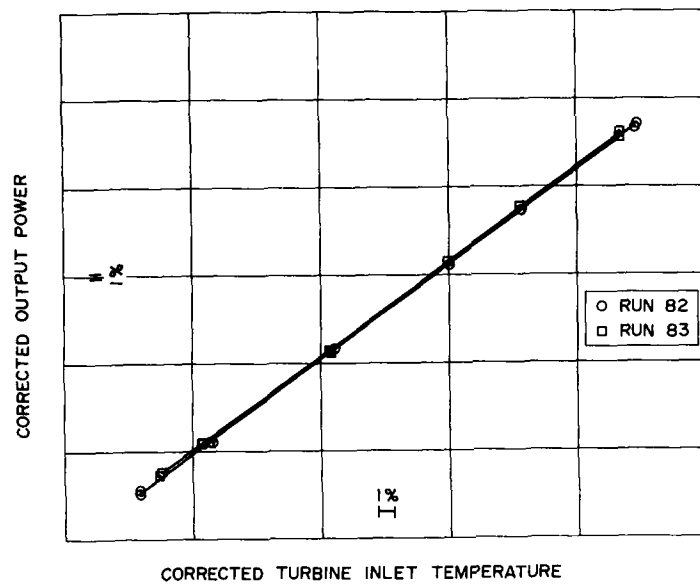


FIGURE 3: DATA QUALITY - CORRECTED OUTPUT POWER

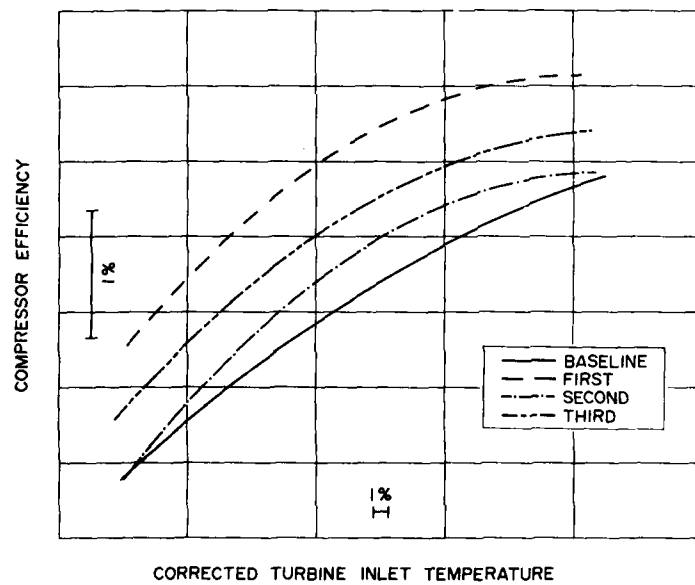


FIGURE 4: ENGINE PERFORMANCE - COMPRESSOR EFFICIENCY VS CORRECTED TURBINE INLET TEMPERATURE

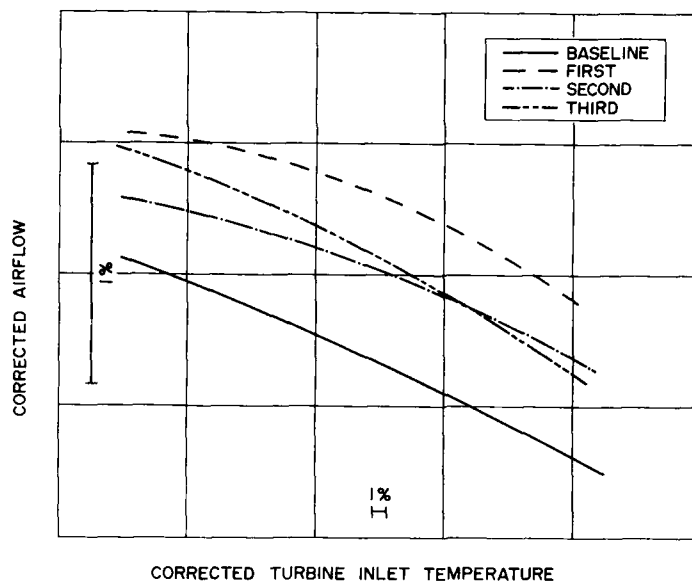


FIGURE 5: ENGINE PERFORMANCE - CORRECTED AIRFLOW VS CORRECTED TURBINE INLET TEMPERATURE

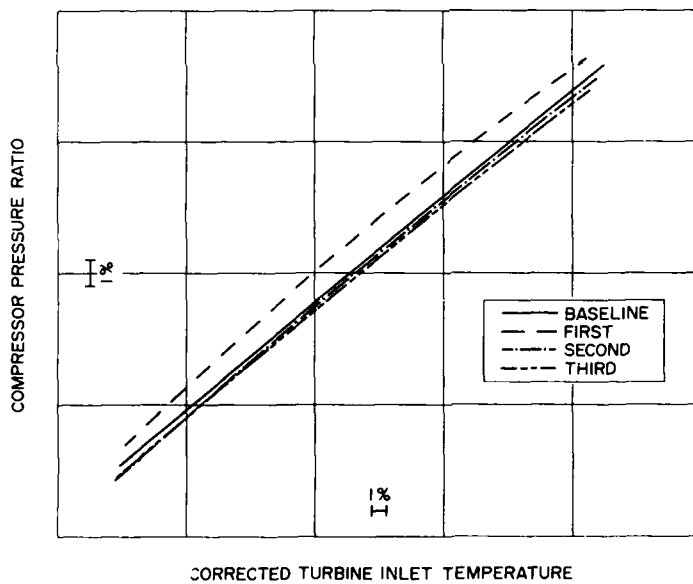


FIGURE 6: ENGINE PERFORMANCE - COMPRESSOR PRESSURE RATIO VS CORRECTED TURBINE INLET TEMPERATURE

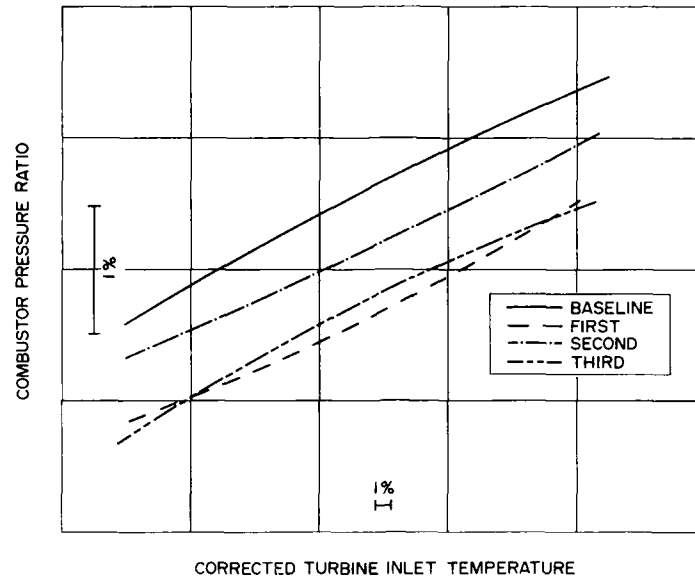


FIGURE 7: ENGINE PERFORMANCE - COMBUSTOR PRESSURE RATIO VS CORRECTED TURBINE INLET TEMPERATURE

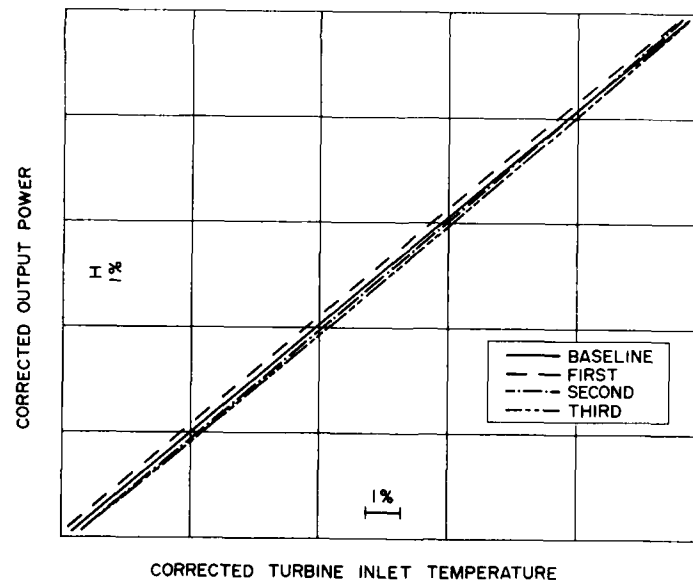


FIGURE 8: ENGINE PERFORMANCE - CORRECTED OUTPUT POWER VS CORRECTED TURBINE INLET TEMPERATURE

Oxidation, Sulfidation, and Hot Corrosion: Mechanisms and Interrelationships

T. A. Kircher
Aerospace Materials Division
Naval Air Development Center
Warminster, PA 18974

Summary

A discussion of the various types of oxide growth laws which describe oxidation of metals and alloys has been given. The formation and maintenance of a dense, adherent oxide scale will result in diffusion-limited scale growth and a parabolic-type rate equation. These protective scales are formed by selectively oxidizing their respective metallic components from a complex base alloy or coating. Exposure of alloys to a sulfidizing or hot-corrosive type environment reduces the ability for protective scales to adhere or recover from scale damage and shortens the time for which an alloy can form a protective scale via selective oxidation.

Introduction

Alloys which are designed for high temperature applications are subject to a wide spectrum of degradation mechanisms, many of which are highly specific to a particular service environment. The mechanisms involved even in simple oxidation of a modern superalloy are complex combinations of surface morphology, microstructure, alloy chemistry, oxygen partial pressure, and so on. Consideration of additional thermochemical reactions made possible by the presence of mixed gas environments or condensed deposits results in a situation which is almost unapproachable without making simplifying assumptions of some kind. Yet from a design lifetime standpoint the applicability of an alloy for some service environment can be reduced to the following evaluation: what is the ability of that particular alloy to function in the particular service conditions without undergoing accelerated and catastrophic degradation? This evaluation recognizes the inevitability of degradation under even the best conditions. Understanding what circumstances result in the transition from an acceptably stable degradation mode to an unacceptably debilitating form of attack can allow the materials engineer to work towards extending the region of time in which the alloy exhibits stable degradation in that service environment.

This paper examines oxidation, sulfidation, and hot corrosion from the standpoint of acceptable vs unacceptable degradation with the intent of emphasizing fundamental aspects common to these important forms of high temperature environmental attack. There are two guidelines which form a framework for understanding high temperature degradation regardless of whether the environment is purely oxidizing, a mixed gas environment, or an environment in which condensed deposits form⁽¹⁾:

- 1) For adequate service life an alloy must form a protective oxide scale. The usual method for accomplishing this is the selective oxidation of a particular alloying element.
- 2) The effect of an environment on component lifetime is primarily the result of reactions which lead to the disruption or prevention of protective oxide formation and subsequent rapid material degradation.

The first section of the paper will discuss oxidation. Specifically, it will explore the various oxide growth laws and the concept of selective oxidation. The second section on sulfidation will discuss protective oxide growth in sulfur-containing gas environments. The third and final section will focus on hot corrosion attack, in particular the effects of condensed deposits and molten salt chemistry on protective oxide formation.

Technical Discussion

A. Oxidation

The oxidation of a pure metal can be broken into a five step sequence as illustrated in Figure 1⁽²⁾. The first step is the adsorption of oxygen onto the metal surface from the gaseous environment. Islands of oxide are formed and lateral growth of these islands quickly occurs in step 2. This lateral growth of surface oxide film is accompanied by oxygen dissolution into the substrate lattice. The formation of a continuous surface film, step 3, is an important step in providing long-term oxidation resistance at elevated temperatures. If the continuous oxide film is stable the growth of the film will be dependant on two factors, namely, the continued availability of oxygen in the atmosphere and the rate of transport of ionic species through the oxide film. Also occurring in this step is the continued dissolution of oxygen into the metal substrate. In some situations the formation of internal oxides or embrittlement of the substrate can represent a far worse condition than metal recession due to uniform surface oxidation. With continued scale growth a variety of local defects can form as shown in step 4. Defect coalescence can create porosity within the scale. Volumetric

or thermal stresses can lead to microcracks at the oxide/substrate interface. Extensive cracking of the oxide scale can also occur due to volumetric stresses, as shown in step 5. This occurs readily when the oxide has a specific volume that differs greatly from that of the substrate metal.

There are three principal rate equations which describe oxidation of metals and alloys. At lower temperatures ($< 500^{\circ}\text{C}$) many metals such as aluminium, copper, and silver exhibit oxide growth behavior which is described by the logarithmic-type rate equation. This describes very thin oxides which form rapidly and then grow slowly with time. Electronic effects dominate transport across these films⁽³⁾. At higher temperatures ($> 500^{\circ}\text{C}$) the growth of oxide scales is usually limited by thermally activated transport processes, or diffusion. The growth rate in such scales is then inversely proportional to the oxide thickness and parabolic-type rate equations are observed. When the oxide scale undergoes extensive cracking or spalling linear-type rate equations develop. A summary of these three types of rate equations is given in Table 1.

It should be noted that diffusion-limited growth can also be observed where a continuous external scale does not form. For this reason metallographic evaluation must always be performed in addition to measuring weight change before oxidation behavior can be accurately characterized.

The formation of a dense, continuous, adherent oxide film which allows suitably slow diffusion-limited kinetics represents the best means for protection of high-temperature alloys. For diffusion-limited growth across a continuous oxide film the growth rate of the oxide layer will be proportional to the flux of ionic species through the oxide film. This flux is proportional to the diffusion coefficient and the oxygen gradient. For a given temperature and oxygen gradient, factors which increase diffusion through the oxide will accelerate the oxidation process.

Diffusion in oxide scales at a given temperature and oxygen pressure is a function of the oxide lattice and defect structure. Ionic species will have lower diffusivities in close-packed lattice structures such as hexagonal-close-packed and face-centered-cubic than in more open lattice structures such as a spinel structure. Point defects related to non-stoichiometry or impurities in the oxide lattice and line defects such as grain boundaries will also effect the overall diffusion rate of reactants through the oxide.

The growth rate of several metal oxides as a function of temperature is shown in Figure 2⁽⁴⁾. For protection of components at elevated temperatures the oxides SiO_2 , Al_2O_3 , and Cr_2O_3 are almost exclusively used. SiO_2 is used to protect components in oxidizing atmospheres to 1700°C . It is the protective oxide which allows MoSi_2 heating elements to function for thousands of hours at 1500°C and higher. Silicide-based coatings are also used to protect refractory metal alloys which are unable to form protective Al_2O_3 scales by selective oxidation. Al_2O_3 scales are the primary means of protection for nickel-base superalloys in gas turbine engines. Cr_2O_3 scales are utilized in many heat-resistant alloys where sulfidation is a major concern. Cr_2O_3 -forming alloys are limited to applications below approximately 1000°C . Above this temperature oxide volatilization is a limiting factor.

In complex alloys such as a nickel-base superalloys the desired protective oxide scale is usually formed by selective oxidation. Selective oxidation is the process by which one (usually minor) alloying element is exclusively oxidized from the bulk alloy substrate to form a pure, protective oxide for the alloy. In this process the relative free-energy of formation of the oxides of the various alloying elements is important. Although external scale formation is a complex function of diffusivities, oxygen solubility, and other thermodynamic/kinetic interactions, the alloying element whose oxide has the lowest free energy of formation will have the strongest driving force to form. Even with favorable thermodynamic conditions, however, formation of undesirable transient oxides can occur which can severely affect the selective oxidation process.

The selective oxidation process can be controlled to some extent by alloy chemistry. Figure 3⁽⁴⁾ shows an oxide map of the equilibrium oxide films which form on a wide variety of nickel-base superalloys at 1100°C as a function of nickel, chromium, and aluminium content. The selective oxidation process can change with time if the protective oxide scale needs to be continuously re-formed. This is true for oxides which spall upon thermal cycling. Such spallation will gradually cause depletion of the desired oxide-forming element from the surface layer and formation of less protective oxides. Referring to the oxide map shown in Figure 3, the surface composition of an alloy which starts out in the Al_2O_3 -forming region of the oxide map will gradually shift towards the Cr_2O_3 and finally NiO region of the map. Coating alloy compositions such as NiCrAlY are designed as reservoirs which are rich in the desired oxide-forming elements. As such, coatings will retard the movement of the surface composition towards regions of less protective oxide formation. The importance of oxide scale adherence in oxidation and hot corrosion behavior is discussed in an earlier paper of this proceedings⁽⁵⁾.

B. Sulfidation

Sulfidation is considered in this paper as the degradation of an alloy by sulfur attack from a gaseous sulfur species such as SO_2 or H_2S . Sulfidation is one specific type of general material degradation which can occur in mixed gas environments. In such

an environment the diffusion of sulfur into the substrate and the formation of internal sulfides can significantly shorten the period of time over which an alloy can form a protective oxide via selective oxidation.

The formation of protective Cr_2O_3 scales in sulfidizing environments has been widely studied. An especially important parameter in the formation of protective oxide scales in sulfidizing environments is the oxygen partial pressure in the gas. Studies have reported on the influence of oxygen partial pressure in a sulfidizing environment on the corrosion products of a wide variety of Fe-Cr-Ni alloys containing >18% Cr⁽⁶⁾. The data indicate the existence of a threshold oxygen partial pressure above which a continuous protective oxide scale develops. The use of an excess parameter, $P_{\text{O}_2}/P_{\text{O}_2}^e$, has been suggested, where P_{O_2} is the oxygen partial pressure in the gas mixture and $P_{\text{O}_2}^e$ is the equilibrium Cr_2O_3 -Cr₂ oxygen partial pressure indicated by the thermodynamic phase stability diagram at the temperature of interest.

Figure 4⁽⁵⁾ shows the degradation of IN 800 over a wide range of temperatures and sulfur partial pressures as a function of this parameter. Samples of IN 800 were exposed for 25 hours and then metallographically examined for sulfidation attack. The figure indicates that irrespective of temperature and P_{O_2} there exists a threshold oxygen partial pressure $P_{\text{O}_2}/P_{\text{O}_2}^e \sim 10^3$ where scale thickness and alloy penetration are negligible. This stable degradation mode is associated with the formation of a continuous, protective Cr_2O_3 scale on the metal surface.

Sulfidation of the substrate will still occur in most cases despite the formation of a continuous external Cr_2O_3 scale. The formation of subscale sulfides is caused by diffusion of sulfur through the oxide scale. This causes scale spallation or cracking, followed by subsequent oxidation of the sulfides and sulfur penetration into the alloy along the grain boundaries. Breakaway sulfidation is associated with chromium depletion of the alloy matrix in the surface region, formation of mixed sulfide phases, and widespread de-scaling of the chromium-oxide.

C. Hot Corrosion

Hot corrosion is considered in this paper as corrosion in the presence of a condensed phase, or "deposit-modified corrosion"⁽¹⁾. The condensed deposits which characterize hot corrosion attack in Naval gas turbine engines are salts, primarily Na_2SO_4 , which form during combustion of the fuel in the presence of marine contaminants. Hot corrosion attack occurs in the form of aggressive degradation of turbine engine components in the intermediate temperature region of 650-900 °C. Above these temperatures the salt deposits volatilize and hot corrosion is not observed.

The selective oxidation process and the formation and maintenance of protective oxide films is important in understanding hot corrosion reactions. In most cases, the primary impact of condensed environmental contaminants is to shorten the time for which an alloy can form a protective scale via selective oxidation.

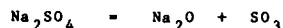
An examination of the hot corrosion degradation sequence reveals that corrosion resistant alloys degrade in the same characteristic sequence. This sequence is represented by the weight change data for two nickel-base superalloys shown in Figure 5⁽¹⁾. There is an initiation or incubation stage, where the alloy is behaving much the same as if there were no deposit. The propagation or accelerated oxidation stage is characterized by accelerated weight gain. This stage represents a situation where the deposit has significantly modified the protective oxide and has attacked the alloy substrate beneath the oxide film. Some researchers insert a transition stage between these stages. A more specific discussion of the role of oxide films in the hot corrosion process is described in an earlier paper in this proceedings⁽⁴⁾.

From the weight change data in Figure 5 it is clear that IN 738 exhibits a much longer initiation stage than the B-1900. If the time scale were expanded, however, the weight change data for the B-1900 would also exhibit the same characteristic stages as the IN 738. It becomes apparent, therefore, that for a particular component one would like to extend the initiation stage as long as possible and remove the component from service before the propagation stage occurs.

In order to understand what conditions lead to transition from the initiation stage to the propagation stage of hot corrosion, it is necessary to examine the effects of condensed, molten salt deposit on the alloy surface. The situation is represented schematically in Figure 6. There are two primary deposit-induced effects⁽¹⁾:

- 1 - The condensed deposit separates the alloy surface from the gaseous environment. The partial pressure of oxygen at the alloy surface is thereby reduced and the selective oxidation process is more difficult. This in turn allows the formation of less protective oxides which have higher transport rates. Additionally, elements in the substrate may react with the deposit, especially the active elements which have a high affinity for oxygen.
- 2 - The protective oxide on the alloy may be dissolved by the deposit. These so-called fluxing reactions occur through electrochemical mechanisms which arise from acid-base conditions in the molten salt.

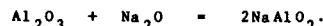
An understanding of molten salt electrochemistry can help alloy and coating designers minimize the potential for hot corrosion attack. The Na_2SO_4 equilibrium



can be characterized as acidic or basic according to the concentrations of the two ionic species, Na_2O and SO_3 . Protective oxides can be dissolved by either acidic or basic conditions. Acidic species such as SO_3 dissolved in the molten deposit can react with oxides as follows:



Basic species such as Na_2O can react with oxides as follows:



The solubilities of various oxides as a function of Na_2SO_4 melt basicity at 927°C are shown in Figure 7(9). The purpose of such studies is to minimize hot corrosion reactions by selection of an alloy or coating which is able to form and maintain a protective oxide despite the presence of a molten salt film. Cr_2O_3 and Al_2O_3 show solubility minima in the acidic region, which is representative of conditions in aircraft gas turbine engines. Co_3O_4 shows a minimum in the basic region. This is consistent with empirical observations of nickel and cobalt base alloys in aircraft gas turbine engine service, where cobalt-based alloys exhibit a much greater susceptibility to hot corrosion attack. SiO_2 has a low solubility which is independent of melt basicity.

Conclusions

A discussion of the various types of oxide growth laws which describe oxidation of metals and alloys has been given. The formation and maintenance of a dense, adherent oxide scale will result in diffusion-limited scale growth and a parabolic-type rate equation. Cr_2O_3 , Al_2O_3 , and SiO_2 scales have the slowest transport rates and are most often utilized as protective scales. These protective scales are formed by selectively oxidizing their respective metallic components from a complex base alloy or coating. Damage or spallation of the scale results in further selective oxidation, gradual depletion of the favorable element from the base alloy, and eventual formation of a less dense, less protective oxide. Exposure of alloys to a sulfidizing or hot-corrosive type environment reduces the ability for protective scales to adhere or recover from scale damage and shortens the time for which an alloy can form a protective scale via selective oxidation.

References

- (1) F. S. Pettit and G. H. Meier, Superalloys 85, TMS-AIME, Warrendale, Pennsylvania, (1985).
- (2) P. Kofstad, High Temperature Corrosion, NACE-6, R. A. Rapp, ed., NACE, Houston, Texas, (1983) 123-138.
- (3) F. P. Fehlner and N. F. Mott, Oxidation of Metals and Alloys, ASM, Metals Park, Ohio, (1970) 37-62.
- (4) R. Hindam and D. P. Whittle, submitted to Oxidation of Metals for publication.
- (5) M. A. DeCrescente and N. S. Bornstein, this proceedings.
- (6) K. Natasen, High Temperature Corrosion, NACE-6, R. A. Rapp, ed., NACE, Houston, Texas, (1983) 336-344.
- (7) R. A. Rapp, Mat.Sci. and Eng., **87**, (1987) 319-327.

Table 1 - "OXIDE GROWTH LAWS"

Figure 1 - "OXIDATION SEQUENCE"

Figure 2 - "OXIDE PARABOLIC RATE CONSTANTS"

Figure 3 - "SELECTIVE OXIDATION IN SUPERALLOYS"

Figure 4 - "OXYGEN PRESSURE EFFECTS"

Figure 5 - "HOT CORROSION KINETICS"

Figure 6 - "DEPOSIT-INDUCED EFFECTS"

Figure 7 - "OXIDE SOLUBILITIES IN MOLTEN Na_2SO_4 "

- *logarithmic-type rate equations*

$$T = K \cdot \log(t) + \text{constant}$$

- *parabolic-type rate equations*

$$T^2 = k_p \cdot t$$

- *linear-type rate equations*

$$T = k_l \cdot t$$

Table 1 - Oxide growth laws which describe oxidation of a metal or alloy.

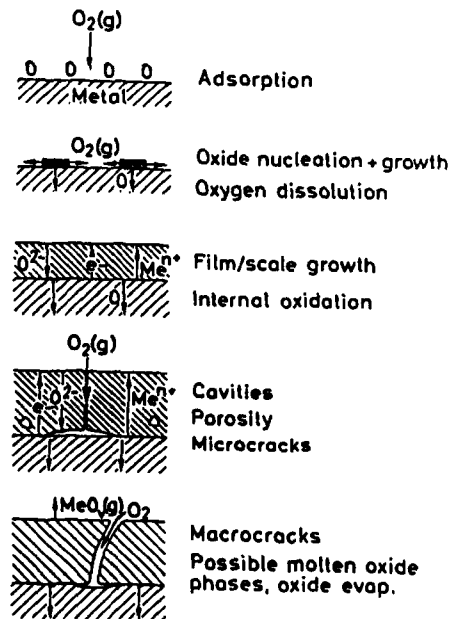


Figure 1 - A schematic illustration of oxidation on the surface of a metal or alloy.

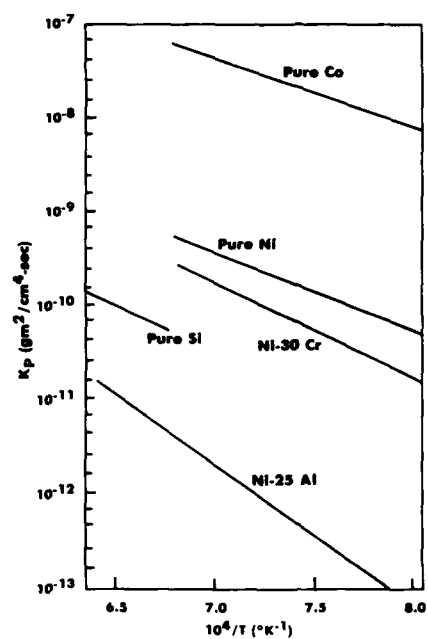


Figure 2 - Parabolic rate constants for various oxides.

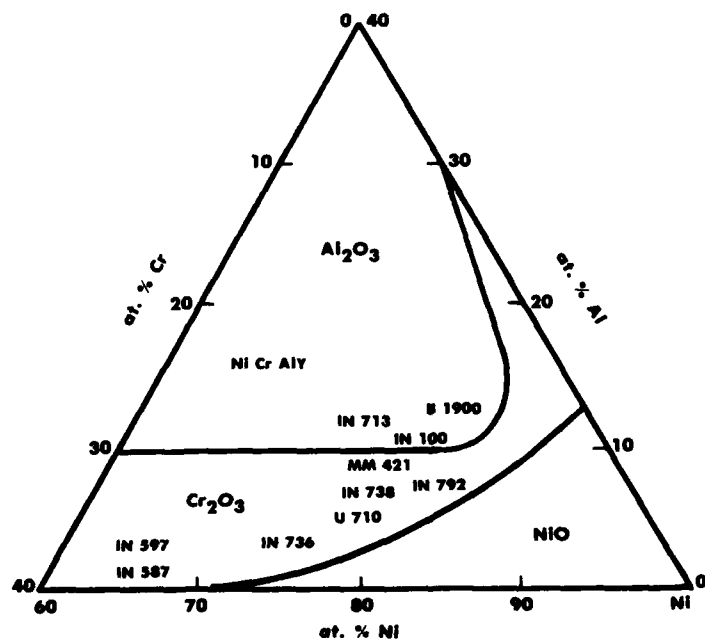


Figure 3 - Map of selective oxide formation on Ni-Cr-Al alloys.

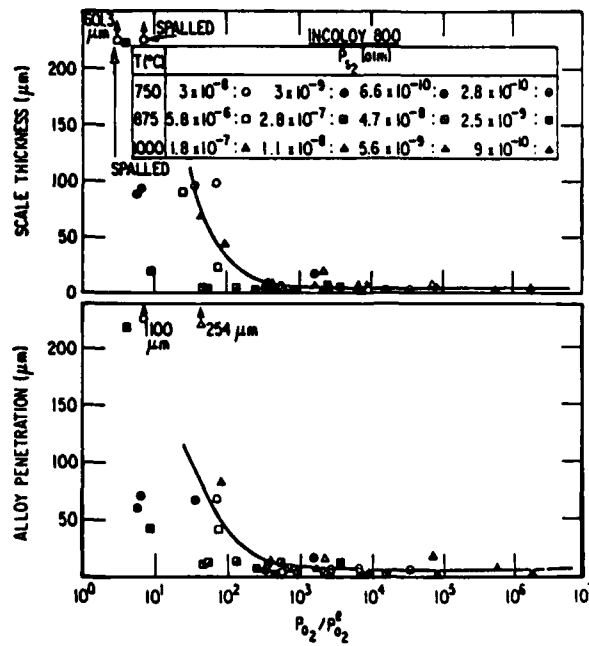


Figure 4 - Effect of oxygen partial pressure on sulfidation of IN 800.

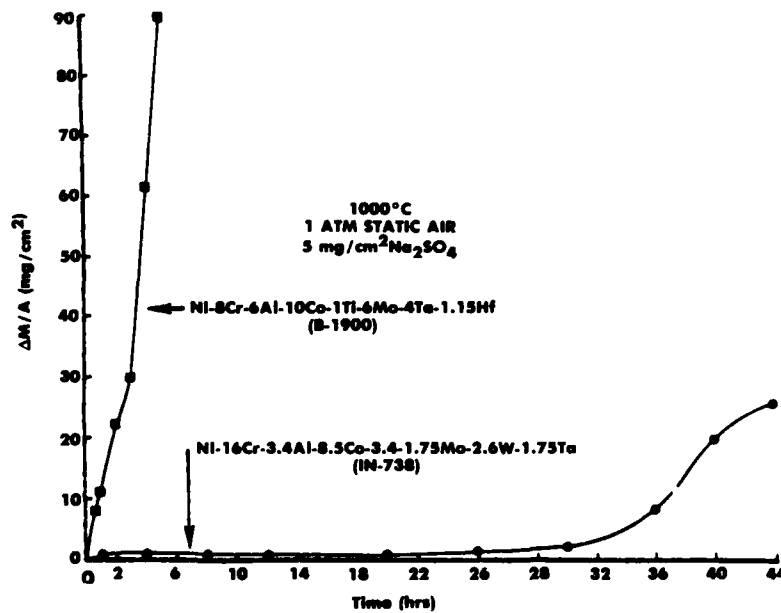
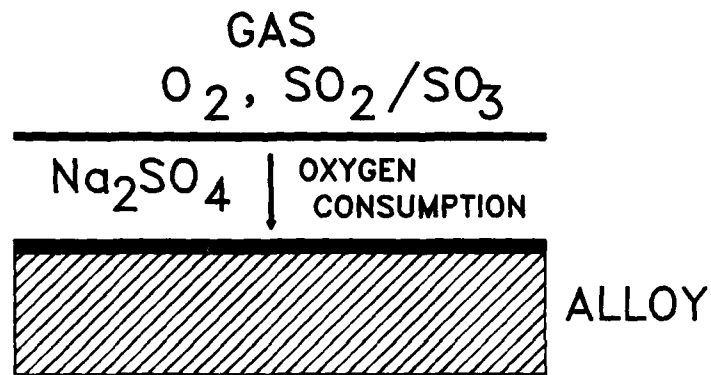


Figure 5 - Specific weight changes for B-1900 and IN-738 during laboratory hot corrosion testing.



- 1 - SEPARATE ALLOY FROM ENVIRONMENT
- 2 - DISSOLUTION OF PROTECTIVE OXIDE
(FLUXING REACTIONS)

Figure 6 - Schematic illustration of effects of a molten salt deposit on the surface of an alloy during hot corrosion.

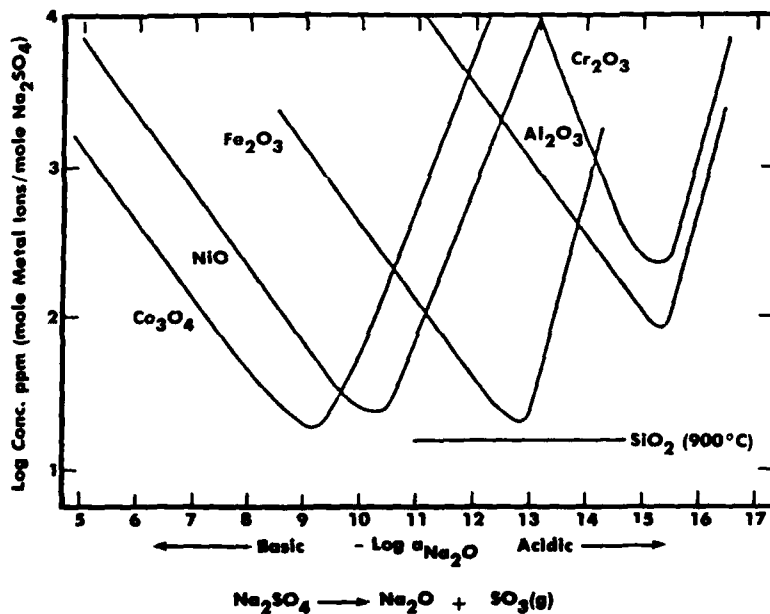


Figure 7 - Solubilities of various oxides in molten Na_2SO_4 at $927^\circ C$ as a function of molten salt basicity.

SCALE ADHERENCE EFFECTS IN OXIDATION AND SULFIDATION

by

M.A. DeCrescente
 Manager of Manufacturing Technology & Process Research
 and
 N.S. Bornstein
 Chief, Materials Process Research
 United Technologies Research Center
 Silver Lane
 East Hartford, Connecticut 06108
 United States

Summary

The most oxidation-resistant gas turbine alloys and coatings form adherent Al_2O_3 oxide scales which slowly thicken and resist spallation when thermally stressed. Work performed at United Technologies Research Center in the period 1966-1972 and by others demonstrated that the onset of sulfidation was also affected by the adhesion of the Al_2O_3 scale. In this paper, the relationship between sulfidation corrosion, and oxide scale adherence as it relates to oxidation resistance will be reviewed.

The sulfidation mechanism research performed at UTRC will be summarized to illustrate the role of Al_2O_3 scale in the sulfidation process; whereas more recent oxidation results of in-house and ONR and NADC-sponsored programs will be presented which demonstrates that sulfur present in gas turbine materials, even at very low concentrations, degrades Al_2O_3 scale adhesion. Finally, results are disclosed which indicate that the very low sulfur-containing materials are extremely oxidation resistant and delay the onset of sulfidation.

Sulfidation Corrosion

A. Background

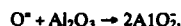
Sulfidation corrosion is the accelerated rate of oxidation of gas turbine materials associated with the presence of a condensed alkali sulfate salt. It is generally agreed that sulfidation corrosion microstructure characterized by the presence of a non-protective oxide scale separated from the unaffected substrate by an alloy-depleted zone containing sulfide precipitates is called Type I; and a microstructure characterized by the absence of the depletion zone and sulfide precipitates is referred to as Type II. Whereas Type I is a broad-front attack, Type II is a pitting attack. Although Type I is generally believed to be the high temperature form of corrosion ($>750^\circ\text{C}$), the temperature range of the two types of corrosion overlap. The similarities and differences in the types of attack are described in the recently published review articles (1,2). The studies presented in this paper deal with Type I corrosion.

B. The Role of Al_2O_3 films in the Sulfidation Process

A typical TGA curve for 1 mg/cm^2 Na_2SO_4 coated B-1900 exposed at 850°C is shown in Figure 1. The weight change in the absence of the salt after 1400 min is significantly less than 1 mg/cm^2 , and in the presence of the salt about 14 mg/cm^2 . The weight change curve for the salt coated specimen is divided into three stages. Stage I is the "incubation period" and is separated from Stage III, "accelerated oxidation" by Stage II the "transition period". During the first Stage (I) of the sulfidation process, Al_2O_3 remains intact, insulating the substrate from reactive Na_2SO_4 . Al_2O_3 may be removed locally (flawed) by any of a number of processes (erosion, impaction, corrosion, spallation) after which the Na_2SO_4 comes into direct contact with the substrate. This is Stage (II), a period of accelerating oxidation. At this point the sodium sulfate reacts with strong sulfide-forming elements in the alloy to raise the oxide ion (O^{2-}) concentration through the reaction:



The O^{2-} which is produced can then react with and remove the Al_2O_3 barrier,



thereby involving a large amount of the surface in the accelerated oxidation process.

The sulfidation process then enters into a period of parabolic oxidation (Stage III) during which the surface area (for oxidation) is maximized and remains constant and whose kinetics are controlled by the conversion of Ni to NiO . Since NiO is the least reactive oxide with respect to O^{2-} it does not react to form NiO_2 and it survives the sulfidation process.

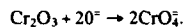
The energy of activation for the sulfidation (Na_2SO_4 -accelerated oxidation) of superalloys is 39 Kcal/mol, similar to that observed for the oxidation of Ni, (Figure 2). A comparable energy of activation is also observed for

Na_2CO_3 -accelerated oxidation of superalloys. In this case, O^* , formed by the equilibrium



prevents the existence of an Al_2O_3 scale leaving NiO the only remaining barrier for oxidation. The duration of each of the sulfidation stages is temperature dependent (3).

The sulfidation inhibition mechanism which involves lowering the O^* concentration was verified using a galvanic cell employing a Na_2SO_4 electrolyte and an electrode reversible to O^* (4). Whereas additions of alkali oxides increased the oxide ion content of Na_2SO_4 , Cr_2O_3 additions were found to decrease the oxide ion content by the chemical reaction,



These observations led to the conclusion that chromium-containing alloys derive their sulfidation resistance through the formation of Cr_2O_3 which lowers the oxide content of Na_2SO_4 below that required for its reaction with Al_2O_3 to form NaAlO_2 . Cr_2O_3 prevents Al_2O_3 scale breakdown by O^* and permits Na_2SO_4 to co-exist with the alloy.

The ability of Cr_2O_3 to inhibit sulfidation corrosion is demonstrated in Figure 3, and the use of chromium compounds which form Cr_2O_3 during combustion to inhibit sulfidation corrosion has been demonstrated in both marine and industrial gas turbine engines (5, 6).

Although chromia and other oxides can regulate the oxide ion content of sodium sulfate, the integrity of the aluminum scale that separates the corrosive salt from the alloy substrate can be compromised other than by chemical dissolution. It is widely accepted that thermal shock is a principle cause of oxide scale spallation and preconditioning the oxide film can influence its resistance to thermal shock. For example, the onset of sulfidation corrosion can be significantly postponed by preoxidizing the alloy so that it forms a more protective oxide scale. Preoxidation of B-1900 for 16 hours at 700°C increases the duration of the incubation period four-fold, Figure 4. However, if the salt-coated alloy is thermally shocked, the specimen immediately enters Phase II of the corrosion process, Figure 4.

This summary of many years of research of the mechanism of sulfidation and its inhibition supports the premise wherein accelerated corrosion does not begin as long as the normally protective Al_2O_3 film remains intact. Chemical dissolution of Al_2O_3 by the oxide ion in equilibrium with Na_2SO_4 is a major method for its removal as are mechanical stresses which develop during thermal cycling. The remaining portion of this presentation deals with an important factor which contributes to adhesion of Al_2O_3 during thermal cycling.

Oxide Scale Spallation

The extraordinary oxidation performance of superalloys and their protective coatings depends upon the retention (adherence) of naturally occurring Al_2O_3 scale. Stresses produced during thermal cycling greatly increase the rate of oxidation of Al_2O_3 -forming alloys and coatings (e.g. Ni-15Cr-6Al), which under isothermal conditions exhibit excellent high temperature oxidation resistance. The importance of thermal stresses with respect to oxide scale spallation is shown in Figure 5, where the weight change of NiCrAl and NiCrAlY exposed at 1150°C is shown as a function of time. Under isothermal conditions, no differences are noted between the oxidation behavior of the two coating alloys. However, in the cyclic mode, the oxide scale that forms on NiCrAl spalls after each cycle and the alloy rapidly loses weight with each consecutive cycle.

The work of Petit (8) and others have led the way in understanding how yttrium additions impart oxidation performance under thermal cycling conditions by maintaining oxide scale adherence. Without yttrium, protective oxide scales spall during thermal cycling, and the benefits they impart are lost. Mechanisms proposed to account for such improved adherence have historically included: (a) the formation of oxide pegs which anchor the scale to the substrate; (7) (b) the prevention of vacancy coalescence at the scale-metal interface by providing alternate coalescence sites; (8) (c) the enhancement of scale plasticity by altering its structure; (9) (d) the alteration of scale growth processes; (10) and (e) the formation of a graded oxide layer. (11)

Most recently, Funkenbusch, Smeggil and Bornstein (12) proposed that sulfur present in the alloy at a low concentration, segregates to and weakens the oxide scale-metal interface, thereby promoting oxide scale exfoliation. This ONR-sponsored work established that the Al_2O_3 /substrate adhesion is ordinarily strong but is weakened as a result of sulfur diffusing to the interface. The role of yttrium is to immobilize the sulfur through the formation of stable yttrium sulfide. Surface segregation studies were conducted employing Auger Electron Spectroscopy (AES) coupled with cyclic oxidation experiments. Samples were heated up to 1000°C in the vacuum of the Auger chamber and the surface composition monitored as a function of time. Typical Auger results for the Ni-15Cr-6Al alloy are shown in Figure 6. At room temperature the concentration of sulfur on the surface is quite low, but at 1000°C , sulfur is a major element on the surface of the alloy.

The surface concentration of sulfur as measured from AES (Figure 7) for NiCrAlY is approximately one fourth of that measured for the NiCrAl, even though the nominal sulfur content of both alloys are comparable (about 40 ppm). The

presence of yttrium sulfur precipitates in the NiCrAlY specimens was confirmed through the use of scanning electron microscopy studies. Some typical results are shown in Figure 8.

The enrichment in sulfur content at the surface of NiCrAl causes the normally protective alumina scale to spall. This conclusion is based upon the results of experiments in which NiCrAl specimens were produced from extremely pure, low sulfur constituents, and then cyclically oxidized. The oxide scale that forms on the surface of NiCrAl (containing 20-30 ppm S) is weakly bonded, consequently the alloy exhibits large weight losses when cyclicly exposed at elevated temperatures. However, the oxide scale that forms on the surface of NiCrAl prepared from extremely high purity stock is adherent, and the cyclic oxidation behavior of the alloy is comparable to that of the NiCrAlY alloy, (Figure 9). The sulfur content of the high purity NiCrAl is 2-3 ppm.

This comparison clearly indicates that scale adherence is greatly enhanced in low sulfur NiCrAl. Furthermore, the adherence of the alumina scale in NiCrAl with 2-3 ppm sulfur is comparable to that of NiCrAlY.

The relationship between sulfur, yttrium and oxide scale adherence is further demonstrated in the data presented in Figure 10. There is a small positive change in weight when NiCrAlY, containing 40 ppmS, (Alloy C) is cyclicly exposed in air at 1150°C since an adherent oxide scale is formed. However, the results are quite different for NiCrAl containing the same amount of sulfur (Figure 10, Alloy A). Within 600 hours, it had lost more than 15 mg/cm² as the Al₂O₃ film is repeatedly formed and spalled. Similar experiments were conducted with materials containing larger quantities of sulfur. The sulfur content of these alloys was approximately ten-fold higher. As shown in Figure 10, whereas the higher sulfur content of the NiCrAl alloy (Alloy B) did not result in a large reduction in its oxidation resistance, it did bring about a marked deterioration in the performance of the NiCrAlY alloy (Alloy D). Larger amounts of sulfur cause the alloy to behave as if it had no yttrium. The excellent oxidation resistance typical of NiCrAlY is restored to the sulfur-contaminated NiCrAlY alloy by increasing its yttrium content. These experiments support the precept that the role of yttrium is to immobilize the sulfur.

These observations coupled with the AES results previously described, indicate the Al₂O₃ film that forms on NiCrAl is normally protective but is made less adherent when sulfur present in the alloy thermally diffuses to the metal/oxide interface.

The "Sulfur Effect" on Coatings

A beneficial feature of the overlay coatings is that the compositions which are applied are independent of the superalloy substrates. However, as shown in Figure 11, their oxidation resistance of the PVD coating appears to be dependent upon substrate alloy composition even though there is no evidence of interdiffusion of substrate and coating constituents. It is felt that this variability is related to the relative sulfur activity of the substrates. However, this hypothesis is unverified since no correlation exists to relate composition to sulfur activity for these multi-constituent alloys. Some isolated conditions exist which indicate sulfur in the substrate influences coating behavior.

For example, it is found that laser melting of overlay coatings has a profound effect on oxidation performance during cyclic burner rig testing. The surface of a test specimen exposed 100 hours (100 cycles) at 1000°C in a cyclic burner rig is shown in Figure 12. At the completion of the test, the oxide film on the laser processed surface was extremely thin and very adherent. However, the opposite surface which was not laser processed exhibited a mottled surface indicative of the repetitive Al₂O₃ spallation and reformation process occurred over the test period. The benefits imparted by laser melting are however temperature dependent. The improvements obtained at 1000°C are greater than those at 1200°C. It was initially rationalized that the superior performance of the laser-processed surface was related to the unique microstructure associated with rapid solidification. However, AES showed evidence that laser melting lowered the surface sulfur content as shown in Figure 13.

It was concluded that although the sulfur concentration of the coating was reduced by laser processing, it was reestablished by diffusion from the higher sulfur activity substrate. Higher temperatures favor the rate at which the sulfur levels are restored.

In summary, it is now established that the alumina scale that forms on alloys is very protective and sulfur an impurity present at trace levels causes the normally adherent oxide scale to spall. The role of yttrium and other reactive elements is to react with and immobilize sulfur, thereby reducing its activity in the alloy. Under NADC-sponsorship it remains to be demonstrated that an improvement in sulfidation resistance can be achieved by improving scale adherence through control of alloy and coating sulfur activity.

References

1. J. Stringer, *Materials Science and Technology*, July 1987, Vol. 3.
2. N. S. Bornstein, ONR Contract N00014-88-M-0013, *Literature Review of Inhibition for Vanadate Attack*, June 1988.
3. N. S. Bornstein, M. A. DeCrescente and T. Sturiale, *AFML 50th Anniversary Corrosion of Military and Aerospace Equipment Technical Conference*, Denver, CO, Sulfidation of a Nickel Base Superalloy, May 23-24, 1967.

4. N. S. Bornstein, and M. A. DeCrescente, *Investigation of Sulfidation Mechanism in Nickel Base Superalloys*, Contract N00600-68-C-0639, April 1969.
5. N. S. Bornstein and A. Mitchell, *Fighting Sulfidation with a Chromium Bearing Fuel Additive*, ASME 76-GT-82, 1982.
6. M. A. DeCrescente, N. S. Bornstein and C. A. Blizzard, *Fuel Additions to Inhibit Sulfidation*, SAE 760919, December 1976.
7. D. P. Whittle, and J. Stringer, *Philos Trans. R. Soc., London Ser. Vol. A295*, pp. 309-329, 1980.
8. J. K. Tien, and F. S. Pettit, *Met. Trans.*, Vol. 3, pp. 1587-1599, 1972.
9. J. E. Antill, and K. A. Peakall, *J. Iron Steel Inst.*, Vol. 205, pg. 1136-1142, 1967.
10. F. A. Golightly, and F. H. Scott and G. C. Wood, *Oxid. Met.*, Vol. 10, pp. 163-187, 1976.
11. H. Pfeiffer, *Werkst. Korros*, Vol. 8, pp. 574, (1957).
12. A. W. Funkenbush, J. G. Smeggil and N. S. Bornstein, *Trans, AIME*, Vol. 16A, June 1985.

FIG. 1 OXIDATION AND SULFIDATION OF B-1900 AT 850°C

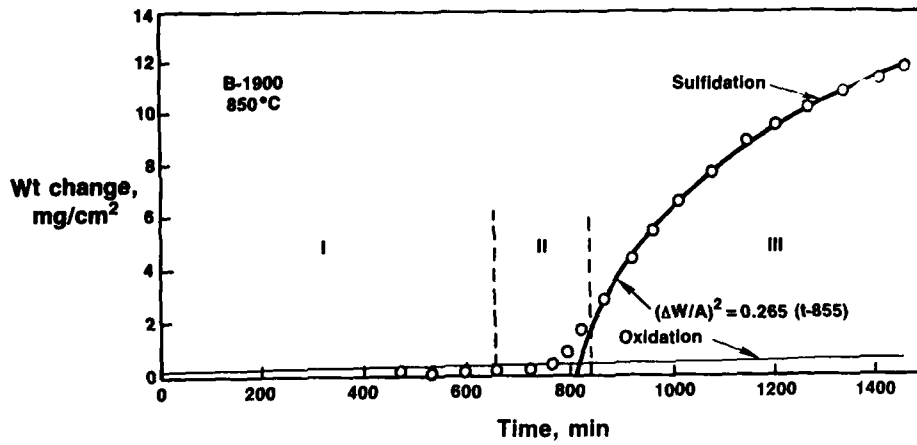


FIG. 2 ACTIVATION ENERGY FOR HOT CORROSION OF B-1900 ALLOY

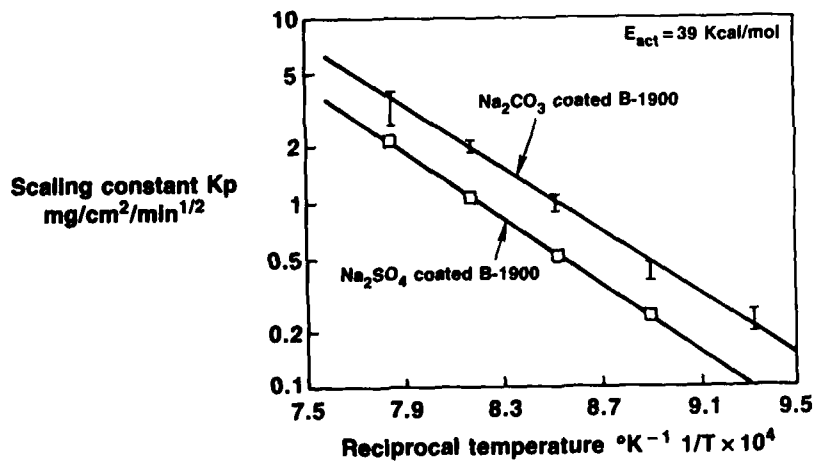


FIG. 3 CHROMIUM OXIDE ATTENUATES SULFIDATION CORROSION

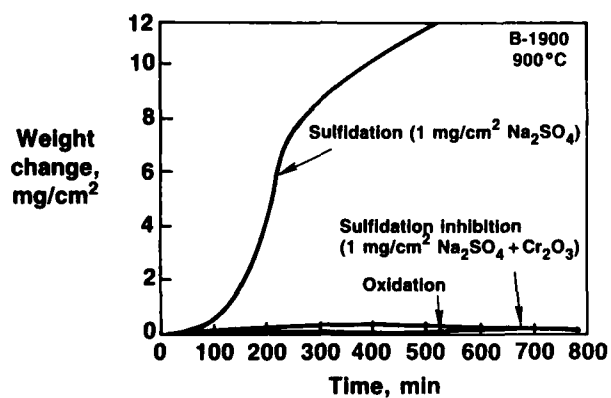


FIG. 4 THE ONSET OF SULFIDATION IS AFFECTED BY OXIDE SCALE PRECONDITIONING

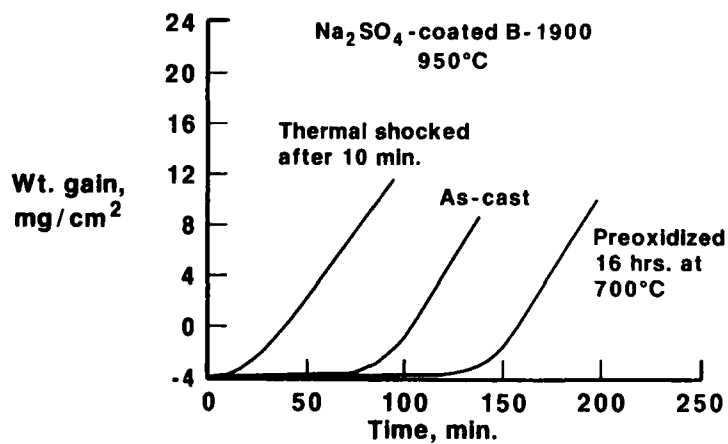


FIG. 5 YTTRIUM GREATLY ENHANCES OXIDE SCALE ADHERENCE OF NiCrAl AT 1150°C

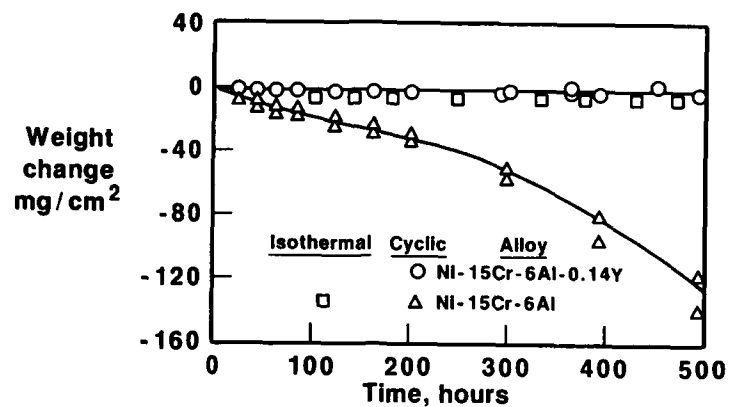


FIG. 6 AUGER SPECTRA OF NI-15Cr-6Al

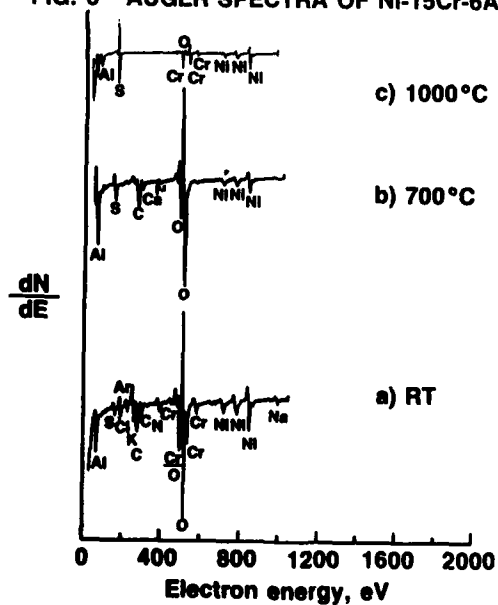


FIG. 7 YTTRIUM DECREASES SULFUR SURFACE CONCENTRATION

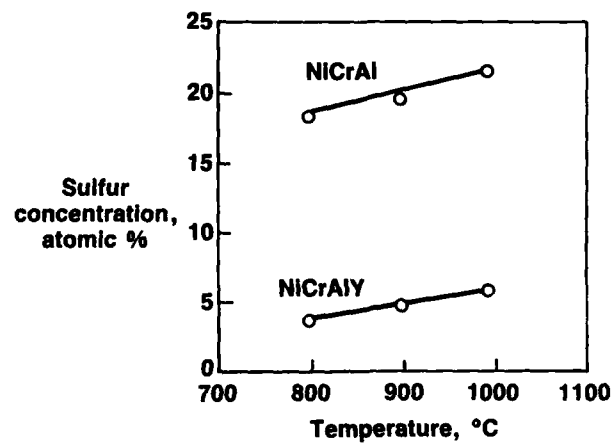
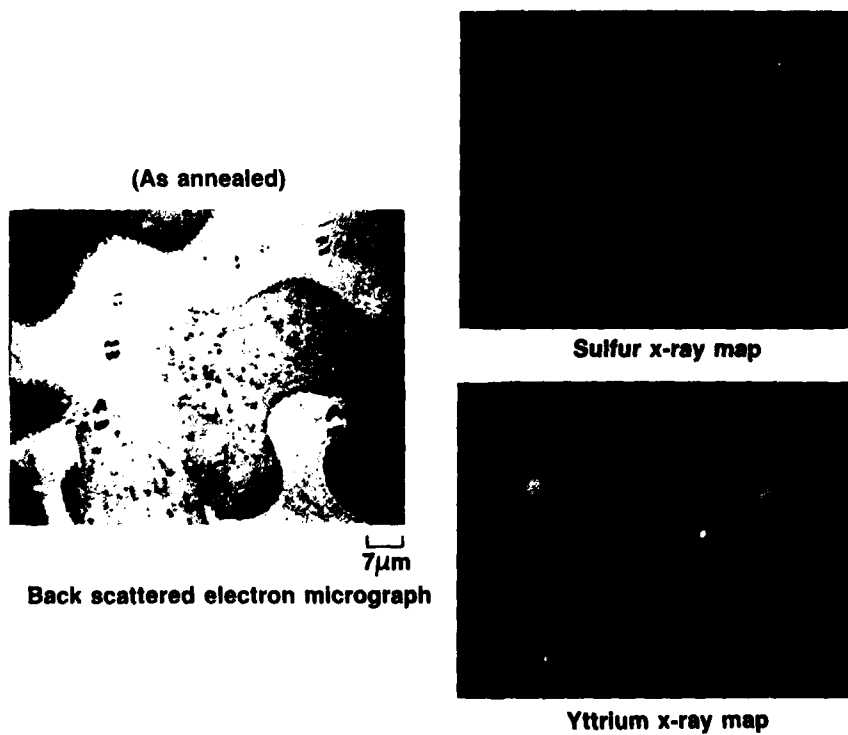
FIG. 8 YTTRIUM AND SULFUR RICH INCLUSIONS EXIST IN
NI-15Cr-6Al-1Y ALLOY

FIG. 9 CYCLIC OXIDATION PERFORMANCE OF COATING ALLOYS IMPROVED BY REDUCING SULFUR

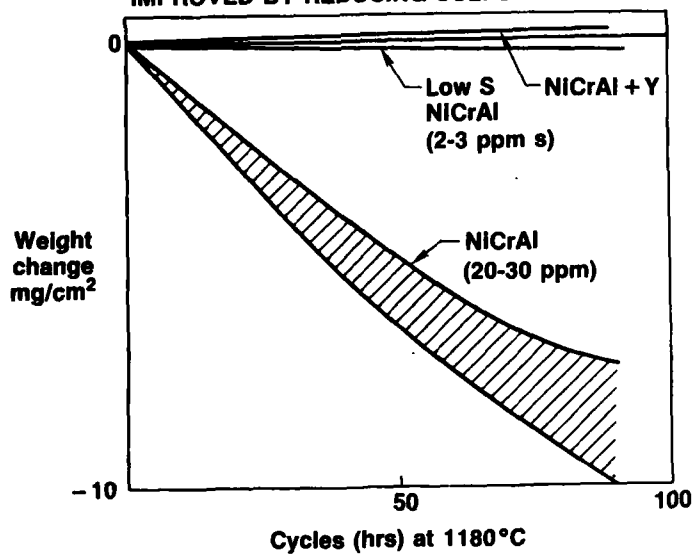


FIG. 10 SULFUR INCREASES OXIDATION RATES. YTTRIUM NEGATES SULFUR EFFECT

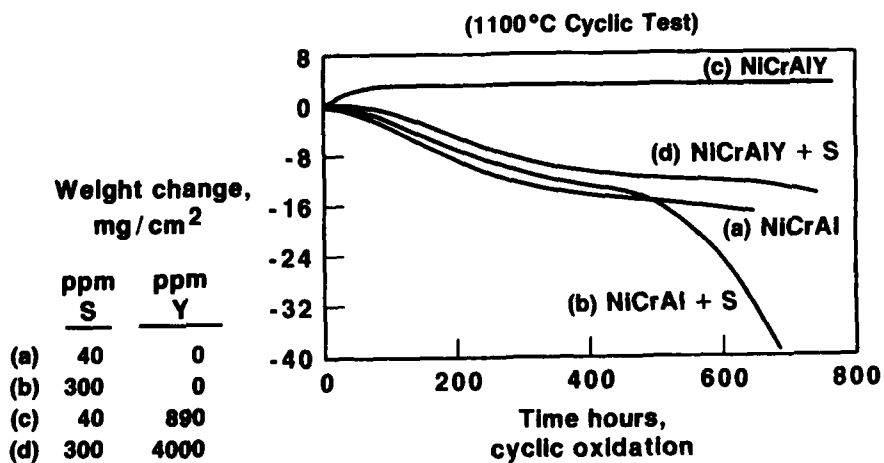


FIG. 11 BURNER RIG TEST RESULTS OF NiCoCrAlY COATED ALLOYS AT 1180°C

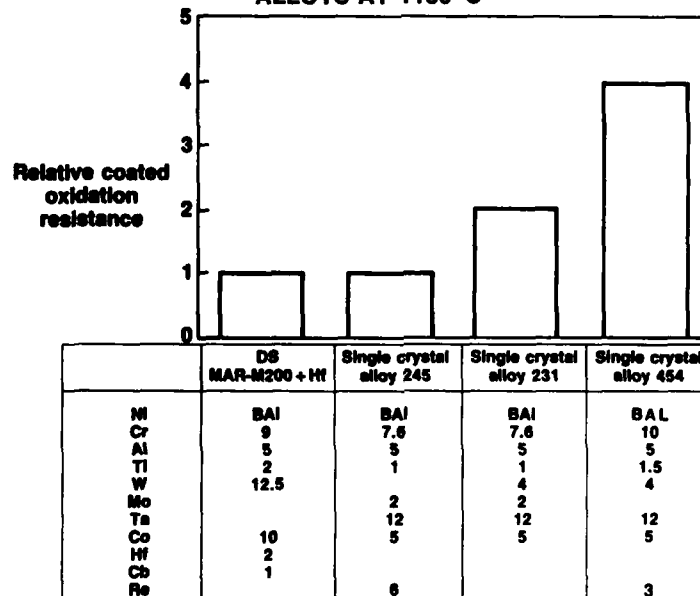


FIG. 12 LASER SURFACE MELTING IMPROVES OXIDATION RESISTANCE

1000°C-100 hrs, cyclic burner rig tests

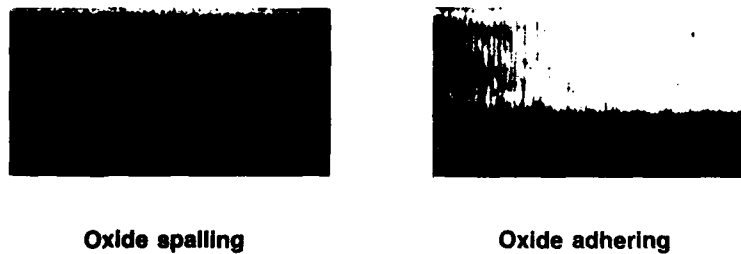
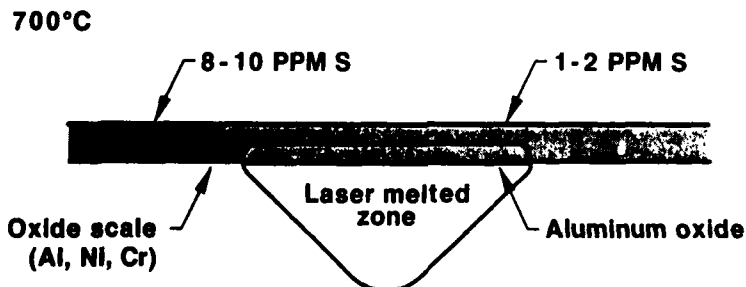


FIG. 13 LASER SURFACE REMELT REDUCES SULFUR CONTENT



MOLTEN SALT INDUCED HIGH TEMPERATURE DEGRADATION OF THERMAL BARRIER COATINGS

Serge ALPÉRINE

*O. N. E. R. A. Materials Science Department
B. P. 72, 92322 Chatillon Cédex, FRANCE*

ABSTRACT

Thermal barriers are now fairly well known as a new generation of protective coatings for components of the hot sections of conventional, diesel and turbine engines. The more performing system is a duplex coating consisting of a stabilized zirconia top coat ($\text{ZrO}_2 + \text{CaO}$, MgO , Y_2O_3 or CeO_2) generally air plasma sprayed on a $\approx 100 \mu\text{m}$ thick MCrAlY bond coat. The service degradation modes of such coatings have been extensively studied during the past ten years. Their failure mechanisms are generally thought of in terms of thermomechanical stress, thermal expansion coefficient mismatch and bond coat high temperature oxidation. Efforts are thus made to design ceramic and bond coat composition, microstructure and processing parameters, according to these requirements. However, degradation of thermal barrier coatings by hot corrosion processes and, more generally, by fused salt thin films related phenomena, should also be taken into account. In this paper, a review is given of the degradation modes that can be encountered when partially stabilized zirconia coatings are exposed to intermediate temperature range (from 650 to 950 °C) and sulphur and/or vanadium containing atmosphere. The interaction of the salt film with the coating is threefold : a chemical acidic or alkaline dissolution of the zirconia stabilizing oxide (CaO , MgO , Y_2O_3 or CeO_2) may occur, provoking zirconia tetragonal to monoclinic phase transformation and subsequent coating spallation on cooling. Fused salt may diffuse inside the ceramic microcracks network and solidify on cooling with a generation of extra stress inside the coating. Fused salt diffused throughout the microcracks network down to the ceramic/bond coat interface may also affect the MCrAlY bond coat according to the well described type I and type II hot corrosion processes. Careful distinction should be made between the working conditions encountered in diesel engines and marine turbines (relatively moderate temperature range and less refined fuel) and those involved in aircraft turboengines (higher temperature range and cleaner kerosene). An illustration of the hot corrosion resistance of a ZrO_2 -8wt% Y_2O_3 /NiCrAlY thermal barrier coating, plasma sprayed on a single crystal superalloy substrate, in a typical aircraft turbine environment (850 to 950 °C, Na_2SO_4 contamination) is given. Although no chemical destabilization of the ceramic coating occurred, thermomechanical failure and bond coat significant hot corrosion at temperatures as high as 950 °C could be observed.

INTRODUCTION

Thermal barriers are now fairly well known as a new generation of protective coatings for components of the hot sections of conventional, diesel and turbine engines. They consist essentially of a thick, thermally insulating layer of ceramic material (300 to 1500 μm) deposited on the metallic components to be protected. When the components are cooled internally, this layer provides a 50 to 150 °C temperature gradient between the inner and outer skin of the ceramic coating (figure 1); it also offsets temperature transients due to fast changes of engine regime (figure 2). The resulting effect is a possible increase of turbine or engine efficiency (increase of outlet gas temperature, reduction of component cooling fluxes) and/or components lifetimes (decrease of metallic parts skin temperature). Depending on the application envisaged, the service temperature of thermal barrier coatings (TBC) can be as low as 650 or 750 °C (diesel engines and marine turbines) and as high as 1100 or 1200 °C (hot stages of aircraft turbine engines).

Candidate ceramics for such applications must meet various criteria : low thermal conductivity, high thermal expansion coefficient (to minimize the mismatch between the ceramic part of the coating and the metallic substrate, which generates very high compressive stress in the ceramic on cooling) and superior chemical stability. Until now, the principal family of ceramic materials envisaged for thermal barrier coatings is that of partially stabilized zirconias (PSZ). Depending on the application, ZrO_2 is partially stabilized with alkaline earth oxides [1,2] (CaO , MgO) for the lower temperature range, or other oxides such as Y_2O_3 , CeO_2 and Yb_2O_3 [3-5] for the higher temperature range. The elaboration conditions also are of paramount importance for the integrity of the coating.

Only porous and/or microcracked coatings can accommodate the thermal expansion coefficient mismatch between ceramic and substrate ; such *porosity* and/or *microcrack network* can be obtained by physical vapor deposition (EB-PVD) [6] or air plasma spraying [7]. The presence of a ductile metallic bondcoat is also required for stress accommodation ; low pressure plasma sprayed MCrAlY alloys (M = Ni and/or Co and/or Fe) are generally used for this purpose [8], with the secondary benefit of providing an efficient protection of the substrate against the aggressivity of high temperature environment (high temperature oxidation and molten salt induced hot corrosion).

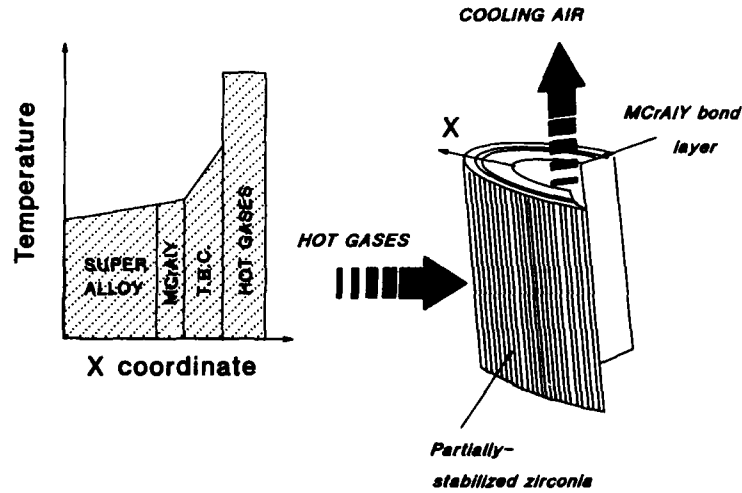


Figure 1 : Thermal barrier coatings ; schematic view representation of temperature gradients for internally cooled components

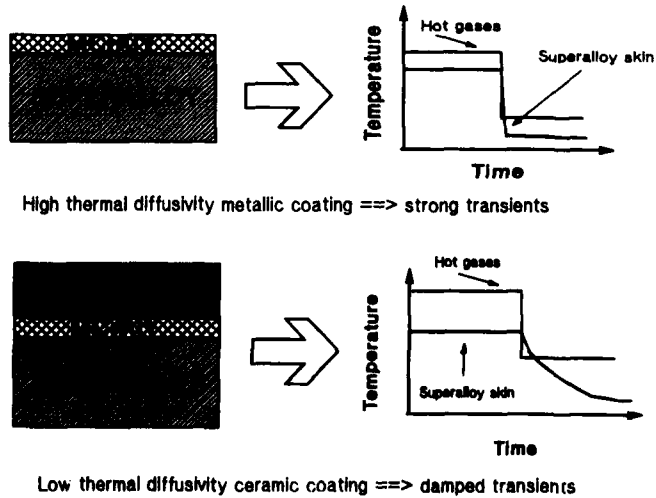


Figure 2 : Thermal barrier coatings : effect of the ceramic layer on temperature transients

The interaction of sulfate and vanadate molten salt films (issued from fuel impurities), at elevated temperatures, with the duplex MCrAlY + PSZ thermal barrier coatings is the matter dealt with in this paper. From the elements briefly recalled in the above paragraphs, it is possible to describe such an interaction according to three different approaches. A first approach -- which is the object of most concerned literature -- is to consider chemical interactions between the salt film and the zirconia coating. A second one takes into account a physical interaction between the same. A third approach is related to fused salt diffusion in the ceramic microcracks network and subsequent chemical attack of the MCrAlY bondcoat. These three forms of interaction will be detailed and reviewed with special emphasis on rare earth oxides stabilized PSZ. Distinctions will be made, whenever possible, between the different types of degradation expected according to the coatings composition (namely the nature of the stabilizing oxide) and environment (temperature, fused salt composition). Finally an illustration will be given through the description of cyclic hot corrosion tests performed in the laboratory, simulating 'aeronautic conditions', on yttria stabilized zirconia coatings.

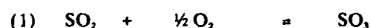
CERAMIC / FUSED SALTS CHEMICAL INTERACTION

More about gaseous and fused salt films environment...

Fused salt films are the consequence of more or less complex chemical reactions taking place between high temperature oxygen and nitrogen environment, ingested solid particles (such as sodium chloride, ashes or carbon residues) and impurities present in the engine fuel (such as sulphur, vanadium and to a lesser extent magnesium). The result of such reactions is the formation of various ionic compounds having relatively low melting points on the one hand, and of highly corrosive gaseous species on the other hand. At elevated temperatures, the former melt and may be retained by capillary forces at the surface of exposed components (as thin films) whereas the latter may dissolve into the fused salt film, according to thermodynamics, and therefore alter its acido-basic properties and its chemical reactivity. Obviously, if one wishes to examine and rationalize the chemical composition and the physical, chemical and electrochemical properties of such films, the relevant parameters are the atmosphere and fuel compositions (impurity levels), the working temperature *as it is in all parts into contact with both the salt and the exhaust gases* (which sets the solubility of gaseous species and corrosion products in the fused salt) and eventually the local pressure (which may alter such physical properties of the salt as melting point, vapor pressure and viscosity).

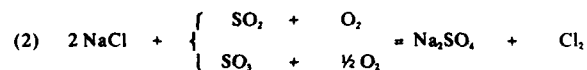
In this paper, we will limit ourselves to considering fused salt films build-up in an oxygen containing atmosphere, in the presence of ingested sodium and sulphur and/or vanadium fuel impurities. In such conditions the following compounds may form :

- (i) SO₂ and SO₃ gases in equilibrium :



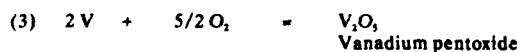
This equilibrium is shifted on the left hand side the higher the temperature. Typically, the equilibrium SO₃/SO₂ ratio in air is 6.08 at 627°C and only 0.11 at 927°C [9]. It is to be noted that the actual SO₃/SO₂ ratio may be lower than the equilibrium value due to kinetical limitation.

- (ii) Formation of sodium sulfate :



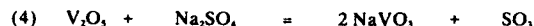
Under one atmosphere Na₂SO₄ is liquid between 884°C and about 950°C where it decomposes. Sodium chloride impurities present in marine turbines may lower significantly its melting point.

- (iii) Formation of vanadium compounds :



V₂O₅ is a very acidic oxide that melts at 690°C ; it can exchange Na₂O molecules with sodium sulfate (Na₂O being the most alkaline specie in Na₂SO₄ melts) and form many types of sodium vanadates less and less acidic as the number of exchanged Na₂O molecules increases [10]. One of the

most common sodium vanadate present in vanadium containing sodium sulfate melts is *sodium metavanadate*, NaVO_3 .



Sodium metavanadate also has a low melting point (630°C).

Zirconia stabilization

The major chemical interaction between plasma-sprayed PSZ and molten salt films relates to the zirconia stabilization concept. At 1 bar pressure, zirconia is crystallized according to three distinct polymorphs [11]: a high temperature cubic phase with fluorite structure (between 2340 and 2720°C) deforms into a lower temperature tetragonal phase ($1170^\circ\text{C} < T < 2340^\circ\text{C}$). At temperatures below 1170°C the tetragonal phase martensically transforms into a low temperature monoclinic phase [12]. This $t \rightarrow m$ transformation gives rise to an important volume increase (between 4 and 9 % according to the different authors) which causes any metal-zirconia bond to disrupt and thus prevents the use of pure zirconia for thermal barriers.

The $t \rightarrow m$ transformation is associated with a decrease of Zr^{4+} ions coordination (from 8 in the c and t phases to 7). If one partially substitute some tri- or divalent cations (Ca^{2+} , Mg^{2+} , Y^{3+} , Yb^{3+} , etc...) to Zr^{4+} in the ZrO_2 cationic sublattice by mixing ZrO_2 with the appropriate quantity of the corresponding oxides, the associated oxygen vacancies injection can prevent the occurrence of such a transformation, enabling the cation sublattice to retain a coordination of eight at low temperature. The same result can be obtained with oxides made of tetravalent cations where a cubic phase with coordination eight is maintained at low temperature (CeO_2). Note that such explanations are rather schematic and do not fully explain all ZrO_2 -oxides binary phase diagrams.

The materials thus obtained are called 'partially' (PSZ) or 'fully stabilized zirconias' (FSZ) depending on the quantity of stabilizing oxide introduced; in the PSZ the $t \rightarrow m$ transformation occurs at a lower temperature whereas in the FSZ it is completely offset (cubic phase is retained at room temperature).

Partial binary equilibrium phase diagrams of zirconia with CaO , MgO and Y_2O_3 (ZrO_2 -rich region) can be seen on figure 3, 4 and 5 respectively [13,2,14].

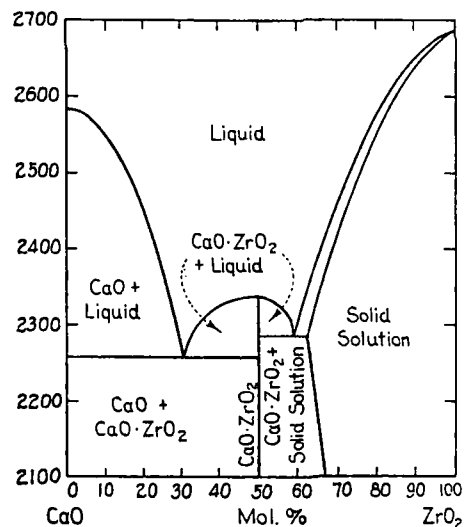


Figure 3: Equilibrium partial phase diagram of ZrO_2 - CaO (ZrO_2 -rich section) [13]

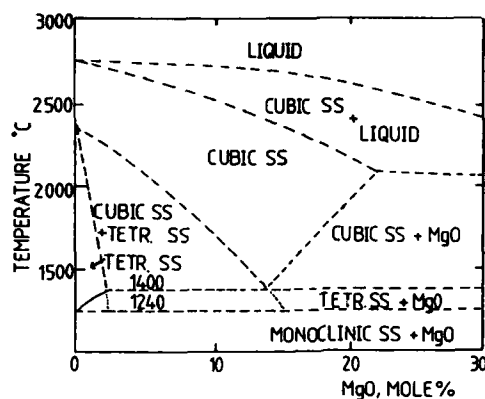


Figure 4: Equilibrium phase diagram of ZrO_2 - MgO (ZrO_2 -rich section) [2]

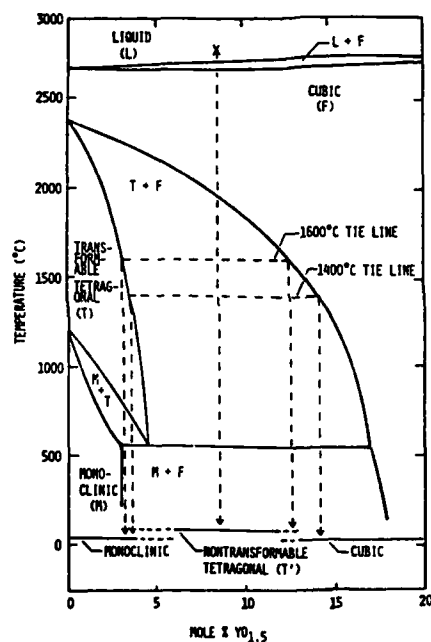
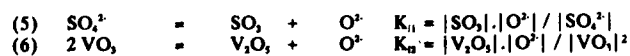


Figure 5: Partial phase diagram of ZrO_2 - Y_2O_3 (ZrO_2 -rich section) [3]

Possible reactions between the fused salt medium and the oxides

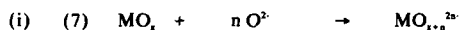
The chemical interaction between ZrO_2 , CaO , MgO , Y_2O_3 or CeO_2 and the fused salts essentially relates to the concept of oxoacido-basicity developed by Lux and Flood [15]. In sodium sulfate and/or vanadate melts the acido-basic equilibria can be written as follows:



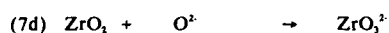
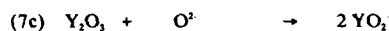
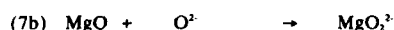
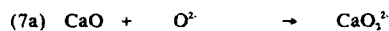
where $|X|$ represents the activity of specie X in the melt. The equilibrium constants K_i are thermodynamically set by the mass action law and temperature dependant. For instance, in pure alkaline sulfate melts, $K_1 = 10^{-22}$ at 707°C [16] and 10^{-19} at 900°C [17].

The basicity of the melt is expressed by the quantity pO^{2-} ($-\log|O^{2-}|$) measured on a logarithmic scale between 1 and pK , (just as the pH of aqueous solutions is measured at standard temperature between 1 and 14). The higher pO^{2-} , the higher the acidity of the melt. A direct consequence of equations (5) and (6) is that the melt is all the more acidic that SO_3 and/or V_2O_5 contents are high. An indirect consequence is that, at higher temperatures or lower oxygen partial pressure, equilibrium (1) is shifted towards the left hand side and the melt is more basic.

If one considers an oxide MO_x in contact with the melt, two different acido-basic reactions may take place :



which is a *basic dissolution* of the oxide ; relevant examples are :

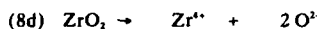
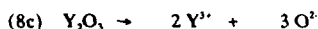
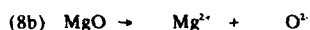


Such a basic dissolution will occur when the melt is more basic than the oxide (low pO^{2-} or very acidic oxides)

(ii) *Acidic dissolution* of the oxide :



or for the oxides involved in TBC :



Such an acidic dissolution will take place when the melt is more acidic than the oxide (high SO_3 or V_2O_5 contents or very basic oxides).

The amphoteric behaviour of many oxides in contact with sulfate/va-nadate melts can be illustrated by plotting the metal element solubility versus pO^{2-} . The curves such as that schematically presented on figure 6 can derive from thermodynamical calculations or from experimentation ; they all show a sharp minimum which corresponds to 'equal acidobasicity' of the oxide and the melt. The solubility of the metal on both side of this minimum is to be understood as cationic (acidic dissolution) and anionic (basic dissolution). From the knowledge of the value and the position of this solubility minimum of a given oxide on the acido-basic scale of a given fused salt at given temperature and P_{O_2} , valuable information can be derived concerning its dissolution mechanism. The chemical stability of different oxides in the same environment can also be compared if the $S = f(pO^{2-})$ curves are known.

Many authors performed solubility measurements of such oxides as NiO [18], Cr_2O_3 [19], Al_2O_3 [20], Fe_2O_3 [21] and Co_3O_4 [20] because the behaviour of such oxides in contact with fused salt deposits is of paramount importance for the understanding of classical hot corrosion phenomena of superalloys protected by passivating metallic coatings (aluminides or MCrAlY coatings). More recently Zhang and Rapp performed solubility measurements, at 900°C under 1 bar oxygen atmosphere, in pure Na_2SO_4 and $Na_2SO_4 - 30 \text{ mol\% } NaVO_3$ of CeO_2 (both melt compositions) and Y_2O_3 ($Na_2SO_4 - NaVO_3$ melt only) [22]. Equivalent data for Y_2O_3 in pure Na_2SO_4 at 927°C in 0.2 bar oxygen atmosphere are also available (experimental conditions are not very much different) [23]. The corresponding solubility- pO^{2-} curves are reproduced on figure 7 and 8 respectively. The comparison of these two curves gives the following information :

- (i) CeO_2 is significantly less soluble than Y_2O_3 in pure sodium sulfate.
- (ii) The acid-base properties of CeO_2 differ significantly in the two melts. The solubility minimums almost differ by two orders of magnitude. The presence of NaVO_3 in Na_2SO_4 shifts this minimum on the basic side of the $p\text{O}^{2-}$ scale, which means that CeO_2 behaves as a weaker acid. On the other hand the acid-base properties of Y_2O_3 seem to be less sensitive to vanadate additions.
- (iii) For both oxides, the fact that the slope of the acidic dissolution branch varies when NaVO_3 is added to Na_2SO_4 indicates that the acidic dissolution reaction differs in that case: Ce_2VO_4 (resp. YVO_4) forms instead of $\text{Ce}(\text{SO}_4)_2$ (resp. $\text{Y}_2(\text{SO}_4)_3$). The basic dissolution reactions remain the same (slope of the 'basic branch' unchanged).

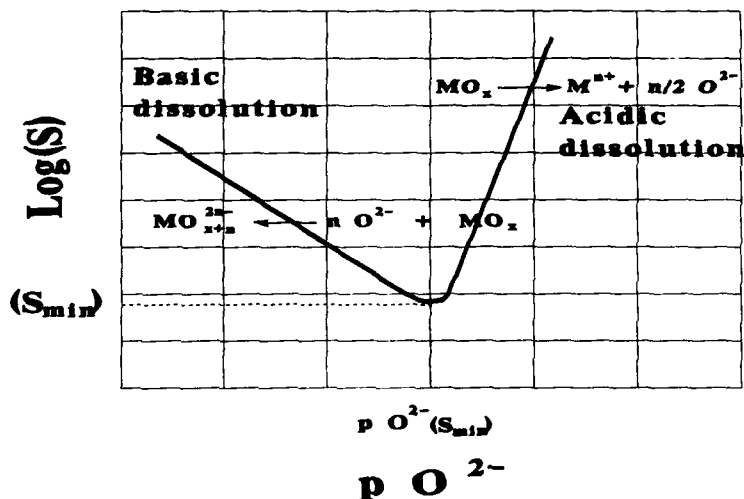


Figure 6 : Solubility - $p\text{O}^{2-}$ curve of an oxide MO_x in a fused salt medium

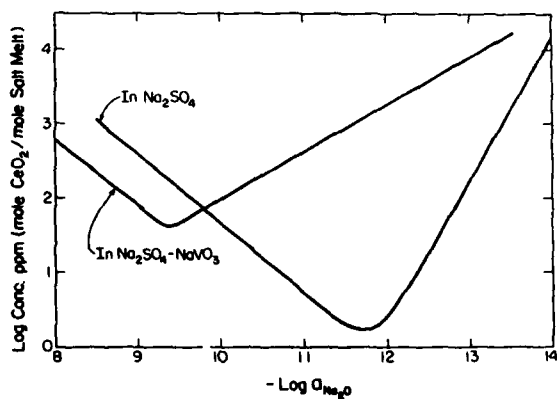


Figure 7 : CeO_2 solubility - $p\text{O}^{2-}$ curves in pure Na_2SO_4 and in Na_2SO_4 -30 mol% NaVO_3 at 900°C , under 1 bar oxygen [22]

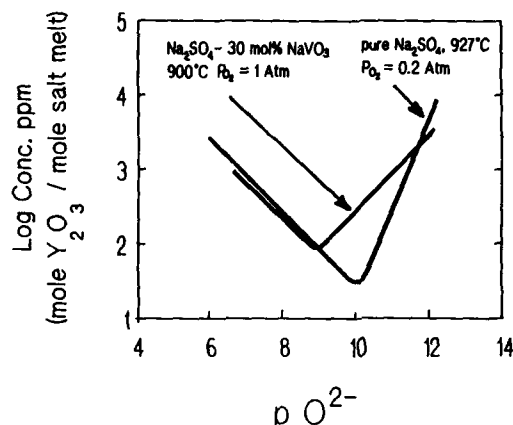


Figure 8 : Y_2O_3 solubility - pO_2 curves in pure Na_2SO_4 at $927^\circ C$ under 0.2 bar oxygen [23] and in Na_2SO_4 -30 mol% $NaVO_3$ at $900^\circ C$, under 1 bar oxygen [22]

Oxide/fused salt interface -- leaching phenomena

Let us consider the interface between the ceramic coating and the fused salt : it consists of the ceramic microcracks network, that the liquid salt has filled, down to a certain depth (figure 9a). Let us now consider the acidic dissolution of a given oxide, say Y_2O_3 (equation 8c) at the interface (ZrO_2 dissolution is not to be taken in real consideration). If we also consider that oxygen is renewed with some difficulty at the salt film surface, then equilibrium (1) is locally shifted so that SO_3 partial pressure vanishes at the fused salt/gas interface (figure 9b); in the same way the surface of the salt medium becomes less acidic (pO_2 decreases). There is a positive gradient of $[O^{2-}]$ within the salt film and a concomitant negative gradient of Y^{3+} solubility (figure 9b). The consequence is that the Y^{3+} cations formed by acidic dissolution of Y_2O_3 at the oxide/salt interface, which migrate towards the salt/gas interface, experience a strong solubility decrease ; thus, Y_2O_3 precipitates in the outer zone maintaining a $|Y^{3+}|$ gradient in the salt film and provoking further dissolution of the oxide at the oxide/salt interface. This leaching phenomenon has first been described by Rapp & Goto in the case of high temperature corrosion of superalloys and may be related to a general criterium [24] :

$$(9) \quad \left[\frac{\partial S}{\partial x} \right]_{x=0} < 0$$

where S is the anionic or cationic oxide solubility of the metallic element in the melt and x the euclidian coordinate perpendicular to and originating at the oxide/salt film interface (figure 9b).

The above paragraphs show that, if certain conditions of temperature and fused salt acidity are met, important depletion of the zirconia stabilizing oxides can take place. Local $t \rightarrow m$ transformation occurs which generates higher levels of stress upon cooling, crack growth and further fused salt penetration. This destabilization phenomenon is the major chemical interaction between TBC and the fused salt films.

Only a relatively limited number of publications are available reporting of experimentation on these phenomena. The experimental approaches approximately fall into four categories :

- (i) Experiments on pure oxides
- (ii) Experiments on bulk PSZ
- (iii) Furnace tests on coatings (plasma sprayed PSZ + plasma sprayed MCrAlY)
- (iv) Burner rig tests on TBC

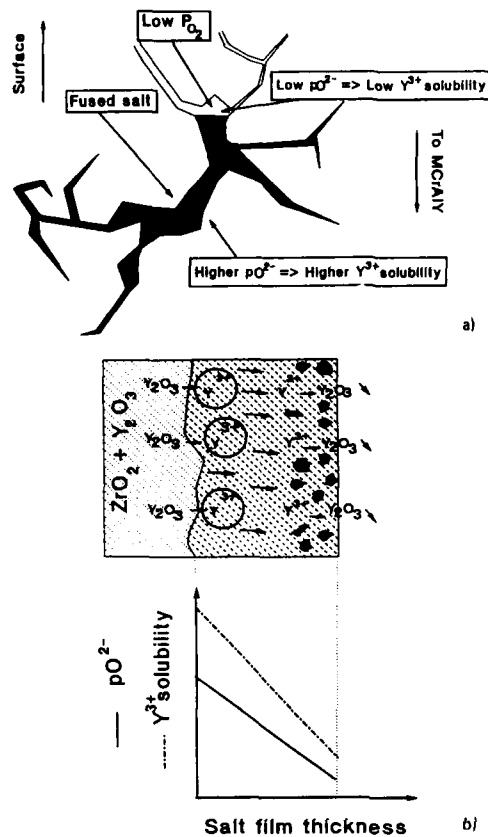


Figure 9 : Acidic leaching of Y_2O_3 in TBC :
 a) fused salt penetration in the microcracks network of the ceramic with low P_{O_2} at the salt/gas interface
 b) Y_2O_3 dissolution-precipitation mechanism inside the fused salt film ; corresponding pO^{2-} and Y^{3+} solubility gradients

Pure oxides

Jones and al. have studied the reactivity of ZrO_2 , CeO_2 [25] and Y_2O_3 [26] with sodium sulfate between 700 and 950 °C, under a SO_2 partial pressure varying between 0.5 and about 2800 Pa. The tests performed were of the 'crucible' type, in which oxide powder is added to Na_2SO_4 powder to form equimolar mixtures and heated 24 hours under a controlled air + SO_2 atmosphere. It appears that in the presence of such large quantities of sodium sulfate, the major reaction mechanism is one of **acidic oxide sulfation** leading to the formation of $\text{Zr}(\text{SO}_4)_2 \cdot \text{Na}_2\text{SO}_4$, $\text{Ce}(\text{SO}_4)_2 \cdot \text{Na}_2\text{SO}_4$ and $\text{Y}_2(\text{SO}_4)_3 \cdot \text{Na}_2\text{SO}_4$ mixed fused salts respectively. The reactivity of ZrO_2 is however limited to very high SO_2 partial pressures (unrealistic for gas turbine environments). Both other oxides do form eutectics with Na_2SO_4 that melt below 800 °C. Y_2O_3 is more reactive than CeO_2 (sulfation at 800 °C takes place at low $P_{\text{SO}_2} \approx 5 \text{ Pa}$ in the case of Y_2O_3 and at P_{SO_2} about 100 times higher for CeO_2). This reactivity sequence compares well with the respective acidity of the three oxides ($\text{ZrO}_2 > \text{CeO}_2 > \text{Y}_2\text{O}_3$) : the more acidic the oxide, the more acidic the melt has to be, to be able to attack it (the higher P_{SO_2} required for sulfation).

The same authors also have performed crucible tests to measure the high temperature reactivity of various oxides (among which ZrO_2 , CeO_2 and Y_2O_3) with vanadium compounds and vanadate/sulfate mixed fused salts [10]. The general philosophy is, indeed, that the reactivity is controlled by the difference of acidity between the oxide and the melt as summarized in figure 10. The addition of sulfate to vanadate modify the acidity of the melt, according to the value of P_{SO_2} in the above atmosphere.

		— INCREASING ACIDITY —>		
		Na_3VO_4	NaVO_3	V_2O_5
INCREASING ACIDITY ↓	Y_2O_3	NR	YVO_4	YVO_4
	CeO_2	NR	NR	CeVO_4
	ZrO_2	NR	NR	ZrV_2O_7 (BUT SLOWLY)
	GeO_2	$\text{Na}_4\text{Ge}_3\text{O}_{20}$	$\text{Na}_4\text{Ge}_3\text{O}_{20}^{(*)}$	NR
	Ta_2O_5	NaTaO_3	$\text{Na}_2\text{Ta}_4\text{O}_{11}$	$\alpha\text{-TaVO}_5$
		NR = NO REACTION		
		(*) AS PPT FROM H_2O SOL'N		

Figure 10 : Reactivity of pure oxides with various fused salts [10]

Bulk PSZ (mixed oxides)

This category of experiments differs from the previous one in the sense that one deals with actual alloyed ceramics. The activities of the different oxides may here depart from unity (case of pure oxides). Also the kinetics of reactions may significantly differ in the case of bulk materials exposed to molten salt media and in that of high specific surface oxide powders.

Nagelberg has studied the high temperature interaction of sintered ZrO_2 - 8wt. % Y_2O_3 samples with molten Na_2SO_4 and various Na_2SO_4 - NaVO_3 mixtures at 900°C under controlled O_2 + SO_2 atmosphere ($25\text{ Pa} < P_{\text{SO}_2} < 5000\text{ Pa}$) [27]. Again the tests were of the 'crucible' type. The progression of a zirconia monoclinic transformation front due to surface destabilization is observed (acidic leaching of Y_2O_3). The rate of progression is parabolic with time (within a good approximation), leading to the conclusion that the kinetic limiting factor is fused salt anionic diffusion inside the ceramic. The derived parabolic rate constants increase appreciably with increasing P_{SO_2} (K_p being proportional to P_{SO_2} in an extended P_{SO_2} range) and with the metavanadate content in the melt (K_p being proportional to $|\text{VO}_3|^{1/2}$). No appreciable ZrO_2 dissolution was observed.

Jones and al. studied the corrosion by vanadate salts between 700 and 900°C . of CeO_2 and Y_2O_3 stabilized zirconia massive samples elaborated through various processing routes (sintering, rapid solidification and single crystals) [28] and compared the results with those obtained on pure oxide in a previous study mentioned above [10]. Both 'crucible' and 'salt-spray' tests (salt deposit of $3\text{-}5\text{ mg/cm}^2$) were this time performed. The most surprising result is that CeO_2 stabilized zirconia suffers deeper vanadate attack than Y_2O_3 stabilized samples in equivalent conditions, which is contradictory to the behaviour of the pure oxides in the same environment [10].

One has to draw the conclusion that the acido-basicity of oxides does differ whether they are pure or mixed with a zirconia matrix. It seems also that the ceramic-to-salt molar ratio can play a significant role in controlling the extent of corrosion. These two assumptions set strong limits regarding the capacity of crucible test, on the one hand, and tests on pure oxides on the other, to give information that can be representative of thermal barrier hot corrosion resistance. Indeed, the role played by such important parameters as accessibility of the fused salt and concentration gradients in the films are thus ignored.

TBC laboratory testing and burner rig tests

Testing plasma sprayed TBC has the advantage of reproducing the interaction between the ceramic microcrack network and the fused salt film. It can be done in furnaces under controlled atmosphere (N_2 + O_2 + SO_2/SO_3) and salt deposition conditions (salt composition and film thickness), with monitored sample weight gains. It can also be done in burner rigs with a continuous inlet of fuel contaminants. In the latter case, however, the complexity of the environment prevents very precise degradation analysis of the coating.

Only few 'furnace testing' of TBC are reported. The authors generally focus on zirconia chemical destabilization. A general conclusion [29,30] is that Y_2O_3 acidic dissolution in PSZ only occurs in the presence of vanadium contamination, or with very acidic sodium sulfate melts (0.1% or 1% SO_2/SO_3 in air); MgO stabilized coatings generally degrade more rapidly in the same environment.

PHYSICAL INTERACTION BETWEEN CERAMIC AND FUSED SALT

Physical interactions between the fused salt environment should also be taken into consideration. Most of them relate to the very peculiar role played by the ceramic microcracks network in the thermochemical resistance of TBC. The plasma sprayed ceramic porosity can be seen as the result of two distinct phenomena during the elaboration process. The individual molten ceramic powder grains spread on the cooled substrate as they rapidly solidify (with columnar grain growth) and stack up like tiles (figure 11a), with some probable sintering points. The free space left between the droplets constitutes a more or less interconnected 'primary' microcracks network [31]. Microstructural observations also suggest [32] that the droplets experience transversal fragmentation upon cooling (figure 11 b), thus forming a 'secondary' microcracks network. It is believed that these networks somehow allow the ceramic to sustain the high compressive stresses it is submitted to on cooling, by a macroscopic deformation of the ceramic, sum of the partial closure of transversal microcracks [33].

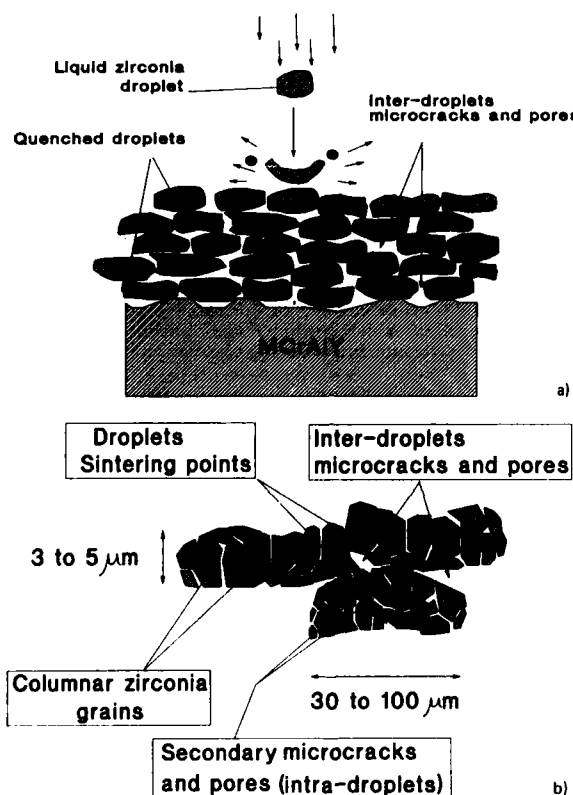


Figure 11 : Plasma sprayed zirconia microcracks networks :

a) formation of the 'primary network'

b) columnar grain growth inside the droplets and partial sintering ; 'secondary network'

If liquid salt, drained by capillary forces, penetrates some of the microcracks at high temperature, the solidification of the salt on cooling will prevent them to even partially close. Part of the benefit of the microcracks network will then be lost and the thermomechanical degradation of the coating will be more rapid. Such effects have been described by Hodge et al. [34]. Let us consider a 300 μm thick PSZ coating with a total porosity of 16% and an open porosity of 14%, which seem reasonable orders of magnitude [35]. The volume accessible to the fused salt for a unitary coating surface of 1 cm² is around 4.2 mm³. If the fused salt contamination rate in service is around 10 μg/cm².h for aeronautic turbines and 100 μg/cm².h for marine turbines [36], the volume of salt

deposited in 100 hours lies between ≈ 0.7 and 7 mm^3 . This means that, if capillarity allows salt penetration, about 16% of the accessible microcracks could be obturated in 100 h in aeronautic conditions; in marine turbines environment 100% of the accessible microcracks would be obturated in but 60 h. This calculation is obviously very crude, but suggests that an acceleration of the classical thermomechanical failure mechanism could actually take place in the presence of fused salt deposits. This phenomenon would be all the more important that thermomechanical solicitations take an important part as a degradation mode compared to chemical destabilization; in other words it is more likely to be noticeable in aeronautic turbines (high working temperatures, limited chemical interactions) than in marine turbines and diesel engines.

Another type of interaction can be thought of. PSZ are ceramic materials with exceptional toughness, which limits the propagation rate of small cracks under high stresses (thermomechanical fatigue). Several studies have shown that there may be a strong influence of the environment on ceramic or glasses crack growth [37]. The presence of adatoms such as water molecules [38] at the crack tips can dramatically lower the subcritical crack growth parameters of the material. If fused salts -- or salt vapors at very elevated temperatures -- penetrate at the tip of lateral cracks (parallel to the zirconia/MCrAlY interface) such an effect could maybe take place and again accelerate the thermomechanical degradation of the coating. No experimental work has been published, however, that supports this assumption.

CHEMICAL INTERACTION BETWEEN MCrAlY AND FUSED SALT

The third type of interaction between molten salts and TBC that should be taken into account is an interaction between the MCrAlY bond coat and the fused salt medium. Indeed, since the fused salt can diffuse inside the microcracks network of the ceramic, after a certain period of time it will be in contact with the bond coat at the bondcoat/PSZ interface. The chemical interaction between the fused salt and the metal alloy can no longer be described as purely acido-basic, since the MCrAlY oxidizes, forming a protective alumina and/or chromia scale [8]. Further interactions between the protective oxides and the melt relate to the acidic and basic fluxing concepts described above on the one hand, and to metal cations and/or oxygen diffusion promoting oxide growth on the other. Oxide spallation due to thermal cycling and consecutive fused salt penetrations provoking alloy sulfidation are also possible. All these phenomena have been extensively studied as a key to the understanding of hot corrosion of MCrAlY coated superalloys [39,40] and will not be detailed here. Relevant consequences concerning thermal barrier coatings are twofold: in the short run, the protective alumina scale considerably strengthens the MCrAlY/PSZ interface; in the long run, however, severe degradations of the MCrAlY and eventually the underlying superalloy can occur.

HOT CORROSION STUDY OF A THERMAL BARRIER COATED SINGLE CRYSTAL SUPERALLOY

The use of TBC in aeronautic turbine engines is generally planned for components working at very high temperatures (typically 1100°C and higher), significantly above the range of classical hot corrosion. However, some components may *locally* experience lower temperatures and subsequent salt deposit; the same can also happen at intermediate engine regimes. Furnace cyclic hot corrosion tests of typical aircraft components materials are presented. The same tests performed in the absence of fused salt deposit (cyclical oxidation) are reported as a reference.

Experimentals

The samples substrate is a CMSX-2 single crystal superalloy of nominal composition: Ni bal-5 Co-8 Cr-0.5 Mo-8 W-5.5 Al-1 Ti-6 Ta (weight percents). The rods were elaborated under $60^\circ\text{C}/\text{cm}$ temperature gradient with a solidification rate of 9.6 cm/h . They were heat treated 3 h at 1315°C in hydrogen for γ' dissolution and air quenched. Samples consist of 12mm diameter, 4mm high flat cylinders. The bond coat is low pressure plasma sprayed NiCrAlY (AMDRY 963 powder of nominal composition Ni-23 Cr-6 Al-0.4 Y, weight percents). The bond-coat consists of two $50 \mu\text{m}$ thick layers, sprayed successively with powders of equal composition but different granulometry (for the external layer, coarser powder was used to increase bond-coat roughness and consequent ceramic to metal adherence). Surface preparation of the samples, transferred arc cleaning parameters, plasma spraying parameters and diffusion post-treatments are described elsewhere [41]. The thermal barrier is air plasma sprayed ZrO_2 -8wt.% Y_2O_3 . The thickness of the ceramic coating is $400 \mu\text{m}$ deposited in two steps starting from MEL PSZ powder. The surface preparation operations and air plasma spray parameters are detailed in [41].

High temperature testing of these samples was performed at 850 and 950°C . Thermal cycling between 200°C and the test temperature is insured by an automatic device; each cycle runs as follows. The samples are introduced into a furnace maintained at the test temperature (temperature rise in about ten minutes for the samples) and remain at constant temperature for one hour

; they are then withdrawn and quenched with forced air convection until they reach 200°C (in about four minutes) and finally reintroduced for the next cycle.

Cyclic oxidation tests are run in air in separate furnaces. For hot corrosion tests, sodium sulfate contamination is added : the samples are coated with Na_2SO_4 by spraying a 80g/l aqueous solution of this salt on the test pieces heated at about 200°C. Sodium sulfate is renewed every 50 to 100 cycles, so as to obtain a contamination rate of $10 \mu\text{g}.\text{cm}^2.\text{h}^{-1}$. Visual observation and weight variation measurement are performed every 20 cycles during the first 100 cycles and every 50 cycles from there on. Optical microscopy, SEM/EDS analysis and X-ray diffraction measurements were performed on as sprayed and corroded samples.

Results

As sprayed samples

A cross section of as sprayed samples can be seen on figure 12. X-ray diffraction indicates that the as sprayed PSZ is mainly composed of the metastable, non transformable, high yttrium content t' phase [42], quenched from the cubic state during plasma spraying. No monoclinic phase was observed in as sprayed samples.

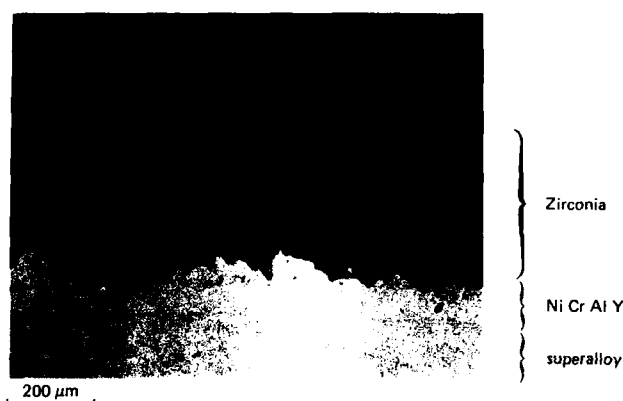


Figure 12 : TBC coating on CMSX-2 superalloy ; as sprayed

850 °C degradation

The mass variation of the samples as a function of the number of cycles can be seen on figure 13. The samples exposed to sodium sulfate show external macrocracks on their edges after about 300 cycles. This local phenomenon, which is being accentuated until 900 cycles are reached, accounts for the important weight losses sustained by the samples. After 900 cycles, the flat faces of the sample do not show any external macrocrack. No evidence of PSZ desatabilization was found (XRD diagrams are unchanged). A cross section of such a sample can be seen on figure 14. At this temperature, a thin but continuous alumina layer has developped at the NiCrAlY/Zirconia interface. Beneath this alumina layer, some Cr_2O_3 is present. Internal oxides and sulfides can be seen in the NiCrAlY, but this penetration is limited to the upper layer of the bond coat (50 μm).

The samples exposed to an oxidizing environment, only suffer a very moderate and regular weight gain, corresponding to the formation of a protective alumina layer at the PSZ/NiCrAlY interface. Very few oxide penetrations are observed after 650 cycles (figure 15) and the coating is still very healthy.

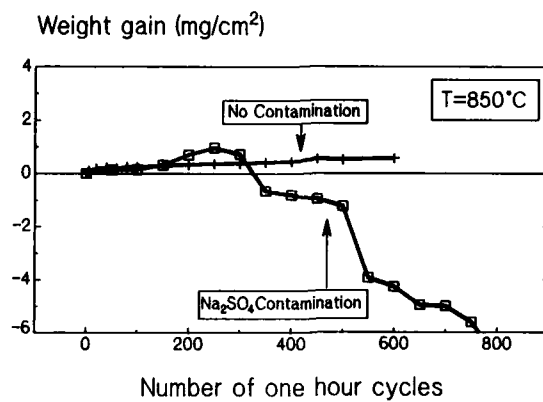


Figure 13: Degradations at 850 °C ; weight gain curves for oxidised and corroded samples

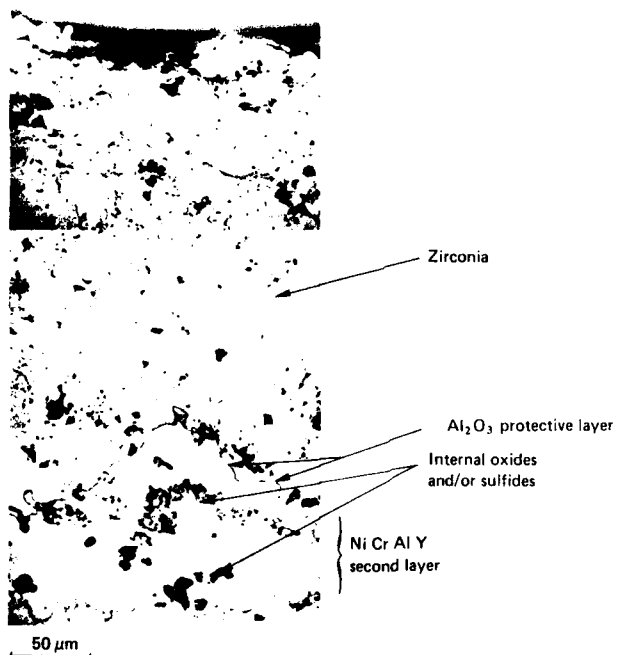


Figure 14: Cross section of a sample flat side after 900 cycles of corrosion at 850 °C

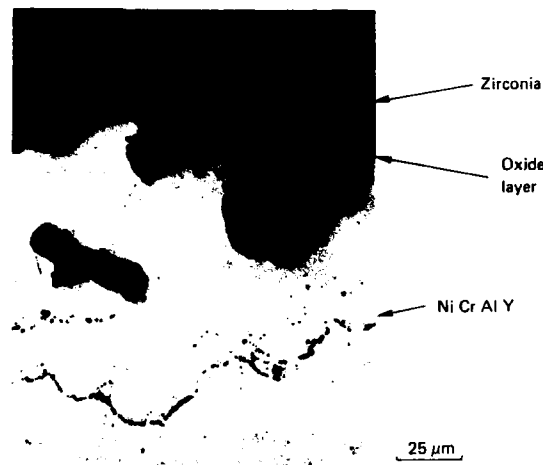


Figure 15: Cross section of a sample flat side after 650 cycles of oxidation at 850 °C ; detail of the zirconia/NiCrAlY interface

950 °C degradation

The weight gain versus number of cycle curves of corroded and oxidized samples at 950 °C can be seen on figure 16. Samples exposed to fused salt environment experience a weight gain during the first 25 cycles corresponding to fast alumina growth at the metal/oxide interface. Significant weight losses are then observed ; after 200 to 300 cycles, zirconia pieces falls off from the edges of the samples, rendering weight measurements difficult to interpret. After but 100 cycles, circular macrocracks are visible along the edges of the cylinders (figure 17), whereas none can be seen on the flat sides. Major cracks run parallel to the metal oxide interface some ten micrometers above, as often observed. After 300 cycles, poorly protective oxides such as $\text{Ni(Al,Cr)}_2\text{O}_4$ spinels have grown inside the NiCrAlY bond-coat. After 550 cycles, deep pits are present in the NiCrAlY, almost reaching the substrate in some places. The cristallographic structure of zirconia has scarcely changed during this test : until 400 cycles X-ray diffractograms are identical to those obtained on as-sprayed specimens ; from then on very small amounts of monoclinic phase (≈ 1 wt.%) can be detected. The diffractograms taken in the outer zone of the zirconia layer are identical to those taken in the inner zone of spalled ceramic fragments.

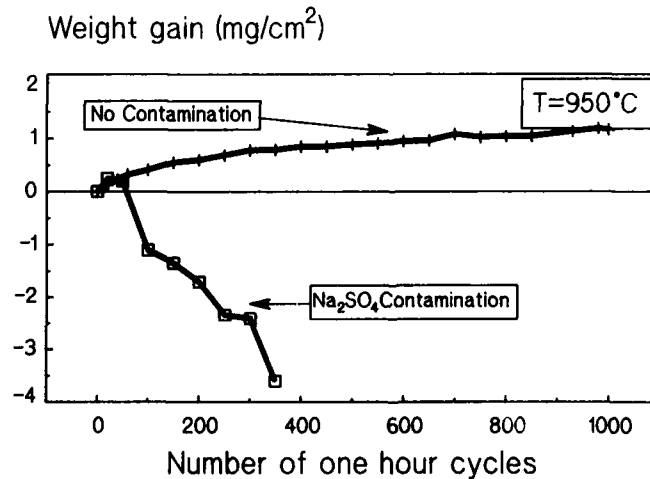


Figure 16: Degradations at 950 °C ; weight gain curves for oxidised and corroded samples

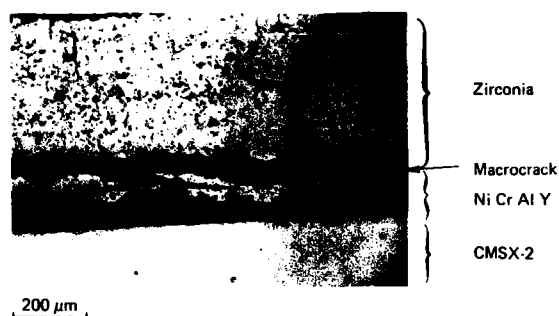


Figure 17 : Cross section of a sample edge after 100 cycles of corrosion at 950 °C

Oxidized samples show a very good resistance to thermal cycling at 950 °C (figure 16). Even after 1000 cycle, no spallation of the ceramic occurred, despite the usual presence of circular macrocracks on the samples edge. Only limited internal oxidation has taken place after 300 cycles, which seem to evolve very slowly until 1000 cycles.

DISCUSSION

One of the first conclusions that can be drawn from these experiments, is that, in this particular case, almost no chemical interaction between the PSZ and the fused salt has taken place (no zirconia destabilization). This is not very surprising if one considers the acidobasicity of pure Na_2SO_4 in the absence of SO_2/SO_3 external adduction : pure Na_2SO_4 is a very weakly buffered medium in which pO^2 lies about 10 at 900 °C [17]. This value is very close to the minimum solubility of pure Y_2O_3 at 927 °C in pure Na_2SO_4 (figure 8). If one supposes that neither the pO^2 scale extension (pK, value), nor the position of this solubility minimum vary a lot between 850 and 950 °C (which sounds reasonable), and that the solubility of Y_2O_3 allied to ZrO_2 is not very different from that of the pure oxide, very limited dissolution of Y_2O_3 was to be expected, which is confirmed by our data. However, our observations show very significant differences between the samples thermally cycled in the presence or in the absence of Na_2SO_4 contamination. This clearly indicates that one or more of the other degradation modes envisaged above has taken place.

The differences between the environmental resistance of the bond coat in the presence and the absence of salt contamination clearly show that some fused salt has found its way through the microporosity of the ceramic to the ceramic/metal interface and has attacked the bond-coat. The bond-coat chemical composition is such, however, that it is well suited to resist such hot corrosion.

If one considers thermomechanical fatigue of the coating, one has to distinguish between the flat sides of the samples where the solicitations are relatively moderate because the temperatures of the tests are moderate compared to 1100 °C -- for which the coating is designed -- and the edges where local small curvature radii can induce stress concentration. Only few thermomechanical damages are seen on the flat sides, which renders difficult to appreciate the role played by the fused salt in such a degradation. On the other hand, the presence of Na_2SO_4 seem to dramatically aggravate thermomechanical degradations in the stressed regions of the samples, at 850 °C as well as at 950 °C. The 850 °C effect is probably related to microcrack obstruction by solid sulfate on cooling (as described above). However, at 950 °C, most of the sulfate should have decomposed and very limited effects should have been observed. Two interpretations of this 950 °C effect can thus be proposed : the first relates to an influence of penetrating sulfate vapor at the microcrack tips provoking subcritical crack growth. The other one is an eventual remanence of molten sulfate at temperatures higher than the usual 900 °C, due to increased local pressure (capillary forces inside small pores for instance). We do not have at the moment direct proofs confirming one of these assumptions.

GENERAL CONCLUSION

Thermal barriers coatings are complex materials involving thermomechanical resistance of very heterogeneous bonds (ceramic-metal), which can only be obtained by sophisticated elaboration processes and carefully designed elaboration parameters (such as bond-coat and ceramic compositions and plasma spray parameters). Partially stabilized zirconia is the most important family

of ceramics envisaged for thermal barrier applications. The interaction of such coatings with fused salt films in high temperature corrosion environment, is also a complex multifold phenomenon.

Such an interaction can be of a chemical nature. It can be rationalized by using the Lux-Flood fused salt oxoacido-basicity concept. Various oxide solubility measurements in different fused media at different temperatures and O_2 partial pressures are required as a base of discussion. These measurements have been accompanied by many burner-rig or laboratory tests on pure or mixed oxides. The following points can be made :

- (i) *There is no significant interaction between ZrO_2 and the fused salt environment envisaged (sulfates and/or vanadates)*
- (ii) *Chemical interaction mainly consists of an acidic dissolution of the zirconia stabilizing oxide, which causes zirconia tetragonal to monoclinic transformation and coating failure on cooling.*
- (iii) *This acidic leaching phenomenon is of paramount importance for marine and industrial turbines where the environment is more acidic due to higher vanadium content in the fuel (higher vanadate concentrations in the melt) and/or higher sulfur contents (higher P_{SO_2} in the melt). Cerium oxide seems to be more resistant in this environment than yttrium or magnesium oxide.*
- (iv) *TBC functioning in aeronautic turbines do not suffer zirconia destabilization (cleaner fuels).*

Corrosion of the MCrAlY bond-coat can be a secondary source of degradations for thermal barrier coatings. According to the temperature range and fuel composition, type I or type II hot corrosion can take place. However, MCrAlY bond-coats are well designed to resist such attacks, especially if it is low pressure plasma sprayed.

Finally, physical interaction between the ceramic layer and the salt film can also be encountered (microcrack obstruction and/or subcritical crack growth enhancement in the ceramic), aggravating the typical thermomechanical failure of the TBC. The effect is all the more spectacular that the thermomechanical stress on the coating is high (the higher the temperature -- without exceeding the salt decomposition temperature -- and the frequency of cycling). Such effects could be observed at temperatures as high as $950^\circ C$. This third family of fused salt induced effects could be highly deleterious to complex shaped components with local low curvature radii.

ACKNOWLEDGMENTS

The author gratefully acknowledges the help of L. Lelait for fruitful discussions and R. Mévrel for reviewing the manuscript.

REFERENCES

- [1] J.M. Marder, T.E. Mitchell & A. H. Heuer, *Acta, Metall.* **31** (3) (1983), p.387-395
- [2] C. F. Grain, *J. Am. Ceram. Soc.*, **50** N° 6 (1967), p.288-290
- [3] R. A. Miller, R. G. Smialek and Garlick, *Science and Technology of Zirconia, Adv. of Ceramics*
- [4] P.A. Siemers & D. W. McKee, US patent N° 4,328,285
- [5] S. Stecura, *Thin solid films*, **150** (1987) p. 15-40
- [6] J.W. Fairbanks, R.J. Hecht, *Materials Science and Engineering*, **88** (1987) 321-330.
- [7] S. Stecura, NASA TM 78976 (1976).
- [8] R. Mévrel and R. Morbioli First international Congress 'High-Tech-Materials and Finishing' Berlin, March 12-14 1989
- [9] K. H. Stern & E.L. Weise *Natl. Stand. Ref. Data Ser., Natl. Bur. Stand.*, N° 7 (Sulfates), 1966
- [10] R. L. Jones, C. E. Williams & S. R. Jones, *Journal. of electrochem. Soc.* **133** N° 1 (1986), p.227-230
- [11] A. H. Heuer, M Rühle, *Science and Technology of zirconia, Adv. in Ceramics* **12** (1985), p. 1-13
- [12] E. C. Subbarao, *Science and Technology of Zirconia, Adv. in Ceramics*, **2** (1981) p. 1-24

- [13] V. S. Stubican, J. R. Hellman, Science and Technology of Zirconia, Adv. of Ceramics **3** (1981) p.25
- [14] M.G. Scott, J. Mat. Sci., **10** (1975), p.1527-1535
- [15] H. Lux, Z. Elektrochem., **45** (1939) p.303
- [16] L.M. Gribaudo, J.J. Rameau, Rev. Intern. Hautes Tempér. Réfract.-Fr, **20** (1983), p.89
- [17] C. A. C. Sequeira, M. G. Hocking, Brit. Corr. J., **12** (1977), p.157
- [18] D. K. Gupta & R.A. Rapp, J. Electrochem. Soc., **127** (1980), p. 2194
- [19] Y. S. Zhang, J. Electrochem. Soc., **133** (1986) , p. 655
- [20] P. D. Jose, D. K. Gupta & R.A. Rapp, J. Electrochem. Soc., **132** (1985), p. 735
- [21] Y. S. Zhang & R.A. Rapp, J. Electrochem. Soc., **132** (1985), p.734
- [22] Y. S. Zhang & R. A. Rapp, Corrosion-Nace, **43** N° 6 (1987), p. 348-352
- [23] M. L. Deanheart & K. H. Stern, J. of Electrochem. Soc., **129** N° 10 (1982), p. 2228-2232
- [24] R. A. Rapp, K. Goto, in 'Proc. of the Fused salt Symp. II', J. Braunstein Editor, The Electrochemical Soc., Princeton (1979)
- [25] R. L. Jones, S.R. Jones and C. E. Williams, J. Electrochem. Soc. **132** N° 6 (1985), p. 1498-1501
- [26] R. L. Jones, D. B. Nordman & S. T. Gadomsky, Metallurgical Trans. A, **16a** (Feb. 1985), p. 303-306
- [27] A. S. Nagelberg, J. Electrochem. Soc., **132** N° 10 (1985), p. 2502-2507
- [28] R. L. Jones & C. E. Williams, Surf. and Coatings Technol. **32** (1987), p. 349-358
- [29] D. W. Mc Kee & P. A. Siemers, Thin Solid Films, **73** (1980), p. 439,445
- [30] J. W. Vopgan, & A. R. Stetson, NASA CR-167852, Jan. 1982
- [31] D. S. Suhr, T.E. Mitchell & R. J. Keller, Science and Technology of zirconia, Adv. in Ceramics **12** (1985), p. 503-517
- [32] L. Lelait & S. Alperine, to be published
- [33] D. L. Ruckle, Thin Solid Films, **73** N° 2 (1980), p.455-461
- [34] P. E. Hodge, R. A. Miller & M. A. Gedwill, Thin Solid Films, **73** N° 2 (1980), p.447-453
- [35] F. Gitzhofer, Thesis, Limoges, 1988
- [36] C. Duret-Thual, R. Morbioli & P. Steinmetz, 'A guide to the control of high temperature corrosion and protection of gas turbine materials', O. Morocutti Ed. Comission of the European Communities, 1986
- [37] R. F. Pabst & G. Popp, Fracture Mechanics of ceramics 5, Plenum publishing, 1983, p.305-315
- [38] W. Tradinik, A. Bornhauser & R. F. Pabst, Fracture Mechanics of ceramics 5, Plenum publishing, 1983, p.317-336
- [39] R.A. Rapp, Corrosion-Nace, **42** N° 10 (1986), p.568-577
- [40] P. Steinmetz, C. Duret & R. Morbioli, Mat. Sci. and Techn., March 1986 **2**, p. 262-271
- [41] S. Alperine & P. Steinmetz, R.T. ONERA N° 5/3673M, Jan. 1987
- [42] C. A. Anderson & T. K. Gupta, Science and Technology of zirconia, Adv. in Ceramics **3** (1981), p. 184-201

HIGH TEMPERATURE OXIDATION OF Al-Li ALLOYS

by

P G Partridge
Materials and Structures Department
Royal Aerospace Establishment
Hampshire GU14 6TD UK

SUMMARY

Lithium additions increase the oxidation rate of Al-alloys in the solid and liquid states. At elevated temperatures in the solid state lithium diffuses rapidly through the aluminium alloy and through oxidised surfaces to become oxidised preferentially at the oxide/air interface where it forms non-protective oxidation products. The consequent lithium depletion causes changes in the near surface microstructure and hardness to depths of up to 800 μm depending on the temperature and exposure times. Depleted surface layers can lead to substantial reductions in the strength of thin sections. Procedures for minimising lithium depletion during processing of Al-Li alloys are discussed.

Oxidation in the liquid state is important in casting, in fusion welding and in rapid solidification processing and the behaviour of Al-Li alloys under these conditions is described.

1 INTRODUCTION

The development of Al-Li alloys with low density and high specific modulus is well documented in the International Al-Li Conferences over the period 1980-1987¹⁻³. The alloys are normally produced by the ingot chill casting route, but rapid solidification processing (gas atomisation or planar flow casting) and mechanical alloying techniques are also being developed. The compositions of some commercial and experimental alloys are listed in Table 1 together with their processing routes. There have been several excellent reviews of the microstructure, processing^{8,9} and mechanical properties^{1-2,10} of Al-Li alloys and these aspects will only be referred to in this paper when relevant to the oxidation behaviour. A feature of all Li-containing Al-alloys is their reactivity at elevated temperatures with oxygen or water vapour. In the solid state the rate of oxidation can be one or two orders of magnitude greater than for Li-free alloys and explosive reactions can occur with molten Al-Li alloys in contact with water. It is therefore a tribute to the aluminium industry that the problems associated with the manufacture of Al-Li alloys have been overcome and large ingots are now becoming available for conversion to rolled, forged and extruded products¹¹.

The potential reduction in weight and hence cost savings predicted for Al-Li alloy structures has led to rapid application of Al-Li alloys in the aerospace industries. The effect of elevated temperature oxidation during heat treatment is therefore of particular interest. Several papers have dealt with the elevated temperature oxidation of Al-Li alloys in various environments (Table 2) but many aspects require further investigation and there are conflicting reports on the basic oxidation behaviour and on the effect of oxidation on mechanical properties. A review of some of the published data is presented in this paper and their significance for the commercial processing of Al-Li alloys is discussed.

2 OXIDATION OF Al-Li ALLOYS IN THE SOLID STATE

Surface oxidation products are readily visible on the surface of Al-Li alloys after exposure at $\sim 500^\circ\text{C}$ for times greater than 20 minutes. Coincident with the surface oxidation the following changes occur in bands below the surface:-

i Lithium and sometimes magnesium depletion.

ii Depletion of δ' (Al_3Li) precipitate in peak aged and of δ (Al_3Li) precipitate in overaged Al-Li alloy.

iii Recrystallisation and grain growth in unrecrystallised sheet.

iv Reduction in hardness.

v Formation of pores or LiH particles.

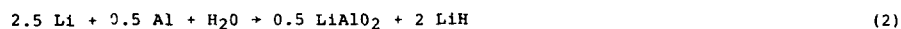
The oxidation products formed on Al-Li alloys and the experimental evidence for the sub-surface changes are described below.

A summary of the oxidation studies reported for binary and ternary Al-Li alloys is given in Table 2. These have included exposure to vacuum and various gaseous environments (eg air, Ar, H_2 , N_2 and CO_2/N_2 and O_2/Ar mixtures) in dry and moist conditions at temperatures up to 580°C and for times up to 50 h. Weight gain data and X-ray and electron beam analytical techniques have been used to relate the surface

oxidation products to the oxidation conditions. Oxidation was found to be sensitive to moisture^{13,19,21} which could lead to an increase in hydrogen content^{13,21,24}.

2.1 Surface Oxidation Studies

Lithium oxidises preferentially at the free surface of Al-Li alloys and many oxidation reactions are thermodynamically favoured²¹. The following reactions 1 - 4 are in order of decreasing ΔG , the free energy change, and lead to the products most frequently detected on Al-Li alloy surfaces:-



The mass and volume changes that occur when lithium metal is converted to these solid oxidation products are given in Table 3. A substantial increase in weight occurs in all the examples with the greatest increase for the Li_2CO_3 phase and only Li_2O has a volume ratio less than unity.

Ahmad²³ investigated the oxidation of 8090 alloy at the SHT temperature (530°C) in air. The early stages of oxidation were studied by Auger electron spectroscopy (AES) with depth profiling using inert gas ion sputtering; the sputter etching rate was ~ 20 nm/min. An elemental distribution depth (sputtering time) profile for a ground and etched surface is shown in Fig 1; the surface is completely covered by Al_2O_3 . The effect of annealing in air for times up to 30 min at 530°C is shown in Fig 2. After annealing for short times (<10 min) Al and Mg oxides coexist, however after 30 min the outermost surface is completely covered by oxidised Li with Mg only appearing after 10 min sputtering. With increasing time more Li diffuses from the bulk to the surface and is preferentially oxidised, whilst the rate of Mg oxidation slows down. Li appears to diffuse faster than Mg through both the metal and oxide. The oxide $\text{AlLi}_5\text{AlO}_5$ increased with time, but Li_2CO_3 was present after 5 min and became the dominant oxidation product; after 60 min γLiAlO_2 was detected.

Holdway and Bowen²⁶ also found Li_2CO_3 to be the dominant oxidation product on 8090 in air; X-ray intensities after 15 min and 1 h at 530°C are shown in Figure 3. Only the spinel γLiAlO_2 and Li_2CO_3 were detected. Other studies on 8090 at 500°C²⁰ suggested Li_2O occurred in dry air and LiAlO_5 in moist air. Results obtained for 2090 alloy oxidised at 550°C in dry and moist air showed γLiAlO_2 , δLiAlO_2 and Li_2CO_3 . Thus in the commercial alloys a variety of oxides have been reported even for the same alloy, but the dominant oxidation product in the presence of O_2 or moisture after long exposure times at 530°C appears to be Li_2CO_3 .

These results differ from earlier X-ray results obtained on binary and ternary Al-Li alloys by Field et al^{13,17}, who suggested that at 530°C Li_2CO_3 would be replaced by γLiAlO_2 in dry air and by mixed spinels in moist air. Furthermore these workers concluded that oxidation was controlled by nucleation and growth of the oxidation products at the metal/oxide interface, whereas all recent studies on commercial alloys have concluded that Li depletion and oxidation is controlled by bulk diffusion of Li^{18,23}.

Differing results have also been reported for the behaviour of Mg in commercial alloys. Fox et al^{18,27} found surface depletion of Mg in 8090 was, like Li, controlled by bulk diffusion to the surface. Russian workers also reported Mg depletion in O1420 alloy (Al-5 Mg-2 Li)¹². However Ahmad²³ using 8090 bar after SHT in a salt bath or in air at 530°C found no significant Mg loss, although Mg appeared to be lost during thermo-mechanical processing. Similarly only Li was severely depleted from an Al-2.9 Li-1.5 Cu-2 Mg-0.15 Zr alloy ingot annealed in dry argon for 12 - 48 h at 543°C⁸. Further work is required to clarify these results.

The oxidation products on Al-Li alloys are permeable to Li and the Li_2CO_3 film appears as a brittle loosely adherent coating which is usually cracked. A deliberately damaged Li_2CO_3 film is shown in Figure 4; the surface beneath the film appears undamaged by oxidation and the original mechanical polishing scratches (at A) and grain boundary grooves were visible. A number of workers have noted that Li_2O , LiH and Li_2CO_3 films were removed by washing in water^{21,23,24} whilst the spinels were unaffected.

It is interesting to note that after exposure in vacuum at 530°C no surface oxidation products were detected optically (Fig 5) or by X-ray diffraction (Fig 6) but Li depletion occurred²⁵; under these conditions Li must be lost at the surface by sublimation. Subsequent exposure of the same surface for 1 min in air at 530°C produced the normal discontinuous oxidation products (Fig 7) and after 1 h the continuous Li_2CO_3 film was detected (Fig 6). Thus the amount of oxidation product may not indicate the extent of Li loss. Much of the published work referred to above involved long exposure times and thick surface films. In practice heat treatment times for thin sheet are kept to a minimum to reduce lithium depletion of the surface^{18,28-30} and to avoid contamination of surfaces prior to solid state diffusion bonding. The latter is particularly important in the development of high strength diffusion bonded joints in combination with superplastic forming of thin sheet. Experiments have been carried out to investigate the surface contamination of 8090 alloy sheet after exposure times up to 1 min at 530°C in moist air

or argon²⁵. After 1 min little continuous film formation had occurred, but rapid oxidation was observed at isolated sites aligned in the rolling direction as shown at low magnification in Fig 7. The morphology of the oxidation products at these sites varied from hemispherical or conical mounds about 25 μm diameter and 25 μm high (Fig 8a) to longer conical shaped growths up to 1 mm long (Fig 8b) or filamentary growths ~ 10 μm diameter and 1 mm long (Fig 8c); growth rates were estimated to be ~ 2 $\mu\text{m/s}$. The growths in Fig 8b-c are similar to those reported elsewhere^{37,9} and identified as γLiAlO_2 . When these oxidation products were removed from the surface by ultrasonic cleaning, pits were found beneath the growths (Fig 8d). The sites of rapid oxidation coincided with the position of insoluble Cu or Fe containing particles (possibly Al_6Cu , Li , or Al_7CuFe) in stringers. The pit depths were 10 - 20 μm with up to 18×10^3 pits/ cm^2 .

The above summary emphasises the need to combine high resolution analytical and electron optical techniques in order to understand the oxidation behaviour of Al-Li alloys.

2.2 Effects of oxidation on subsurface microstructure and microhardness

In unrecrystallised 8090 sheet the evidence for Li loss at elevated temperatures is usually taken to be the occurrence of recrystallisation and grain coarsening and a reduction in hardness below the sheet surface. The coarse grained region in as received sheet is typically about 20 μm deep as shown at A in Fig 9a. With increasing exposure time to 12 h at 530°C the surface density of the $\{100\} \langle 100 \rangle$ texture in 8090 sheet increased from <2 to 14 whereas the overall grain growth increased the $\{110\} \langle 100 \rangle$ texture³¹. Mechanical polishing or chemical milling can remove this soft depleted layer as shown in Fig 9b.

Curves of hardness v depth for sheet SHT for 20 min or 4 h at 530°C is shown in Fig 10¹⁸. Prior removal of the surface layer reduces the depletion depth after 20 min oxidation, but had little effect on the depth after 4 h oxidation.

The effect of SHT temperatures of 480°C, 520°C and 575°C on the hardness gradient in 5 mm sheet is shown in Fig 11¹⁸. Depletion occurred at all temperatures, but the depth at which the parent metal plateau hardness was reached increased and the hardness gradient decreased with increasing temperature. Fox et al^{18,27} showed the measured normalised Mg concentration versus depth curve was in good agreement with the microhardness curve. Lithium loss was not measured but calculated assuming the surface was an infinite sink for Mg and Li solute and the relationship for diffusion was^{18,23}:

$$C_{(xt)} = C_0 \operatorname{erf} \left(\frac{x}{2 \sqrt{Dt}} \right) \quad (1)$$

Where C_0 = alloy Li content, $C_{(xt)}$ = concentration of Li at a distance x from the surface at time t , t = time, D = diffusivity of Li in Al. Theoretical concentration profiles for both Li and Mg were in good agreement with the microhardness curves²⁷.

Indirect confirmation of Li solute depletion was provided by observations of precipitate density as a function of depth. After 1 h at 530°C the precipitate largely responsible for the hardness in 8090 alloy, δ' (Al_3Li), was absent to a depth of ~ 30 μm . This was believed to be the region in which the Li concentration was <1 wt % Li. Mg depletion led to a low Mg/Cu ratio and the possibility of θ' precipitation. In recrystallised sheet Li loss may occur in the absence of grain coarsening which depends on processing and thermal history³¹. It should also be noted that the depth of Li loss cannot be deduced from the depth of the recrystallised layer which is much less than the depth of the soft layer determined by microhardness^{27,32} ie.

depth precipitate free zone (30 μm)	< depth recrystallised layer (60 μm)	< depth of low microhardness region (100 μm)
--	---	---

Some depletion depths determined by microhardness for various heat treatments are listed in Table 4. An example of the relative depletion depth determined by microhardness measurement and the depth of the coarse recrystallised grain microstructure determined metallographically is given in Fig 12 for 3 mm thick 8090 sheet SHT for 4 h at 560°C in air.

Fox²⁷ measured the microhardness on transverse sections (LT/ST) of 8090 unrecrystallised sheet after SHT at 530°C in a salt bath. Measurements were made in directions parallel to the elongated grains (LT) and perpendicular to this direction (ST) with the results shown in Fig 13. Similar hardness curves were obtained after 20 min with a plateau at a depth of 120 μm , but after 4 h different shaped curves were obtained with a greater plateau depth in the LT direction (350 μm) compared with the ST direction (25 μm). Corresponding X-ray depletion profiles for Mg confirmed the plateau depths, but showed continuously increasing Mg with increasing depth. These results suggested that the greater depletion in the LT direction was caused by the more rapid diffusion of Li and Mg along grain boundaries; support for this explanation was provided by the preferential formation of LiH at grain boundaries in 8090 sheet exposed at 530°C in H_2 ²⁵. However recrystallisation and grain growth can also be produced in unrecrystallised 8090 sheet by local cold work at for example a guillotined edge, as shown at A in Fig 14; at B recrystallisation associated with solute depletion at the sheet surface is much less. Thus surface recrystallisation and low hardness may not always indicate solute depletion.

Comparisons have been made between SHT of 8090 in air and in salt baths at 530°C^{23,27}; the depletion depths in terms of the microhardness were the same in both environments, although the shape of the microhardness curves differed slightly²³. However elsewhere salt bath heat treatment is reported to reduce the depleted layer depth by $\frac{1}{3}$ to $\frac{1}{3}$ ^{12,30}, presumably by reducing the heat treatment time. An addition of 60% LiNO₃ to the NaNO₃ bath reduced the near surface depletion slightly after 4 h at 590°C without affecting total depletion depth²⁷. Severe loss of Li was reported during ageing of Al-2.3 Li-2.8 Cu alloy in a salt bath at 190-235°C³⁵. After 20 min and 4 h at 530°C in a salt bath 8090 sheet showed large pores and blisters below the alloy sheet surface; the latter caused expansion of sheet in the thickness direction²⁷.

There was evidence that Li loss in 8090 sheet was less in argon^{18,27}. In a study of Al-3 wt % Li alloy³⁶ Li loss was significantly less in an argon sealed environment than in a vacuum sealed environment after 11 h at 550°C (Fig 15). This suggests that in sealed high pressure argon, O₂ or moisture is gettered by Li and argon pressure reduces the rate of Li loss. The effect was particularly apparent in the STA condition (Fig 16); the depletion depth was greater in air (Fig 16a) than in a sealed vacuum or a dynamic vacuum (Fig 16 b-c) environment and was very small in a sealed argon environment (Fig 16d).

An X-ray and microhardness study carried out on 8090, 8091, 2090 and 2091 showed²⁶ that after 1 h at 530°C in air the depletion depth was similar in all alloys at 200 μ m. A linear relationship was obtained for depletion depth x (in μ m) for times (t) up to 24 h. With 8090 sheet and for the normal SHT temperature of 530°C the depth of the depleted layer x (μ m) could be related to the exposure time t (minutes) by:-

$$x = 14.85 \sqrt{t} + 48 \quad (2)$$

A similar relationship was reported for 01420 alloy at 450°C and 500°C for $t = 1$ h to 100 h and for exposure in air, salt bath and for an Al electroplated surface¹². The X-ray intensity measurements for Li₂CO₃ differed in the 8000 and 2000 series Al-Li alloys with greater intensities for 8090 and 8091; this was attributed to the higher Li contents in these alloys. It was concluded however that the maximum or integrated peak intensities for Li₂CO₃ in the angular range 20-33°/2 θ could be a viable non-destructive technique for monitoring Li depletion with an accuracy limited by the accuracy of the microhardness measurements. But a wide range of values have been reported for Li depletion depths even for similar exposure conditions²⁶ as shown in Table 4.

The depletion depth measured in an 8090 forging exposed to 438°C is shown in Fig 17³³. Much longer exposure times are possible at this lower temperature before significant depletion occurs (Table 4). In Al-Li ingots or castings homogenisation treatments may involve a combination of long times and progressively higher temperatures in order to avoid incipient melting⁸. The depletion depth determined for a cast alloy is shown in Fig 18³⁴. No significant depletion was found in the as cast state, but increasing depletion occurred at 500°C in an air circulating furnace. After 20 h a low but constant hardness plateau was obtained compared with a progressively increasing hardness curve at shorter times. These results imply that for SHT times often used for Li free Al-alloys (up to 48 h) depletion depths greater than 0.6 mm would be obtained.

The effect of environment on Li-depletion depths (determined by chemical analysis and optical microscopy) is shown in Fig 19⁸. Dry N₂ produced the smallest depletion depth and a coating of Li₂CO₃ whilst wet N₂ produced the largest depletion depth and a coating of LiAlO₂. No difference was found between dry, wet or laboratory air and the depths were all less than in wet N₂.

2.3 Effect of Oxidation on Weight Gain and Porosity

The increase in mass when lithium containing oxidation products are formed (Table 3) has been used extensively to monitor the oxidation behaviour of Al-Li alloys. The effect of Li content on the weight gain in wet air at 500°C is shown in Fig 20a¹⁹; the rate of weight gain increased with increase in Li content and the curves appeared to be parabolic. The corresponding curves showed that the rate of weight gain was substantially less in dry air (Fig 20b). For similar Li contents (3 wt %), the weight gain for binary Al-Li was 10x that for a binary Al-Mg alloy and a further factor 10 increase was obtained for Al-Li alloys in moist air¹³.

The effect of various atmospheres on the weight gain of Al-2.7 wt % alloy at 520°C has been reported¹⁷. For dry air, N₂ or 20% O₂/dry air the weight gains were similar. Water vapour dominated the oxidation kinetics regardless of the carrier gas and led to breakaway oxidation after ~ 3 h in wet O₂/Ar gas. Trace alloying additions of Be, Ca and Bi at 10³ and 1000 ppm did not significantly reduce the oxidation of Al-3% Li. The effect of magnesium and copper additions to Al-Li alloy reported by Gregson³⁷ is shown in Fig 21; magnesium had a slight effect (compare curves 1 and 2) but the Li content had the greatest effect on the weight gain.

The weight gain for the commercial alloys (DTDXXXA equivalent to 8090 and DTDXXXB \approx 8091) are shown in Fig 22¹⁹; the rate of weight gain in dry air compared to 8090 appeared to be greater for the 8091 alloy initially and then became similar. Both alloys appeared similar in wet air, showing a transition from parabolic to accelerated oxidation after 2 h. The weight gain was greater than for the binary alloys and this was attributed to the magnesium content. Copper caused only a slight increase in weight gain.

When depletion depth (defined by microhardness) and weight gain data are compared the surprising result is that moisture did not effect the depletion depth although it increased the weight gain. Thus the weight gain cannot be used to determine the Li depletion depths or oxidation rates^{19,21}.

The weight gain data for commercial 2090 alloy has been determined in the temperature range 200 - 550°C in (i) dry air (<10 ppm H₂O), (ii) moist air (2200 ppm H₂O), (iii) dry 20 vol % CO₂/80 vol % N₂, (iv) 10% CO₂/10% N₂ (v) dry N₂ (Fig 23)²¹. For all temperatures and atmospheres the weight gain versus time curves were initially parabolic changing to linear after 1.7 - 5 h. Note that some oxidation occurred below 400°C when the weight gain increased in the order 5, 1, 2, 3, 4. Above 400°C 1 and 5 caused the lowest gains, and then the weight increased in the order 4, 3, 2. Porosity was found in cross-sections after heating in air, and increased with increase in moisture content or temperature. Based upon thermodynamic data it was difficult to account for the sensitivity to moisture in the reactions with Al-Li alloys. The moisture effects may be an indirect effect of volume changes in the oxidation products, and porosity and disruption of the films by H₂²¹.

Micropores and increased H₂ content have been reported for oxidised Al-Li alloys by many workers. Li was the dominant factor influencing porosity in 01420 alloy¹². Surface H₂ contents of 0.8 - 1.2 cm³/100 g were 2x that in the bulk and 4 - 5x that of pure Al.

Bands of subsurface porosity have been found in 8090 sheet¹⁰ and forgings³². The depth of the bands and the Li depletion depth increased together with increase in the SHT time at 530°C in air; the bands always occurred at about the maximum depth of the depleted layer. The results obtained by Dickinson et al²⁴ in a careful metallographic study of oxidised Al-3 wt % Li plate and 2090 alloy may explain many of the confusing observations of porosity in Al-Li alloys^{12,10,32}. They found both porosity and LiH particles could be obtained depending on the environment. LiH formed in preference to H₂ porosity when H₂O vapour <10 - 100 ppm, but in high concentrations of H₂O vapour or H₂, porosity occurred. LiH was found to dissolve in water or ethanol. Thus the sites of LiH in metallographic samples polished in these media could appear as pores. The displacement of the bands of LiH particles ("porosity") to progressively increasing depths with increasing SHT time can be explained by the diffusion of Li to the surface. When the Li concentration around the LiH particles falls below a critical concentration the LiH particles dissolve, liberating H₂ which diffuses deeper into the alloy to reform LiH. In practice the diffusion of H₂ through the surface films may be a complex process dependent on the properties of the oxide films. For example in the presence of a continuous Li₂O film, H⁺ will require anion vacancies in the lattice for transport and this would be the rate limiting step for H₂ diffusion. Also the state of the lithium may effect the lattice mismatch, since the Li atom (1.5 Å) has a much larger radius than Li⁺ (0.6 Å)³⁸. In a recent review of hydrogen effects in advanced materials it was noted that whereas Al alloys are not considered sensitive to hydrogen, the behaviour of Al-Li alloys is not yet clearly defined³⁹.

3 OXIDATION OF Al-Li ALLOYS IN THE LIQUID STATE

3.1 Ingot and component casting

Lithium confers a greater reactivity to aluminium melts than any other alloying element⁴⁰. Impurities such as O₂, H₂O vapour, CO₂, and N₂ occur in all furnace atmospheres and with an Al - 3 wt % Li alloy at 740°C in dry and moist atmospheres the formation of LiOH, LiOH.H₂O, (neither of which normally occur in the solid state) and the dominant Li₂O and Li₂CO₃ phases were detected. Aluminium oxides were absent at this Li concentration but were found on melts with <1% Li. In an Al-Mg-Li-Be alloy at 710 - 720°C Li₂O dominates but was non-protective; 0.2% Be reduced the rate of oxidation after 90 min⁴⁰. No nitrides were detected even in dry N₂. Additions of Be, La, or Y did not inhibit oxidation of Al-Li binary and when O₂ or H₂O vapour concentration exceeded ~30 ppm the oxidation rate was similar in all protective atmospheres. Thus only high purity gases are likely to reduce Li oxidation in a melt⁴¹.

Production of aerospace Al-Li alloys on a large scale usually involves a process of semi-continuous vertical direct chill (DC) casting to convert molten metal to solid ingot. The coolant (usually water) impinges directly on to the skin of a partially solidified ingot. Skin fracture can lead to molten metal reacting with the coolant. Molten Al-Li alloys explode more violently with water than other Al-alloys. The energy released (KJ/kg) increased exponentially with increasing Li content above about 3 wt % Li leading to potentially dangerous conditions⁴¹. The explosive conditions are complex and involve the evolution of large volumes of H₂ gas produced by water/metal reaction. The thermal conductivity for molecular H₂ is 10 times greater than for water at 100°C; the increased heat transfer coefficient is believed to contribute to the increased energy yield with Al-Li alloys.

Because of the reactivity of molten Al-Li alloys, in the casting of components special attention must be paid to the refractories and atmospheres to avoid loss of Li and H₂ contents up to 50 times that found in other Al-alloy castings. The hydrogen reaction appears to be independent of other alloying elements in the Al-Li alloys. Compared with data for wrought alloys there is little work reported on Al-Li casting alloys, although material utilisation should be improved and since casting factors effectively increase the weight penalty, reductions in alloy density are particularly attractive for castings.

Metal/mold reactions have been investigated using an Al-2.5% Li alloy with Mg and Cu additions⁴². No reaction was obtained with an iron mould, but severe interactions were obtained with sodium silicate bonded sand. The subsurface layer of the casting in contact with the sand contained large gas bubbles. When sodium silicate was replaced with resin a dramatic reduction in the reaction was obtained; although a carbonaceous layer was formed the casting quality was equal to that for the iron mould. The reduced reactivity was attributed to the absence of water associated with the silicate binder. Ceramic coatings such as Al_2O_3 and SiC on the resin bonded sand mould prevented carbonaceous film formation but their lack of permeability led to gas bubbles in the metal near the ceramic coatings. Further developments are expected in cast Al-Li alloy technology.

3.2 Rapid Solidification Processing (RSP)

Some of the potential benefits of RSP, common to most alloy systems, are reduced segregation, refinement of the microstructure (smaller grain and dispersoid sizes) and large departures from equilibrium constitution (high solute supersaturation, non-equilibrium phases)⁴³. All the RSP techniques such as gas atomisation, mechanical alloying and chill casting (melt spinning, spraying and splat cooling) have been applied to Al-Li alloys with the objective of achieving a greater reduction in density or increase in modulus⁴⁴. It may be possible for example to increase the Li content above 2.7 wt % (the limit for ingot metallurgy) without causing embrittlement^{45,46}. RSP Al-Li alloys may also have the advantage of not requiring a stretching operation prior to ageing and so be particularly suitable for forgings.

However the consolidation of RSP Al-alloy products has presented many problems because of the surface oxide, hydroxide or carbonate film formed on the powders or particles. These films become semi-continuous films or stringers after consolidation and lead to low toughness.

Contamination by oxidation products depends upon cooling rate and on the partial pressures of O_2 and H_2O during RSP, storage and handling. These oxidation problems are greater for Al-Li alloys. For example the surface oxide film thickness was greater (15 - 50 nm) on atomised powder and melt spun Al-3 Cu-2 Li-1 Mg alloy ribbon than on Li-free alloys⁴⁶. Oxide or carbonate films on prior powder particle boundaries were a dominant factor in controlling the fracture toughness of consolidated melt spun ribbon in Al-3.4 Li-0.8 Cu-0.4 Mg-0.5 Zr alloy⁴⁵; increasing the particle size, reduced the particle surface area to volume ratio and increased toughness. However cooling rates also affect oxide film thicknesses. The finer the particle size in gas atomised powders the greater the cooling rate and the thinner the oxide film. On melt spun ribbon the oxide film was a factor 2 thicker on the top surface than on the bottom roll face surface and thicker on thicker ribbons, because of slower cooling rates. In general the larger melt spun particles size translate to small surface/volume ratio, which tends to minimise effects due to surface oxides on ribbon compared with atomised powder products⁴⁴. Mechanically alloyed (MA) Al-Li alloy powders tended to have thicker oxide than inert gas atomised powder⁴⁷; also when exposed to ambient conditions MA powders tended to reabsorb more moisture and form thicker hydrated surface oxides.

In melt spun Al-3 Li alloy containing 2 or 10 wt % Be⁴⁶ the as spun oxide films were 10 - 50 nm thick and increased to 2.5 - 3 μm after 20 min at 500°C in air. Even in the high Be alloy, Li oxidised preferentially at 500°C although BeO is the most stable oxide; Li was concentrated in the top surface of the oxide above a Be-rich oxide layer. Thus rapid Li diffusion through the oxide film suggested kinetic rather than thermodynamic factors alone dictated the oxidation behaviour.

Vacuum atomised high Li alloys containing 4-5 wt % Li were much more reactive than Al-3 wt % Li⁵. Li-rich inclusions aligned in stringers in consolidated material increased the notch sensitivity and led to local rapid oxidation pitting during SHT at 588°C for 1 h. Liquid dynamic compaction was used to reduce the contamination; the oxide content was reduced to 20 ppm compared with 600 - 1000 ppm in conventional powder extrusions⁴⁸. During superplastic deformation at 590°C under 2.1-2.8 MPa gas pressure the Li loss was small (4 wt % to 3.8 wt % Li from density measurements), which suggested Li loss would not be a problem at strain rates $>6 \times 10^{-4} \text{ s}^{-1}$. However density data may not be adequate for assessing Li loss.

Early attempts at making Al-Li/SiC composites by the Osprey inert gas spray deposition process produced porosity of ~10% compared with <5% for non-Li alloys⁴⁹. Oxidation of Al-Li was often associated with hydrogen evolution and high H_2 contents (10 - 50 w ppm compared with 0.4 w ppm for ingot material) were a feature of extrusions produced from various Al-3 wt % Li RSP products⁵⁰. Vacuum annealing was ineffective in removing H_2 from the extrusions. Since the H_2 was believed to originate from hydroxides on particle surfaces caused by reactions with ambient atmospheres, improved powder cleanliness and degassing was recommended.

3.3 Fusion welding

There is considerable interest in fusion welding of Al-Li alloys by gas tungsten arc (GTA), gas metal arc (GMA) and electron beam (EB). However all Al-Li alloys are susceptible to weld porosity and Li depletion in the weld zone. In 2090 alloy the problem was greater for thin sections⁵¹. In 01420 alloy GTA welded using 3 passes with 01420 filler metal, the H_2 and Li contents fell together in the surface analysed across a transverse section of the weld (Fig 24) and increased together from bottom to top of the

weld; it was suggested that this coincidence may be caused by LiH formation⁷. In GTA welded 8090 alloy the use of 8090 filler reduced the Li loss in the weld⁵². The porosity was attributed to hydrogen derived from moisture associated with surface films formed either during SHT or during exposure at room temperature for times greater than 20 h after machining. To reduce the porosity it is recommended that an 0.2 - 0.3 mm deep surface layer be machined or chemically milled from the surface immediately before welding. For alloy 01420 vacuum degassing at 450°C for 24 h at 10^{-2} - 10^{-3} torr or in high vacuum (at 10^{-5} torr) significantly reduced or eliminated porosity ($H_2 < 0.2$ ml/100 g)⁵³. It was also reported that in the 01420 alloy LiH formed as low as 450°C and rapidly at 710 - 720°C.

3.4 Salt Bath Heat Treatment

In sodium nitrate salt baths the rate of reaction of Al-Li alloys becomes rapid above the liquidus temperature particularly for Li contents greater than 4%⁵⁴. For example at near eutectic composition (9.7% Li) considerable gas evolution preceded violent eruption and pyrotechnic displays at a temperature of 616°C, the liquidus temperature. However commercial Al-Li alloys with Li contents <3% were melted in a salt bath with no signs of reaction. It was concluded that all Al-Li alloys may be safely heat treated below the liquidus temperature in salt baths up to 600°C.

4 EFFECT OF Li DEPLETION ON MECHANICAL PROPERTIES

Strength reduction will clearly depend on the depth of the lithium depleted layer. This is dependent primarily on the temperature and the total exposure time eg for multiple SHTs a limit of 2 extra SHTs (of 20 min each) has been applied to sheet⁵⁵. When considering mechanical properties the effect of other sheet processing variables must also be considered eg

- i Pre-chemical milling or etching to remove depleted layer produced during sheet manufacture.
- ii Initial microstructure eg the size, shape and orientation of the grains.
- iii Heat treatment environment eg atmosphere, salt bath composition, argon gas pressure and O_2 or moisture content.
- iv Post - heat treatment process eg chem-milling.

The strength reduction will also depend on the sheet thickness and forming techniques. A given depletion depth may be insignificant in thick sections but become significant in very thin sheet. Unique factors associated with superplastic forming of thin sheet, such as prolonged treatment times⁵⁵, simultaneous decrease in sheet thickness and increase in surface roughness⁵⁶ all tend to enhance the effect of or increase Li loss. When formed into a die, Li loss may be asymmetrical through the sheet thickness, being less at the surface in contact with the die. The loss of Li on as forged surfaces of precision forgings is of some concern, but Li loss may be avoided in conventional closed die forgings³³. (Note that Al-Li alloys with higher Cu contents may be quench rate sensitive and changes in strength caused by Li loss may be obscured by changes in cooling rates.)

In comparing the magnitude of the reduction in strength reported by different authors the type of test piece and whether it is partly machined after heat treatment must be taken into account. For a sheet test piece machined at the edges, the tensile strength is given by

$$\sigma = \sigma_o - \frac{2}{w} (\sigma_o - \sigma_d) x \quad (1)$$

where σ_o = strength of undepleted alloy, σ_d = strength of depleted region, w = thickness of sheet. If x is the depth at which Li is depleted to 2/3 of its original value, then $x \approx 1.5 (Dt)^{1/2}$ where D = diffusivity of Li in Al, t = SHT time and

$$\sigma = \sigma_o - \frac{3}{w} (\sigma_o - \sigma_d) (Dt)^{1/2} \quad (2)$$

Combining equations (2) and (3):-

$$(\sigma - \sigma_o) = - \frac{3}{w} (\sigma_o - \sigma_d) \left(\frac{x - c}{m} \right) D^{1/2} \quad (4)$$

where m and c are constraints depend on temperature. The strength reduction $(\sigma - \sigma_o)$ is proportional to the depleted layer depth and increases with $\sqrt{\text{time}}$.

Tensile and proof strength data for 8090 sheet obeyed the $t^{1/2}$ relationship after SHT in air or in a salt bath before or after anodising^{28,29}; the curves for SHT in air are shown in Fig 25. The strength reduction coincided with an increase in elongation. Some test pieces exposed for the maximum time were machined to remove the depleted layer before testing; those test pieces exposed in air regained the bulk strength, indicating the fall in strength was caused by the depleted layers. Anodised test pieces did not regain the full bulk strength after machining. In the salt bath the rate of loss of strength was only slightly less than in air. In a salt bath heat treatment times may be half that in air with a corresponding reduction in the depletion depth of 1/2 to 1/3^{12,30}. Early results suggesting anodising before SHT suppressed Li loss⁸ were not confirmed at longer exposure times²⁹.

Higher temperatures might be considered for diffusion bonding. Some stress/strain curves for 0.9 mm thick sheet after high temperature exposure are shown in Fig 26. The reductions in strength and the corresponding depletion layer depths are shown in Table 5 and Fig 12. At these high temperatures reductions in strength of up to 27% were obtained compared with a reduction of only 6% after the specified STA treatment applied to the 0.9 mm thick sheet. It may be possible to reduce Li loss during bonding at the high temperatures by stack bonding the sheet followed by superplastic forming at lower temperatures. Much smaller reductions in strength were obtained after identical high temperature SHT of thicker (4 mm) sheet (Table 5). This indicates that the bulk strength was not effected by the heat treatment and that, as expected, similar depletion depths on thicker sections have much less effect on static strength.

Since the reported depletion layer depths may differ by a factor 2, care should be taken in using these data to predict the reduction in strength. Furthermore the hardness in the depleted layer depends on composition and heat treatment, since some solid solution and precipitation hardening does occur in this region as shown schematically in Fig 27. More quantitative data are required relating Li depletion depths, heat treatment and processing variables to the mechanical properties of Al-Li alloys.

5 DISCUSSION AND CONCLUSIONS

Users of Al-Li alloys are well aware that Li depletion occurs during processing and heat treatment. However Li depletion depth data are not always reported, even when high temperatures are used for example with powder alloys. This suggests that the importance of Li depletion is not always appreciated. There is a surprisingly large variation in the reported depletion depths for similar exposure conditions, from which it is not clear whether this is caused by a variation in the rate of Li loss or in the measurements by different operators.

Volume changes and thermal stresses caused cracking of surface films on Al-Li alloys and the surface area may be increased by porosity associated with hydrogen^{21,22,24} or Kirkendall diffusion²². These factors and the occurrence of all the oxidation products together in surface films, preclude the use of gravimetric data for determining oxidation rates for Al-Li alloys^{19,21,20}, nor can the depth of the lithium depleted layer be used to predict oxide layer thickness as suggested elsewhere⁸. Furthermore the use of X-ray diffraction data to relate the amount of each oxidation product to the oxidation conditions is made difficult by the lack of sensitivity at low volume fractions²³, by the variety of oxidation products, by the large changes in oxide thickness over small distances on the alloy surface²¹ and by subsequent reactions of the oxidation products in air at room temperature²¹.

A knowledge of the Li depletion is particularly important when thin sections are used or when long processing times or high temperatures are involved. Li depletion appears to be limited only by the bulk diffusion rate and is therefore controlled by the exposure time and temperature. Prior surface treatment, different atmospheres or salt bath heat treatment appear to have little effect on the Li depletion depth after long times. However there is evidence that sealed inert gas pressure heat treatment may reduce the rate of Li loss and salt bath heat treatment may allow shorter exposure times compared with heat treatment in air. Avoiding exposed metal surfaces by keeping sheets in contact with die surfaces or stacking sheets could also reduce lithium loss during heat treatment. To prevent H₂ pick-up hydrated surface films must be removed prior to heat treatment and moisture must be eliminated from the environment. Further studies are required to investigate the factors that effect the rate of lithium loss and the mechanism of oxidation in particular alloys, and the conflicting data on magnesium loss should be examined. Finally the development of a rapid, reliable and accurate NDE method for measuring Li depletion is required for quality control on incoming sheet and for monitoring Al-Li products during in-house processing.

REFERENCES

Conferences

- II 2nd Intern. Al-Li Conference Monterey USA Met. Soc AIME 1984.
- III 3rd Intern. Al-Li Conference Oxford UK Inst. Metals 1986.
- IV 4th Intern. Al-Li Conference Paris France J Physique 48 1987.
- 1 C J Peel, B Evans, D McDermid, III p.26.
- 2 P Meyer, B Dubost, III p.37.
- 3 F E Bretz, " : Sawtell, III p.47.
- 4 N J Kim, D J Skinner, K Okazaki, C M Adam, III p.78.
- 5 P J K Meschter, R J Lederich, J E O'Neal, III p.85.
- 6 P S Gilman, J W Brooks, P J Bridges, III p.112.
- 7 J R Pickens, T J Langan, E Barta, III p.137.

- 8 R F Ashton, D S Thompson, E A Starke, F S Lin, III p.66.
- 9 E A Starke, W E Quist, AGARD - Structures and Materials Panel 67th Panel Meeting Mierlo Oct 1988.
- 10 A F Smith, IV p.C3-49.
- 11 R Grimes, T Davis, H J Saxty, J E Fearnon, IV p.C3-11.
- 12 I N Fridlyander, V S Sandler, T I Nikd'skya, R A Savinkov, I N Roschina, Russian Met 2 175 (1978).
- 13 D J Field, E P Butler, G M Scamans, Proc 1st Intern. Al-Li Confer. (Met. Soc. AIMME) 1981 p.325.
- 14 A Csanady, J Kurthy, J Mater. Sci. 16 2919 (1981).
- 15 A Csanady et al, Corrosion Sci. 22 689 (1982).
- 16 A Csanady et al, Ibid 24, 237 (1984).
- 17 D J Field, G M Scamans, E P Butler, II p.657.
- 18 S Fox, H M Flower, D S McDarmaid III p.263.
- 19 M Burke, J M Papazian III p.287.
- 20 J M Papazian, R L Schulte, Met. Trans. 17A 635 1986.
- 21 K Wefers, F A Mozelewski, Proc. 8th Intern. Light Metals Confer. Vienna 1987 p.744.
- 22 J M Papazian, J P W Wagner, W D Rooney, IV p.C3-513.
- 23 M Ahmad, Met. Trans. 18A 681 (1987).
- 24 R C Dickinson, K R Lawless, E Wefers, Scripta Met. 22 917 (1988).
- 25 P G Partridge, N Chadbourne, J Mater. Sci. In the press.
- 26 P Holdway, A W Bowen, RAE Tech. Rep. 88059 (1988).
- 27 S Fox, PhD Thesis, Imperial College London 1987.
- 28 J M Papazian, G G Bott, P Shaw, 17th National SAMPE Tech. Confer. 1985 p.688.
- 29 J M Papazian, G G Bott, P Shaw, Mater. Sci. Eng. 94 219 (1987).
- 30 D Constant, M Doudeau, P Meyer, AGARD Al-Li Confer. Mierlo (1988).
- 31 A W Bowen, RAE Tech. Memo. 1099 (1987).
- 32 A F Smith, IV p.C3-629.
- 33 D T Markey, R R Biederman, A J McCarthy, III p.173.
- 34 A F Smith, III p.164.
- 35 J C Huang, A J Ardell, III p.455.
- 36 H Ueda et al, J Jap. Inst. Metals 49 562 (1985).
- 37 P J Gregson, PhD Thesis, Imperial College, London 1983.
- 38 O K Krikorian, High Temperatures - High Pressures 20 183 (1988).
- 39 H G Nelson, SAMPE Quarterly Oct. p.20 (1988).
- 40 L V Tarasenko et al Russ. Metall. 2 174 (1980).
- 41 F M Page, A T Chamberlain, R Grimes, IV p.C3-63.
- 42 C H Tong et al IV p.C3-117.
- 43 F H Froes, W E Quist, S K Das, MPR June p.392 (1988).
- 44 W E Quist et al III p.625.
- 45 N J Kim, R L Bye, S K Das, IV p.C3-309.
- 46 A Joshi, J Wadsworth, A E Vidoz, Scripta Met. 20 529 (1986).

- 47 G H Narayanan et al II p.517.
 48 P J Meschter et al IV p.C3-317.
 49 J White et al IV p.C3-347.
 50 P J Meschter, J E O'Neal, R J Lederich, II p.419.
 51 R P Martukanitz, C A Natalie, J O Knoefel, J Metals Nov p.38 (1987).
 52 M R Edwards, V E Stoneham IV p.C3-293.
 53 J R Pickens, J Mater. Sci. 20 4247 (1985).
 54 E R Clark, P Gillespie, F M Page III p.159.
 55 C J Peel et al II p.363.
 56 P G Partridge, D V Dunford, Intern. Confer. Superplasticity and Superplastic Forming, Blaine Washington August 1988.

ACKNOWLEDGEMENTS

The author is grateful to D Dunford for help with the experimental work and to Drs Holdway and Bowen for access to their work on γ -ray measurement of depleted layers and to Dr McDarmid and A J Shakesheff for helpful discussions on the microstructure and processing of Al-Li alloys.

© Controller Her Majesty's Stationery Office London 1989

TABLE 1 COMPOSITION AND PROCESSING ROUTE FOR SOME Al-Li ALLOYS

Production Route	Alloy	Composition wt %						Specific Gravity	Reference
		Li	Cu	Mg	Fe	Si	Zr		
Ingot	LITAL A ¹	2.4	1.2	0.54	0.08	0.03	0.14	2.54	1
	8090 ²								2
	CP271 ²								
	LITAL B ¹	2.4	1.93	0.76	0.07	0.09	0.12	2.55	1
	8091								
	2090	2.09	2.68	0.05	0.12	0.03	0.11	2.60	1
	ALITHALITE ³								3
	2091	2.1	2.11	1.54	0.05	0.05	0.08	2.58	2
	CP274 ²								
	01420 ⁴	2.05		5.09	0.06	0.06	0.08	2.47	7
Melt spun	678 ⁵	3.22	0.54	3.07			0.83		4
Powder atomised		4.10		1.0			0.2		5
Mechanically alloyed	IN905XL	1.5		4.0	+ 1.2C + 0.4 O			2.58	6

1 LITAL Alcan UK. 2 CP27X Cegedur Pechiney, France. 3 ALITHALITE Alcoa USA.
 4 Russia. 5 Allied Corp USA. 6 Novamet Aluminium, USA.

TABLE 2 SUMMARY OF OXIDATION STUDIES ON Al-Li ALLOYS

Alloy Composition wt %	Test piece dimensions	Surface Conditions	Atmosphere	Temperature	Time	Data or Technique	Reference
Al-Mg-Li Al-2 Li	1.6-2 mm thick sheet	-	Air Salt bath	450-550°C	1-100 h	XD ED H ₂ content Hardness	12
Al-3 Li Al-4.2 Li Al-3 Li-2 Mg	0.2 mm thick sheet	Electropolished + 14 days in air	20% O ₂ /Ar dry and wet	480-575°C	30 min-5 h	Weight gain TEM ED SEM	13
Al-Zn-Mg + 0.19 Li	0.5 mm thick sheet	Electropolished	Vacuum	350-500°C	1-1 h	Weight gain TEM	14
Al-Zn-Mg + Cr, Cu or Li trace additions	0.5 mm thick sheet	Electropolished	Vacuum air	400-500°C	0.5-4 h	X-ray SIMS AES	15
Al + trace additions	Foil	Pre-oxidised at 240-400°C 2-16 h	90% RH air	40°C	0-16 days	X-ray SEM EPMA SIMS	16
Al-Li alloys + trace additions	0.2 mm thick sheet	Electropolished + 14 days in air	20% O ₂ /Ar Lab air N ₂ wet and dry	350-575°C	30 min-5 h	Weight gain SEM	17
8090	3 and 5 mm thick sheet	Ground polished pickled anodised	Dry Argon air	480-575°C	20 min-4 h	Hardness EDS (Mg loss) Fatigue Tensile Metallography fractography	18
Al-Li Al-Li-Zr Al-Li-Cu-Zr 8090/8091	0.38 mm thick sheet	Electropolished + 4 weeks in air	Dry or wet air dry Argon	500°C	1 h, 3 h	Weight gain tensile bend hardness	19

TABLE 2 SUMMARY OF OXIDATION STUDIES ON Al-Li ALLOYS (cont'd)

Alloy Composition wt %	Test piece dimensions	Surface conditions	Atmosphere	Temperature	Time	Data or technique	Reference
8090 8091	7 and 7.8 mm sheet	Electropolished + 1 day air	Air wet and dry, Argon	500°C	1, 4, 16 h	Li probe weight gain metallography	20
2090	1 mm thick sheet	Ground	Air, and CO ₂ /N ₂ , dry and moist, dry N ₂	200-550°C	0-16.6 h	Weight gain XD H ₂ content SEM	21
8090 8091 2090	7 mm thick plate 7.8 mm " " 12.5 mm plate extrusion 6.25 x 37 mm	As received ground electropolished sand blasted rolled	Vacuum H ₂ Argon Dry and moist air	500°C	1-6 h	Metallography	22
8090	Extruded bar, 1-3 mm thick test pieces	Etched	Air	530°C	2.5 min-1 h	Hardness EDS (Mq loss) AES XPS SEM XD ⁺	23
Al-3 Li 2090	1/4 in plate machined to 3 mm diameter	Electropolished	Air, dry and moist H ₂	550°C	12 h	SEM fractography	24
8090	2.5 mm sheet	Ground Electropolished	Air } Dry Argon } and wet H ₂ vacuum	530°C	0 - 1 h	Metallography SEM	25
8090 8091 2090 2091	1.6-2.0 mm " " 1.5 mm " sheet	Ground	Air	530°C	5 m-50 h	Hardness XD	26

XD = X-ray diffraction, ED = electron diffraction, TEM = transmission electron microscopy
SEM = scanning electron microscopy, EDS = energy dispersive X-ray analysis, AES = Auger electron spectroscopy,
XPS = X-ray photo-electron-spectroscopy, SIMS = secondary ion mass spectrometry.

TABLE 3 MASS AND VOLUME RATIOS FOR LITHIUM OXIDATION²¹

Oxidation product	Product mass Metal mass	Product volume Metal volume
Li_2O	2.10	0.57
LiAlO_2	1.94	1.12
Li_2CO_3	5.32	1.35

TABLE 4 EFFECT OF HEAT TREATMENT ON LITHIUM DEPLETION DEPTH DETERMINED BY MICROHARDNESS MEASUREMENTS

Material	Solution Heat Treatment in Air		Depletion Depth μm	Reference
Unrecrystallised 8090 sheet (3 mm)	530°C	20 min	100	18
	530°C	4 h	210	
8090 sheet (0.9 mm). Surface machined before heat treatment	530°C	20 min	47	RAE
	560°C	4 h	204	
8090 sheet, as rolled.	500°C	1 h	50-60	19
8090 sheet As received. 2.07 mm	530°C	30 min	160 \pm 30	26
		1 h	190 \pm 30	
		2 h	220 \pm 40	
		4 h	260 \pm 20	
		24 h	600 \pm 50	
8090 bar (air and salt bath)	530°C	1 h	80	23
8090 forging	438°C	6 h	25	33
		8 h	240	
2091 die forging	526°C	8 h	240	32
Al-1.5 Li-2.9 Cu-2.1 Mg Casting	510°C	2 h	250	34
	510°C	24 h	800	

TABLE 5 EFFECT OF HEAT TREATMENT IN AIR ON THE TENSILE PROPERTIES OF
0.9 MM AND 4 MM THICK 8090 SHEET

4 mm sheet machined to 0.9 mm thick				4 mm thick sheet			
Heat Treatment Conditions	Tensile Strength σ MPa	Reduction in Strength $\frac{\sigma - \sigma_0}{\sigma_0}$	Depletion Depth (Micro-hardness) μm	Heat Treatment Conditions	Tensile Strength σ	Reduction in Strength $\frac{\sigma - \sigma_0}{\sigma_0}$	Depletion Depth (Micro-hardness) μm
1) STA + surface machined to remove depleted layer	428 (σ_0)		0	1) As received + aged	434 (σ_0)		
2) 1) + STA	402	6%	47	2) 1) + STA	428	1.4%	55
3) 1) + 570°C 1 h + STA	350	16.4%	78-94	3) 1) + 570°C 1 h + STA	393	9.5%	
4) 1) + 580°C 1 h + STA	332	22.4%	172-183	4) 1) + 580°C 1 h + STA	398	8.3%	
5) 1) + 560°C 1 h + STA	314	27%	204	5) 1) + 560°C 1 h + STA	398	8.3%	252

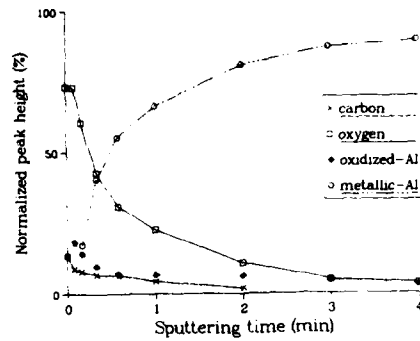


Fig 1 Auger elemental distribution - sputtering time profiles for 809 extruded bar in the ground and etched condition. [23]

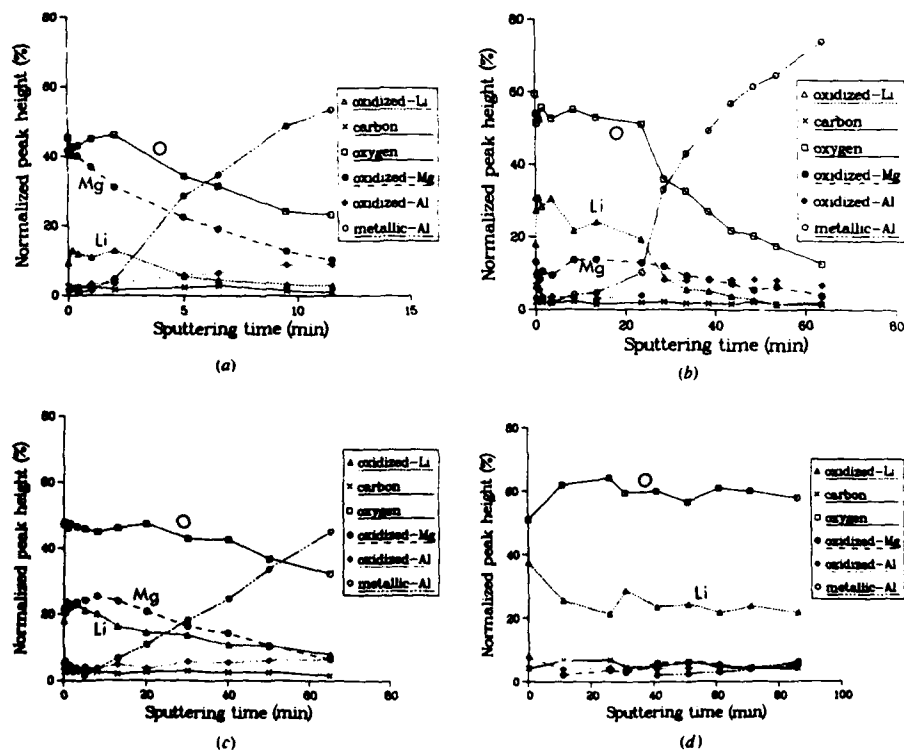


Fig 2 Profiles for 8090 extruded bar after oxidising in air at 530°C for (a) 2.5 minutes (b) 5 minutes (c) 10 minutes (d) 30 minutes. [23]

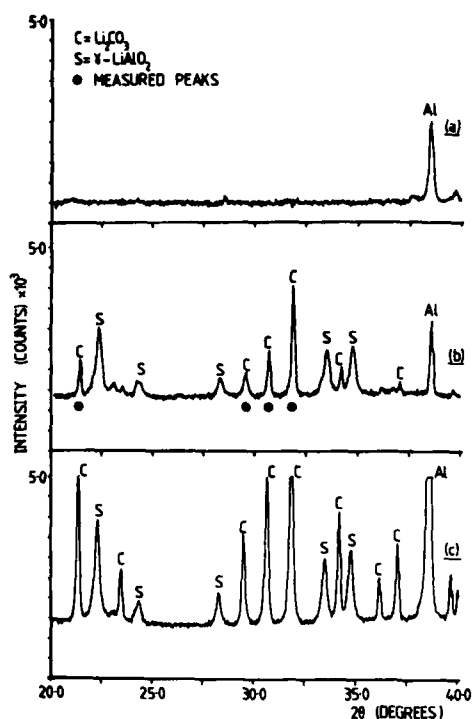


Fig 3 X-ray diffractograms for 2.1 mm 8090 alloy sheet, (a) as received and after SHT at 530°C for (b) 15 minutes (c) 1 h. [26]

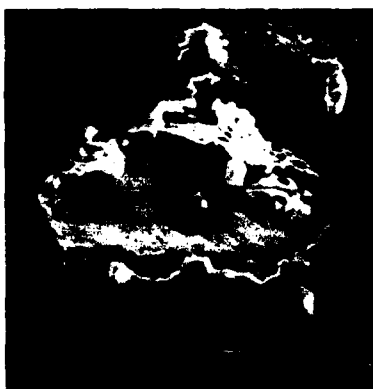


Fig 4 Unrecrystallised 2.5 mm 8090 sheet after 1/2 h in vacuum at 540°C and 1 min in air at 530°C showing fractured Li_2CO_3 film. [25]

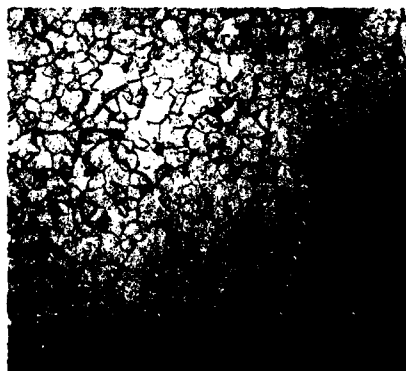


Fig 5 Recrystallised 2.5 mm 8090 sheet after 1/2 h in vacuum at 540°C. [25] x100

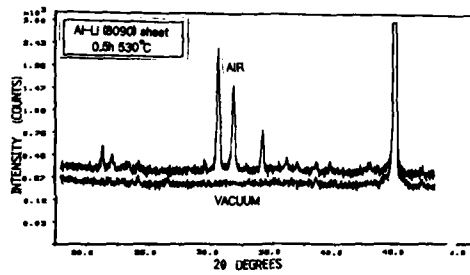


Fig 6 X-ray intensities for 2.5 mm 8090 sheet after $\frac{1}{2}$ h in vacuum and after further $\frac{1}{2}$ h in air.

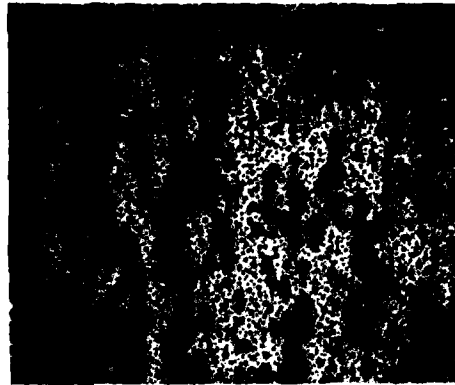


Fig 7 Ground surface of 2.5 mm unrecrystallised 8090 sheet after 1 min at 530°C in air x50.



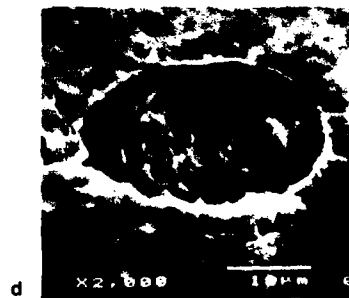
a



b



c



d

Fig 8 Unrecrystallised 2.5 mm 8090 sheet, after exposure at 530°C in (a) electro-polished surface in moist argon for 1 minute, (b) (c) ground surface in air for 10 minutes (d) recrystallised sheet, electro-polished surface after 1 minute at 530°C in moist air and ultrasonic cleaning in water. [25]

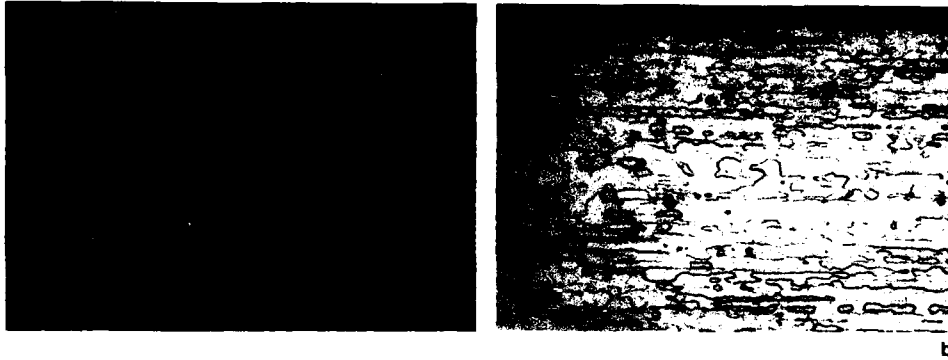


Fig 9 Unrecrystallised 2.5 mm 8090 sheet
in (a) as received condition
(b) after surface polishing x500.

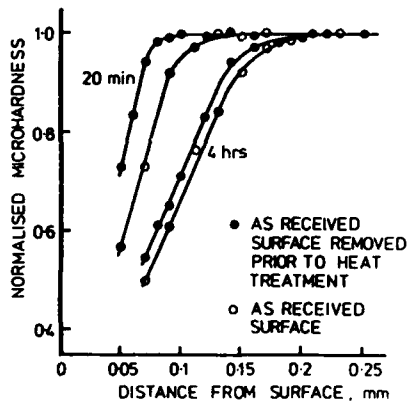


Fig 10 8090 5 mm sheet, microhardness v distance curves for as received and polished surfaces. [18]

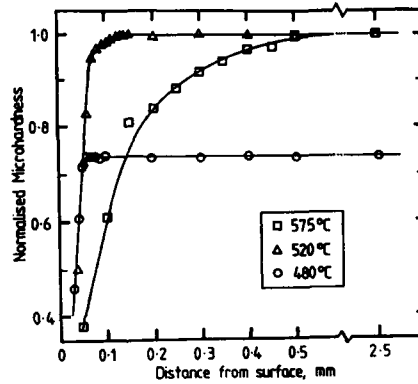


Fig 11 8090 5 mm sheet polished surface showing effect on microhardness of 1 h at various temperatures in air. [18]

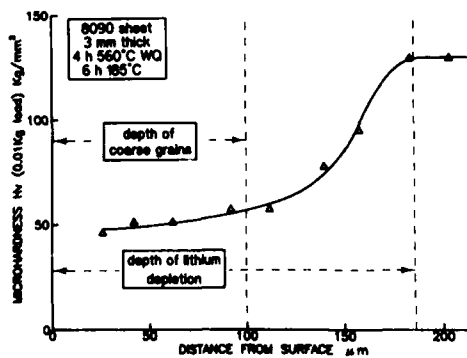


Fig 12 8090 3 mm unrecrystallised sheet, ground surface showing depths of recrystallised and low hardness bands.

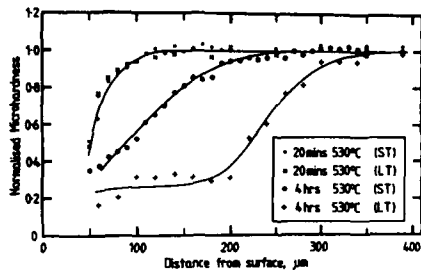


Fig 13 8090 unrecrystallised sheet microhardness after 530°C in a salt bath. [27]

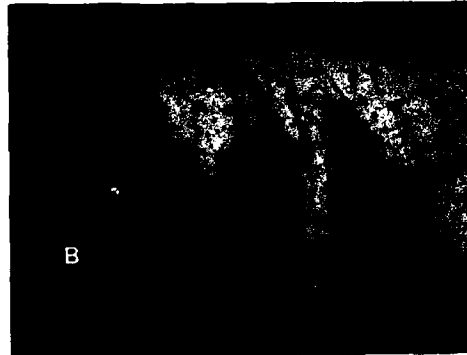


Fig 14 8090 3 mm unrecrystallised sheet, ground surface at B, guillotined edge at A after 31 minutes at 530°C in air. x250

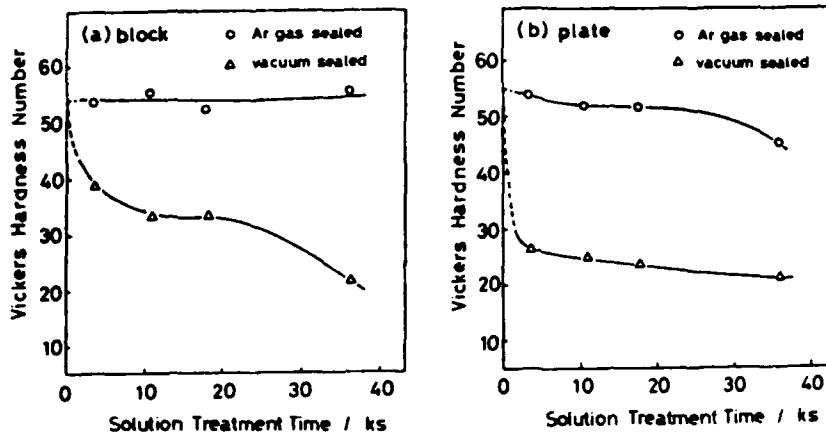
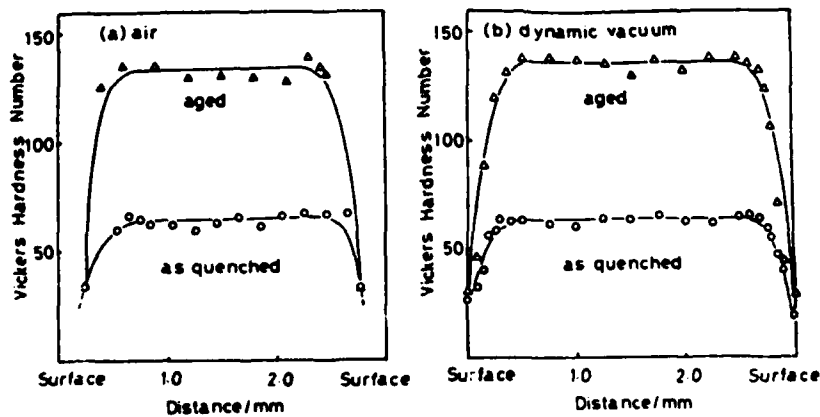


Fig 15 Al-3.12% Li alloy (a) block $3 \times 3 \times 10$ mm and (b) plate $0.2 \times 3 \times 20$ mm, microhardness after exposure at 550°C for times up to 10 h. [36]



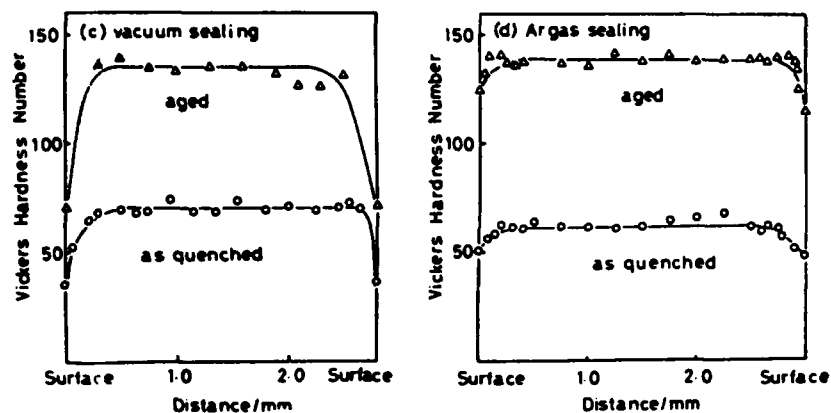


Fig 16 Al-3.12 wt % Li after SHT 550°C 3 h + WQ aged 200°C for 16 h (a) in air (b) dynamic vacuum (c) vacuum sealed (d) argon gas sealed. [36]

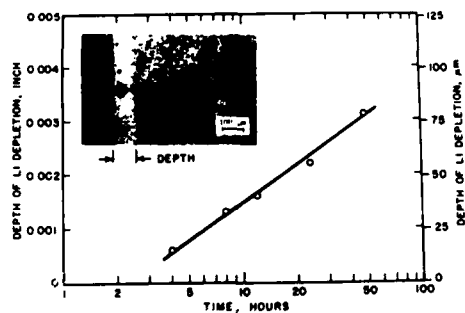


Fig 17 8090 forging, depletion depth after exposure at 438°C in air. [33]

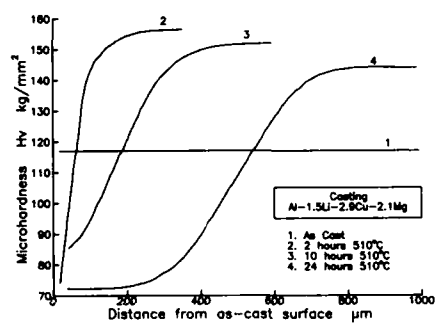


Fig 18 Depletion depth in Al-Li alloy casting. [34]

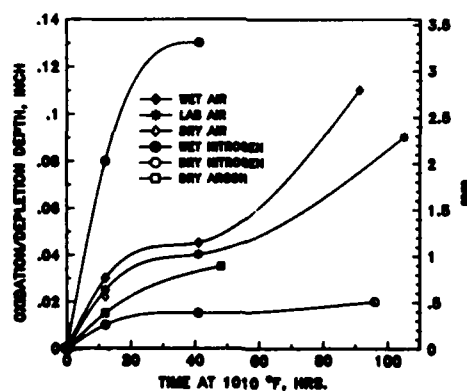


Fig 19 Depletion depth in Al-2.9% Li-1.5% Cu-2.0% Mg-0.15 Zr-alloy ingot during homogenization at 543°C in different atmospheres. [8]

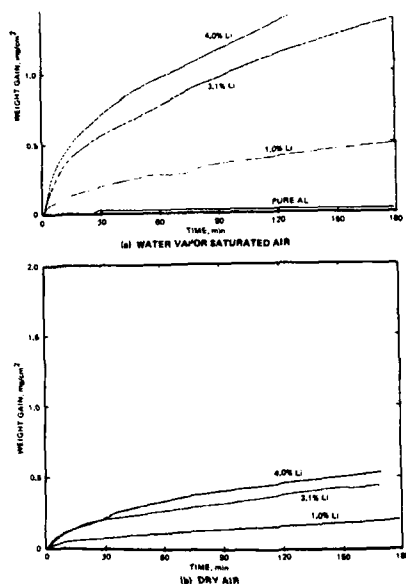


Fig 20 Effect of lithium content on weight gain of Al-Li alloys at 500°C in (a) water saturated air (b) dry air. [37]

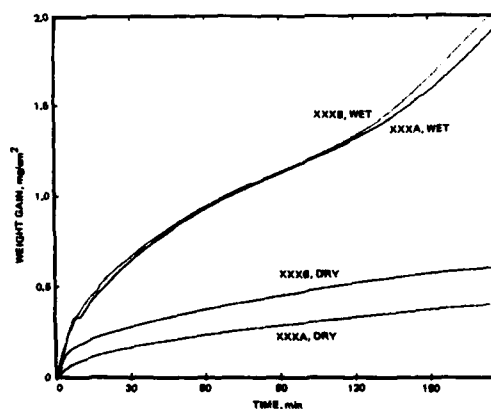


Fig 22 Weight gain of 8090 and 8091 alloys in wet and dry air at 500°C. [19]

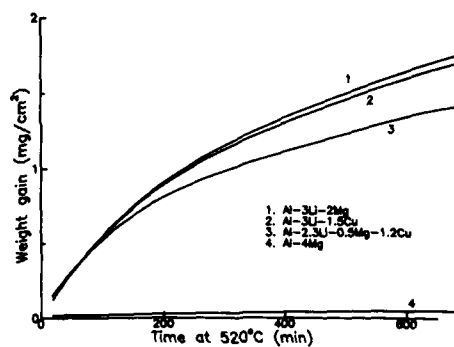


Fig 21 Effect of alloy content on weight gain of Al-Li alloys at 520°C. [37]

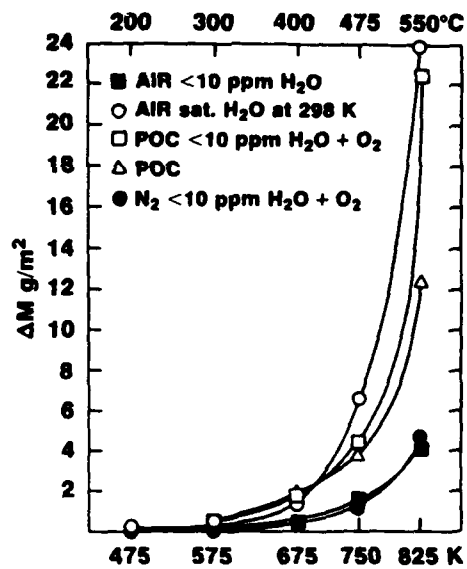


Fig 23 2090 1 mm sheet mechanically polished showing the effect of temperature on weight gain after 3.3 h in various atmospheres. [21]

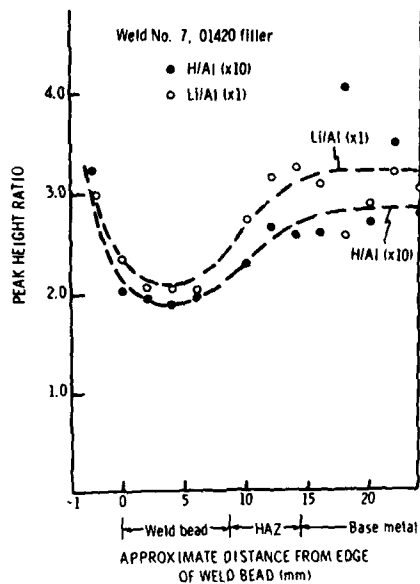


Fig 24 Secondary ion mass spectroscopy (SIMS) peak height profiles for Li and H normalised to Al across a transverse section of 01420 TIG weld, bead made using 01420 filler. [7]

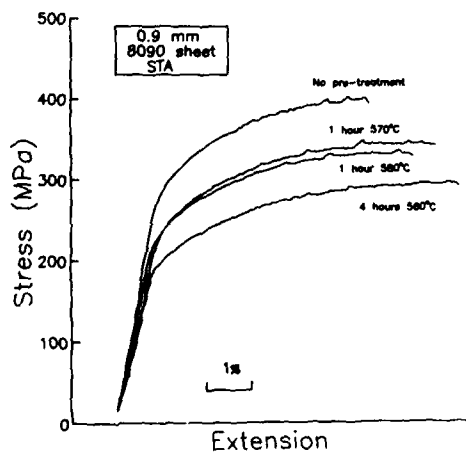


Fig 26 8090 0.9 mm sheet machined from 4 mm sheet. Effect of different solution heat treatments in air on tensile stress/strain curves in -T6 condition.

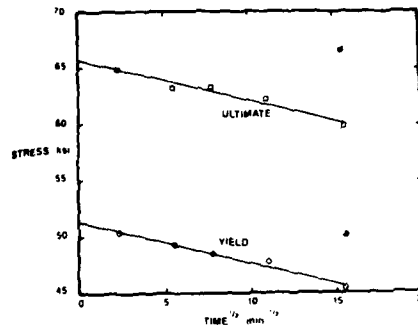


Fig 25 As received 1.6 mm 8090 sheet showing effect of time at SHT (530°C) in air and ageing (WQ, 190°C 16 h) on tensile properties. Closed symbols for samples surface machined after heat treatment. [29].

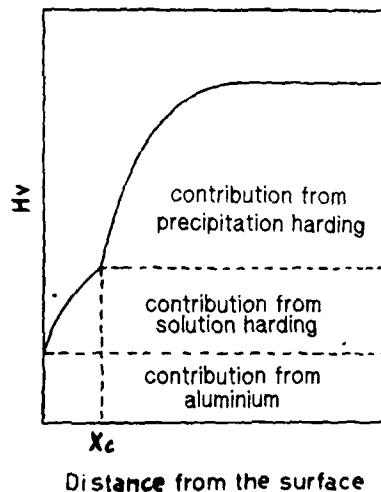


Fig 27 Schematic diagram of contributions to hardness in depleted layer.

FRETTING WEAR AND FRETTING FATIGUE AT TEMPERATURES UP TO 600°C

by

R B Waterhouse
Department of Metallurgy and Materials Science
University of Nottingham
Nottingham NG7 2RD
UK

SUMMARY

Raising the temperature increases the oxidation rate of most alloys. The thicker oxide film prevents metal-to-metal contact and reduces the coefficient of friction. On ferrous materials a type of oxide layer develops which was first observed in high temperature unidirectional sliding and, because of its smoothness, was given the name "glaze oxide". Both high temperature and sliding are necessary for its formation. The result is that the wear is much reduced and also fatigue strengths are increased. It is only stable at the high temperature. If the temperature falls to room temperature it is soon completely disrupted. The evidence is that the alloys which are capable of forming the "glaze oxide" are those on which an oxide with a spinel structure can develop. The appearance of the oxide is a smooth, grooved outer surface, with a granular structure underneath. If the oxide is damaged it is soon repaired. Titanium alloys do not develop this type of oxide. Surface modification by implantation of Ba and Bi ions has produced significant improvements in the tribological behaviour of these alloys in high temperature fretting.

INTRODUCTION

The features that distinguish fretting wear from unidirectional or reciprocating sliding wear are the very small amplitude of the relative movement, and as a result, the slow velocity of movement, typically of the order of $\mu\text{m/s}$ rather than m/s . The amplitude of motion, known as slip, at which fretting can be said to have become reciprocating motion is controversial. There is, however, a marked increase in the specific wear rate in the region 30 to 75 μm , Fig. 1(1). Damage has been reported at amplitudes of less than 1 μm . One consequence of the small amplitude is that any debris that is formed remains in situ and does not escape easily from the contact. Often features on one of the surfaces such as machining marks are imprinted on the other surface.

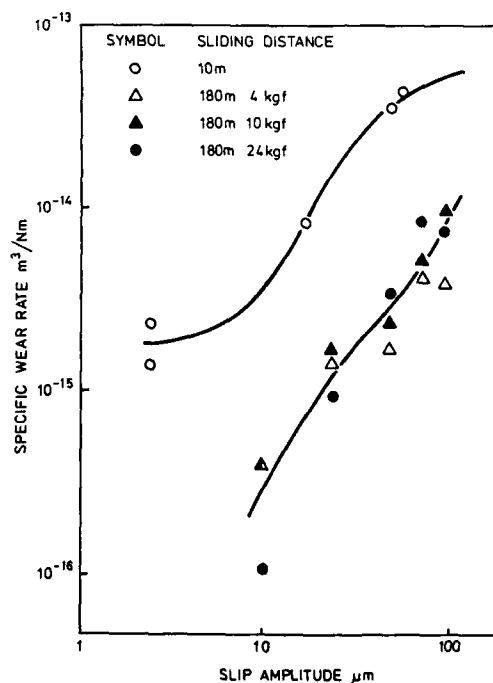


Fig. 1. Specific wear rate vs. slip amplitude.

In nearly all cases of fretting the two contacting surfaces are clamped together and are nominally stationary with respect to each other. The movement arises from vibration or, more commonly, due to one of the members of the contact being cyclically stressed, i.e. undergoing fatigue. In such cases slip occurs only over part of the contacting surfaces so that there is a boundary between the slip and non-slip areas. This boundary is frequently the initiation site for fatigue cracks. Examples of possible fretting situations are press-fits e.g. turbine discs on rotating shafts, or connections such as dove-tail or fir-tree fixings of turbine blades to the turbine disc. Fretting also occurs between the snubbers on the blades but this has the purpose of damping vibration of the blades. In the gas turbine aero-engine these events are occurring in a high temperature oxidising atmosphere which exerts a powerful influence on the process.

One of the early quantitative explanations of fretting was that due to Uhlig.(2). His explanation was the asperities on one surface scraped off the oxide film on the opposing surface during a half cycle and the oxide film grew again ready to be scraped off in the next half cycle, Fig. 2. He assumed a logarithmic growth law which meant that there would be a pronounced frequency effect, Fig. 3a and b, which he found in his experiments on mild steel at room temperature. At higher temperatures the oxide film grows much more quickly on most alloys so that on the Uhlig theory the formation of debris would be much greater. However, the first experiments on high temperature fretting by Burdicks and Ashford showed that this was not the case, and in fact the fretting wear of mild steel showed a marked transition to a lower wear rate in the region of 150°C(3). Shortly after this Taylor found that fretting stainless steel in carbon dioxide at a temperature of 650°C disrupted the normally protective Cr_2O_3 film and exposed a much faster growing oxide film with a spinel structure.(4). Fortunately this also exhibited low wear properties and also low friction. Similar films had been discovered in the high temperature unidirectional sliding of a number of alloys by Stott and he gave them the name "glaze" oxides because of their extremely smooth surface(5).

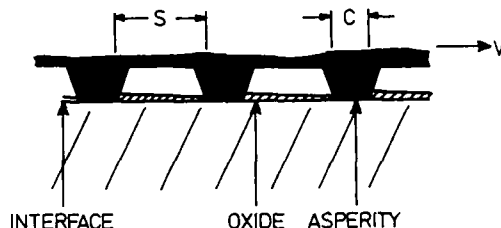


Fig. 2. Model of fretting wear process.

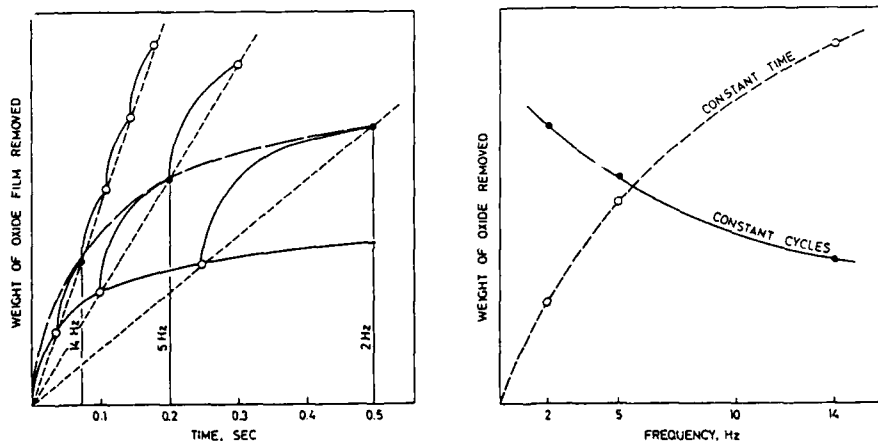


Fig. 3. Effect of frequency on (a) oxide growth rate; (b) wear rate.

The reason that fretting lowers the fatigue performance of materials is that the mechanical action disrupts air-formed oxide films in the early stages and promotes intimate metal to metal contact, often with the formation of local welds. This results in regions of local high strain fatigue with the rapid initiation of fatigue cracks. If the fretting motion is the result of cyclic stressing then these cracks will propagate and lead to failure. It has recently been shown that if there is a residual tensile stress

in the surface or just below it the cracks can propagate under these conditions and may lead to failure⁽⁶⁾. The effect of increased temperature on the fatigue properties of most alloys is to reduce them particularly if creep becomes an added component of the process. However, the reduction in coefficient of friction by the growth of oxide films will reduce the local alternating shear stresses resulting from the fretting action and make the initiation of a fatigue crack more difficult.

These considerations are now examined in the light of the high temperature fretting behaviour of a number of materials.

FRETTING WEAR AT HIGH TEMPERATURES

Nickel and nickel-based alloys

Swikert and Johnson⁽⁷⁾ found that the fretting wear of Inconel 600 was an order of magnitude less at 260°C compared with room temperature due to the protective action of the thicker oxide film. Bill⁽⁸⁾ showed that the fretting wear of Inconel X-750 and Rene-41 steadily decreased up to a temperature of 500°C and then was constant at this value up to 816°C. The wear volume reduction was 70% for the Inconel and 90% for the Rene. The behaviour was attributed to the protection afforded by the chromium rich oxide films on these alloys which contain 15 to 20% Cr. Further work on experimental nickel-chromium alloys to which additions of up to 5% Al were made, indicated that the alloying additions considerably improved the resistance to fretting compared with pure nickel⁽⁹⁾. Fig. 4 compares Bill's results with results

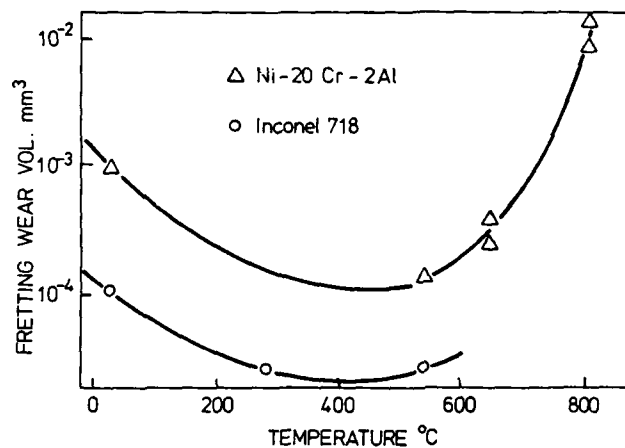


Fig. 4. Wear vs. temperature for Ni-20Cr-2Al and Inconel 718.

obtained in the author's laboratory on Inconel 718⁽¹⁰⁾. The increase in wear rate above 540°C was attributed to creep of the material. The reduction in fretting wear was assumed to be due to the formation of spinel type oxides which could be NiOCr_2O_3 and NiOAl_2O_3 in the experimental alloy and also NiOFe_2O_3 and FeOCr_2O_3 in the case of the Inconel. Fig. 5 illustrates how these changes are reflected in

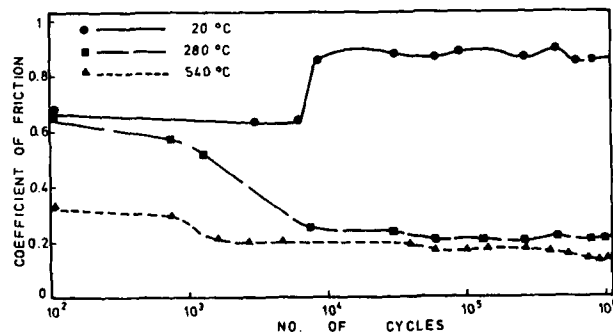


Fig. 5. Coefficient of friction vs. number of cycles for Inconel 718 at 20°, 280° and 540°C.

the friction behaviour(11). Kayaba has used friction/cycles curves to determine the number of cycles to develop the glaze oxide over the whole of the contacting areas, Fig. 6(12). The value of N^* depends both on frequency and temperature, Figs. 7 and 8. Transfer of material from one surface to the other occurs in the initial stages but ceases when the glaze oxide is developed.

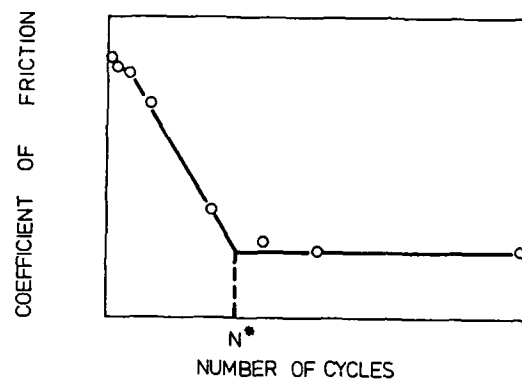


Fig. 6. Determination of number of cycles, N^* , to form glaze oxide.

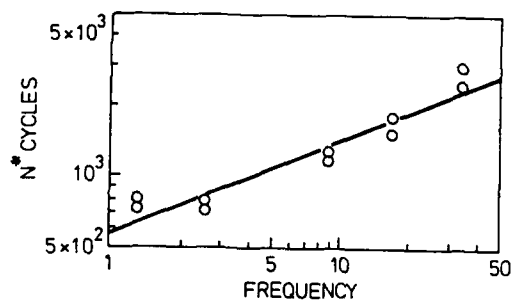


Fig. 7. Variation of N^* with frequency.

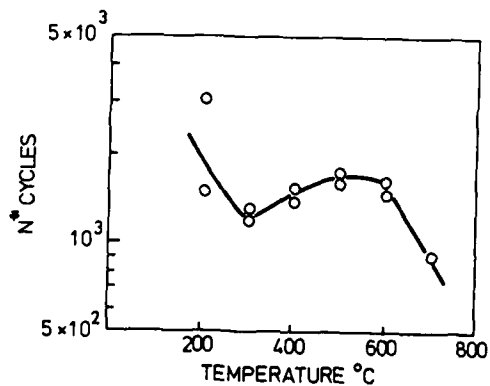


Fig. 8. Variation of N^* with temperature.

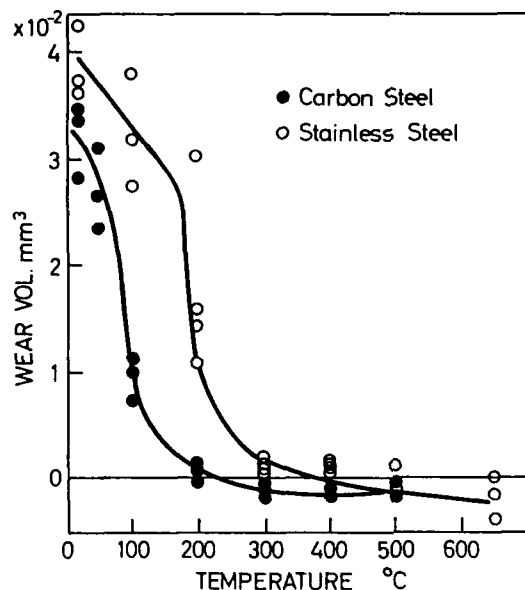


Fig. 9. Fretting wear vs. temperature for 0.45C steel and stainless steel 304.

Iron and Iron-based alloys

Hurricks studied the fretting behaviour of mild steel up to 500°C. He found a transition at 200°C at which the wear became very low(13,14). Below this temperature the typical reddish brown debris was visible but above this temperature the debris was compacted into smooth areas with a hardness of 1000 VHN. Between 200 and 500°C the wear continued to fall. Surface finish was found to be a significant factor at temperatures above 380°C, the wear being greater the rougher the initial surface. Above 380°C Fe_3O_4 is the major constituent of the oxide, and has the spinel structure referred to earlier. Fig. 9 shows the fretting wear curves for a 0.45C steel and austenitic steel 304 with the marked transitions at 100°C and 200°C respectively(15). These transitions are again attributed to the formation of the spinel oxide Fe_3O_4 which is verified by quantitative X-ray analysis. These authors have compared the effect of temperature on fretting wear with its effect on unidirectional sliding for these two steels and find that the specific wear volume above the transition temperature is a factor of 10 lower for the carbon steel in fretting and a factor of 40 lower for the stainless steel(16). The difference is explained by the different way in which the glaze oxide is formed in fretting, namely by the build up of transferred layers of oxide. Similar formation of multi-layers of oxide was found in fretting of another stainless steel, 321, in CO_2 in the temperature range 350 to 650°C(4). At higher applied loads the fretted surfaces appeared to be smoother which was taken as evidence that the glaze oxide had some plasticity at these temperatures.

The author has investigated an austenitic stainless steel containing nitrogen and has found that at temperatures above 400°C the smooth glaze oxide was formed with corresponding falls in the coefficient of friction and the wear vol me, Figs. 10 and 11(17). The oxide was identified as the spinel $NiOCr_2O_3$ by X-ray analysis but chemical analysis confirmed that it contained some iron.

Titanium and Titanium alloys

Bill(18) investigated the fretting of high purity titanium at temperatures up to 650°C. The wear volume increased as the temperature was raised to 500°C but then fell sharply, Fig. 12. The rise in wear rate was ascribed to the softness of the substrate and the thinness of the oxide film. The fall at higher temperatures was due to a change in kinetics of oxide film formation resulting in much thicker films. Swikert and Johnson(7) report that fretting wear of the alloy Ti6Al4V was very severe at room temperature with considerable galling. At 280°C the wear was an order of magnitude less although the coefficient of friction was similar at both temperatures. The author found that the coefficient of friction tended to fall with increasing number of cycles at room temperature but rose at 400 and 600°C, with the result that the final values were little different at the various temperatures.(11) The wear volumes were similar at slip amplitudes of 10μm, but at an amplitude of 40μm the wear at 20°C was 30 times greater than the wear at temperatures between 200 and 600°C where the wear was very similar, Fig. 12. The author has studied four other titanium alloys intended to be used at elevated temperatures, namely IMI 500, 879 and 829(19). At room temperature all showed coefficients of friction of around 0.6 falling to 0.15 at 600°C with very little wear damage at this temperature. However, the glaze oxide seen on the nickel and iron alloys was not detected. The opinion was that the oxide films, although protective, were very thin whereas the glaze oxides appear to be the result of more rapidly growing oxides. In general their composition was TiO_2 although occasionally other constituents of the alloys

were detected such as Al_2TiO_5 on 550 and ZrTiO_4 on 829(20). Efforts to develop a glaze oxide on these alloys are described in a later section.

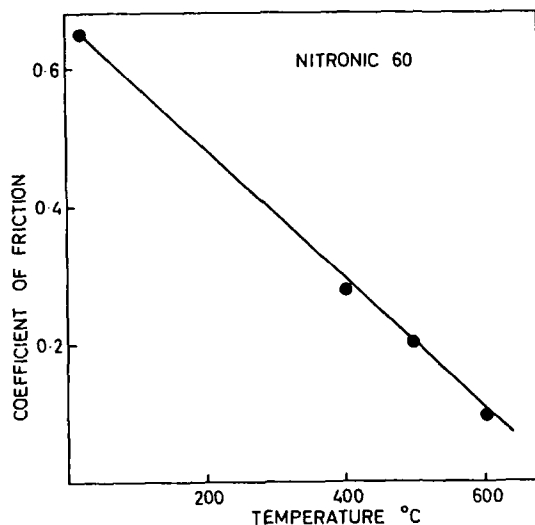


Fig. 10. Friction vs. temperature for stainless steel Nitronic 60.

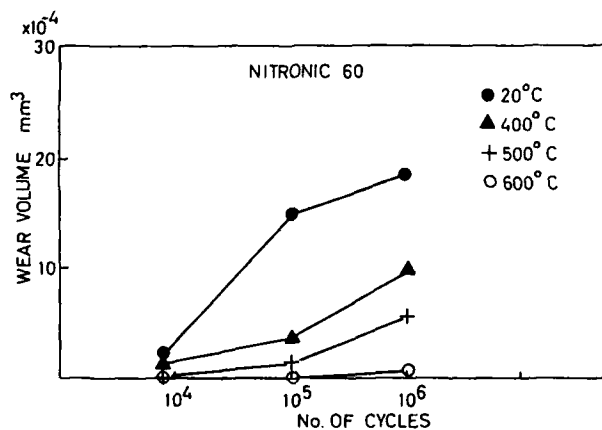


Fig. 11. Fretting wear vs. temperature for stainless steel Nitronic 60.

FRETTING FATIGUE AT HIGH TEMPERATURES

Nickel-based alloys

The author has studied the fretting fatigue of Inconel 718 at temperatures up to 700°C but at this temperature creep was becoming appreciable and so the tests were limited to 20, 280, 540°C. The tests were carried out in fluctuating tension with a mean stress of 550 MPa. The fatigue curves are shown in Fig. 14(21). The strength reduction due to fretting was 2.29 at 20°C but reduced to 1.20 at 540°C. At the intermediate temperature the fatigue strength was low at 10⁷ cycles but the fatigue life was increased at higher stresses. The improvement was due to the development of the glaze oxide but at 280°C a certain minimum amplitude was necessary to form the glaze. This was estimated at 22μm, since the slip amplitude depends on the applied fatigue stress. The glaze oxide formed at 540°C was perfect but the glaze formed at 280°C exhibited cracks and areas where the glaze had spalled. The virtue of the glaze

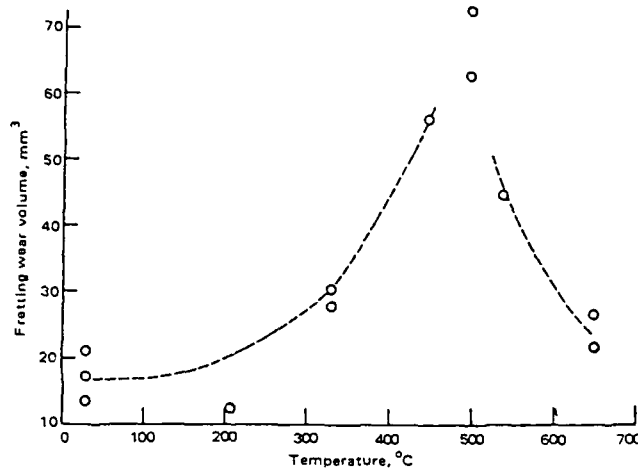


Fig. 12. Fretting Wear of pure titanium vs. temperature.

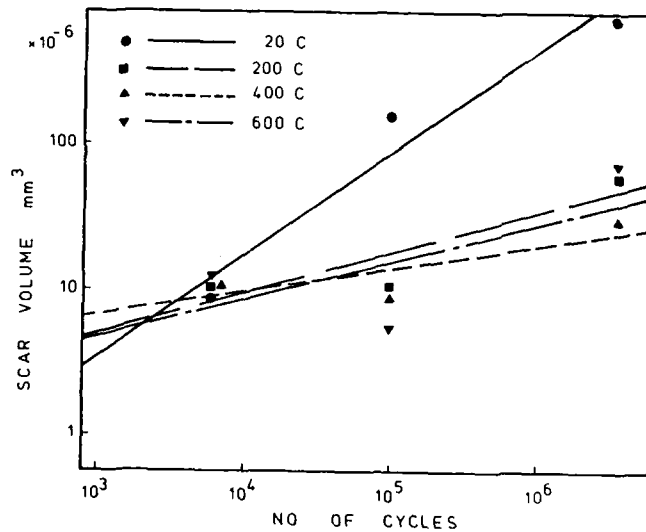


Fig. 13. Fretting wear of Ti-6Al-4V vs. temperature.

oxide is that it can renew itself if it breaks down. Since temperature fluctuations are certain to occur in a gas turbine aero-engine, some tests were carried out where the glaze was developed at 540°C and then the temperature dropped and the fretting continued at room temperature. Under these circumstances the glaze afforded no protection and was rapidly disrupted so that the point fell close to the room temperature fatigue curve(22).

Iron-based alloys

There is little information here although the author has carried out fatigue tests on the stainless steel 316. Fig. 16 shows that again there is a considerable increase in fretting fatigue strength as the temperature is raised.

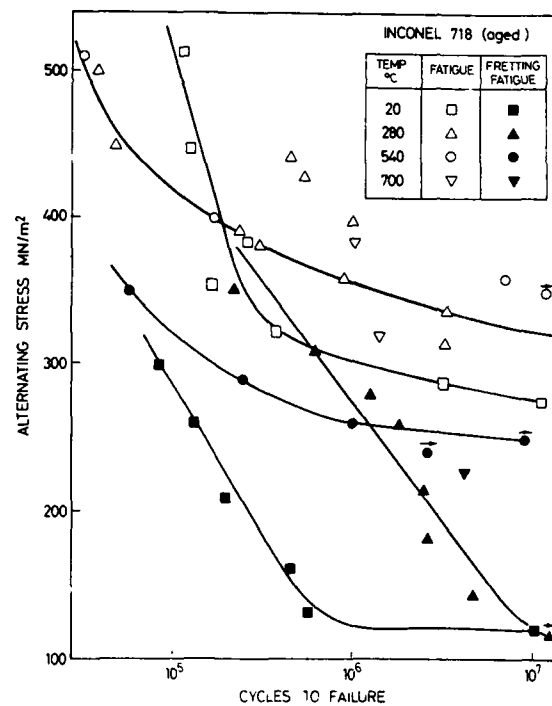


Fig. 14. Fatigue and fretting fatigue curves for Inconel 718 at 20°, 280° and 540°C.

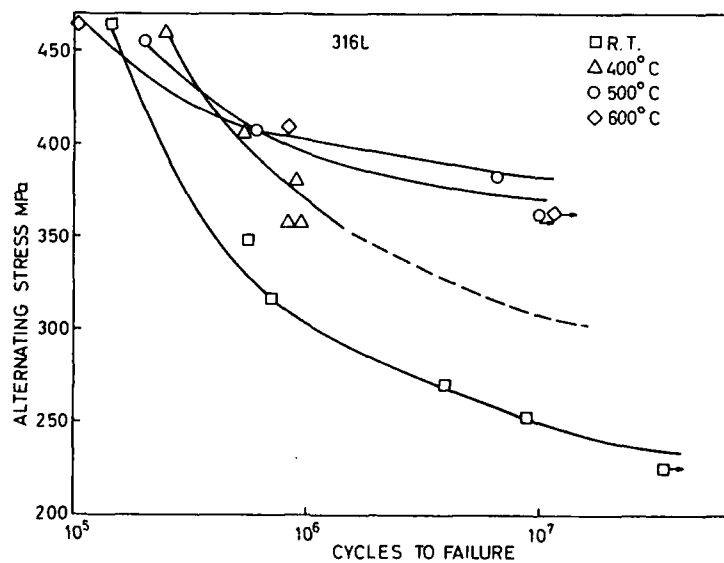


Fig. 15. Fretting fatigue curves for stainless steel 316L at 20°, 400°, 500° and 600°C.

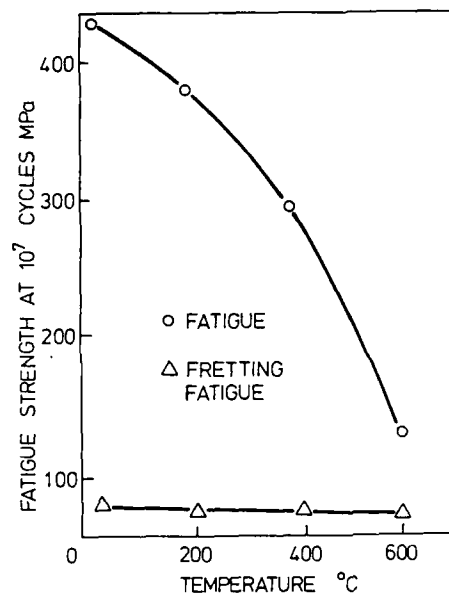


Fig. 16. Fatigue and fretting fatigue strength at 10^7 cycles of Ti-6Al-4V vs. temperature.

Titanium alloys

The author has investigated the fretting fatigue of the alloys Ti6Al4V IMI 318(23) and IMI 829(24). The latter was specifically designed as a creep resistant alloy. The fatigue strength of the 318 alloy at 10^7 cycles with a mean stress 247 MPa are shown in Fig. 16. The fatigue strength falls with increasing temperature. With fretting the fatigue strength is uniformly low at all temperatures. Similar results for IMI 829 are shown in Fig. 17, the mean stress being 280 MPa. Again the fatigue strength falls with temperature although the fretting fatigue strength does show some increase with temperature. Although areas of smooth oxide are visible they show frequent evidence of cracks and spalling and do not appear to have the characteristic properties of the glaze oxide found on nickel and iron alloys. It appears that both these alloys would be unsatisfactory if suffering fatigue at these temperatures whether or not fretting was involved.

SURFACE TREATMENTS TO IMPROVE HIGH TEMPERATURE FRETTING PROPERTIES

One method of achieving this would be to apply a coating which itself has the necessary composition to form the glaze oxide under the operating conditions. Sprayed molybdenum has been found effective when applied to steel at temperatures up to 300°C(25). Above this temperature rapid oxidation and volatilisation of the oxide occurred. For higher temperature applications sprayed coatings of Fe-13Cr, Fe-18Cr-8Ni and Ni-5Al were applied to a low alloy steel and tested at room temperature, 475 and 700°C for resistance to fretting wear(26). The coatings containing iron and chromium gave very low wear rates at the two higher temperatures with evidence of glaze formation. The Ni-5Al coating was only effective at 700°C. A composite coating of Fe-13Cr + Ni-5Al however did give good protection at both temperatures.

Some consideration has been given to modifying the surface of the titanium alloys to produce an oxide similar to the glaze oxide(27). The method chosen was ion implantation. The first ion implanted was barium as it was hoped that oxidation would result in the formation of $BaTiO_3$ since this has the perovskite structure which is not unlike the spinel structure which is a feature of the glaze oxides. It did give some reduction in coefficient of friction but the oxide layer was extremely thin. The other ion implanted was bismuth since this was thought to increase the oxide thickness. Extremely low coefficients of friction were recorded at temperatures of 500 and 600°C, Fig. 18, and the wear was immeasurable. This process showed considerable promise but resources have not been available to see if it is as effective in fretting fatigue.

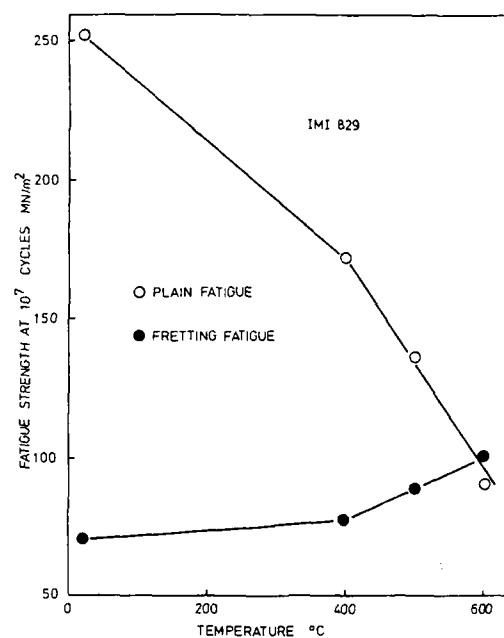


Fig. 17. Fatigue and fretting fatigue strength at 10^7 cycles of IMI829 vs. temperature.

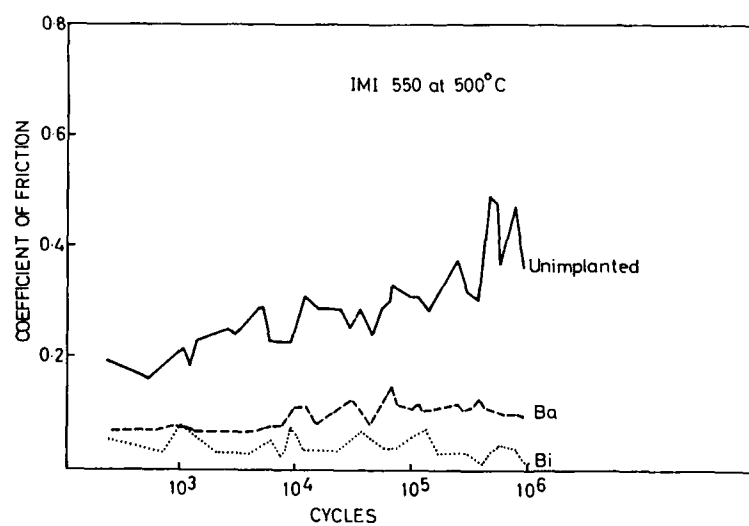


Fig. 18. Effect of ion implantation on the coefficient of friction of IMI550 at 500°C.

DISCUSSION

The effect of the glaze oxides on reducing fretting damage is due to their excellent protective properties in preventing wear damage and also the low friction which reduces the alternating shear stresses in the contact zone. Since they are formed from the constituents of the alloys themselves they have the unique feature of being self repairing if any spalling occurs. Sections through a glazed surface indicate that the layer is often as thick as 10 μ m and may have a layer-like structure. Similar oxide layers found in reciprocating sliding experiments have been described by Lin as a stable adherent, thermally softened oxide layer on the load-bearing areas⁽²⁸⁾. The low friction is attributed to their low shear strength and the relatively high strength of the substrate. The common feature is the spinel structure which is a cubic close-packed arrangement of oxygen ions with the metal cations in interstitial positions. The oxides formed on titanium alloys do not have this structure, and this fact together with their limited thickness in this temperature region precludes the formation of glaze oxide. It has been suggested that the glaze oxide is only formed on alloys where oxide growth is entirely by cationic conduction, which is not the case with titanium alloys, but this theory has yet to be tested experimentally. Implantation with barium and bismuth ions did not produce any detectable change in the oxide composition but bismuth appeared to increase the thickness of the oxide layer. Whether such oxides would be self-repairing if breakdown occurred during wear is uncertain.

CONCLUSION

Alloys containing iron and/or chromium are capable of forming, under fretting conditions at high temperatures, a form of oxide which exhibits low friction and low wear. The low friction reduces the likelihood of crack initiation in fretting fatigue. If breakdown does occur the film is able to regenerate itself from the constituents of the alloy. The structure of these protective oxides is that of a spinel. Such oxides are not formed on titanium alloys and it has been suggested that surface modification by ion implantation, particularly by bismuth ions, gives such low friction and wear values to warrant further investigation.

REFERENCES

1. Waterhouse, R. B., Fretting Wear, proc. Conference Wear of Mats, March 30 - April 1 1981, San Francisco, ASME, New York, (1981), 17.
2. Uhlig, H. H., Mechanisms of fretting corrosion, J. Appl. Mech. 21 (1954) 401.
3. Hurricks, P. L. and Ashford, K. S. The effect of temperature on the fretting wear of mild steel, Proc. Instn. Mech. Engrs. 184 Pt 3L (1969-1970) 165.
4. Taylor, D. E., Hardisty, F. B., Waterhouse, R. B. and Nehru, A. Y. The fretting wear of an austenitic stainless steel in air and carbon dioxide at elevated temperatures, Wear 56 (1979) 9.
5. Stott, F. H., Lin, D. S. and Wood, G. C. The structure and mechanism of formation of the 'glaze' oxide layers on nickel-based alloys during wear at high temperatures, Corr. Sci. 13 (1973) 449.
6. Kuno, M., and Waterhouse, R. B. The effect of residual stress and temperature on the fretting of bearing steel, Proc. Conf. Leeds-Lyon, 6-9 September 1988, Leeds, in the press.
7. Swikert, M. A. and Johnson, R. O. Friction and wear under fretting conditions of materials for use as wire friction dampers of compressor blade vibration, NASA TN-4630 (1968).
8. Bill, R. C. Fretting of secondary seal ring candidate materials in air at temperatures to 816°C, NASA TN-D7073 (1972).
9. Bill R. C. Fretting of nickel-chromium-iron alloys at temperatures to 816°C, NASA TN-D-7570 (1974).
10. Waterhouse, R. B. and Taylor, D. E. High temperature fretting and wear of like metal contacts, Rev. High Temp. Mat. 4 (1980) 259.
11. Hamdy, M. M. and Waterhouse, R. B. The fretting wear of Ti-6Al-4V and aged Inconel 718 at elevated temperatures, Wear 71 (1981) 237.
12. Kayaba, T., Iwabuchi, A. and Kato, K. Fretting wear of Ni-Cr alloy at high temperature, Int. Edn. J. Jap. Soc. Lub. Engrs. 5 (1984) 47.
13. Hurricks, P. L. The fretting wear of mild steel from room temperature to 200°C, Wear 19 (1972) 207.
14. Hurricks, P. L. The fretting wear of mild steel from 200 to 500°C, Wear 30 (1974) 189.
15. Kayaba, T. and Iwabuchi, A. The fretting wear of 0.45% C steel and austenitic stainless steel from 20 to 650°C in air, Wear 74 (1981-1982) 229.
16. Iwabuchi, A., Hori, K. and Kudo, H. The effect of temperature on wear of S45C and SUS 304, Int. Edn. J. Jap. Soc. Lub. Engrs. 9 (1988) 29.
17. Waterhouse, R. B. The fretting wear of nitrogen-bearing austenitic stainless steel at temperatures to 600°C, J. of Tribology 108 (1986) 359.
18. Bill, R. C. Fretting of titanium at temperatures to 650°C in air, NASA TN-D-8048 (1975).
19. Waterhouse, R. B. and Iwabuchi, A. High temperature fretting wear of four titanium alloys, Wear 106 (1986) 303.

20. Waterhouse, R. B. and Iwabuchi, A. The composition and properties of surface films formed during the high temperature fretting of titanium alloys, Proc. JSLE Int. Tribol. Conf., July 8-10, Tokyo (1985) 53.
21. Hamdy, M. M. and Waterhouse, R. B. The fretting fatigue behaviour of a nickel-based alloy (Inconel 718) at elevated temperatures, Proc. Conf. Wear of Mats., April 16-18 1979 Dearborn ASME, New York (1979) 351.
22. Hamdy, M. M. and Waterhouse, R. B. The stability of the protective glaze oxide formed during high temperature fretting of an aged nickel-base alloy Inconel 718, Proc. Conf. Wear of Mats., March 30 - April 1 1981. San Francisco, ASME, New York (1981) 546.
23. Hamdy, M. M. and Waterhouse, R. B. On glaze formation on Ti-6Al-4V alloy during fretting fatigue at elevated temperatures, Key Engng. Mats. A7 (1985) 1.
24. Hamdy, M. M. and Waterhouse, R. B. The fretting fatigue behaviour of the titanium alloy IM1829 at temperatures up to 600°C, Fatigue of Engng. Mats. and Structs. 5 (1982) 267.
25. Overs, M. P., Harris, S. J. and Waterhouse, R. B. The fretting wear of sprayed molybdenum coatings at temperatures up to 300°C, Proc. Conf. Wear of Mats., April 16-18 1979, Dearborn, ASME, New York (1979) 379.
26. Overs, M. P., Harris, S. J., and Waterhouse, R. B. Development of coatings based on Fe-Cr-Ni-Al for resisting fretting wear in the temperature range 20-700°C, Wear 74 (1981-1982) 315.
27. Waterhouse, R. B. and Iwabuchi, A. The effect of ion implantation on the fretting wear of four titanium alloys at temperatures up to 600°C, Proc. Conf. Wear of Mats., April 14-18 1989, Vancouver, ASME, New York (1985) 471.
28. Lin, D. S., Stott, F. H. and Wood G. C. The effects of elevated temperatures in the friction and wear behaviour of some commercial nickel base alloys, ASLE Trans. 17 (1974) 251.

EFFECT OF PROTECTIVE COATINGS ON MECHANICAL PROPERTIES OF SUPERALLOYS

Rémy MEVREL, Jean-Marie VEYS*

O.N.E.R.A., Materials Science Department, B.P. 72, 92322 Châtillon Cedex, France
*S.T.P.A., Ministry of Defense, France.

ABSTRACT

Superalloys employed in hot sections of gas turbine engines are generally designed in terms of high temperature mechanical and/or thermal properties such as creep, mechanical and thermal fatigue. Their use in the aggressive environment of combustion gases requires their protection by a coating, most commonly an aluminide coating or an MCrAlY overlay. In this paper we give a brief review of the possible effects of the presence of a protective coating on the mechanical properties of superalloy substrates.

The superalloy microstructure, and therefore its mechanical performances, particularly in creep, can be altered by the heat treatments associated with the coating deposition process. As a result, proper care must be taken when selecting a coating for a specific superalloy substrate. Interdiffusion phenomena taking place between coating and substrate at high temperature during service may decrease the load bearing section of the superalloy and, as a consequence, may degrade its creep lifetime. Examples will be given of the possible effects of coating/substrate interdiffusion on the creep life of single crystal CMSX2 (no effect) and in the case of a directionally solidified eutectics superalloy (significant degradation). It is to be added though that in the long run, the presence of a coating can enhance the creep life of a substrate due to its protective effect against high temperature corrosion. As regards the fatigue behaviour, several studies, in the U.S.A. and in Europe, have shown that the presence of a coating (aluminide or MCrAlY overlay) may in some cases degrade the mechanical and thermomechanical performances of superalloy substrates. The interpretation of these data remains at present limited because the intrinsic properties of protective coatings are still insufficiently studied.

1. INTRODUCTION

For use in hot sections of gas turbine engines, a superalloy is generally selected for specific properties such as creep, fatigue, whether mechanical or thermal. Due to the interaction with the aggressive environment of the combustion gases which can provoke the degradation of these properties, the superalloy components must be protected by a coating. The most used coatings are aluminide-based [1], MCrAlY overlays [2], and zirconia-based thermal barrier coatings [3]. However, a coating may affect the mechanical properties of the superalloy substrate it protects in several ways: alteration of the alloy microstructure during the heat treatments associated with the coating cycle, formation of non-load-bearing regions or of brittle phases because of interdiffusion phenomena during coating application or in service at high temperature, suppression of environmental degradation,...

Several reviews have been published concerning the influence of protective coatings on the mechanical properties of superalloys [4-6]. In this paper, after considering the different factors which can affect the mechanical behaviour of coated systems, we will review some recent experimental results.

2. CONSIDERATIONS ON THE MECHANICAL PROPERTIES OF COATED SYSTEMS

2.1. Coating as non-load-bearing section

Coatings are generally considered as non-load-bearing material. This is all the more justified that, at temperatures ranging between 800°C and 1100°C, which are typical operating superalloy

temperatures in gas turbine applications, the coating mechanical resistance is low as will be seen below. This fact has to be taken into account when calculating the effective stress supported by the substrate alloy. For example, during the formation of an aluminide coating, part of the substrate is transformed into β -NiAl-based material. This reduces the effective load-bearing section of the superalloy substrate. It has been calculated [7] that the formation of a typical 60 μm low activity aluminide coating on a 1 mm thick IN100 component results in a 9% increase in stress supported by the non affected alloy and, as a consequence, a reduction by a factor 2 of the creep lifetime at 850°C. Such an effect does not occur with MCrAlY overlay coatings, provided interdiffusion phenomena remain limited during exposure at elevated temperature.

In addition, it has to be mentioned that for rotating components a coating is an overload due to centrifugal forces, particularly in the case of thermal barrier coatings.

2.2. Compatibility of coating process with alloy heat treatments

Mechanical properties of modern superalloys, such as creep strength, are strongly dependent on their microstructure (in particular the γ' -Ni₃Al morphology and distribution [8]). This microstructure is to a great extent determined by the heat treatments. It is therefore essential that the heat treatment associated with the coating thermal cycle be compatible with the quality heat treatment cycle required by the alloy. Table 1 shows for example that for CMSX-2, the thermal cycle of a high activity aluminizing process is compatible with the heat treatment of the alloy, whereas a low activity is not, because of the slow cooling rate due to the thermal inertia of the pack. In this case, it has been demonstrated that an additional heat treatment is required to restore the proper γ' microstructure.

Quality heat treatment	Heat treatments associated with aluminizing	
	Low activity	High activity
CMSX-2		
2-3 h. T : 1280°C to 1320°C AC	16 h. at 1050°C SC	4 h. at 750°C SC
15 h. at 1050°C AC or 4-6 h. at 1100°C AC		16 h. at 1050°C AC
15-24 h. at 850°C AC		

Table 1 : Quality heat treatments of CMSX-2 and typical thermal cycles associated with aluminizing processes (AC = air-cooled, SC = slow cooling in pack).

An advantage of gas phase aluminizing over pack cementation processes, as emphasized by [9], is the possibility of high cooling rate. On the other hand, MCrAlY coatings obtained by EB-PVD or plasma-spraying, are generally heat treated to improve their adhesion and density ; this treatment can easily coincide with a quality heat treatment of the alloy.

2.3 Intrinsic mechanical properties of coating materials :

2.3.1. Aluminide coatings

These coatings are generally obtained by a cementation process during which aluminium is brought upon the substrate surface where it reacts and forms a β -NiAl or -CoAl based coating. Coating thicknesses are determined by solid state diffusion laws (proportional to square-root of time) and for durations compatible with industrial practice, they range between 50 and 100 μm . The structure of these coatings can be very complex as illustrated by figure 1, rendering extremely difficult the evaluation of their intrinsic mechanical properties.

Investigations carried out on extruded pure β -NiAl [10] have shown that this phase exhibits a brittle behaviour at low temperature, up to a so-called DBTT (ductile-brittle-transition-temperature), typically

600°C. This is explained by the operation of only three independent slip systems, of the form $\{hk0\} \langle 001 \rangle$, less than the minimal five required by Von Mises criterium for generalized plastic deformation. At high temperature, diffusion-related mechanisms can be effective, for example dislocation climb, and the material becomes ductile. It has to be noted though that apparently no published data exist on the mechanical behaviour of bulk materials having as complex compositions and structures as aluminide coatings. Most experimental results reported in the literature concern the evaluation of DBTT determined on coated specimens (fig. 2).

It is important to keep in mind that the properties of β -NiAl may depend on a variety of factors such as grain size, composition, strain rate, ... As regards the influence of grain size for instance, Schulson et al. [11] have carried out tensile tests on polycrystalline β -NiAl at 400°C and shown that below a critical size (20 μm), its ductility increases sharply with decreasing grain size, reporting tensile elongation of up to 40%. According to these authors, in fine-grained aggregates, the stress required to nucleate cracks is less than that corresponding to their propagation. The cracks propagate only after some plastic flow has occurred.

2.3.2. MCrAlY alloys

MCrAlY alloys deposited by plasma spraying under controlled atmosphere, to prevent any oxidation, are generally constituted of a $\gamma(\gamma')$ matrix containing a fine dispersion of β -NiAl phases. Yttrium is practically insoluble in these phases and is generally found in a M_2Y -type phase or an yttrium-containing oxide.

The possibility of fabricating MCrAlY specimens by low-pressure-plasma-spraying (LPPS) [12-14] or by hot isostatic pressing [15] has permitted to gather experimental data on the mechanical behaviour of alloys representative of overlay coatings. It was shown in [14] for example, that bulk LPPS NiCoCrAlTaY alloy presents two deformation behaviours between room temperature and 800°C, as revealed by tensile (fig. 3), microhardness and torsion tests. Up to about 500°C, it exhibits low fracture elongation (lower than 2%) and high strength; above 550°C, its strength decreases and its ductility increases sharply. At 800°C a superplastic behaviour could be shown for strain rates ranging from 10^{-4} to 10^{-3} s^{-1} . Similarly, Wood et al. [15] have shown that the tensile strength of a fine-grained (5-10 μm) NiCoCrAlY alloy obtained by HIP of alloy powders, remains high up to about 600°C (yield strength higher than 800 MPa) and sharply decreases at higher temperatures, with a correlative rise in ductility.

The low cycle fatigue behaviour of an LPPS NiCoCrAlY (PWA 276) coating alloy has been investigated by Gayda et al. [16]. At 1050°C, the life of the NiCoCrAlY alloy is significantly greater than that at 650°C and this is attributed to a slower transgranular crack growth.

2.4. Residual stresses

Residual stresses may arise at different stages during the coating processing: initial surface treatment of the substrate alloy, solidification of molten powder particles during plasma spraying, ... It is generally thought, however, that these stresses may be relaxed during the post-coating heat treatment and therefore that the main source of residual stress comes from the thermal expansion mismatch between coating and substrate. Thus for a positive expansion mismatch of $2 \cdot 10^{-6} \text{ } ^\circ\text{C}^{-1}$ between coating and substrate, a temperature drop of 1000°C will provoke a 0.2% tensile deformation in the coating, which is considered to be a maximum value by [5]. Few residual stress values are reported. Wood [15] determined by X-ray diffraction tensile stresses of 225 and 60 MPa in a fully processed CoNiCrAlY and an aluminide coating respectively, the substrate being SX60A in both cases.

2.5. Interdiffusion phenomena

Coating and superalloy substrates generally have widely different compositions, each of them selected for different purposes: protection against oxidizing environment on the one hand and high temperature mechanical properties on the other. The chemical potential gradients of the different elements (Ni, Al, Cr, ...) across the coating/substrate interface will cause interdiffusion phenomena to occur, and these

effects will be all the more important that the temperature is elevated. As a consequence, several transformations can take place in the subcoating zone of the superalloy substrate with a resulting loss of load-bearing section :

- transformation of the initial γ/γ' microstructure into γ/β in the case of CoCrAlY/Ni-base superalloys [17, 18],
- alteration of the γ' distribution,
- modification of the distribution of grain-boundary strengthening elements (carbon,...)[19],
- formation of brittle phases which may be crack initiation sites or an easy paths for crack propagation.

The consequences of such effects can be minimized by carefully selecting a coating composition compatible with that of the substrate, which is possible in the case of MCrAlY coatings because of the flexibility allowed by the deposition processes.

3. EXPERIMENTAL RESULTS ON COATED SYSTEMS

A protective coating may alter the mechanical properties of a superalloy substrate it is applied on, as a result of factors exposed above. It must be stressed however that in the long run, a coating, if adequately protective, will isolate the superalloy from the environment (oxidizing combustion gases, molten salt deposits) and will limit or suppress the corrosion-induced mechanical degradations. In a study on thin section René 80 specimens, precorroded during 500 hours in an engine atmosphere, Kaufman [20] has thus shown that the presence of a coating, whether aluminide or MCrAlY, improves the creep lifetime (at 980 and 1080°C) by factors ranging between 2 and 6, as well as the fatigue resistance at room temperature (220 to 280 MPa).

Components in gas turbine engines experience complex mechanical and thermal solicitations. The data concerning the mechanical behaviour of components in service are most often proprietary or, if mentioned in publication [21, 22], they are often incomplete, with lack of detailed knowledge of precise operating conditions.

The evaluation of the influence of coatings on the mechanical properties of superalloys is most often carried out with simple tests such as creep, thermal or isothermal fatigue, sometimes thermomechanical fatigue, thought to be representative of service conditions.

3.1. Creep

3.1.1. Conventional superalloys

A number of studies carried out on equiaxed superalloys such as IN 100 or IN 738 [6, 23] did not show any marked effect of a protective coating on the creep resistance of these systems provided that the quality heat treatments of the superalloys are carried either during coating application or after, and that the coating section is not taken into account in the calculation of the load bearing section. Restall [24] mentions an important reduction in creep lifetime of IN738 and IN792 thin sections (0.76 mm thickness) protected by a simple or by a Pt-modified aluminide (from 290 h down to 50 hours at 850°C in the case of IN738LC for instance). It is not clear however how the load-bearing section was determined in this work.

3.1.2. Directionally solidified superalloys

Figure 4 shows clearly on a Larson-Miller plot that the creep properties of single crystal superalloy CMSX-2 are not affected by the presence of an aluminide coating or a low-pressure-plasma-sprayed NiCoCrAlYTa coating. The insensitivity of the creep resistance of this superalloy to the presence of a coating may be attributed to :

- the compatibility between coating cycle and the standard heat treatments of the alloy, thus ensuring that the reinforcing γ' phase is present with the optimum distribution.

the very limited interdiffusion phenomena observed between coating and substrate both during coating application and during tests at the highest temperatures. Metallographic examinations showed that the thickness of substrate affected by interdiffusion is less than 30 μm after 990 hours at 1050°C; this would correspond to a maximum overload of 5 MPa if this zone is supposed to support no charge [25].

It is to be noted that Wood and Restall [26] observed cracks in a platinum-modified aluminide coating at the end of a creep test tested at 760°C, but not at higher temperatures. The cracks in the coating, however, do not propagate into the substrate which was single crystal SX60A.

In the case of a directionally-solidified eutectics, Cotac 784, coated with an LPPS NiCoCrAlYTa coating, it has been shown [27] that interdiffusion phenomena result in the formation of an extended γ subcoating region in which the NbC fibres are degraded. This zone is much less creep resistant than the rest of the specimen. The presence of this coating markedly lowers the creep strength, with a lifetime reduction of 20 to 30% at 900°C and up to 50% at 1100°C. In this case it would be necessary to reconsider the coating composition, in particular concerning the chromium content, in order to minimise the interdiffusion effects and the resulting fibre degradation.

To summarise this paragraph, it should be kept in mind that provided the standard heat treatments are respected and little interdiffusion occurs in service or during coating application, no effect are to be expected except a possible favourable influence in the long run, because of the suppression of environmental degradation.

3.2. Mechanical fatigue

Fatigue in gas turbine engine components results from thermal and mechanical stresses. Low cycle fatigue is caused by centrifugal loading during start-up and shut-down procedures. High cycle fatigue effects are provoked by vibrations.

Evaluating the influence of a protective coating has been the topic of early studies. For example, Vidal et al. [28] have noted that a low activity aluminide coating very slightly improves the high cycle fatigue lifetime of cast IN713 alloy at 700°C.

3.2.1. High cycle fatigue

High cycle fatigue tests involve stress cycling a specimen with a deformation remaining largely in the elastic domain. In the case of a coated specimen, the coating thickness is always thin compared to the substrate diameter, and the solicitation on the coating is a deformation cycle imposed by the substrate deformation. Therefore for given test conditions, a coating behaviour is expected to be better for a higher yield strength and/or a lower Young's modulus. It is also important to avoid premature crack initiation sites by an appropriate surface treatment.

For conventional superalloys, due to the large scatterband of high cycle fatigue results typical of unprotected substrates, it is sometimes difficult to define an influence of a coating, as emphasized by Pichoir et al. [23] for example. For these systems, the cracks initiate on large internal defects (pores...) with subsequent propagation to rupture, whether the substrate is coated or not.

Schneider et al. [29] investigated the effect of a Pt-modified aluminide coatings on the hcf behaviour of cast IN738LC and IN939 at 850°C. As shown on figure 5 for IN738LC, the lifetimes of coated specimens lie within the scatterband of the lifetimes of uncoated IN738LC. An aging treatment or precorroding the specimens in slag significantly lowers the lifetimes at low stress levels. It is not clear however, if this last test can be representative of simultaneous mechanical solicitations and corrosive aggression.

The situation is better defined with more advanced directionally solidified superalloys. Graham and Woodford [30] investigated the effect of three plasma sprayed coatings on the high cycle fatigue

resistance of NiTaC3 at room temperature, 600°C and 900°C. The reduction in fatigue life is found to be sensitive to the coating composition and stress level. A Ni-20Cr coating exhibits relatively good fatigue resistance at high cyclic stress levels because of its ductility, but exhibits a poor fatigue strength at low stress levels. The higher strength coatings (Ni-20Cr-10Al-2Hf-0.1C and Ni-20Co-20Cr-10Al-2Hf-0.1C) are superior at low stresses, but crack early at high stresses. At 900°C, the coatings has little effect on fatigue life.

Veys [31] evaluated the effects of coatings on the high cycle fatigue behaviour of a single crystal superalloy, CMSX-2, and a directionally-solidified eutectics, Cotac 784. Both an aluminide coating and a LPPS NiCoCrAlYTa coating markedly lower the high cycle fatigue resistance of CMSX-2 at 870°C (fig. 6), the lifetime being all the more reduced that the stress is high. This is attributed to the early cracking of the coatings and the subsequent crack propagation into the substrate, leading to the eventual failure of the specimen. In contrast, the failure of uncoated CMSX-2 involves crack initiation on internal defects (pores, inclusions). It should be noted that the CMSX-2 superalloy employed in that study had relatively high mechanical fatigue properties, having been solidified in laboratory conditions. The drop in lifetime for materials processed in industrial conditions might not be therefore so important. It is likely however that even in this case early cracking would occur in the coating.

Wood and Restall [26] reported results concerning rotating bend high cycle fatigue (50 Hz, 380 and 560 MPa) on NiCoCrAlY-coated single crystals, MMT143 and SX60A, at temperatures ranging between 400 and 1000°C (fig. 7). They note that increasing temperature :

- decreases the number of cycles to crack initiation,
- increases the number and surface length of coating cracks,
- lessens the significance of those cracks, especially at low stresses.

Moreover they observed that a polishing treatment increases the lifetime at low temperature but does not have any marked effect at 800°C.

A qualitative interpretation can be proposed for both extreme cases : low stresses and low temperature on one hand, high stresses and high temperature on the other. At low temperature and low stresses, the coating is solicited in elastic cyclic deformation; this corresponds to long lives in the absence of surface defects, which explains why a polishing treatment can improve the performances. At high stresses and high temperatures, the yield stress of the coating material is low and the coating is cycled in plastic deformation; this corresponds to shorter lives (early cracking). In this case a surface defect has little influence since plastic deformation can relieve the stress concentration it may cause. Once the coating is cracked, the remaining life is determined by the crack propagation rate inside the substrate alloy. This rate, on the whole decreases with increasing temperature, this effect being more pronounced at low stresses. This is generally explained by environmental effect (oxidation at the crack tip limits the crack opening displacement) and by the effect of temperature on the crack tip plasticity; obviously, the oxidation effect is expected to be important for long lives at high temperatures, and this corresponds to low stresses.

The fact that early cracking occurs at temperatures around 800°C or 900°C may be an aggravating factor for hot corrosion degradation : in this temperature range, sodium sulfate may condense on blade surfaces and penetrate through these crack, abolishing the beneficial effect of the protective coating.

It is important to note that the structure and composition of a protective coating changes during operation at high temperatures : aluminium is consumed by oxidation, the initial $\gamma + \beta$ structure of an MCrAlY coating therefore transforms into $\gamma + \gamma'$ and in the end to γ -solid solution of nickel; this is accompanied by grain growth. No study however seems to have been published on these effects, the durations of tests performed being too short for these phenomena to be significant.

3.2.2. Low cycle fatigue

In this type of test, the specimen is stressed at a level above the conventional yield stress, which explains the low cycle number at rupture, generally lower than 10^6 cycles, and with lower frequency (0.033 to 1 Hz) than for high cycle fatigue. The degradation modes are very similar to those observed in thermal fatigue.

Wood [15] reports an alteration of strain-controlled low cycle fatigue of a single crystal superalloy at room temperature, due to the presence of overlay and aluminide coatings. The fatigue properties at 800°C were not affected.

Recent tests at 950°C performed by CEAT (unpublished data) on NiCoCrAlYTa-coated IN100 and DS200 Hf showed no alteration of low cycle fatigue resistance at 950°C.

3.3. Thermal and thermomechanical fatigue

Thermal fatigue results from temperature cycling during start-up and shut-down procedures. Few experimental results are published, some of them having been reviewed by Nicoll et al. [32].

Recent efforts [33-36] have concentrated on thermomechanical fatigue tests which combine mechanical strain controlled cycling and temperature cycling; these tests offer a better simulation of the complex strain-temperature-time experienced by gas engine components in service. Moreover, thermomechanical fatigue may now be a major limiting factor in turbine vanes and blades [37], in particular for highly stressed thin-walled components.

Swanson et al. [35, 36] are developing life prediction models with emphasis on applicability to thermomechanical fatigue conditions. These models are based on the development of individual constitutive models of coatings (PWA286 : NiCoCrAlYSiHf and PWA273 low activity aluminide) and PWA1480 single crystal substrate, for which commercial production experience already exists. Results of out-of-phase tests carried out between 427 and 1038°C indicate that at strain ranges greater than 0.5%, the overlay-coated specimens have longer lives than do those coated with the aluminide, the reverse being true at lower strain range. It is interesting to note that similar results had been obtained by Bain [33] on a single crystal superalloy coated with a CoCrAlY alloy or an aluminide and tested in slightly different conditions.

5. CONCLUSION

As emphasized by Wood [15], little work has been done to determine in depth what coating properties are of importance in controlling the mechanical behaviour of coating/substrate system. The studies in this field have mainly dealt with the identification of degradation modes and the experimental evaluation of the incidence of coatings on few mechanical properties of as-coated substrates. It is important to remark that coatings are found as crack initiation sites in a variety of test conditions, the cracks thus formed propagating subsequently into the substrate material and leading eventually to failure. Neither the evolution of the coating composition in service nor the presence of corrosive products are taken into account. Some attempts at modelling the coating/superalloy system have been recently published [36]. However, the lack of data relative to the coating intrinsic mechanical properties, mainly in the case of the widespread aluminides (simple or modified), seems to have delayed the development of an adequate description of these systems. As a consequence, the possibility of tailoring the coating composition and/or structure to improve the mechanical properties of the coating/substrate composite does not seem to have been fully exploited.

REFERENCES

1. Mévrel R, C. Duret and R. Pichoir, Pack cementation processes, Mat. Sci. Technol. 2(1986)201-206.
2. Mévrel R. and R. Morbioli, MCrAlY coatings, Proc. First Int. Congress on High-Tech-Materials and Finishing (1989)204-216.
3. Bürgel R. and I. Kvernes, Thermal barrier coatings, in High Temperature Alloys for Gas Turbine and other Applications 1986 (Reidel) 327-356.
4. Schneider K.H. and H.W. Grünling, Mechanical aspects of high temperature coatings, Thin solid films, 107(1983) 395-416.

5. Grünling H.W., K. Schneider and L. Singheiser, Mechanical properties of coated systems, *Mat. Sci. Engng*, 88(1987) 177-189.
6. Strang A. and E. Lang, Effect of coatings on the mechanical properties of superalloys, in *High Temperature Alloys for Gas Turbines 1982* (Reidel), 469-506.
7. Hauser J.M., C. Duret and R. Pichoir, Influence des traitements de protection sur les propriétés mécaniques des pièces en superalliage. AGARD CP 312.
8. Caron P. and T. Khan, Improvement of creep strength in a nickel-base single-crystal superalloy by heat treatment, *Mat. Sci. Engng* 61(1983)173-194.
9. Gaujé G. and R. Morbioli, in *High temperature protective coatings* (ed. S.C. Singhal). The Met. Soc. of AIME (1983) 13-26.
10. Ball A. and R.E. Smallman, *Acta Met.* 14(1966)1349.
11. Schulson E.M. and D.R. Barker, A brittle to ductile transition in NiAl of a critical grain size. *Scripta Met.* 17(1983)17.
12. Smith R.W., *Thin solid films* 84(1981) 59-72.
13. Hebsur M.G. and R.V. Miner, High temperature tensile and creep behaviour of low-pressure plasma-sprayed NiCoCrAlY coating alloy, *Mat. Sci. Engng* 83(1986) 239-245.
14. Veys J.M., A. Rivière and R. Mévrel, Mechanical properties of LPPS NiCoCrAlYTa alloy, in *First Plasma-Technik Symposium* (Lucerne, 1988), Edit. H. Eschnauer, P. Huber, A.R. Nicoli and S. Sandmeier, vol.2, 115-124.
15. Wood M.I., The role of coatings in the fatigue of superalloy single crystals. *Proc. First ASM Europe Technical Conference on "Advanced Materials and Processing Techniques for Structural Applications"*. (Paris, 7-9 sept. 1987) (ONERA, 1987) 179-188.
16. Gayda J., T.P. Gabb and R.V. Miner, Low cycle fatigue behaviour of a plasma-sprayed coating material, *Int. J. Fatigue* 8(4) (1986) 217-223.
17. Mévrel R. and C. Duret, Interdiffusion effects between protective coatings and superalloy substrates, in *Coatings for Heat Engines*, NATA Advanced Workshop (Acquafredda di Maratea, 1984) 595-612.
18. Mazars P., D. Manesse and C. Lopvet, Interdiffusion of MCrAlY coatings with substrates, in *High Temperature Alloys for Gas Turbines and other Applications 1986* (Reidel, 1986) 1183-1192.
19. Strang A., E. Lang and R. Pichoir, Practical implications of the use of aluminide coatings for the corrosion protection of superalloys in gas turbines. AGARD SMP, CP356, 11/1-11/35 (1983).
20. Kaufman M., Examination of the influence of coatings of thin superalloy sections, *NASA CR* 1215(1972).
21. Cocking J.A., N.A. Burley and G.R. Johnston, The degradation of aluminide-coated first stage blades in the engines of a light military helicopter, *High Temperature Technol.* 4(4) (1986)175-190.
22. Meetham G.H., Service experience with protective coatings in industrial, marine and aero-gas turbines, in *Coatings for Heat Engines*, NATA Advanced Workshop (Acquafredda di Maratea, 1984), 219-238.
23. Pichoir R., J.M. Hauser, Etude de l'influence des méthodes de protection et des revêtements sur le comportement des superalliages en fluage et en fatigue. DGRST N°79-7-1419 (1981).
24. Restall T.E., The effects of protective coatings on the mechanical properties and corrosion behaviour of UDS nickel superalloys. Final report of project 3UK14. COST 50-3(1985).
25. Veys J.M. Thèse de Docteur Ingénieur (Poitiers, 1987).
26. Wood M.I. and J.E. Restall, The mechanical properties of coated nickel based superalloy single crystals, in *High Temperature Alloys for Gas Turbines and other Applications* (Liège 1986), *****.
27. Veys J.M. and R. Mévrel, Influence of protective coatings on the mechanical properties of CMSX-2 and Cotac 784, *Mat. Sci. Engng* 88(1988) 253-260.
28. Vidal G., P. Galmard and B. Genty, *La recherche Aérospatiale*, 1970-3 (1970), 177-179.
29. Schneider K., H. Von Arnim and H.W. Grünling, Influence of coatings and hot corrosion on the fatigue behaviour of nickel-based superalloys. *Thin solid films*, 84(1981) 29-36.
30. Graham D.E., D.A. Woodford, The influence of overlay coatings on high-cycle fatigue of an advanced tantalum carbide strengthened eutectic composite. *Metall. Trans.* 12A (1981) 329-336.
31. Veys J.M. and R. Mévrel, Creep and high cycle fatigue properties of coated CMSX-2, in *Advanced Materials and Processing Techniques for Structural Applications*, ASM Technical Conference (Paris 7-9 sept. 1987).

32. Nicoll A. and U.W. Hildebrandt, Thermal fatigue of coated superalloys, in Environmental Degradation of High Temperature Materials (The Inst. of Metall., 1980) 6/27-6/37.
33. Strangman T.E. PhD thesis.
34. Bain K.R., The effect of coatings on the thermomechanical fatigue life of a single crystal turbine blade material, AIAA-85-1366 (1985) 1-6.
35. Swanson G.A. et al., Life prediction and constitutive models for engine hot section anisotropic materials program. NASA CR 174952 (1986).
36. Swanson G.A. et al., id., NASA CR 179594 (1987).

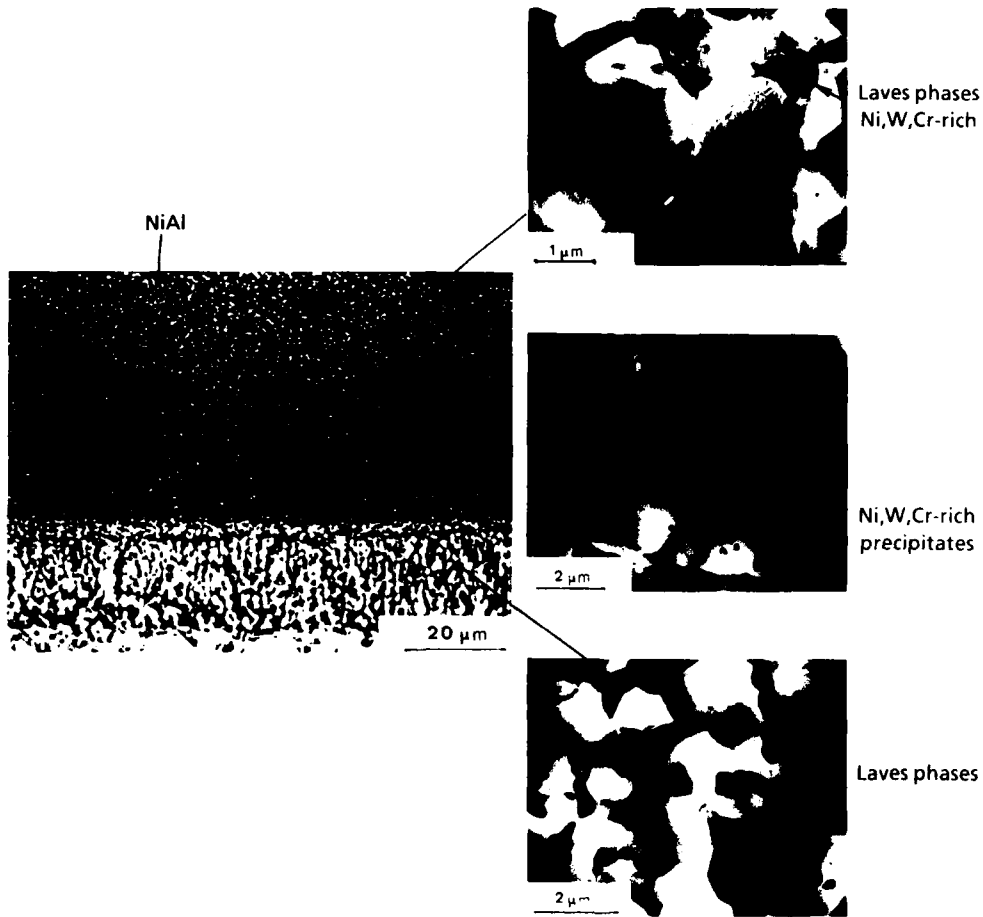


Figure 1 : High activity aluminide coating on CMSX-2 [25].

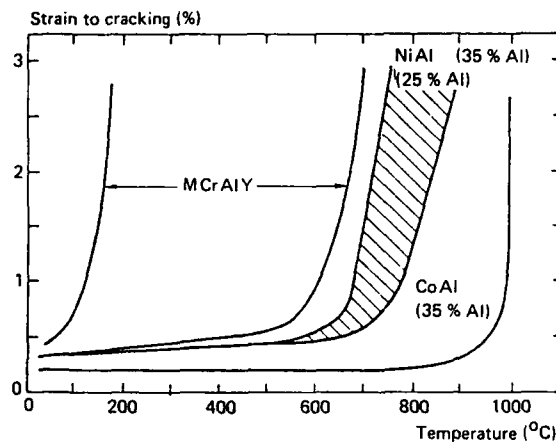


Figure 2 : Influence of composition on ductility of protective coatings [19]

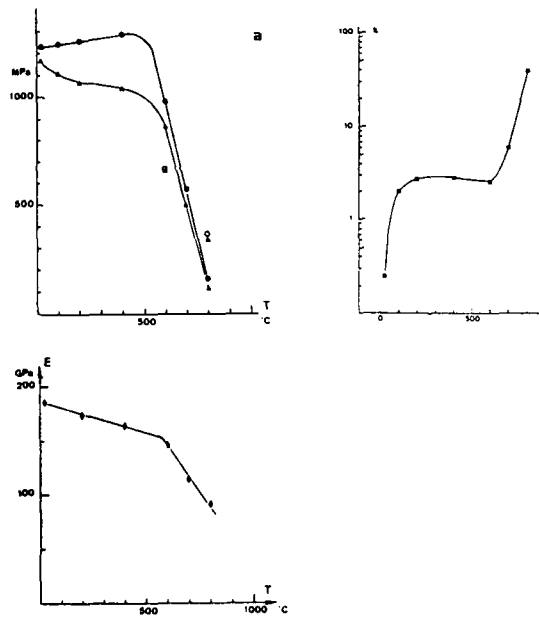


Figure 3a : Tensile properties of LPPS NiCoCrAlYTa alloy as a function of temperature [14].

- a) Ultimate tensile strength (●), 0.2% yield strength (▲)
 - b) Elongation to rupture (■)
 - c) Young's modulus (◆)
- The open symbols correspond to vacuum cast NiCoCrAlYTa alloy

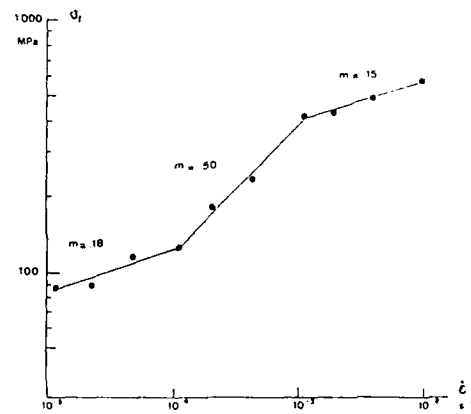


Figure 3b : Flow stress of LPPS NiCoCrAlYTb alloy as a function of strain rate at 800°C; m is the strain rate sensitivity. [14]

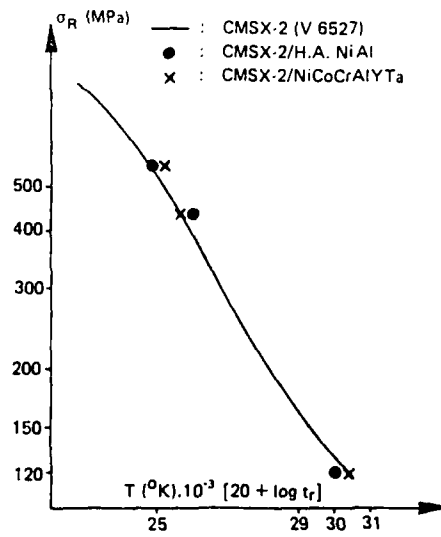


Figure 4 : Influence of protective coatings on creep properties of CMSX-2 [25]

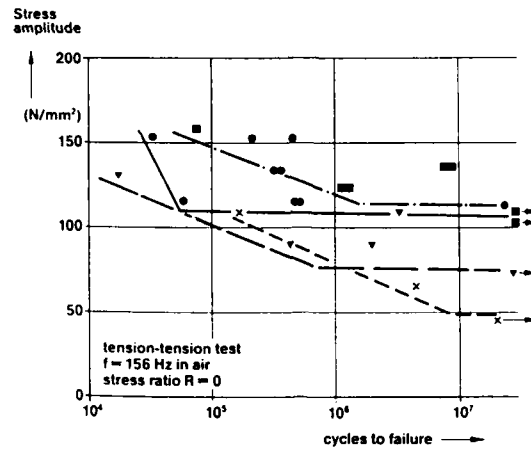


Figure 5 : Results of HCF tests of IN 738 LC at 850°C ($f = 156$ Hz in air; $R = 0$)
 —●—, uncoated; —■—, LCD2 coated; —▲—, LDC2 coated and aged 5000h
 at 850°C; —x—, LDC2 coated and pre-corroded for 1000h at 850°C in slag [29]

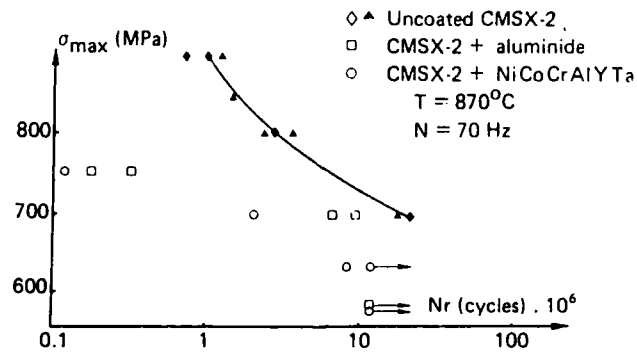


Figure 6 : High cycle fatigue properties of coated CMSX-2 [25]

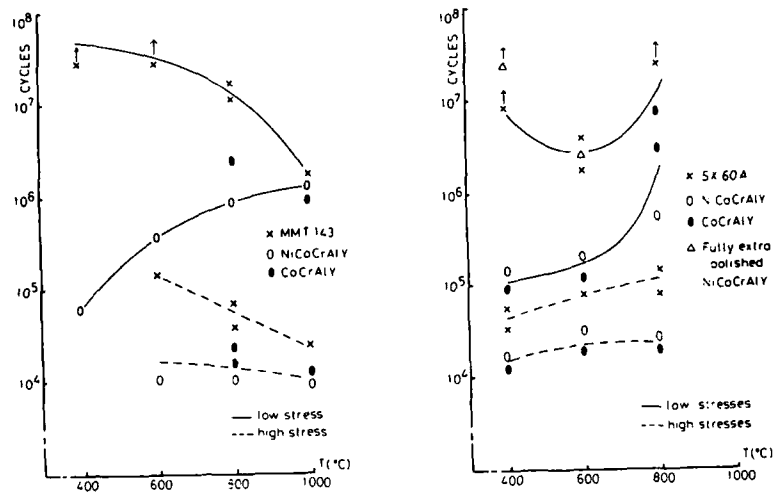


Figure 7 : Cycles to failure - temperature for coated and uncoated MMT143 and SX60A [26].

MICRODAMAGE TO CERAMIC SURFACES UNDER SLIDING CONDITIONS

BY

P. J. Kennedy and A. Conte
Naval Air Development Center
Warminster, PA (USA) 18974

SUMMARY

Fretting studies were performed on silicon nitride in order to ascertain the effect of small amplitude slip (0.1 to 10 micrometers) on ceramic wear. The results of this study indicate that the small amplitude fretting of silicon nitride on silicon nitride is primarily controlled by tribochemical reaction forming a soft silicon oxide layer. This reaction was not observed to any measurable extent at slip amplitudes of less than 3 micrometers. The tribochemical reaction was initially observed at the edge of the contact region and then progressed toward the center of the contact zone. The reacted material in the contact zone tended to flow out of the high pressure region to form a debris pile-up outside of the contact area. The wear ratio was found to be $4 \times 10^{-5} \text{ m}^3/\text{Nm}$.

INTRODUCTION

The tribology of ceramics and in particular the effect of small amplitude fretting (0.1 to 10 micrometers) on ceramic wear are important considerations in the design of bearings for future turbine engine applications. A certain amount of elastic deformation occurs during rolling bearing contact applications and this contributes to slip which in turn can be responsible for bearing failure. The initial aim of this study was to determine the effect of slip on bearing life and in particular, to determine if there was a critical slip amplitude or similar value that defined a lower limit below which no surface damage would occur. This value represents a parameter that could be incorporated in future ceramic bearing designs. Other objectives included the determination of the effect of atmosphere, number of fretting cycles and load on the small amplitude fretting of ceramics.

The primary material investigated in this study was silicon nitride since it is one of the most promising materials for use in high temperature bearing applications. Previous studies have provided a significant insight into the low amplitude slip fretting mechanism for metals and it was felt that this knowledge would provide a basis for comparison and thus provide a greater understanding of the effect of surface stresses on ceramic damage.

EXPERIMENTAL

The configuration of the ceramic ball and flat that was used in this study is shown in Fig. 1. The ball specimens were grade 5, 12.7 mm diameter balls made from either Norton's uniaxially hot pressed NC-132 or hot isopressed NBD-100 silicon nitride. The flat specimens were in the form of small cylinders 8 mm in diameter and 2 mm in height. The flat specimens made from silicon nitride were then hand polished using a diamond polishing medium. Both the ball and flat specimens were washed in boiling stoddard solvent and rinsed in petroleum ether prior to testing. The test specimens were then inserted into a fretting test rig producing the specimen configuration shown in Fig. 1. Testing was normally performed using an applied load of 88 N. This test rig which was operated at 210 Hz, was previously described². Most conventional wear test devices using a ball on flat type of specimen arrangement would normally generate fretting wear by imparting a linear oscillatory motion to one of two contacting specimens under load conditions. The length of this back-and-forth displacement would be defined as the slip amplitude. Accurately reproducing extremely small amplitude slip conditions with this type of linear displacement would be extremely difficult. Alternately, a similar type of fretting motion can be produced by using an angular displacement rather than a linear displacement. Loading of a ball against a flat, as shown in Fig. 1 produces a circular Hertzian contact region which defines the actual damage or wear area. Under normal test conditions, the contact area would have a radius of approximately 0.15 mm. During testing, the ball specimen is held stationary and an oscillatory twisting type of motion through an angle, θ , is imparted to the flat specimen. The actual amount of twist needed to produce a slip amplitude of 1 micrometer is very small and amounts to 0.007 rad/micrometer or 0.4 degree/micrometer. This motion was about the Z-axis which is normal to and through the center of the ball/flat contact region. The slip amplitude at the edge of the ball/flat contact area can be easily calculated knowing the magnitude of the angle of twist and the radius of the contact area. The primary experimental variables were the angle of twist or slip amplitude, the normal load and the duration of test. In previous testing, fretting specimens were analyzed after 2.3 million fretting

cycles. In this study, the majority of test specimens were analyzed after 12,600 fretting cycles.

A typical wear scar, resulting from the oscillatory torsional motion of a ball against a flat, is illustrated in Fig. 2. The outer diameter of the wear scar can be calculated using the Hertz equations. The inner diameter would be dependent on normal and shear stresses. This can be illustrated by considering a ball resting on a flat plate under elastically loaded conditions. This will produce a normal stress distribution over the ball/flat contact area. This stress would be zero at the edge of the contact and a maximum in the center. Application of a shearing or twisting force to the flat produces a shear stress distribution that would have a maximum near the edge of the contact area and a minimum in the center. Estimates of the shapes of these distributions are shown in Fig. 2. The action of these two opposing forces can produce microslip in the Hertzian contact region.

Relative motion or sliding requires that the applied shearing force must exceed the product of the static coefficient of friction and the normal load. The inner dash lines in Fig. 2 represent a radius which can be defined as the locus of those points at which the ratio of the shear to normal stress is exactly equal to the static coefficient of friction. Thus, relative motion or sliding can only occur at radii greater than the inner radius shown in Fig. 2 or outside of the inner dash line region. This region is referred to as the slipped region. Inside of the dash lines, the converse will hold true and the shearing force will always be less than the product of the normal stress and coefficient of friction and thus, all motion will be taken up elastically. This is normally referred to as the locked region. Slip can not be directly calculated along the radius of the wear scar using the applied angle of twist. At the edge of the locked region, no motion can occur since all applied motion will result in elastic deformation. Elastic deformation effects must also be taken into consideration at all other points in the wear scar region except at the edge of the slipped region. At this point the normal stress is equal to zero and no elastic deformation can occur. In this work, slip was calculated at the edge of the Hertzian contact region.

RESULTS

Initial experiments were concerned with elucidating the fretting mechanism for silicon nitride against itself under small amplitude (0.1 to 10 micrometers) slip conditions. Wear scars formed on silicon nitride were unlike those that were formed on metals under similar conditions. Some of these unusual characteristics are shown in Fig. 3. This photomicrograph consists of a series of overlays of photographs taken of the slip region on a flat specimen. The lower left hand corner shows the undamaged locked region whereas, the upper right corner shows the undamaged ceramic surface outside of the wear region. This wear scar was formed under 88 N load using an angle of twist equal to 2 micrometers slip at the edge of the Hertzian contact area. Testing was done for 3 hours at 210 Hz. The photomicrographs show that the slip region is characterized by the formation of smooth grooves that start at the edge of the locked region as extremely fine lines that increase in breadth with increasing radial distance from the center of the scar. This general trend in wear scar width is reasonable because theory indicates that the amount of slip would be zero at the edge of the locked region and would be a maximum at the edge of the wear scar. At the edge of the locked region, the pressure would theoretically be great enough to insure that all motion would be taken up elastically. As we increase in radial distance from the edge of the locked region, the amount of slip would increase to the calculated amount at the Hertz radius since pressure decreases with increasing radial distance.

An examination of Fig. 4 suggests that groove widths approach the applied slip amplitude (dash line). Plots of groove width as a function of radial distance for two separate wear scars were made. A typical plot is shown in Figure 4. In both this plot and a plot of groove width for a higher amplitude slip, results indicated that the groove width is equal to $1/2$ the applied slip amplitude at the Hertz radius. It had previously been suggested that a significant amount of applied slip would be lost in the moving mechanical components of the test rig when applied slip amplitudes were extremely small (4). This possibility was investigated by attaching a flag in the position where the ball would normally touch the flat specimen so as to measure actual movement at the point. Under these conditions, the slip amplitude calculated from the applied slip amplitude was equal to the measured slip amplitude. These tests suggest that this value of 0.5 is real and may be associated with the thickness of the glassy film that forms on both the ball and flat specimen during testing. The data points in Fig. 4 are the average of 3 separate readings. It is difficult to determine the general effect of a decreasing normal stress on applied slip from this data.

The wear scar pattern shown in Fig. 3 requires slip amplitudes greater than 3 micrometers and total slip distances in excess of 1 meter. The initial intent of this investigation was to determine if there was a critical slip amplitude that was associated with the onset of surface damage. Comparison of surface profiles of wear scars at different slip amplitudes indicates that significant surface damage did not occur below 3 micrometers. Only extremely mild surface changes, perhaps associated with the build up of a tribofilm, were observed in a slip amplitude range of 0.1 to 3 micrometers. In a previous study with metals, this mild surface damage appeared as a dark staining on the surface of the specimens². This mild damage was dependent on

both slip amplitude and total distance traveled. For example, no wear scar was observed after testing at 0.1 micrometer for 3 hours but was observed at 6 hours. From visual observation of damage as a function of both total sliding distance and slip amplitude, it appears that mild damage is dependent on both parameters, but it is more dependent on slip amplitude than on total sliding distance.

The "sun burst" pattern shown in Fig. 3 is formed in a thin layer of glassy material. The relative softness of this layer is shown in Fig. 5. This wear scar contains several indentor marks. The type of indentor mark formed outside of the wear area is shown in photo (B) and is characterized by very sharp edges. It can be seen that the indentor marks inside the wear area (photos C and D) are quite different and are characterized by the extrusion of plastic-like material in the form of thin sheets of debris. It is interesting to note the rivulet pattern in photo D and the presence of loose debris in this groove. These thin sheets of debris were then lifted from the surface using a plastic film technique and analyzed using TEM. Analysis of the energy loss spectrum indicated the presence of silicon and oxygen. Nitrogen was not detected. This suggests that the material covering the slip region was a form of silicon oxide.

The development of this tribofilm appears to be associated with a tribochemical reaction occurring at the edge of the Hertzian contact area. The way in which this was determined was unusual. Three dimensional maps of the wear scar developed from multiple surface profiles using a surface contacting or stylus type instrument are shown in Fig. 6 for different wear scars formed at 4.48 micrometers slip but tested for varying periods of time. The short 1 minute test shows the development of two circular mounds of debris without any indications of debris removal from the surface. The runs at 10 minutes and 180 minutes showed the expected wear track that defines the slip region. This build-up phenomena was also found in a wear scar at 2 micrometers slip for 10 minutes. Surface contours were then determined on these same specimens using an optical laser based system. The surface profile obtained using the optical method on the same specimen shown in photograph (A) of Fig. 6 showed the expected groove rather than a debris pile-up. This optical data is compared with the stylus based data in Fig. 7. This difference was at first, very surprising and both surface profiling instruments were re-evaluated and found to be accurate. One logical explanation for the apparent difference in surface profiles would be that the wear process initially involves the development or growth of a transparent tribochemical film around the edge of the ball flat contact region. The groove shown in the optical surface tracing would not be detected by the stylus measuring system since it is filled with material or, conversely, the transparent material filling the groove would be invisible to the optical surface profiling equipment. As the wear process proceeds, large particles of debris are broken down in the slip region and extruded out to the outer edge of the contact area. This debris is in the form of string-like material in the contact region. Near the low pressure edge of the contact region, the debris breaks down to small spherical particles that either maintain their shape or coalesce into a partially transparent glassy material that can form a lip around the wear scar.

At higher amplitude slip, the wear process appears to be characterized by formation of a tribochemical layer followed by a general wearing away of the surface from the outside edge in towards the locked region. At very low amplitude slip, the mechanism might be somewhat different. Photomicrographs of the slip region formed by slip amplitudes less than 1 micrometer suggest delamination of thin surface flakes of material approximately 10 micrometers in length. This may be due to the presence of a thin tribochemical film less than 1 micrometer in thickness on the wear surfaces of both the ball and flat specimen.

The principal aim of this investigation was to determine the effect of slip amplitude on the fretting of silicon nitride components. In addition, we were interested in the degree of surface damage under fretting conditions. Wear ratios, calculated from wear volume data, were 2×10^{-16} at 1 and 10 minutes and then decreased to $6 \times 10^{-17} \text{ m}^3/\text{Nm}$ at 180 minutes. This decrease in the wear ratios with time would be expected since the pressure distribution would change as the amount of debris removed from the slip region increased. After extended testing, the pressure distribution would change so that the entire load would be supported by the locked region. In terms of wear rate, this value would be about 2 orders of magnitude lower than the commonly report value^{5,8} but this is probably due to test conditions which involve a pressure distribution rather than an applied load, a slip amplitude dependent on radial distance and the exclusion of atmosphere from the wear track.

CONCLUSIONS

From the results of our experiments, the following conclusions can be drawn.

(1) The wear ratio for silicon nitride fretting was found to be approximately $2 \times 10^{-16} \text{ m}^3/\text{Nm}$ or about two orders of magnitude less than that reported for sliding wear.

(2) Although wear scars were formed at slip amplitudes less than 0.1 micrometers, surface profile measurements indicated that 3 micrometers represents a critical slip amplitude for silicon nitride in that slip amplitudes greater than this were required for significant surface damage or measurable wear volumes.

(3) Slip amplitudes of about 1 micrometer can produce delamination of very thin flakes of material from the surface of silicon nitride specimens in the "as received" condition. This is an important consideration in the use of ball specimens.

(4) The initial step in the fretting wear of silicon nitride involves a tribochemical reaction to form a silicon oxide glassy layer. This glassy material was found to cover the entire wear track.

REFERENCES

1. P. J. Kennedy, S., J. Calabrese and M. B. Peterson, Microdamage in sliding contacts, *Wear*, 121 (1988) 223-238.
2. P. J. Kennedy, M. B. Peterson and L. Stallings, A study of surface damage at low amplitude slip, *ASLE Trans.* 27(4) (1984) 305 - 312.
3. H. Deresiewicz, Contact of elastic spheres under an oscillating torsional couple, *J. Applied Mech.*, Trans. ASME, 76 (1954) 52-56.
4. Y. Berthier, Ch. Colombie, L. Vincent and M. Godet, Fretting wear mechanisms and their effects on fretting fatigue, *ASME Journal of Tribology*, 110 (1988) 517-524.
5. D. C. Cranmer, Wear surface analysis of silicon nitride, *Lubrication Engineering*, 44 (1988) 975-980.
6. S. Jahanmir and T. E. Fischer, Friction and wear of silicon nitride lubricated by humid air, water, hexadecane + 0.5 percent stearic acid, *STLE Trans.* 31,1 (1987) 32-43.

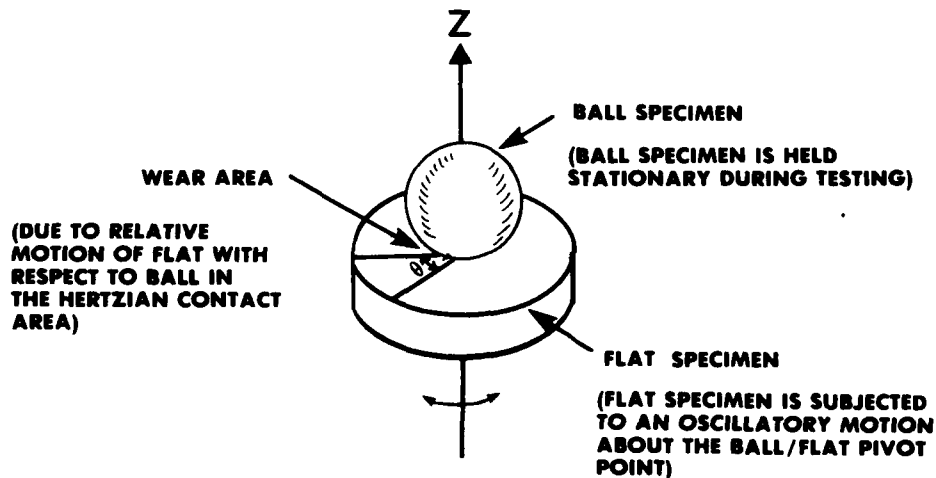


Figure 1. Specimen configuration and motion.

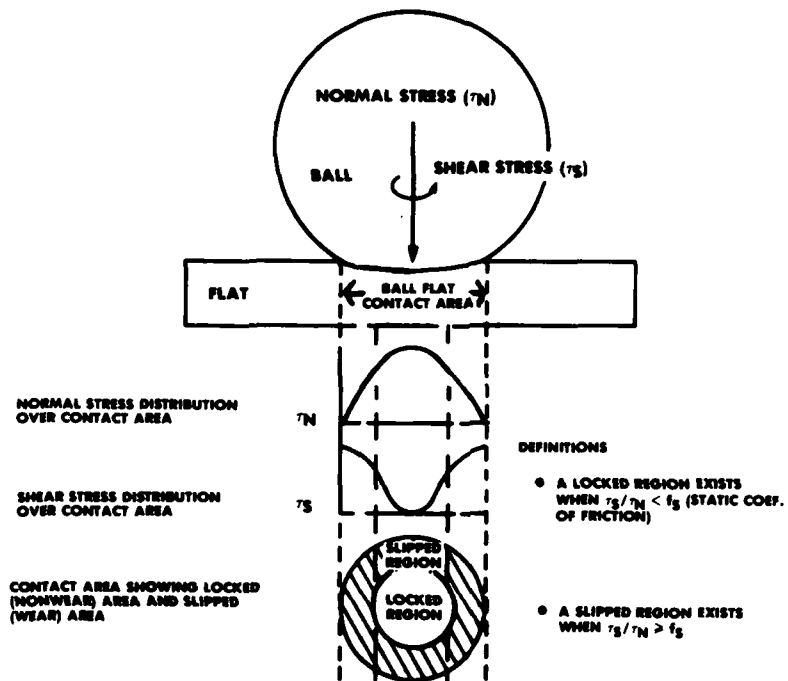


Figure 2. Ball-on-flat configuration showing relationship of shear and normal stresses to scar dimensions.



Figure 3. Wear scar formed on silicon nitride showing radial groove formation.

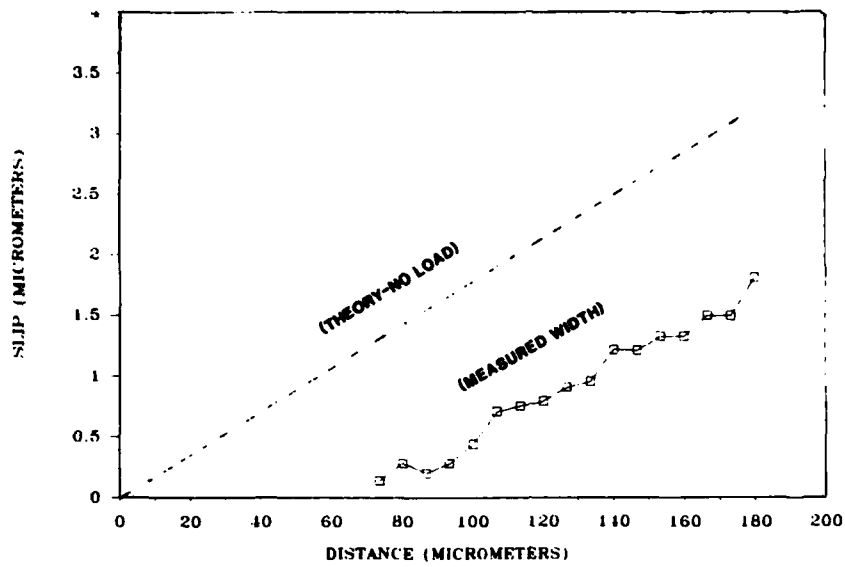


Figure 4. Width of wear scar grooves as a function of radial distance.

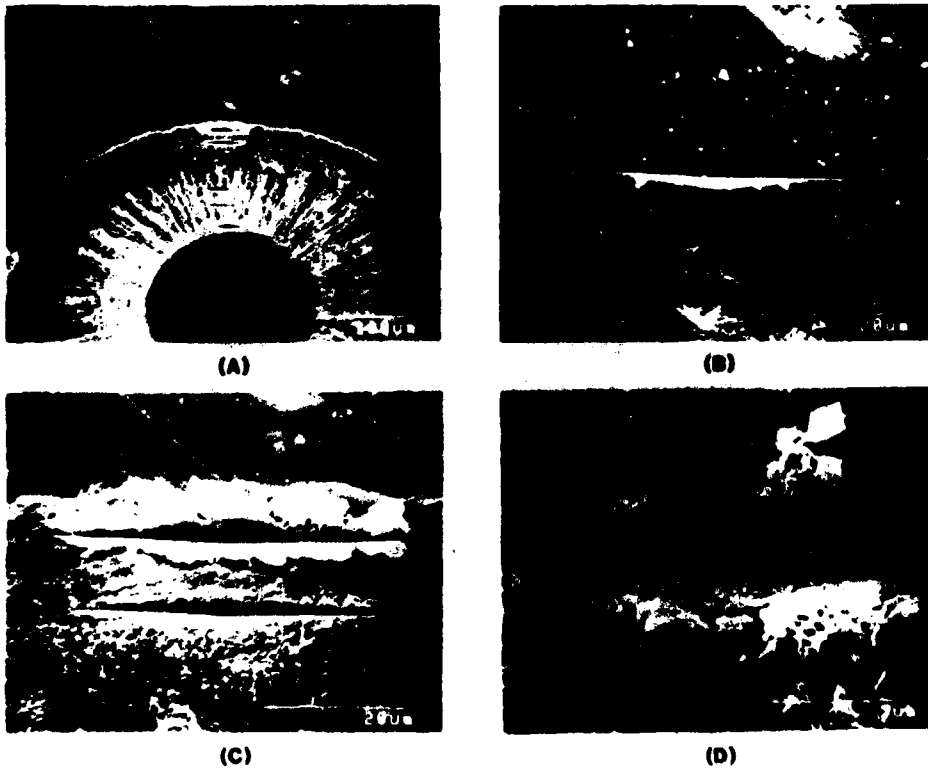


Figure 5. Indenter marks in wear scar region.

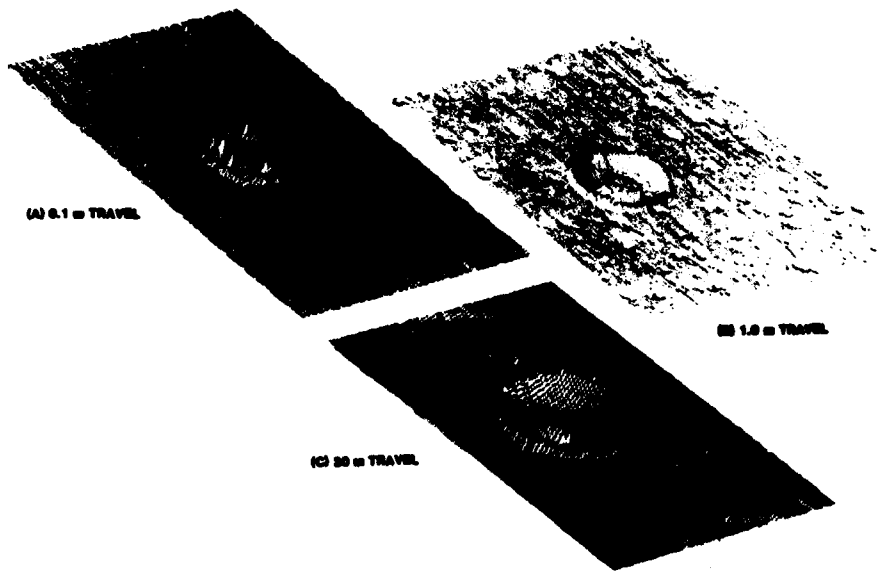


Figure 6. Surface profiles of wear scars obtained with a stylus-based profilometer.

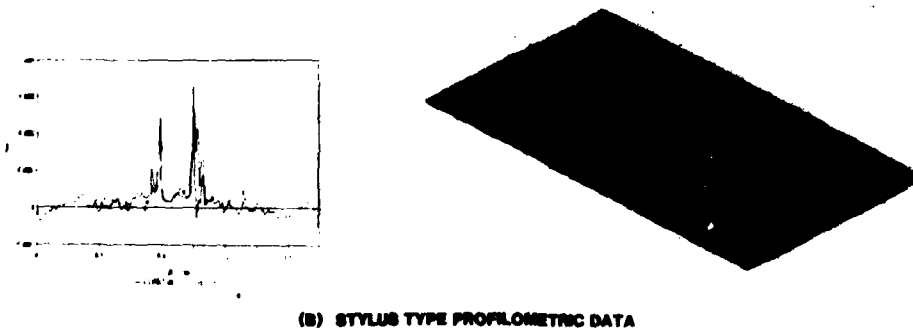
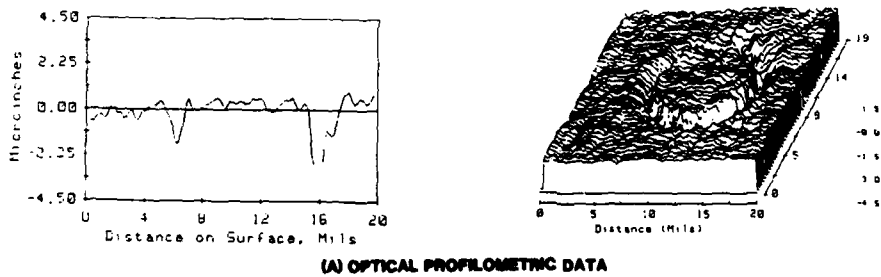


Figure 7. A comparison of stylus-based surface profile data with optical-based surface profile data.

**FRETTING FATIGUE STRENGTH OF Ti-6Al-4V AT ROOM AND ELEVATED TEMPERATURES
AND WAYS OF IMPROVING IT**

by

Rainer Schäfer and Walter Schütz

IABG
Einsteinstraße 20
D-8012 Ottobrunn

SUMMARY

The high sensitivity of titanium alloys to fretting fatigue has to be taken into account when oscillatory relative motion occurs in joints of fatigue loaded components, e.g. in the connection of the disc with the blades in compressors of aircraft engines. Against this background fretting fatigue behaviour of Ti-6Al-4V was investigated at room temperature and service temperature (350°C) as well by testing flat specimens under fatigue loading and simultaneous fretting applied by a special fretting apparatus.

The results show a complex system of parameters affecting fretting fatigue resistance: Fretting fatigue resistance decreases with increasing contact pressure and increasing amplitude of slip, down to a certain limit value for each. Other parameters investigated here are surface finish and stress ratios. The lowest value of fretting fatigue limit found in this work was about 20% of the original fatigue limit of the unfretted material. Elevated temperature (350°C), however, had little additional detrimental effect.

Among several methods to improve fretting fatigue resistance, shot peening and coating are also employed in compressor components. By shot peening the fretting fatigue limit could be increased by more than a factor of two, by coating with PVD systems by nearly a factor of two.

LIST OF SYMBOLS

a:	"strain length", characteristic length of fretting assembly influencing amplitude of slip
p:	clamping pressure, nominal contact pressure
p/σ_{max} :	relative clamping pressure
s_a :	amplitude of slip
F_a :	amplitude of fatigue load
F_m :	mean load
F_n :	clamping force
N:	number of cycles to failure
N_u :	ultimate number of cycles
R:	stress ratio, $R = \sigma_{min}/\sigma_{max}$
σ_a :	amplitude of fatigue stress
σ_{max} :	maximum fatigue stress
σ_{min} :	minimum fatigue stress

1 INTRODUCTION

Fretting is defined in [1] to stand for "wear phenomena occurring between two surfaces having oscillatory relative motion of small amplitude". Fretting can produce damage by fretting wear or fretting corrosion.

Fretting fatigue means "the combined action of fretting and fatigue, a situation where the actual wear damage can be slight" [1], but the fatigue resistance can decrease considerably, down to about 10% of the original values in extreme cases [1-5].

The sensitivity to fretting fatigue is specific for a certain material, i.e. different materials are sensitive to fretting fatigue to different degrees. Compared to many other metals, titanium alloys have been shown to be especially sensitive, in contact with materials of the same type, as well as in contact with other metals. This sensitivity results in a considerable decrease of fatigue resistance due to fretting.

This situation has to be taken into account when titanium alloys are used for producing fatigue loaded components where fretting can also occur. In consideration of the specific advantages of titanium alloys - high strength and low density - efforts are made to improve the fretting fatigue resistance in order to extend the applicability of these alloys.

An important application of titanium alloys are components of aircraft engines. Since the service temperature of titanium alloys is limited (300°C to 450°C) depending on the type of alloy, compressor components are produced from titanium alloys. Shaft-hub connections, bolted joints, and, above all, the joints of the rotating discs with the blades are subject to fretting fatigue loading [6-8].

Figure 1 shows, schematically, the dovetail of a compressor blade where fretting fatigue damage has been observed [7]. The contact pressure results from the centrifugal force, the slip and fatigue loading are induced by the flutter of the blades in the gas stream.

The problems described above and the actual damage were the reason for the following investigations. The aim was to improve the understanding of the complex mechanisms of fretting fatigue and to look for measures to improve fretting fatigue resistance of titanium alloys.

Test material for the following experimental investigations was Ti-6Al-4V, the most frequently used titanium alloy. Tests were carried out at room temperature and at elevated temperature as well. According to the service conditions the elevated test temperature was chosen to be 350°C.

2 EXPERIMENTAL INVESTIGATIONS

2.1 METHODS

The complexity of stressing and damaging mechanism in fretting fatigue in connection with the multiple affecting factors prevent analytical solutions of the actual problems [3, 9, 10]. Therefore most of the fretting fatigue research work puts the main emphasis on experimental work.

Compared to the actual situation in service the experimental procedures have to be simplified in order to be able to define and to vary parameters and to obtain reproducible test results. A survey of various experimental methods and test setups is given in [1] and [11], some special additional arrangements are described in [12-14].

The assembly shown in Figure 2 was used in numerous test series, e.g. in [3, 4, 7, 15-19], due to its simple design, facilitating the systematic variation of contact pressure and slip amplitude. Fretting pads shaped similar to a bridge are clamped to the fatigue loaded flat specimen. The slip amplitude develops from the relative motion between specimen and fretting pads caused by the cyclic elongation of the flat specimen during fatigue loading. The slip amplitude can be varied within certain limits by varying the length $2a$ of the bridge.

This "bridge" assembly may have an - at least theoretical - disadvantage: since the position of the bridge in the axial direction is not fixed, it is not absolutely sure that the relative motion of all four contact points will be equal and will occur simultaneously. One contact point might weld and prevent motion in this point. This would double the slip amplitude in the other contact point of the bridge. In consequence the scatter of results might increase and reproducibility and comparability of results might be reduced.

To avoid such possible effects a modified test assembly was used for the majority of the tests. This modified assembly, shown in Figure 3, has only one contact point on each side of the specimen so that slip can occur only here. The slip amplitude can be varied, similar to the bridge assembly, by varying the length of the arms.

To anticipate one result of the following tests: under the given conditions, the "bridge" assembly supplied results of a quality similar to the modified assembly.

2.2 SPECIMENS AND FRETTING PADS

Flat specimens as shown in Figure 4 were chosen for the fretting fatigue tests with the fretting system shown in Figure 5. This system contains fretting pads with a cylindrical fretting area mounted in the supporting "bridge", cf. Figure 2, or "arm", cf. Figure 3, of the respective fretting assembly. The cylindrical shape of the fretting area was chosen to avoid edge effects. The contact surface of the pads was machined by precision turning and polished with fine abrasive paper resulting in a roughness R_a of approximately 0.5 μm .

The surface finishing of the flat specimens was varied for the purpose of evaluating the effect on fretting fatigue resistance, cf. chapter 2.6.1.3 and 2.7.2.

2.3 TEST SETUP

The main components of the test assembly are the loading frame with electronic load cell for measuring the clamping force, and, for the tests at elevated temperature, the surrounding heating chamber fed with hot air from a heater fan, see Figure 6. The test temperature was measured and controlled via thermo-couples on the specimen surface. This assembly was mounted in an electro-mechanical resonance machine, loading the flat specimen in axial direction.

2.4 TEST MATERIAL

Flat specimens and fretting pads were machined from a 7 mm thick plate of Ti-6Al-4V in the annealed condition. Chemical composition and characteristic mechanical properties are compiled in the Tables 1 and 2.

2.5 TEST PROCEDURE

Most of the fretting fatigue tests were carried out at a fatigue stress ratio of $R = 0.1$. Test frequency was about 150 Hz. The test temperatures were chosen to be room temperature and 350°C.

The fretting pads were clamped to the flat specimen with defined constant force. The nominal contact pressure was calculated from the clamping force and the area of the fretting scar measured on the pads after the test.

Due to the cylindrical surface of the pads the contact is theoretically line shaped at the very beginning of the test. It was observed, however, that a plane contact area was formed due to abrasive wear in a very short time. Continuing the test, this area is enlarged more and more slowly, so that contact pressure may be regarded to be approximately constant during most of the test duration.

Evaluation of contact area would be problematic, even if pads with plane contact surface were used: the actual contact area is different from the nominal area in the most cases, at least in the first test period.

In all tests the clamping pressure p was related to the maximum fatigue stress, and this ratio p/σ_{max} was introduced as a parameter.

2.6 RESULTS

2.6.1 BASIC EFFECTS ON FRETTING FATIGUE RESISTANCE

2.6.1.1 CLAMPING PRESSURE

The S-N-lines in Figure 7 demonstrate the effect of clamping pressure (nominal contact pressure) on fretting fatigue resistance.

By increasing the clamping pressure the fretting fatigue strength is continuously reduced down to a certain lower limit, which obviously is reached at a relative clamping pressure p/σ_{max} of approximately 0.4. The individual results, omitted in Figure 6, show a rather small scatter.

The relation between fretting fatigue strength and clamping pressure is illustrated in Figure 8, showing the fretting fatigue limit at 10^7 cycles depending on the relative clamping pressure. It can be seen more clearly in this diagram, that beyond a certain limit of relative clamping pressure (approximately 0.4 in this actual case) the fretting fatigue strength will not be reduced further. For simulating the worst conditions all the following tests were carried out with a relative clamping pressure of approximately 0.4.

2.6.1.2 AMPLITUDE OF SLIP

The amplitude of slip is influencing the fretting fatigue strength to a degree similar to the influence of contact pressure. The parameter in Figure 9 is the distance between the contact points at the "bridge" assembly (Figure 2) or the arm length of the modified assembly (Figure 3).

The amplitude of slip depends essentially on this length "a", but in addition depends on the fatigue stress amplitude, on the clamping pressure, and on the coefficient of friction.

Figure 10 shows the dependency of the fretting fatigue limit at 10^7 cycles on the slip amplitude, measured in the first period of the fretting fatigue test or extrapolated from measurements. Even if the slip amplitude is not constant during the test (due to the probably changing coefficient of friction) this representation leads to the conclusion that also a limit value of slip amplitude exists beyond which the fatigue strength - under constant other conditions - will not decrease further.

The results confirm the complexity of the problem "fretting fatigue" and the interaction of different factors with synergetic effects. Figures 11 and 12 demonstrate, for example, the interaction of slip amplitude and clamping pressure: in spite of a relatively big slip amplitude producing severe abrasive wear the fatigue strength is hardly reduced if the clamping pressure is low, Figure 11. In contrast to this, Figure 12 shows that high clamping pressure and a small slip amplitude produce very little abrasive wear but have an extremely detrimental effect on fatigue strength.

2.6.1.3 SURFACE FINISHING

The different fretting fatigue resistance of specimens with a milled surface ($R_a = 0.8 \mu m$) and those with a ground surface ($R_a = 0.6 \mu m$), already visible in Figures 8 and 10, is demonstrated more extensively in Figure 13. The ground specimens always show lower fretting fatigue resistance compared to the milled specimens under equal other conditions.

Trying to interpret this difference, at least two interacting effects have to be taken into consideration: The higher friction forces measured in the first test period on ground specimens and the less favourable residual stresses near the surface. Measuring residual stress near the surface by radiography resulted in compressive stresses with maximum values of 500 MPa on the milled specimens, but only 200 MPa on the ground specimens, cf. Figure 19. It is well known [7,20] that grinding can also produce residual tensile stresses.

2.6.1.4 STRESS RATIO

The effect of stress ratio on fretting fatigue resistance was checked with one test series at $R = 0.5$. A considerable effect was only found at low numbers of load cycles, the effect at high numbers is negligible, see Figure 14.

2.6.1.5 TEMPERATURE

Fatigue and fretting fatigue resistance of Ti-6Al-4V are obviously less affected by elevated temperatures of up to $350^\circ C$, see Figure 15. An interesting result is the increase of the fretting fatigue limit at high numbers of cycles in the case of the ground specimens at $350^\circ C$ compared to room temperature. Obviously, the fretting conditions can be improved in special cases at elevated temperature, probably due to changing tribologic conditions. Relaxation of residual stresses should still be a secondary effect at this temperature [21].

2.6.2 FRACTURE APPEARANCE

Fretting fatigue failure is induced by local damage in the contact zone. Small cracks, propagating first in oblique orientation to the surface, develop from such damage. One or several of these small cracks propagate during cyclic loading, change to a direction normal to the cyclic load direction [1,9,15] and finally cause failure.

A typical crack origin and the first part of the corresponding fracture surface are shown in a longitudinal section in Figure 16 and in an SEM fractograph in Figure 17. In parallel to the dominating crack secondary cracks can also be seen. Part of the fretting debris, oxidized by tribo-chemical reactions, remains on the fracture surface, see Figure 16.

Fretting fatigue resistance is essentially determined by the mechanism of crack initiation and propagation in the first phase. As soon as the crack reaches a certain depth its propagation rate will depend only on the effective fatigue stress intensity factor range and no longer on the fretting conditions at the surface. In this phase the high stress concentration at the crack tip will result in continuous crack propagation even under comparatively low stress amplitudes.

Following current interpretation, crack initiation and propagation in the first phase are governed by multiaxial stresses in the surface area. The compressive stress due to the clamping pressure and the tensile and shear stresses caused by the frictional force are superimposed on the stress produced directly by the fatigue load. The shear stress component is claimed to be the most effective factor [18,22].

2.7 MEANS TO IMPROVE FRETTING FATIGUE RESISTANCE

2.7.1 GENERAL

Following the current interpretation that, as described above, the multiaxial stress in the surface area is decisive for failure initiation, two alternative methods of improving fretting fatigue resistance are conceivable in principle:

- Increase of allowable stress by improving material properties which affect strength in the surface area
- Reduction of effective stress. Service loads, i.e. fatigue load and clamping load, seldom can be reduced. What remains is to reduce the frictional force by reducing friction coefficient and adhesion respectively.

An effective method for increasing the allowable stresses of components is to generate residual compressive stresses and strain hardening effects in the critical surface area by plastic deformation [23]. From several different methods applied in practice, shot peening stands out because of flexible handling and applicability also for components with complicated shape. The method also could be employed for local treatment of compressor blades.

Another possible method is coating. An ideal coating would supply increased strength of the surface area and reduced friction and wear, covering in this way both alternative principle methods mentioned above. Coating also in principle is applicable for compressor blades.

Other methods to reduce friction - use of liquid or solid lubricants or intermediate layers - would not be applicable in disblade connections or would require modifications in design.

2.7.2 SHOT PEENING

The positive effect of shot peening on fretting fatigue resistance at room temperature was demonstrated for several applications [7,24]. The following results include results from tests at elevated temperature in addition.

The flat specimens, Figure 4, were shot-peened over the gage length. For optimizing peening parameters the shot size and Almen intensity were varied. Coverage was 100% in all cases. According to the results of these optimization trials, see Figure 18, peening shot M1 110 h and an Almen intensity of 0.24 mm A2 were chosen for preparing the specimens for the following tests. Measuring residual stress distribution by radiography, see Figure 19, resulted in maximum compressive stress of approximately 750 MPa near the surface.

The tests on specimens, shot-peened with optimized peening parameters, resulted in a considerably improved fretting fatigue resistance, see Figure 20. The fretting fatigue limit at 10^7 cycles was improved by more than a factor of two compared to the untreated milled specimens. That means a level of about 70% of the original fatigue limit can be reached under fretting conditions by shot-peening.

Residual stresses can be relaxed when local yield strength is approached by the service-induced stresses. Additional tests with elevated mean stress at $R = 0.33$ and $R = 0.5$ gave no indication for a beginning relaxation: The decrease of the allowable stress amplitude due to the increased mean stress is similar to untreated specimens with and without fretting as well, see Haigh diagram in Figure 21.

Figures 22 and 23 show the appearance of the shot-peened surfaces and fretting scars of specimens failed in fretting fatigue tests.

2.7.3 COATING

In cooperation with MTU several types of coatings were chosen for fretting fatigue tests from the following points of view:

- applicability for compressor components
- good results from fretting wear tests or fretting fatigue spot checks [7,16,24,25]

Galvanic copper coatings and other copper containing coatings showing favourable results in previous MTU tests [16] were not investigated further in this work. The practical use of copper coatings would be problematic anyway because of a possible detrimental effect of abraded copper particles on high-temperature-resistant alloys in the hot turbine parts.

The test programme included different types of other coatings. In any case the flat specimens were coated, and partly the fretting pads as well. The following coatings were investigated:

- Nickel diffusion layer applied by electroplating. Thickness appr. 50 μm , hardness 500 to 1000 HV 0.025. Fretting pads were uncoated.
- Cobalt chromium oxide ($\text{Co+Cr}_2\text{O}_3$) dispersion coating, consisting of a Co-matrix applied by electroplating, with embedded solid Cr_2O_3 particles with 2 to 5 μm grain size. Thickness appr. 15 μm , hardness appr. 450 HV 0.025. Fretting pads were uncoated.
- Two types of PVD (Physical Vapour Deposit) titanium nitride coatings, one applied in a thickness of appr. 5 μm by ion plating, the other by high performance sputtering in a thickness of appr. 2 μm on an intermediate layer from pure titanium. Hardness of both types was 500 to 600 HV 0.025. Fretting pads were partly coated, partly uncoated.
- PVD chromium nitride (CrN) coating, applied by high performance sputtering. Thickness appr. 10 μm , hardness appr. 1000 HV 0.025. Fretting pads were coated as well.
- Two other PVD coatings: A titanium carbo-nitride system (TiCN) and a titanium aluminium nitride (TiAlN) system. Thickness appr. 5 μm each. Fretting pads were coated as well.

From all these coatings only three did improve fretting fatigue resistance at room temperature and/or 350°C compared to the untreated material:

- the CrN coating
- the ion plated TiN type (pads coated as well)
- the ($\text{Co+Cr}_2\text{O}_3$) dispersion coating

Figures 24 and 25 show the degree of improvement. The best results, achieved with the CrN coating at 350°C, nearly doubled the fretting fatigue limit compared to the untreated material. The level of the shot-peened specimens, however, could not be reached.

An interesting result is the increase of fretting fatigue resistance at elevated temperature, compared to RT, measured on these coating systems. Different factors can be responsible for this effect: Obviously the fretting conditions can be improved at elevated temperatures by reducing friction coefficient and adhesive wear. In the case of the ($\text{Co+Cr}_2\text{O}_3$) coating an orientated oxide developing at elevated temperature is supposed to have such a beneficial effect [25,26]. The fretting zone appears smooth and shining, Figure 26. The specimens coated with CrN present a relatively smooth fretting zone as well with only a few wear scars, Figure 27.

Another positive effect is probably the increase of ductility in some coatings. Early initiation of cracks due to stress concentrations can be avoided or hindered if the coating is able to relax by local plastic deformation.

If fatigue stress and clamping pressure exceed a certain level abrasive or adhesive wear will increase and cracks will be initiated, see Figures 28 to 31.

High contact pressure and shear stress also produce plastic cyclic deformation in ductile coatings, Figures 28 and 29. In less ductile coatings the first stage of damage are multiple cracks, as can be seen in Figures 32 and 33.

The reasons why the other coatings failed at rather low stress are different: Some coatings, e.g. the nickel diffusion coating, are too brittle and failed by early crack initiation, other coatings had insufficient wear resistance and were removed rapidly.

2.7.4 SUMMARIZED RESULTS

The main results achieved with methods for improving fretting fatigue resistance as described above are compiled in Figure 34, demonstrating that shot peening is superior to the coatings investigated here. But by coating the fretting fatigue limit could also be improved by nearly a factor of two compared to the untreated material.

3 CONCLUSIONS

The fretting fatigue mechanism is very complex and still difficult to analyse.

Fatigue behaviour under multiaxial stress (crack initiation, crack propagation), tribological conditions (friction, wear) and chemical reactions (oxidation) have to be regarded as well. All efforts to improve fretting fatigue resistance have to consider this situation.

The investigations described above demonstrate that promising methods to improve fretting fatigue resistance of Ti-6Al-4V for application in compressor components of aircraft engines can be developed. Both basic methods investigated here - shot peening and coating - have special characteristics to be judged specifically for each individual case. One important aspect is the reliability which demands uniform quality since even a single defect may initiate a fatigue crack resulting in failure.

ACKNOWLEDGEMENTS

This research work has been supported by a grant of the Ministry of Research and Technology (BMFT) of the Federal Republic of Germany which should be acknowledged here.
The authors also thank MTU, Munich, for preparing the coated specimens and supplying expert advice.

REFERENCES

- [1] Waterhouse, R. B.:
Fretting Corrosion
Pergamon Press 1972
- [2] Funk, W.:
Der Einfluß der Reibkorrosion auf die Dauerhaltbarkeit zusammengesetzter Maschinenelemente
Diss. TH Darmstadt D 17, 1968
- [3] Julius, A.:
Reibkorrosion - Zum Mechanismus des Reibdauerbruchs
Forschungshefte Forschungskuratorium Maschinenbau, Heft 18, 1972
- [4] Kreitner, L. und H. W. Müller:
Die Auswirkung der Reibdauerbeanspruchung auf die Dauerhaltbarkeit von Maschinenteilen
Konstruktion 28 (1976), S. 209 - 216
- [5] Harris, W. J.:
The Influence of Fretting on Fatigue
AGARD-CP-161, 1975
- [6] Johnson, R. L. and R. C. Bill:
Fretting in Aircraft Turbine Engines
AGARD-CP-161, 1975
- [7] Adam, P., E. Broszeit und K. H. Kloos:
Schwingungsverschleiß an Turbinenwerkstoffen
TRIBOLOGIE, Band 1, Springer-Verlag, 1981
- [8] Gräter, R. and H. Huff:
Fatigue Behaviour of Titanium Material in Aircraft Engines Titanium, Science and Technologie
Proc. 5th Int. Conf. on Titanium, Munich, Sept. 10-14, 1984, Vol. 2, pp. 1269 - 1273
- [9] Hoepfner, D. W.:
Environment Effects in Fretting Fatigue
In: Waterhouse, R.B.: Fretting Fatigue Applied Science
Publishers Ltd., 1981
- [10] Bill, R. C.:
Review of Factors that Influence Fretting Wear
ASTM STP 780, 1982, pp. 165 - 182
- [11] Funk, W.:
Ein Prüfverfahren zur Untersuchung des Einflusses der Reibkorrosion auf die Dauerhaltbarkeit
Materialprüfung 11 (1969) N. 7, S. 221 - 227
- [12] Reeves, R. K. and D. W. Hoepfner:
An Apparatus for Investigating Fretting Fatigue in Vacuum
Wear 45 (1977), pp. 127 - 134
- [13] Poon, C. and D. W. Hoepfner:
Apparatus for Studying Fretting Fatigue in Vacuum
Rev. Sci. Instrum. 50 (2), Febr. 1979, pp. 171 - 176
- [14] Starkey, W. L.:
A New Fretting Fatigue Testing Machine
In: Corrosion Fatigue: Chemistry, Mechanics and Microstructure
University of Connecticut, NACE-2 (1972), pp. 642-645
- [15] Broszeit, E., K. H. Kloos and B. Schweighöfer:
The Fretting Fatigue Behaviour of the Titanium Alloy Ti-6Al-4V, Titanium, Science and Technologie
Proc. 5th Conf. on Titanium, Munich, Sept. 10 - 14, 1984, Vol. 4, pp 2171 - 2178
- [16] Adam, P., M. Paripovic und M. Thoma:
Schutzschichten gegen Schwingungsverschleiß im Triebwerksbau
TRIBOLOGIE, Band 4, Springer-Verlag, 1982
- [17] Waterhouse, R. B.:
The Effect of Fretting Corrosion in Fatigue Crack Initiation
In: Corrosion Fatigue: Chemistry, Mechanics and Microstructure, University of Connecticut,
NACE-2 (1972), pp. 608 - 616

- [18] Edwards, P. R.:
The Application of Fracture Mechanics to Predicting Fretting Fatigue
In: Waterhouse, R.B.: Fretting Fatigue, Applied Science Publishers Ltd., 1981
- [19] Broszeit, E., K. H. Kloos and B. O. Schweighöfer:
Fretting Fatigue Testing with a Fretting Bridge Equipment. Stress Analysis, Amplitudes of Slip, Reliability
Titanium, Science and Technology
Proc. 5th Conf. on Titanium, Munich, Sept. 10 - 14, 1984, Vol. 4, pp. 2179 - 2186
- [20] Franz, H. E.:
Röntgenographische Ermittlung der bei der Oberflächenbearbeitung von TiAl6V4 und TiAl6V6Sn2 entstehenden Eigenspannungszustände
VDI-Berichte Nr. 313, 1987, S. 453 - 462
- [21] Vöhringer, O., Th. Hirsch and E. Macherauch:
Relaxation of Shot Peening Induced Residual Stresses of TiAl6V4 by Annealing or Mechanical Treatment
Titanium, Science and Technology
Proc. 5th Int. Conf. on Titanium, Munich, Sept. 10 - 14, 1984, Vol. 4, pp. 2203 - 2210
- [22] Waterhouse, R. B.:
Theories of Fretting Processes
In: Waterhouse, R. B., Fretting Fatigue, Applied Science Publishers Ltd., 1981
- [23] Schütz, W.:
Shot Peening of Components to Improve Fatigue Strength
In: Shot Peening - Science, Technology. Application
DGM-Verlag, Oberursel, 1987
- [24] Waterhouse, R. B. and Saunders, D. A.:
The Effect of Shot Peening on the Fretting Fatigue Behaviour of Austenitic Stainless Steel and a Mild Steel
Wear, 53, (1979), pp. 381 - 386
- [25] Thoma, M. und P. Büniger:
Verschleißschutz für temperaturbelastete Bauteile durch Dispersionsschichten
Galvanotechnik 75 (1984), Nr. 4, S. 425 - 430
- [26] Thoma, M.:
Wear Protection of Engine Parts at High Temperatures by a Co+Cr₂O₃ Dispersing Coating
21st Annual Airline Plating and Metal Finishing Forum, Atlanta, Georgia, February 18 - 21, 1985
ISSN 0148-7191, 1985, SAE INC.

Table 1: Chemical composition of Ti-6Al-4V.
Values from producer's certificate.

Element	Al	V	Fe	C	N ₂	O ₂	H ₂
Content in weight %	6.2	4.0	0.16	0.014	0.014	0.170	0.007

Table 2: Basic mechanical properties

Property \ Test temperature	RT	350 °C
0.2 % proof stress $R_{p0.2}$ in MPa	1 035	690
Ultimate tensile stress R_m in MPa	1 065	775
Elongation A_5 in %	14	14
Reduction of area Z in %	34	46
Young's modulus E in MPa	115 000	96 000

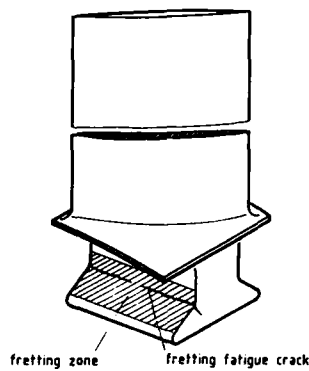


Figure 1: Dovetail of a compressor blade with fretting fatigue damage

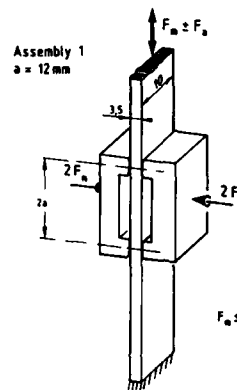


Figure 2: "Bridge" assembly, schematically

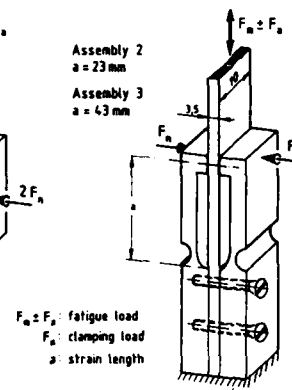


Figure 3: Modified assembly, schematically

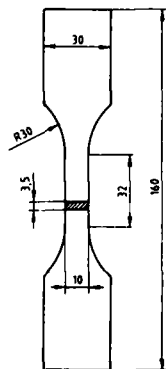


Figure 4: Flat specimen

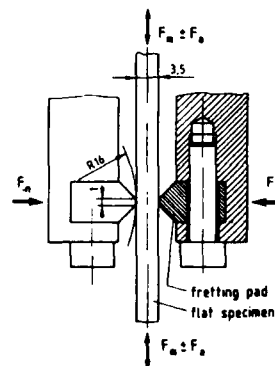


Figure 5: Fretting system

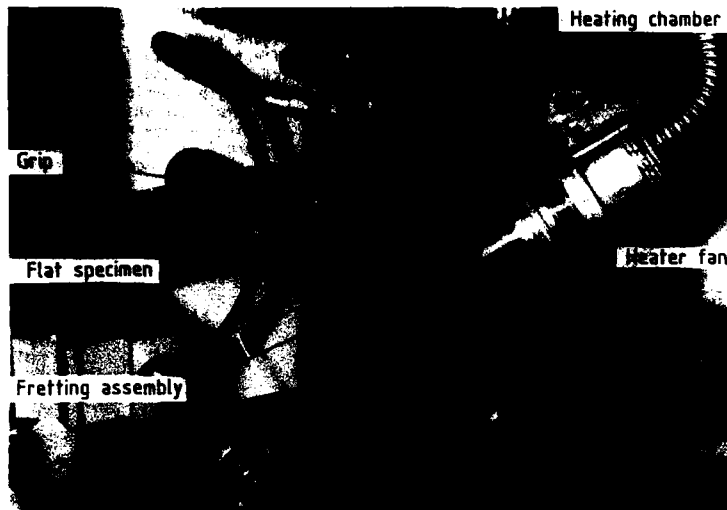


Figure 6:
Test setup (left half of
heating chamber removed)

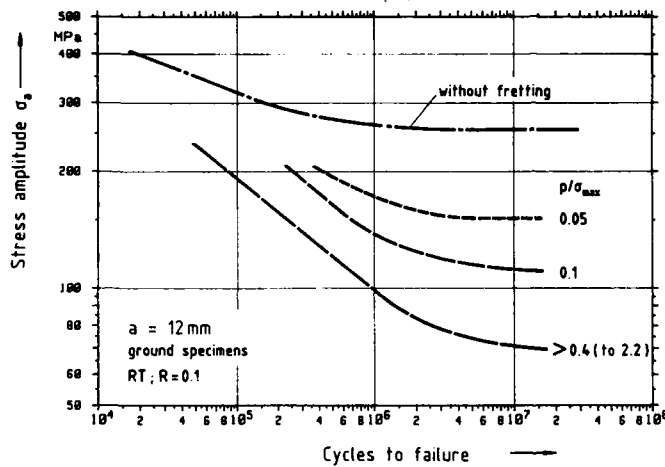


Figure 7:
Effect of clamping pressure
on fretting fatigue resistance

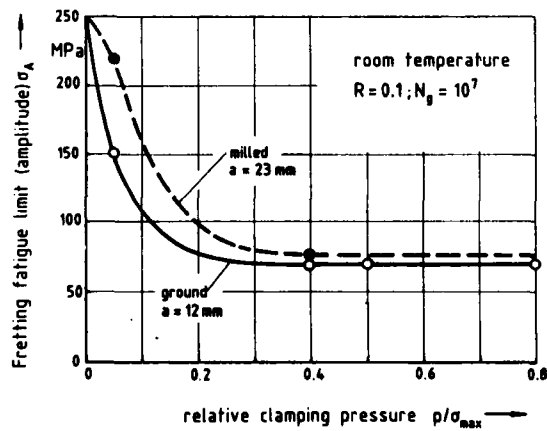


Figure 8:
Fretting fatigue limit at 10^7 cycles in
dependency on relative clamping pressure
Parameter: Surface finishing of flat specimens
(milled and ground)

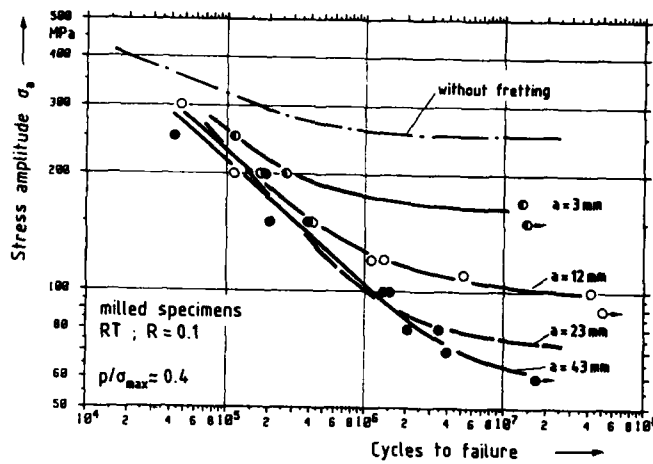


Figure 9:
Effect of length "a"
(cf. Figs. 2 and 3) which is
directly proportional to the
slip amplitude on the
fretting fatigue resistance.
a=3 and 12mm: "bridge" assembly,
a=23 and 43mm: modified assembly

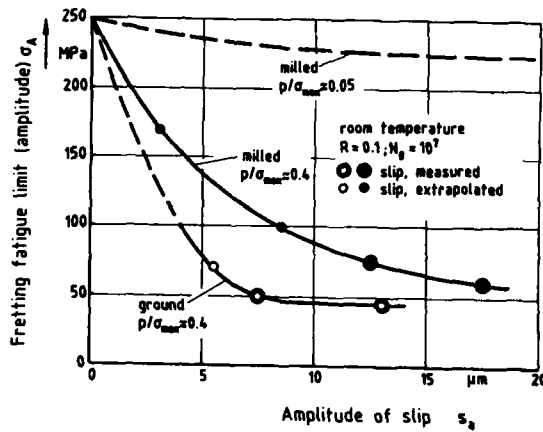


Figure 10:
Fretting fatigue limit at 10^7 cycles
in dependency on the slip amplitude
Parameter: Surface finishing of flat
specimens (milled and ground)

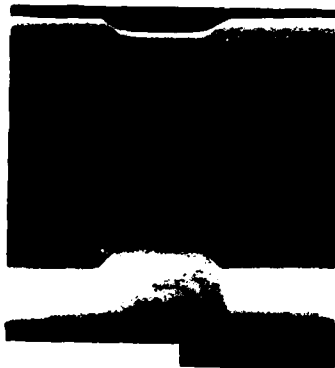


Figure 11: Fretting wear at low clamping
pressure and big slip amplitude
 $p/\sigma_{max} = 0.05$, $s_a = 70 \mu m$
 $\sigma_a = 220 MPa$, $N > 10^7$

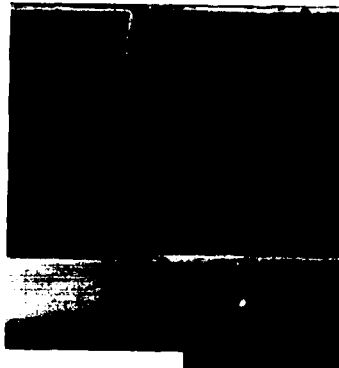


Figure 12: Fretting wear at high clamping
pressure and small slip amplitude
 $p/\sigma_{max} = 0.4$, $s_a = 20 \mu m$
 $\sigma_{max} = 70 MPa$, $N = 8.5 \cdot 10^4$

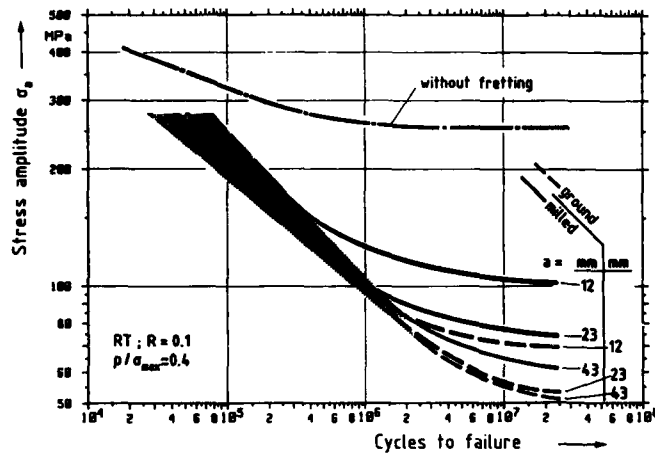


Figure 13:
Comparison of fretting fatigue
resistance of specimens with
milled and ground surface

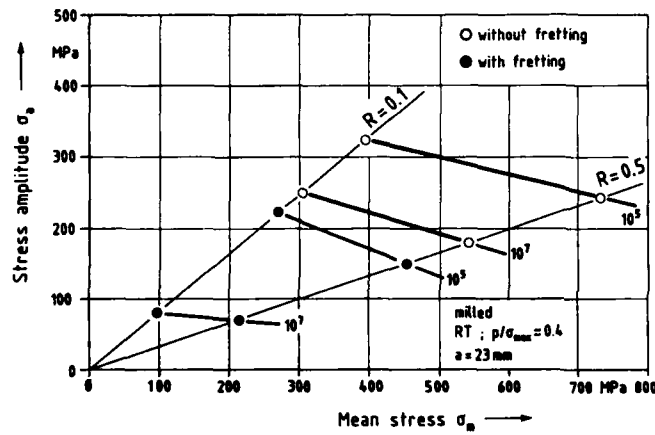


Figure 14:
Amplitude of fatigue and
fretting fatigue strength
in dependency of mean stress

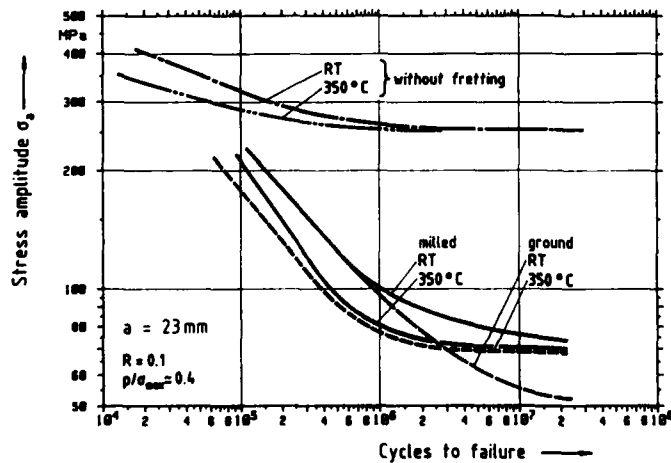


Figure 15:
Effect of elevated
temperature on fatigue
and fretting fatigue resistance

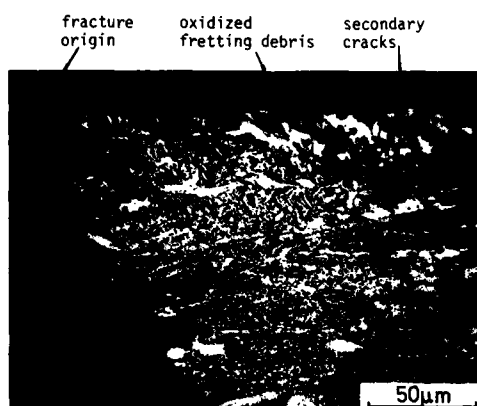


Figure 16: Fracture in milled specimen, tested at RT. Longitudinal section.

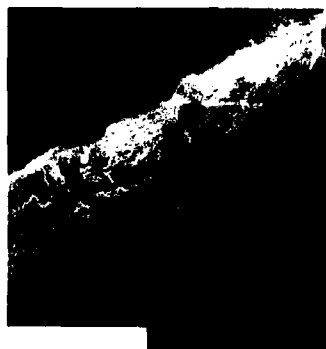


Figure 17: Fretting zone with fracture origin and secondary cracks.

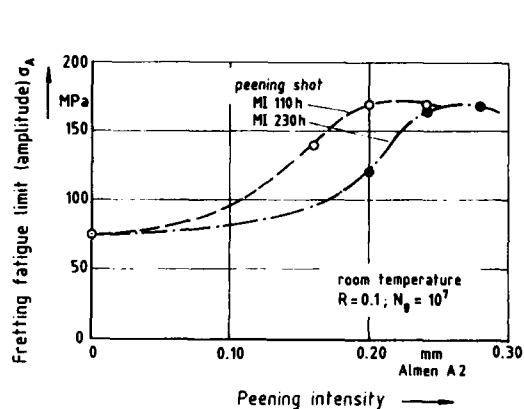


Figure 18: Fretting fatigue limit at 10^7 cycles of specimens shot-peened with different parameters

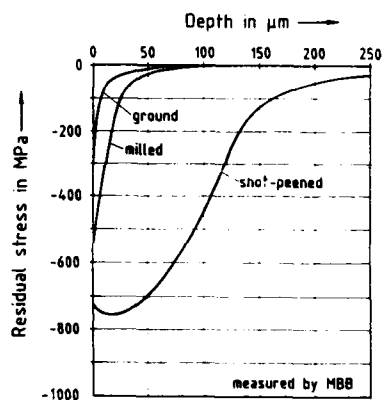


Figure 19: Distribution of residual stress near the surface in axial direction

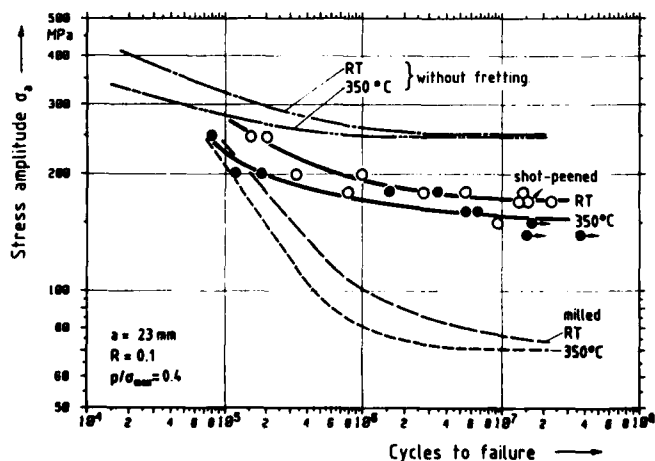


Figure 20: Fretting fatigue resistance of shot-peened specimens. Peening parameters optimized.

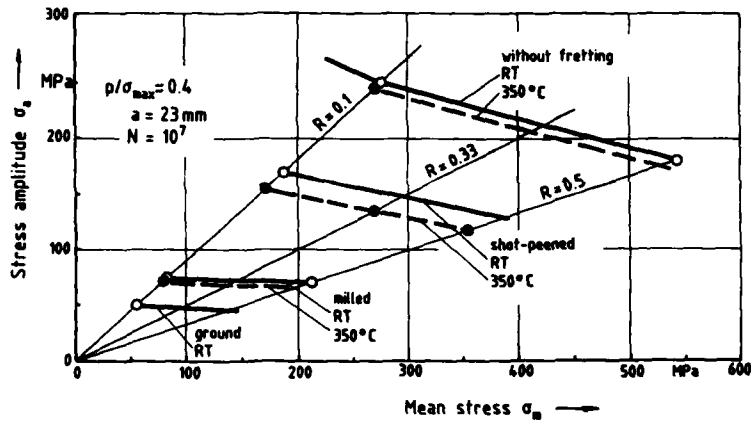


Figure 21:
Haigh-diagram for
fretting fatigue limit
at 10^7 cycles



Figure 22: Shot-peened surface
with fretting scar and fracture
origin.
Specimen tested at RT



Figure 23: Shot-peened surface
with fretting scar and fracture
origin.
Specimen tested at 350°C

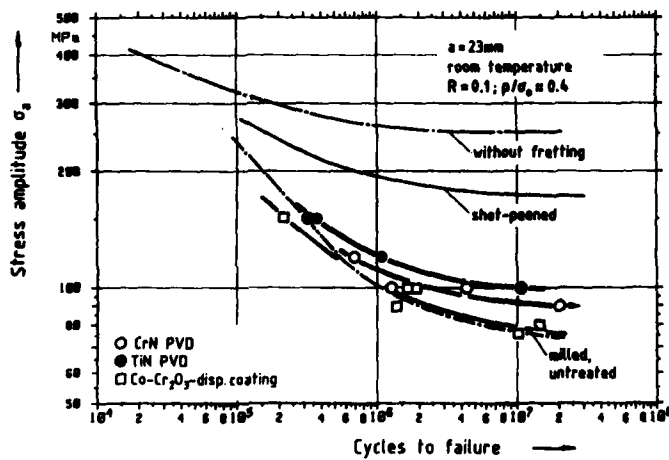


Figure 24:
Fretting fatigue resistance
of coated specimens at
room temperature

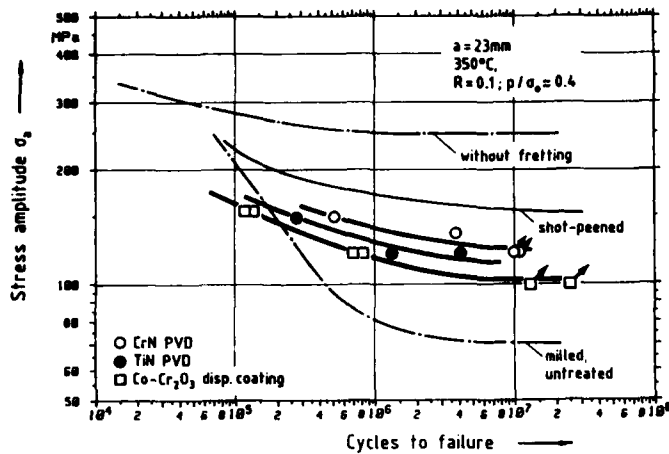


Figure 25:
Fretting fatigue resistance
of coated specimens at 350°C



Figure 26: (Co+Cr₂O₃) dispersion coating
with fretting zone (above).
Specimen tested at 350°C

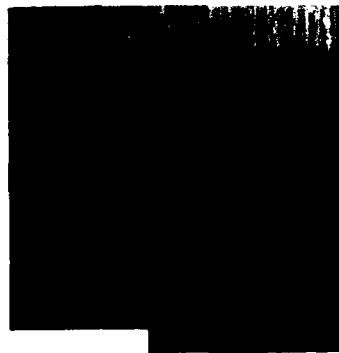


Figure 27: Cr N coating with fretting zone
(in the middle).
Specimen tested at 350°C without
failure.

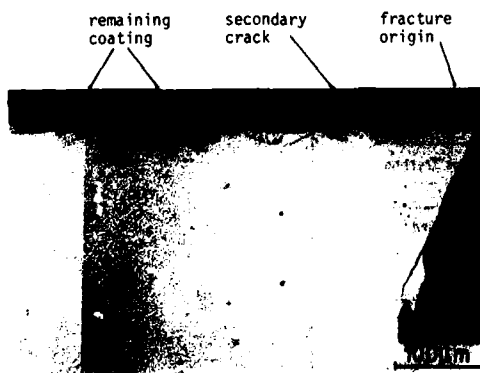


Figure 28: Specimen with (Co+Cr₂O₃)
dispersion coating. Longitudinal
section after failure in test
at 350°C

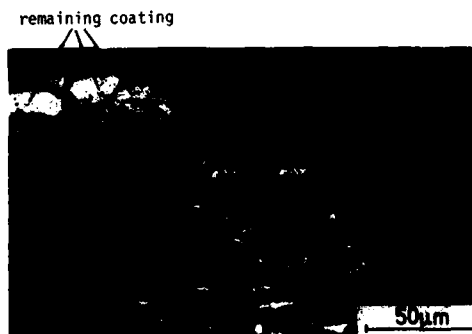


Figure 29: Detail from Figure 28
Section edged



Figure 30: Specimen with Cr N coating after failure in test at 350°C

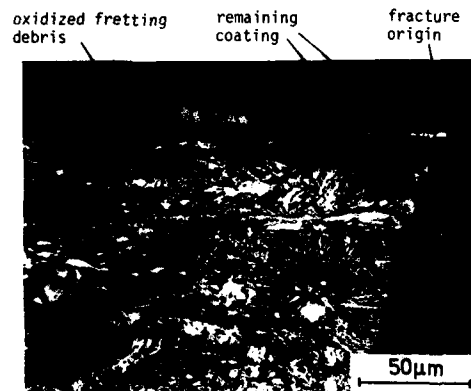


Figure 31: Specimen with Ti N coating. Longitudinal section after failure in test at 350°C

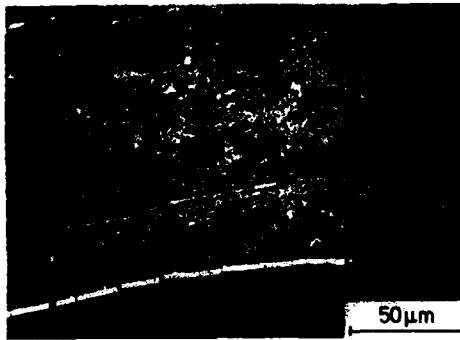


Figure 32: Specimen with Ti N coating. Longitudinal section after failure at 350°C

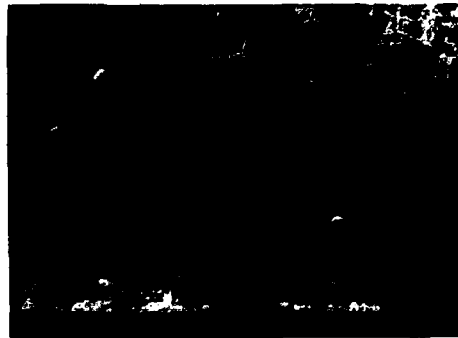


Figure 33: Fretting zone in Cr N coating with multiple cracks

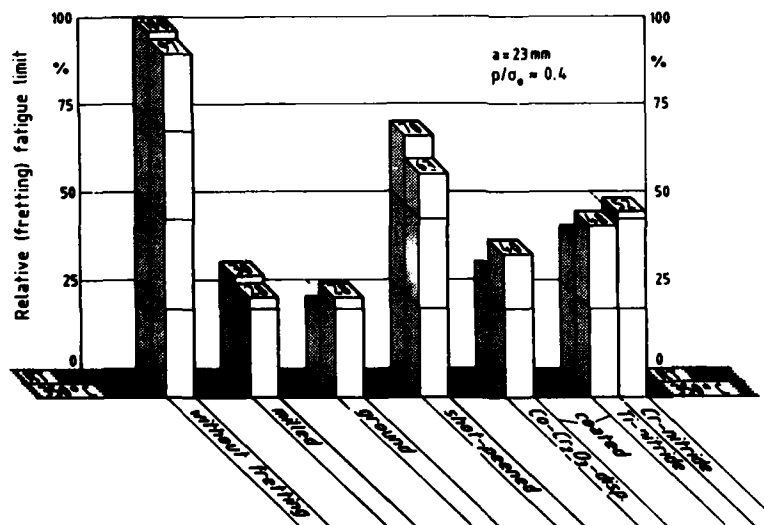


Figure 34: Fretting fatigue limit at 10^7 cycles for different surface finish and treatment

HIGH TEMPERATURE PROTECTIVE COATINGS: RECENT TRENDS

by

Rémy Mevrel
O.N.E.R.A.
Materials Science Department
B.P. 72
92322 Châtillon Cedex
France

Rémy MEVREL

O.N.E.R.A., Materials Science Department, B.P. 72, 92322 Châtillon Cedex, France.

ABSTRACT

A protective coating must meet several criteria : give adequate environmental resistance, be compatible with the substrate, and be applicable. After a brief description of the high temperature protective coatings currently used (simple and modified aluminides, MCrAlY overlays, ceramic thermal barrier coatings,...), a review of recent trends in the coating field is attempted. These trends, which arise from the search for more demanding applications such as higher operating temperatures and the use of low grade fuels, are related to high temperature corrosion degradation mechanisms, mechanical properties of coated components, diffusional stability of coating/substrate systems, the development of alternative coating processes and of more performant ceramic coatings.

1. INTRODUCTION

Materials for high temperature applications are generally selected for specific properties such as strength, creep, mechanical and/or thermal fatigue. During their use at high temperature these properties may degrade as a result of interactions with corrosive environments. One solution to avoid this alteration is to protect the component with a coating. Most high temperature coatings rely on the formation of a protective oxide scale by interaction with the environment. The rôle of this scale is to isolate the coating from the aggressive environment and thereby limit the degradations due to high temperature corrosion. Obviously this scale must fulfill several conditions : be stable, slow-growing, dense, adherent (often in cyclic conditions) and in practical applications only three oxides correspond to these criteria : alumina (Al_2O_3), chromia (Cr_2O_3) and silica (SiO_2). The fact that chromia can form volatile suboxides at temperatures above about 900°C, generally restricts its use at somewhat lower temperatures, especially with high velocity gases. Silica scales confer protection on ceramic coatings (SiC, Si_3N_4 , for example) deposited on carbon-based materials up to about 1800°C [1]. However, the use of silica-former metallic alloys as coatings has been limited. This is largely due to the fact that in order to form a silica scale, a metallic coating must contain a relatively large silicon amount. But silicon, which diffuses rapidly in most alloys, may form low melting phases and/or brittle silicides by interaction with substrate elements. As in the case of chromia forming coating alloys, the use of silica-forming metallic coatings must be restricted to rather low temperatures. These considerations explain why most high temperature coatings (simple or modified aluminides, MCrAlY overlays) rely on the formation of an *alumina scale* to ensure the protection of an underlying component.

Comprehensive reviews on high temperature protective coatings have regularly appeared since the early 70's [1-6]. Our purpose is not to recapitulate the material covered therein but rather, on the basis of published material and some personal communications, to focus on recent trends and to attempt to point out some research perspectives in the first part of this paper. The second part of this paper is devoted to substrate/coating compatibility considerations.

2. MAIN TYPES OF COATINGS

As mentioned above, most coatings rely on the isolation by a "barrier" of the part to be protected from the environment. The rôle of this barrier is to minimize the diffusion of gaseous or liquid species towards the component and conversely to prevent the elemental diffusion from the alloy towards the external surface where they could react. Most generally the barrier is dynamic in the sense that it forms by interaction of the coating with the oxidizing environment. And this is typically the case of coatings, whether metallic or ceramic, which form oxides such as alumina, chromia and silica. However, it is to be noted that inert barriers have been proposed in some cases, for example, silica coatings on steels [7], Ir on C/C [1], thin platinum layers on titanium alloys [8]. Their effective use would imply that a partial absence of coating, due for instance to a coating defect or spalling, is not too detrimental to the component life as the protection cannot then be restored in these systems. Moreover, interdiffusion effects between coating and substrates are supposed to be innocuous as far as the properties of the coated component are concerned.

2.1. Diffusion coatings

2.1.1. Simple diffusion coatings

Aluminide coatings [9, 10] are the most widely used to protect nickel- and cobalt-based superalloys for gas turbine applications. They are generally formed by pack cementation: the components are immersed in a powder mixture in a semi-sealed retort. The retort is then placed inside a furnace and heated at high temperature (between 750°C and 1150°C) under a protective atmosphere. In the case of an aluminizing process, aluminum is transferred from the pack to the substrate surface where it reacts and an aluminide layer forms by diffusion with the substrate. Due to this mode of formation this technique is a particular case of "reactive chemical vapour deposition". Pack cementation is a simple process to operate, easily controlled and inexpensive to run. These advantages justify its wide use for protecting superalloys. But due to its mode of formation, it suffers from several limitations: the range of accessible coating compositions and structures remains rather narrow -- only one element in practice can be transferred in the gas phase from the pack -- and in some applications it would be desirable to enrich the substrate surface not only with aluminium, but also with chromium, yttrium,.... Moreover, the composition and the structure of the substrate alloy can seriously affect the performances of the coating. Other diffusion coatings have been developed: silicon carbide on carbon-based materials [11], silicides on niobium alloys [12]. In the last case the addition elements are generally brought onto the surface in a slurry.

2.1.2. Modified diffusion coatings

As stated earlier, the range of accessible compositions and structures with a pack cementation process is limited. However in several applications, it would be interesting to benefit from the advantages of reactive CVD processes (uniform thickness on complex geometries in particular) but to modify the coating composition in order to improve its corrosion resistance. Different routes have been proposed to modify aluminide coatings: by *pretreatment* or *predeposit* prior the aluminizing process, and by *codeposition*.

A typical *pretreatment* consists in chromizing before aluminizing to obtain a chromium-enriched aluminide coating. Industrially available Cr-modified aluminide coatings include, for instance, C1A (SNECMA) and PWA 32.

Codeposition of two (or more) elements during a single step cementation treatment does not seem to be a widespread technique in industrial practice although it was envisaged a long time ago; reports of combined chromium and silicon cementation of steel were published as early as 1945 [13]. Recent works based on thermodynamic calculations have demonstrated the feasibility of codepositing Cr and Al on nickel base alloys [14, 16b] or on iron-base alloys [15, 16a], as well as Al and Hf [16a, b]. Difficulties seem to remain in the case of the codeposition of Al and an active element such as yttrium, one reason might be the very low solubility limit of this element in nickel- or iron-based alloys. It is to be reckoned that only scarce information are available at the moment concerning the passage to industrial practice (control of cement composition,...). Incorporation of a third element by a *predeposit* has led to the development of the platinum-modified coatings. Most often platinum is electrodeposited as a 8 micron thick layer. After aluminizing, platinum is concentrated in the external region of the coating which is generally constituted of a mixture of PtAl₃ and 8-NiAl enriched in platinum. The addition of platinum improves the resistance of simple 8-NiAl based coatings, particularly against type I hot corrosion.

Recent work by Alpérine et al. [17] indicates that platinum may be advantageously replaced by the chemically similar and less expensive palladium, provided proper care is taken to avoid the coating embrittlement during its processing.

2.2. MCrAlY overlay coatings [18]

MCrAlY alloys whose compositions and structures are entirely independent from the substrate can now be deposited as a result of the development of now well established techniques such as EB-PVD (electron beam physical vapour deposition), and plasma spraying under controlled atmosphere. As a consequence, a wide range of compositions is commercially available as shown in table 1.

Designation	Ni	Co	Fe	Cr	Al	Y	Other
LCO 29		bal.		18	8	.5	
ATD 5		bal.		18	11	.3	
LCO 5		bal.		19	10	.5	
ATD 2		bal.		23	12	.3	
LCO 7		bal.		23	13	.6	
ATD 14		bal.		30	5	.5	
Amdry 961	bal.			17	6	.5	
Amdry 962	bal.			22	10	1.	
ATD 16	bal.			25	12	.3	
Amdry 963	bal.			25	5	.4	
ATD 1	bal.			38	11	.3	
ATD 7	bal.	22		18	12	.3	
ATD 9	bal.	20		42	5	.3	
LN 21	bal.	22		21	7.5	.5	
Amdry 997	bal.	23		20	8.5	.6	4 Ta
LN 34	bal.	0.5		20	11	.5	.5 Mo
LCO 22	32	bal.		21	7.5	.5	
Amdry 995	32	bal.		21	8	.5	
LCO 37	23	bal.		30	3	.5	
Amdry 996	10	bal.		25	7	.6	5 Ta
Amdry 970			bal.	24	8	.4	
ATD 8			bal.	24	11	.6	

Table 1: Examples of MCrAlY nominal compositions (wt.%) which are commercially available [18-21]. (ATD: coatings produced by EB-PVD, Alcoa Temescal; LN and LCO: coatings produced by argon shield plasma spraying, Union Carbide; Amdry: powders available for LPPS, Alloy Metals).

2.2.1. Structure and compositions

MCrAlY alloys are most generally multiphase materials. If the aluminium content is not too high, Ni- and Co-base alloys consist basically of a ductile γ -solid solution (face-centered cubic) containing a dispersion of δ -NiAl or δ -CoAl phase. The actual microstructure can be more complex as shown for example by Frances et al. [22] who have identified γ' , sigma, M'_2Y and Y_2O_3 phases in addition to δ and γ in NiCoCrAlYTa alloys. It is to be borne in mind that the microstructure of MCrAlY alloys may depend on previous heat treatments and cooling rates. If the aluminium content is high enough, the beta phase percolates and contains a dispersion of γ -Ni particles. Such a structure is certainly less favourable in terms of ductility.

It is to be noted that in the Ni-Cr-Al ternary system, a phase transformation can occur at about 1000°C whereby $\gamma + \delta$, stable at high temperature, transforms into γ' -Ni₃Al + α -Cr as represented schematically on figure 1 based on the phase diagrams established by Taylor and Floyd [24]. This reaction is accompanied by a significant volume variation (fig. 1b) which may be deleterious for the mechanical integrity of a coating/substrate system. It is therefore recommended to select an alloy composition outside this field, limiting the aluminium content, or to add cobalt to destabilize γ' formation.

The oxidation behaviour of MCrAlY coating alloys depends on various factors (for a review, see for example [25]): alloy composition, temperature, oxygen partial pressure, time, thermal cycling.

A typical oxidation sequence for an MCrAlY alloy starts with the formation of transient oxides (NiO, spinel...) growing rapidly until a continuous stable oxide layer (chromia or alumina) has formed underneath. The diffusion of oxygen and metallic species being very slow in chromia and even slower in alumina, this layer ensures the oxidation resistance of the alloy. The presence of chromium in these alloys reduces the Al level necessary to form a protective alumina scale. The presence of as little as 5-10 % Cr reduces the amount of Al required from 40 at.% to about 10 at.%.

Alumina scales formed on MCrAlY alloys are not adherent in thermal cycling conditions, presumably as a result of growth and thermal stresses. In order to improve the adherence of the alumina scale, so-called active elements such as Y, rare-earth, ... are incorporated in these alloys in small amounts (less than 1 wt. %). Several explanations have been put forward (see for example [26] for a review) to explain this effect but a controversy still exists relative to the precise mechanism(s) involved. Other elements have been claimed to have the same effect (Hf, Zr...). A recent comparative study [23] showed however that, among Hf, Zr, Y, yttrium is by far the most effective addition element for improving the adherence of alumina scales formed at 1100°C. It is to be noted that this effect is observed whether yttrium is initially present in oxide particles or metallic phases within the coating. It seems in fact that a uniform distribution of these elements is essential. Recently, Gupta and Duval [27] have recommended the addition of both Y and Hf.

A major degradation (termed "hot corrosion") is the accelerated oxidation induced by condensed salts formed by pollutants present in combustion gases. Major contaminants in gas turbines are alkaline sulphates, in particular Na₂SO₄. The degradation modes depend on various factors: temperature range, nature of contaminants, gas composition, alloy composition [5]. Several mechanisms have been proposed (for a review, see [28]).

At relatively high temperature (type I hot corrosion, $T > 800^\circ\text{C}$), the degradation of the scale can take place:

- either by basic fluxing: this affects alumina-forming alloys containing less than about 15% Cr,
- or by acidic fluxing induced by oxides such as MoO₃, WO₃, V₂O₅ formed by oxidation of refractory elements.

At moderate temperatures ($650^\circ\text{C} < T < 800^\circ\text{C}$) another form of hot corrosion (type II, [29]) which affects alloys having low chromium has been reported. It involves acidic fluxing of oxide scales by SO₂ dissolved in molten sulphates in the presence of air.

The presence of chromium is beneficial against all types of hot corrosion. It is thought that Cr₂O₃ acts as a buffer against basic fluxing mechanisms. Moreover, Cr₂O₃ is more rapidly formed than Al₂O₃. About 25 to 40% Cr are required for type II hot corrosion whereas 15 to 20 % Cr are usually recommended for type I [29]. It is to be noted though that too high a chromium content may have deleterious effects on the diffusional stability of the coating/substrate system.

Silicon is particularly good in the case of type II hot corrosion (acidic fluxing) but above about 800°C, it tends to diffuse rapidly into the substrate and may form low-melting phases or brittle intermetallic compounds.

Other addition elements may play a beneficial rôle: tantalum for example, although not particularly good for oxidation resistance, prevents the outward diffusion of elements such as titanium, which are potentially deleterious regarding oxidation resistance, by tying them up, with carbon, in stable MC carbides.

The above considerations justify the wide use of standard NiCoCrAlY-base compositions with about 20% Co, 20% Cr, 8-12% Al and <1% Y (wt. %).

2.2.2. Alternative deposition techniques for metallic coatings

Despite the flexibility they permit, the techniques commercially available to deposit MCrAlY coatings, EB-PVD and plasma spraying under inert atmosphere, remain line-of-sight processes and this, in addition to their relatively high cost, can be a real drawback for coating components having complex shapes. In view of some of the disadvantages of techniques which are in production, alternative processes have been developed, among which electrolytic codeposition and electrophoresis seem the most promising at the moment.

- Electrolytic codeposition

MCrAlY coatings have been obtained by co-electrodeposition of a dispersion of fine CrAlY powder particles and a Co or Ni matrix [30]. This operation can be carried out in a barrel plating unit (fig. 2). The barrel containing the specimens and the powder particles (10 μm diameter) is immersed into a Co and/or Ni conventional bath and rotated. The coated components are subsequently heat treated for alloying and diffusion bonding the coating to the substrate.

This process presents obvious economical advantages: low capital cost (claimed to be an order of magnitude less than existing commercial systems, unit processing cost about half those of competing systems [30]); reliability performances do not seem to have been published as this technique has not yet been scaled up.

- Electrophoresis

This process is based on the migration of fine powder particles suspended in a polar solution under a dc voltage. In the process developed at SNECMA [31, 32], MCrAlY alloy powders with size less than about 40 μm are deposited by electrophoresis on the components to be coated with deposition rates up to 100 $\mu\text{m}/\text{min}$. Figure 3a shows the deposit with controlled porosity obtained at this stage. In order to densify them and adjust the coating composition, the components are then aluminized (vapour phase process). The aspect of an MCrAlY coating obtained in the end is illustrated in figure 3b. With adequate electrode geometry, components with complex shapes can be uniformly coated. Facilities required are relatively simple, so the investment as well as the running costs are much less than for processes such as EB-PVD and plasma-spraying. As shown in figure 3c, these coatings confer a hot corrosion resistance comparable with that of LPPS coatings.

- Cladding

Cladding MCrAlY sheets has been envisaged to produce protective coatings [33]. Early experiments do not seem to have met an overwhelming success. This may have been caused by the very limited Al content of available sheet alloys (conventional forming processes require low Al content) and possibly an inadequate yttrium distribution. It might be interesting to reconsider this technique as MCrAlY ribbons (50 to 100 μm thickness) having satisfactory oxidation-resistant compositions can now be obtained by melt-spinning [34].

2.3. Thermal barrier coatings

Thermal barrier coatings are generally constituted of an oxide layer (thickness ranging from about 300 μm in turbine applications up to about 2 mm in diesel engines) plasma-sprayed on top of an MCrAlY bond layer deposited on the substrate. The benefits of thermal barrier coatings are multiple : higher inlet gas temperatures, lower cooling flow within the metallic component, reduction of temperature transients on the metal surface. All these advantages can result in improved efficiency, extended lifetimes and simplified designs. Such ceramic coatings have been plasma-sprayed onto sheet metal combustor components for more than 15 years. Only recently have they been used in the turbine section of commercial gas turbine engines. Thermal barrier coatings over the entire airfoil of PW4000 turbine vanes were certified in the United States for production use in 1986 [35]. This progress could be achieved by a proper control of porosity, microcrack distribution, and residual stresses in the coating. With nickel-base superalloys having reached their optimum properties, one of the present challenges to significantly increase the gas turbine performance remains to apply these coatings on highly stressed components, such as turbine blades.

2.3.1. ZrO_2 -6 to 8wt.% Y_2O_3

Figure 4 illustrates the typical aspect of the cross section of a thermal barrier coating. Most often the oxide is zirconia-based, whether partially or completely, stabilized with proper additions of Y_2O_3 , MgO or CaO , as ZrO_2 offers a good compromise between low thermal conductivity and high thermal expansion coefficient. Yttria partially stabilized zirconia, containing between 6 and 8 wt.% Y_2O_3 , has been found, empirically [36], to be most resistant in thermal cycling conditions. This composition corresponds to the formation of a metastable tetragonal 't' phase when the cooling rate is sufficiently high, as in plasma spraying which is at the moment the most often used deposition process for obtaining these coatings. With proper parameter adjustment, plasma spraying gives a microcracked structure particularly strain tolerant in compression [37]. This is important as the main degradation mode (spallation) of thermal barrier coatings results from fatigue cracking damage in the ceramic layer near the ceramic/bondcoat interface, induced by thermal strains. It is to be emphasized though that the precise rôle of the 't' phase in terms of crack propagation rate is not clearly understood and basic studies are needed to relate the fine microstructure and phase transformations of TBC with their mechanical properties [38, 39]. Recent engine tests by Sheffler et al. [40], Toriz et al. [41] have proved that thermal barrier coatings obtained by EB PVD may be even more performant than plasma-sprayed ones. This might be due to the well adapted anisotropic microcrack network in PVD columnar deposits.

2.3.2. Rôle of the bond coat

Between the oxide topcoat and the superalloy substrate, an MCrAlY bond coat is required to confer an adequate environmental resistance and to mechanically adapt the oxide layer and the substrate.

- Mechanical adaptation

This mechanical adaptation is more complex than a simple matching of thermal expansion coefficient. Actually the expansion coefficients of MCrAlY alloys are generally higher than for superalloys. The calculation of residual stresses in a purely elastic situation (with experimental elastic moduli) gives values well above the measured ones. In fact, strain accommodation occurs in a large part by plastic deformation of the bondcoat as MCrAlY alloys have a very low flow stress at temperatures above 600°C.

- Environmental resistance

Thermal barrier coatings are dynamic systems in the sense that zirconia topcoat, MCrAlY bondcoat and substrate superalloy interact at high temperature. Figure 5 shows, for example, the thin alumina layer formed at the zirconia/MCrAlY interface after a 100 hour heat treatment at 1100°C. This layer has formed by interaction of aluminium which has diffused from the MCrAlY alloys with oxygen present in the zirconia material. It is interesting to note that the adhesion between these layers (zirconia/alumina/MCrAlY) is sound and that, in practice, spallation rarely occurs at the interfaces. Instead, in thermal cycling tests, failure of TBC happens as shown on figure 6a, by propagation of a main crack inside the zirconia topcoat near the alumina/zirconia interface. The propagation results from compressive stresses arising on cooling in the topcoat because of thermal expansion mismatch. A more extensive oxidation of the bondcoat can lead to the ruin of the barrier as shown on figure 6b as the transformation of the alloy into oxide is accompanied by a volume expansion which generates additional stresses in the zirconia layer. The evolution of the structure and composition of the MCrAlY bondcoat is likely to affect its mechanical properties and as a consequence, to alter its ability to deform rapidly during cooling. This in turn will raise the compressive stress level in the ceramic layer, accelerating the degradation of the coating.

Another degradation mode may occur by hot corrosion with liquid sulfate contaminants. Several mechanisms have been proposed to explain the accelerated degradation of TBC in hot corrosion conditions : destabilization of zirconia, sulfidation of bondcoat, solidification of sodium sulfate in the cracks, crack propagation assisted by sulfate vapours [42].

2.3.3. Modelling

A significant effort at modelling the behaviour and life of thermal barrier coatings is going on especially in the U.S.A., as summarized by Miller [43]. The models developed result from a predominantly phenomenological approach schematically illustrated on figure 7 and involve several empirical parameters. It must be emphasized that, up to now, some areas are still generally poorly described : creep and inelasticity of ceramic and bondcoat, geometry effect (roughness of metal/ceramic interface), oxidation-induced damages, sintering of oxide at high temperature....

2.3.4. Concluding remarks

Thermal barrier coatings should provide the next significant increase in engine performance; Sheffler and Gupta [40] report that a 250 μm thick zirconia layer can reduce metal temperature by as much as 170°C. This may be achieved through the development of more reliable coatings and of thermomechanical modelling. Moreover new ceramic compositions are required for improved coatings resistant to corrosive environments with contaminated fuels and molten salt deposits [45] and, in the long run, for coatings having higher temperature capability than yttria partially stabilized zirconia. Finally new processes for depositing ceramic coatings will have to be developed to protect components having complex geometry.

3. COMPATIBILITY CONSIDERATIONS

Numerous considerations are to be taken into account when selecting or designing a coating for a particular application: they are related to the environment, the coating process, the service conditions and the substrate. Due to the drive for ever increasing temperatures to improve engine performances and the development of advanced superalloys, considerations of coating/substrate compatibility, whether chemical or mechanical, become more and more important.

3.1. CHEMICAL COMPATIBILITY

Coating and superalloy substrates generally have widely different compositions, each of them selected for different purposes: protection against oxidizing environment on the one hand and high temperature mechanical properties on the other. The chemical potential gradients of the different elements (Ni, Al, Cr,...) across the coating/substrate interface will cause interdiffusion phenomena to occur and these effects will be all the more important that the temperature is elevated.

As a consequence, elements from the substrate may diffuse through the coating, reach the external surface and perturb the formation of the protective oxide scale. This is illustrated on figure 8 which represents the weight variations in cyclic oxidation at 1100°C, of different superalloys (IN100, IN738 and CMSX2) coated with the same plasma-sprayed CoCrAlY alloy. The graph clearly shows that after only 250 cycles the coating deposited on IN100 and IN738 suffers extensive damages, which correspond to internal oxidation and subsequent scale spallation as revealed by metallographic examinations. Whereas on CMSX2 the coating lifetime is more than 1000 cycles. Analysis of oxidized samples suggested that in the first two cases, the formation of the alumina scale is perturbed by diffusion of titanium from the substrates toward the external surface. Conversely, interdiffusion may also affect the structure of the subcoating zone in the substrate and therefore alter or modify its mechanical properties. Several transformations can take place:

- transformation of the initial γ/γ' microstructure into γ/δ in the case of CoCrAlY/Ni-base superalloys [46, 47];
- alteration of the γ' distribution;
- modification of the distribution of grain-boundary strengthening elements (carbon,...) [48];
- destabilization of the reinforcing carbide fibres in directionally solidified eutectics [49];
- formation of brittle phases which may be crack initiation sites or easy paths for crack propagation.

These effects which can be important in the case of components with thin sections, can be minimized by carefully selecting a coating composition compatible with that of the substrate. This is possible in the case of MCrAlY coatings because of the flexibility allowed by the deposition processes. Some authors [50] have suggested putting a "diffusion barrier" (generally a stable ceramic material in which metallic diffusion is slow) between coating and substrate to prevent these effects. It is thought however that such intermediate layer might present several drawbacks: poor thermomechanical behaviour due to thermal expansion mismatch, preferential path for oxidation penetration once the diffusion barrier material has been reached by oxygen through a coating defect initially present or induced by local degradation in service.

3.2. MECHANICAL COMPATIBILITY

A protective coating may alter the mechanical properties of a superalloy substrate it is applied on, as a result of factors exposed above. It must be stressed however that in the long run, a coating, if adequately protective, will isolate the superalloy from the environment (oxidizing combustion gases, molten salt deposits) and therefore will limit or suppress the corrosion-induced mechanical degradations. In a study on thin section René 80 specimens, pre-corroded during 500 hours in an engine atmosphere, Kaufman [51] has thus shown that the presence of a coating, whether aluminide or MCrAlY, improves the creep lifetime (at 980 and 1080°C) by factors ranging between 2 and 8, as well as the fatigue resistance at room temperature (220 to 280 MPa).

It is generally accepted that creep properties of superalloys are not affected by a coating provided the standard heat treatments are respected and little interdiffusion occurs in service or during coating application; a possible favourable influence is likely to occur in the long run, because of the suppression of environmental degradation.

The mere presence of a protective coating can significantly alter the fatigue resistance of superalloy substrates. This has been clearly shown for example by Veys [52], Wood [53, 54] in the case of single crystal superalloys. The reduction in fatigue lifetime is related to early cracking in the coating with subsequent propagation inside the substrate. The fact that early cracking occurs at temperatures around 800°C or 900°C may be an aggravating factor for hot corrosion degradation: in this temperature range, sodium sulphate may condense on blade surfaces and penetrate through these cracks, abolishing the beneficial effect of the protective coating.

It is important to note that the structure and composition of a protective coating changes during operation at high temperatures as a result of aluminium consumption by oxidation; the initial $\gamma + \delta$ structure of an MCrAlY coating therefore progressively transforms into $\gamma' + \gamma''$ and in the end to γ -solid solution of nickel; this is also accompanied by grain growth. No study taking these effects into account however seems to have been published, the durations of tests performed being too short for these phenomena to be significant.

Recent efforts [55-58] have concentrated on thermomechanical fatigue tests which combine mechanical strain-controlled cycling and temperature cycling; these tests offer a better simulation of the complex strain-temperature-time cycles experienced by gas engine components in service. Moreover, thermomechanical fatigue may now be a major limiting factor in turbine vanes and blades [37], in particular for highly stressed thin-walled components.

Swanson et al. [57, 58] have been developing life prediction models with emphasis on applicability to thermomechanical fatigue conditions. These models are based on the development of individual constitutive models of coatings (PWA286: NiCoCrAlY SiHf and PWA273 low activity aluminide) and PWA1480 single crystal substrate, for which commercial production experience already exists. Results of out-of-phase tests carried out between 427 and 1038°C indicate that at strain ranges greater than 0.5%, the overlay-coated specimens have longer lives than do those coated with the aluminide, the reverse being true at lower strain range. It is interesting to note that similar results were obtained by Bain [56] on a single crystal superalloy coated with a CoCrAlY alloy or an aluminide and tested in slightly different conditions.

As emphasized by Wood [57], little work has been done to determine in depth what coating properties are of importance in controlling the mechanical behaviour of coating/substrate system. The studies in this field have mainly dealt with the identification of degradation modes and the experimental evaluation of the incidence of coatings on few mechanical properties of as-coated substrates. It is important to remark that coatings are found as crack initiation sites in a variety of test conditions, the cracks thus formed propagating subsequently into the substrate material and leading eventually to failure. Neither the evolution of the coating composition in service nor the presence of corrosive products are taken into account. Some attempts at modelling the coating/superalloy system have been recently published [58]. However, the lack of data relative to the coating intrinsic mechanical properties, mainly in the case of the widespread aluminides (simple or modified), seems to have delayed the development of an adequate description of these systems. As a consequence, the possibility of tailoring the coating composition and/or structure to improve the mechanical properties of the coating/substrate composite does not seem to have been fully exploited.

4. CONCLUSION

Looking back on the historical evolution of high temperature protective coatings it is interesting to note that, generally, the most performant systems, which are in service at the moment, have been developed according to a largely empirical approach. Further development can be expected along this line, for example with the introduction of alternative coating processes for depositing MCrAlY alloys (electrophoresis, co-electrodeposition) or with the replacement of platinum by palladium in modified aluminide coatings. The development of advanced processes however, often requires a more subtle approach (for example involving thermodynamic calculations in the case of codeposition in single step cementation, for instance). More in-depth investigations are needed in order to better understand the degradation mechanisms and therefore be in a position to exploit the full potential of available coating compositions. In this respect more data and modelling are necessary concerning the intrinsic mechanical properties of coatings as well as the thermomechanical behaviour of coated systems. Application of thermal barrier coatings on highly stressed components represent the next challenge for improving significantly gas turbine engine performances. This implies an active research effort in the direction of more reliable coating processes and, depending on applications envisaged, of new systems with higher temperature capabilities or improved hot corrosion resistance.

Finally an increasing activity is noted concerning the development of high temperature materials: titanium alloys having creep strength at temperatures above those for which oxidation resistance is adequate, intermetallic compounds, etc. Formulating new coating compositions and processes is expected to be necessary to ensure the protection of these materials.

ACKNOWLEDGEMENTS

Thanks are due to many people for valuable discussions and suggestions, in particular Serge Alperine and Pierre Josso on Pd-modified aluminide coatings, Patrick Choquet on the oxidation of MCrAl + X coatings, J.-M. Vays on mechanical properties of coated systems, René Morbioli (SNECMA) on electrophoretic deposits and Robert Miller (NASA) on thermal barrier coatings.

REFERENCES

1. J.R. Strife and J.E. Sheehan, Ceramic coatings for carbon-carbon composites, *Ceramic Bulletin*, 67(1988) 369-374.
2. G.W. Goward, Protective coatings - purpose, role and design, *Mat. Sci. Technol.* 2(3) (1986) 194-200.
3. J. Stringer, Design of coatings for high temperature corrosion protection, in *Surface Engineering* (Edit. R. Kossowsky and S.C. Singhal) NATO ASI Series N°85, 561-587.
4. R.A. Miller, Current status of thermal barrier coatings, *Surf. Coat. & Technol.* 30(1987) 1-11.
5. C. Duret-Thual, R. Morbioli and P. Steinmetz, *A guide to the control of high temperature corrosion and protection of gas turbine materials*, Edit. Commission of the European Communities, EUR 10682 (1986).
6. *High Temperature Oxidation Resistant Coatings*, National Academy of Sciences and Engineering Publ (1970).
7. M.J. Bennett, New coatings for high temperature materials protection, *J. Vac. Sci. Technol.* B2(4) (1984), 800-805.
8. S. Fujishiro and D. Eylon, Improved high temperature mechanical properties of titanium alloys by platinum ion plating, *Thin Solid Films* 54 (1978) 309-315.
9. R. Mévrel, C. Duret and R. Pichoir, Pack cementation processes, *Mat. Sci. & Technol.*, 2 (1986), 201-206.
10. R. Mévrel and R. Pichoir, Les revêtements par diffusion, *Mat. Sci. & Engng.* 88 (1987) 1-9.
11. M.-P. Bacos, personal communication.
12. S. Priceman and L. Sama, Reliable, practical, protective coatings for refractory metals formed by the fusion of silicon alloy slurries, *Electrochemical Technology*, 6(9-10) (1988) 315-326.
13. Chromium, Silicon and Aluminum Impregnation of Steel, *The Iron Age*, oct. 18, 1945, 58-61. This article gives an abstract and translation of a report published by A.M. Borzdika in *Stal* 7-8.
14. G.H. Marinissen, Codeposition of chromium and aluminium during a pack process, in *High Temperature Protective Coatings* (ed. S.C. Singhal) 27-35, The Metallurgical Society of AIME (1983).
15. R.A. Rapp, D. Wang and T. Weisert, Simultaneous chromizing-aluminizing of iron and iron base alloys by pack-cementation, *Proc. of TMS-AIME Symposium on Metallurgical Coatings* (Orlando, 1986).
- 16a. B. Nciri, Thèse (Orléans, 1983).
- 16b. G. Leprince, S. Alperine, L. Vandenbulcke and A. Walder, New high temperature resistant NiCrAl and NiCrAl + Hf felt materials, *Mat. Sci. Engng.*, to be published.
17. S. Alperine, P. Steinmetz, P. Josso and A. Costantini, High temperature resistant palladium-modified aluminide coatings for nickel-base superalloys, *Mat. Sci. Engng.*, accepted for publication.
18. R. Mévrel and R. Morbioli, MCrAlY coatings, in *Proc. 1st Internat. Congress on High-Tech-Materials and Finishing* (Berlin, March 12-14, 1989), 205-216.
19. Boone D.H., Physical vapor deposition processes, *Mat. Sci. Technol.* 2(3), (1986) 220-224.
20. Gill B.J. and R.C. Tucker, Plasma spray coating processes, *Mat. Sci. Technol.* 2(3), (1986) 207-213.
21. AMDRY plasma and flame spray powders, Technical notice.
22. M. Frances, M. Vilasi, M. Mansour-Gabr, J. and P. Steinmetz, Etude de l'oxydation de l'alliage NiCoCrAlYTa coulé et projeté au chalumeau plasma sous pression réduite, *Mat. Sci. Engng.* 88(1987) 89-96.
23. P. Choquet, Thèse Doctorat ès sciences (Orsay, 1987).
24. A. Taylor and R.W. Floyd, The constitution of Ni-rich alloys of the Ni-Cr-Al system, *J. Inst. Metals*, 81(1952-3) 451-464.

25. F.H. Stott, The protective action of oxide scales in gaseous environments at high temperature, *Rep. Prog. Phys.* 50 (1987) 861-913.
26. J.L. Smialek, R. Browning, Current viewpoints on oxide adherence mechanisms. NASA TM-87168 (1985).
27. D.K. Gupta and D.S. Duvall, A silicon and hafnium modified plasma sprayed MCrAlY coating for single crystal superalloy, in *Superalloy 1984* (Edit. M. Gell et al.), The Metall. Soc. of AIME (1984), 713-720.
28. R.A. Rapp, Chemistry and electrochemistry of hot corrosion of metals. *Mat. Sci. Engng.* 87 (1987) 319-327.
29. G.W. Goward, Low-Temperature Hot Corrosion in Gas Turbines : a review of causes and coatings therefor, ASME 85-GT-60 (1985) 1-5.
30. Honey F.J., E.C. Kedward and V. Wride, The development of electrodeposits for high-temperature oxidation/corrosion resistance, *J. Vac. Sci. Technol.* A4(6), (nov/dec 1986) 2593-2597.
31. Aboulcam, Gaujé, Grammagnac et Morbioli, Procédé et dispositif pour la réalisation de revêtements protecteurs métalliques. Demande de brevet d'invention N° 2 529 911 (1982).
32. R. Morbioli, Revêtements d'aluminures complexes obtenus par dépôt électrophorétique consolidé par aluminisation, *Mat. Sci. Engng.*, to be published.
33. Protective cladding and coatings for utility gas turbines. Final report EPRI AP-3267 (1983).
34. Duffos F., C. Duret, V. Gossart, M. Kumar, A. Walder, New materials for honeycomb structures with improved resistance to high temperature oxidation, in *High Temperature Alloys for Gas Turbines and other Applications 1986* (Reidel, 1986), part II, 989-998.
35. J.W. Fairbanks, R.J. Hecht, The durability and performance of coatings in gas turbine and diesel engines. *Mat. Sci. Engng* 88 (1987) 321-330.
36. S. Stecura, Optimization of the NiCrAl-Y/ZrO₂-Y₂O₃ thermal barrier system. NASA TM-86905 (1985).
37. T.A. Cruse, S.E. Stewart and M. Ortiz, Thermal barrier coating life prediction model development. *Trans. of the ASME J. of Engineering for Gas Turbines and Power*, 110 (1988) 610-616.
38. R. McPherson, A review of microstructure and properties of plasma sprayed ceramic coatings. *Surface and Coating Tech.*, in press.
39. L. Lelait, S. Alperine, C. Diot and R. Mévrel, Thermal barrier coatings : microstructural evolution during annealing. *Mat. Sci. Engng.*, to be published.
40. K.D. Sheffier and D.K. Gupta, Current status and future trends in turbine application of thermal barrier coatings. *Trans. of the ASME J. of Engineering for Gas Turbines and Power*, 110 (1988) 605-609.
41. F.C. Toriz, A.B. Thakker and S.K. Gupta, Flight service evaluation report of thermal barrier coatings by physical vapor deposition at 5200 hours. To be published.
42. S. Alperine, Molten salt induced high temperature degradation of thermal barrier coatings. This conference.
43. R.A. Miller, Life modelling of thermal barrier coatings for aircraft gas turbine engines. NASA TM 100283 (1988).
44. T.E. Strangman, J. Neumann and A. Liu, Thermal barrier coating life prediction model development. NASA CR-179648 (1987).
45. R.L. Jones, Scandia-stabilized zirconia for resistance to molten vanadate/sulfate corrosion. Presented at ICMC 1989 (San Diego, April 89). To be published.
46. R. Mévrel and C. Duret, Interdiffusion effects between protective coatings and superalloy substrates, in *Coatings for Heat Engines*, NATO Advanced Workshop (Acquafredda di Maratea, 1984) 595-612.
47. P. Mazars, D. Manesse and C. Lopvet, Interdiffusion of MCrAlY coatings with substrates, in *High Temperature Alloys for Gas Turbines and other Applications 1986* (Reidel, 1986) 1183-1192.
48. A. Strang, E. Lang and R. Pichoir, Practical implications of the use of aluminide coatings for the corrosion protection of superalloys in gas turbines. AGARD SMP, CP356, 11/1-11/35 (1983).
49. J.-M. Veys and R. Mévrel, Influence of protective coatings on the mechanical properties of CMSX-2 and Cotac 784, *Mat. Sci. Engng* 88(1988) 253-260.
50. J.P. Coad, D.S. Rickerby and B.C. Oberlander, The use of titanium nitride as a diffusion barrier for MCrAlY coatings. *Mater. Sci. Engng.* 74(1) (1985), 93-103.
51. M. Kaufman, Examination of the influence of coatings of thin superalloy sections, NASA CR 1215(1972).
52. J.-M. Veys and R. Mévrel, Creep and high cycle fatigue properties of coated CMSX-2, in *Advanced Materials and Processing Techniques for Structural Applications*, ASM Technical Conference (Paris 7-9 sept. 1987).
53. M.I. Wood and J.E. Restall, The mechanical properties of coated nickel based superalloy single crystals, in *High Temperature Alloys for Gas Turbines and other Applications* (Liège 1986), 1215-1226.
54. M.I. Wood, The role of coatings in the fatigue of superalloy single crystals. *Proc. First ASM Europe Technical Conference on Advanced Materials and Processing Techniques for Structural Applications*. (Paris, 7-9 sept. 1987) (ONERA, 1987) 179-188.
55. T.E. Strangman, PhD thesis (Univ. of Connecticut, 1978).
56. K.R. Bain, The effect of coatings on the thermomechanical fatigue life of a single crystal turbine blade material, AIAA-85-1366 (1985) 1-6.
57. G.A. Swanson, I. Linask, D.M. Nisley, P.P. Norris, T.G. Meyer and K.P. Walker, Life prediction and constitutive models for engine hot section anisotropic materials program. NASA CR 174952 (1986).
58. G.A. Swanson et al., Id., NASA CR 179594 (1987).
59. M.I. Wood, The mechanical properties of coatings and coated systems. *Mat. Sci. Engng.*, to be published.

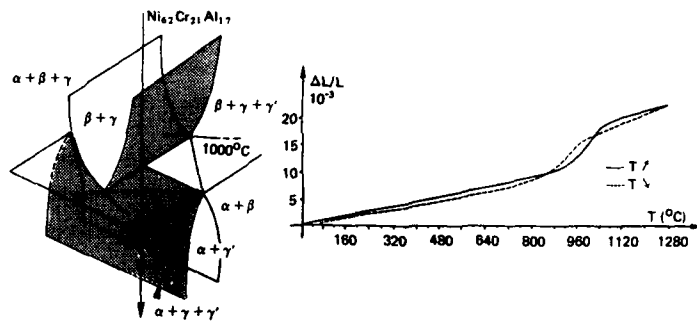


Figure 1 : Partial phase diagram in the Ni-Cr-Al system (a) and thermal expansion data (b) showing the phase transformation at around 1000°C [23].

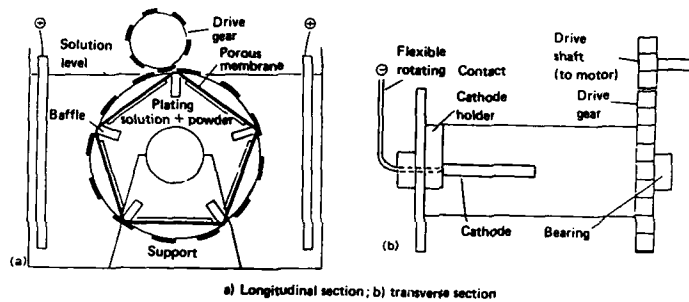


Figure 2 : Schematic diagram of a co-electrodeposition plating unit [9].

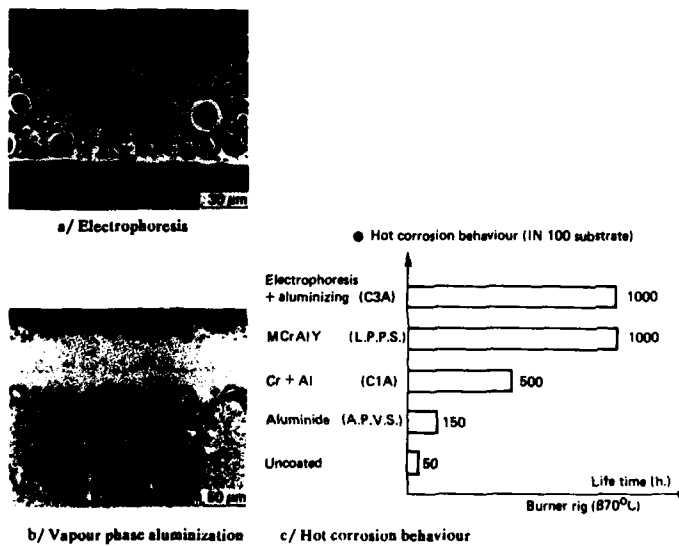


Figure 3 : Cross section of an MCrAlY coating after electrophoresis (a) and subsequent consolidation by vapour phase aluminizing (b). Hot corrosion resistance in burner rig tests, with Na_2SO_4 deposits, at 900°C of various coatings on IN 100 (c) [18].

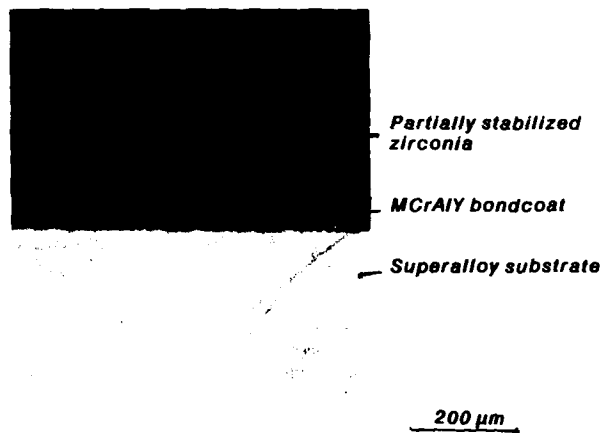


Figure 4 : Typical aspect in cross section of a thermal barrier coating.

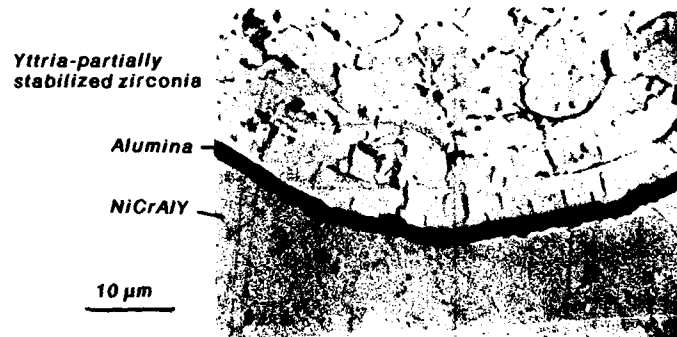


Figure 5 : Alumina layer formed at the zirconia/MCrAlY interface after 100 hours at 1100°C.

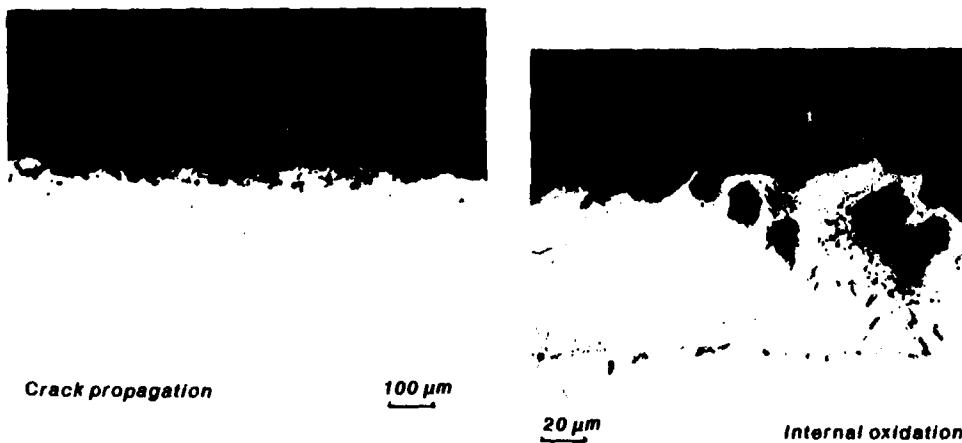


Figure 6 : Typical degradations of a thermal barrier coating : propagation of a main crack parallel to the ceramic/metal interface (a) internal oxidation of bondcoat (b).

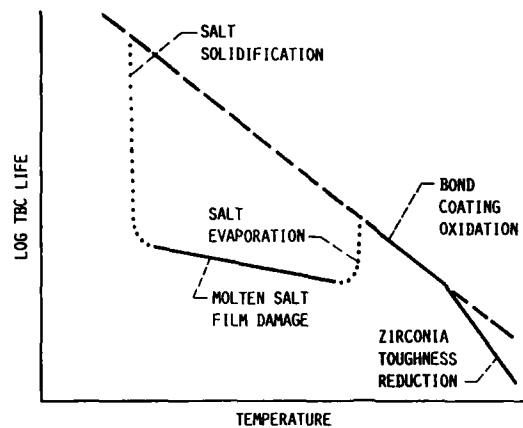


Figure 7 : Schematic representation of thermal barrier coating life as a function of temperature [43, 44]

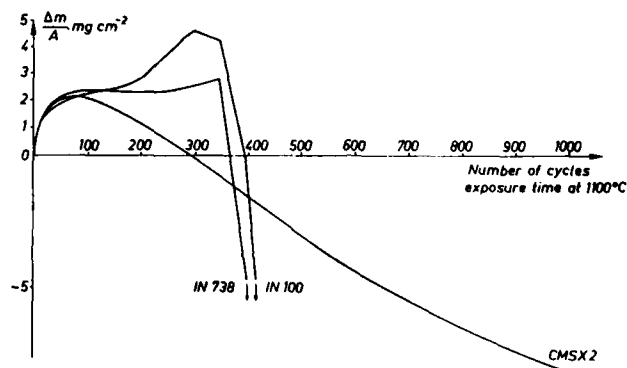


Figure 8 : Cyclic oxidation at 1100°C of a CoCrAlY coating low-pressure-plasma-sprayed on different superalloys [46].

THERMAL SHOCK AND OXIDATION RESISTANCE OF CERAMIC COATINGS

by

J.A.M. Boogers, R.J.H. Wanhill and H.J.C. Hersbach
National Aerospace Laboratory NLR
P.O. Box 153
8300 Ad Emmeloord
Amsterdam
The Netherlands

SUMMARY

Thermal shock and long term oxidation tests on ceramic thermal barrier coatings were done under flight simulation conditions in a burner rig. Three coating combinations were investigated:

- Magnesium stabilised zirconia topcoat with Ni-5 % Al bondcoat
- Magnesium stabilised zirconia topcoat with NiCoCrAlY bondcoat
- Yttrium stabilised zirconia topcoat with NiCoCrAlY bondcoat.

The ZrO_2/Y_2O_3 + NiCoCrAlY combination showed superior resistance to thermal shock and long term oxidation as compared to the ZrO_2/MgO + Ni-5 % Al coating. The long term oxidation resistance of the ZrO_2/MgO + NiCoCrAlY combination was intermediate to that of the other two coatings. Degradation of the coatings was examined in detail, and the practical significance of the results is assessed.

1. INTRODUCTION

There is a continuing effort to increase the operating temperatures of gas turbines in order to improve the efficiency and power output. This means that continued development of high temperature materials, cooling methods and coatings for oxidation and corrosion resistance is necessary.

Ceramic thermal barrier coatings are promising candidates for protecting high temperature components such as combustion chambers, augmentor liners and flame holders. These coatings offer a combination of thermal insulation and high resistance to oxidation and corrosion, thereby enabling better performance and longer service lives. Many ceramics have been investigated, with zirconia (ZrO_2) being given the most attention. However, zirconia undergoes a phase transformation in the turbine temperature regime and the accompanying volume change causes cracking and spalling during thermal cycling. The zirconia therefore must be stabilised. This has led to development of the coating systems ZrO_2 + 18-24 weight % MgO (magnesium stabilised zirconia) and ZrO_2 + 6-8 weight % Y_2O_3 (yttrium stabilised zirconia). These systems represent a good compromise between low thermal conductivity and acceptable thermal expansion mismatch with the metallic substrate [1].

Thermal barrier coatings (TBCs) are commonly applied as two-layer systems consisting of a ceramic topcoat deposited over a metallic bondcoat. As its name implies, the bondcoat provides good adhesion at the interfaces with the ceramic topcoat and metallic substrate. Also the bondcoat has better corrosion resistance than the substrate. Many investigations have shown the potential of TBCs, but it is also clear that their performance depends on component geometry and loads and the environmental conditions.

The F100 engine in service with the Royal Netherlands Air Force (RNLAF) uses a TBC for the combustion chamber and augmentor liner. The TBC is a magnesium stabilised zirconia topcoat with a Ni-5 % Al bondcoat. In service the coating has limited life owing to spalling, and improvements are necessary. Thus an investigation to compare the thermal shock and long term oxidation resistances of the currently used TBC and two possible alternatives has been carried out by the NLR. The alternative TBCs are a magnesium stabilised zirconia topcoat with a NiCoCrAlY bondcoat, and an yttrium stabilised zirconia topcoat with a NiCoCrAlY bondcoat.

2. THE TEST PROGRAMME

An overview of the test programme is given in table 1. Details of the test specimens, the burner rig and testing conditions are given in the following subsections 2.1 - 2.3.

2.1 Specimens

Cylindrical tube specimens with the dimensions shown in table 1 were used for thermal shock tests. The specimens were fabricated by roll-up and welding of Hastelloy X and HS 188 superalloy sheets. The sheet thickness for both materials was 1.2 mm. Chemical compositions of the alloys are given in table 2: these are compared with nominal values [2].

The thermal barrier coatings were applied by air plasma spraying at the RNLAF Jet Engine Depot (DSM Woensdrecht). The intended nominal coating thicknesses were 0.1 mm for the bondcoats and 0.2 mm for the topcoats. These are the specified thicknesses for the F100 combustion chamber and augmentor liner. Actual thicknesses and the chemical compositions of the TBCs are given in table 3. Excepting the ZrO_2/Y_2O_3 topcoat, the coating thicknesses met the nominal specification. The ZrO_2/Y_2O_3 topcoat was consistently thinner than specified. Also the yttrium content of the NiCoCrAlY bondcoats was lower than the nominal specification of 0.5 weight %.

Examples of coated specimens are shown in figure 1. Before testing all specimens were visually inspected for coating deficiencies. None were found. Also the specimens cross-sectioned for coating thickness measurements showed normal structures and porosities, figure 2.

2.2 Burner Rig

The TBCs were tested with a BECON burner rig installed at the NLR. The basic unit of this rig is a laboratory combustor whose operating characteristics closely approximate those of actual gas turbine combustion chambers. A schematic of the BECON rig combustor is given in figure 3. The combustor consists of two sections with independent air systems and an instrumentation ring:

- (1) Primary section:
This is an annular diffuser and a burner liner. Fuel is injected via a pressure-atomising nozzle and homogeneous combustion is achieved by a strong swirl-stabilised recirculation zone.
- (2) Secondary section:
Hot combustion gases are cooled by dilution with air from secondary jets.
- (3) Instrumentation ring:
This is air cooled and enables control of the ignitor, a flame monitor and access ports for injection of pollutants (SO_2 , NaCl , etc.) and erosive particles, if required.

A technical specification for the BECON rig is listed in table 4.

2.3 Test Conditions

The specimens were mounted in batches of 8 in a rotating holder downstream to the burner rig exhaust nozzle. In each batch one specimen was a fully representative "dummy" containing thermocouples brazed into the metallic substrate and the substrate/bondcoat interface. A slip-ring system was used to enable thermocouple measurements to be recorded. The specimens and holder could be moved from the hot gas into a cold air stream to simulate thermal shocks. Also the high temperature testing could be done under flight-by-flight conditions. Movement of the specimens and holder, and all the burner rig operating conditions, were programmed and controlled by a microprocessor.

The thermal shock tests were done using the temperature-time profiles shown in figure 4. The test history consisted of repeated sequences of 30 rapid thermal cycles between 450 °C and 1100 °C plus a 30 minute hold at 940 °C.

The long term oxidation tests were done using the temperature-time profiles shown in figure 5. The test history consisted of repeated 60 minute sequences involving rapid heating (120s) and cooling (60s) between 100 °C and 1050 °C at the beginning and end of each sequence.

For both types of test the burner rig used JP-4 jet fuel. No pollutants or erosive particles were added to the hot gas stream. It should be noted that the temperature-time profiles in figures 4 and 5 are idealised. In practice reasonable approximations were achieved, for example figure 6.

3. RESULTS

A summary of the applied thermal shock and long term oxidation test sequences is given in table 5. As expected, the thermal shock tests were of relatively short duration. The numbers of thermal cycles varied considerably because the specimens were regularly inspected, and serious spalling or lifting of the coating resulted in prompt removal from testing.

3.1 Macroscopic Examination

Visual inspection of the specimens during and after testing led to the qualitative classification of coating damage shown in figure 7. These results indicate the following:

- (1) The $\text{ZrO}_2/\text{Y}_2\text{O}_3 + \text{NiCoCrAlY}$ combination possessed superior resistance to thermal shock and long term oxidation as compared to the $\text{ZrO}_2/\text{MgO} + \text{Ni-5 \% Al}$ coating.
- (2) The long term oxidation resistance of the $\text{ZrO}_2/\text{MgO} + \text{NiCoCrAlY}$ combination was intermediate to that of the other two coatings.
- (3) The choice of substrate apparently influenced the thermal shock resistance. Progressive damage of each TBC combination tended to occur later in coatings on HS 188.

Representative examples of the macroscopic appearances after testing are given in figure 8. The superior resistance of the $\text{ZrO}_2/\text{Y}_2\text{O}_3 + \text{NiCoCrAlY}$ coating to spalling is evident.

3.2 Optical Metallography

Metallographic cross-sections of the specimens were made after testing. A qualitative classification of the observed coating and substrate damage is shown in figure 9, and representative micrographs are illustrated in figure 10. The results are discussed in detail in the following sections 3.2.1 - 3.2.4.

3.2.1 Thermal Shock, 496 Cycles

Specimens coated with $\text{ZrO}_2/\text{Y}_2\text{O}_3 + \text{NiCoCrAlY}$ were undamaged except for slight oxidation of the bondcoat. Specimens coated with $\text{ZrO}_2/\text{MgO} + \text{Ni-5 \% Al}$ showed cracks in the topcoat, the bondcoat/topcoat interface and the bondcoat. Also, the bondcoat was severely oxidised, and slight oxidation of the Hastelloy X substrate had occurred.

3.2.2 Thermal Shock, 1240 Cycles

Specimens coated with $ZrO_2/Y_2O_3 + NiCoCrAlY$ showed cracks in the topcoat and slight oxidation of the bondcoat. The non-spalled areas on HS 188 specimens coated with $ZrO_2/MgO + Ni-5\% Al$ showed progressive deterioration as compared to 496 cycles, see figure 10. However, the substrate had not oxidised.

3.2.3 Long Term Oxidation, 100 Cycles

Specimens coated with $ZrO_2/Y_2O_3 + NiCoCrAlY$ and $ZrO_2/MgO + NiCoCrAlY$ showed cracks in the topcoat and slight oxidation of the bondcoat and substrate. Specimens coated with $ZrO_2/MgO + Ni-5\% Al$ showed cracks in the topcoat, the bondcoat/topcoat interface and the bondcoat. The bondcoat was severely oxidised and slight oxidation of the substrate had occurred.

3.2.4 Long Term Oxidation, 200 Cycles

Specimens coated with $ZrO_2/Y_2O_3 + NiCoCrAlY$ showed cracks only in the topcoat and moderate oxidation of the bondcoat and substrate. Specimens coated with $ZrO_2/MgO + NiCoCrAlY$ showed cracks in the topcoat and the bondcoat/topcoat interface. The bondcoat and substrate were moderately oxidised.

3.3 Scanning Electron Metallography and Analysis

Metallographic cross-sections of untested and tested specimens were investigated by SEM and EDX analysis. Elemental X-ray density maps showed that changes in coating and substrate composition were qualitatively similar for the thermal shock and long term oxidation tests. The choice of substrate did not affect the composition changes in the thermal shock tests. Hence only a selection of the results will be illustrated. Elemental X-ray maps and video images of the untested and tested TBCs are presented in figures 11 - 13. These figures show:

- (1) Testing the $ZrO_2/MgO + Ni-5\% Al$ combination, figure 11, resulted in
 - Cr diffusion from the substrate to the substrate/bondcoat interface
 - Ni diffusion from the bondcoat to the substrate
 - increased O content of the bondcoat, especially at the substrate/bondcoat interface. This change is clearly associated with Cr enrichment at the substrate/bondcoat interface.
- (2) Testing the $ZrO_2/MgO + NiCoCrAlY$ and $ZrO_2/Y_2O_3 + NiCoCrAlY$ combinations, figures 12 and 13, resulted in
 - Cr enrichment of the bondcoat, especially at the substrate/bondcoat and bondcoat/topcoat interfaces
 - Ni diffusion from the bondcoat to the substrate
 - increased O content of the bondcoat. This change is associated with Cr enrichment of the bondcoat.

Concentration changes of other elements were too small to give useful information. However, it is evident from the results that there are broad similarities in the compositional changes arising from both thermal shock and long term oxidation testing.

4. DISCUSSION

4.1 Overview of Coating Performances and Rankings

The TBCs were tested under flight simulation whereby the temperature exceeded 1000 °C only for short times, figures 4 - 6. This is an important consideration because it is generally agreed that magnesium stabilised zirconia is not suitable for long term service exposure above about 1000 °C [1].

On the foregoing basis we conclude that the present test programme demonstrates the superiority of the $ZrO_2/Y_2O_3 + NiCoCrAlY$ combination for service use. This coating was significantly better in its resistance to spalling, which is the main life-limiting problem for the currently used $ZrO_2/MgO + Ni-5\% Al$ combination. However, it is worth noting that metallography of non-spalled areas in the long term oxidation tests, figures 9 and 10, shows little difference between the TBCs with respect to substrate protection. This serves to indicate the importance of high temperature hold times as well as thermal cycling in service [1].

4.2 Coating Degradation and Failure

The most important degradation and failure mechanisms of TBCs are [1,3-5]:

- (1) Topcoat spalling owing to thermal expansion mismatch and destabilisation during thermal cycling.
- (2) Bondcoat oxidation or hot corrosion.
- (3) Reactions with pollutants.
- (4) Erosion-microspalling due to impingement of particles and hot gas.

In the present work the principal degradation and failure mechanisms were most probably limited to topcoat spalling (thermal expansion mismatch) and bondcoat oxidation. Topcoat microspalling occurred in the long term oxidation tests. This was visible as surface roughening, as noted in figure 7.

In more detail figure 14 shows the observed degradation and failure mechanisms according to test type and duration. There are similarities but also distinct differences. The main differences relate to bondcoat cracking and substrate oxidation. Bondcoat cracks occurred late in the thermal shock tests and not at all in the long term oxidation tests. On the other hand, substrate oxidation began relatively early in the long term oxidation tests. Thus TBC protection of the substrate is clearly time-related, as already indicated in section 4.1.

In view of the similar degradation and failure mechanisms of the TBCs tested in the present investigation, we conclude that the choice of bondcoat was crucial. Early failure of the $ZrO_2/MgO + Ni-5\% Al$ combination can be attributed to bondcoat oxidation, whereby the concomitant volume expansion causes stresses leading to topcoat spalling [1].

The elemental X-ray density maps, figures 11 - 13, show that the $Ni-5\% Al$ bondcoat is a relatively poor barrier to oxidation. This is because it contains no chromium, and oxygen has a strong affinity for chromium, which is present in the substrates and also diffuses to the substrate/bondcoat interface. The $NiCoCrAlY$ bondcoat distributes oxygen somewhat more homogeneously, but there is still a concentration of oxygen and chromium at the substrate/bondcoat interface, and also at the bondcoat/topcoat interface.

By itself the concentration of chromium and oxygen - forming Cr_2O_3 - is beneficial to both oxidation and thermal shock resistance [4]. However, in keeping with the policy of increasing the times between overhaul and maintenance it may be worthwhile investigating three-layer TBCs. These have an additional metallic or graded metallic/ceramic layer between the bondcoat and topcoat in order to reduce inward diffusion of oxygen and to assist in accommodating thermal expansion mismatch [1].

5. CONCLUSIONS AND RECOMMENDATIONS

An investigation of the thermal shock and long term oxidation resistances of three ceramic thermal barrier coatings under flight simulation conditions in a burner rig showed that

- (1) The $ZrO_2/Y_2O_3 + NiCoCrAlY$ combination possessed superior resistance to thermal shock and long term oxidation as compared to the $ZrO_2/MgO + Ni-5\% Al$ coating.
- (2) The long term oxidation resistance of the $ZrO_2/MgO + NiCoCrAlY$ combination was intermediate to that of the other two coatings.
- (3) The choice of bondcoat is most important. Early failure of the $ZrO_2/MgO + Ni-5\% Al$ combination can be attributed to bondcoat oxidation leading to topcoat spalling.
- (4) Intact coatings did not differ much in their ability to protect the metallic substrate against oxidation. This is because neither the topcoats [1] nor bondcoats are strong barriers to oxygen diffusion.
- (5) Substrate oxidation is strongly time-dependent. This means that high temperature hold times, as well as thermal cycling, are important to coating performance.

In view of these conclusions we recommend to

- (6) Replace the currently used $ZrO_2/MgO + Ni-5\% Al$ combination with the $ZrO_2/Y_2O_3 + NiCoCrAlY$ coating for the F100 combustion chamber and augmentor liner. This requires evaluation of the plasma spraying conditions to ensure that the ZrO_2/Y_2O_3 topcoat thickness meets the specification.
- (7) Investigate the potential usefulness of three-layer thermal barrier coatings, which should provide improved protection of the metallic substrates against oxidation.

6. ACKNOWLEDGEMENTS

This work was sponsored by the Royal Netherlands Air Force (RNLAf). The technical assistance of P.J. Tromp, H.N. Huisman, T. Hattenberg and R.M. Vermeulen is gratefully acknowledged.

7. REFERENCES

1. R. Bürgel and I. Kvernes, "Thermal barrier coatings", High Temperature Alloys for Gas Turbines and Other Applications 1986, Part 1, D. Reidel Publishing Company, pp. 327-356, 1986: Dordrecht, The Netherlands.
2. C.T. Sims, and W.C. Hagel (Editors), The Superalloys, John Wiley and Sons, pp. 598-599, 1972: New York.
3. P. Hancock, "Degradation processes for ceramic coatings", Advanced Materials Research and Developments for Transport, Symposium IX: Ceramic Coatings for Heat Engines, Les Editions de Physique, pp. 163-179, 1985, Les Ulis, France.
4. H. Herman and N.R. Shankar, "Survivability of thermal barrier coatings", Materials Science and Engineering, Vol. 88, pp. 69-74, 1987.
5. H. Takada, K. Shimotori, H. Baba, T. Suzuki, K. Takahara and T. Yoshida, "Performance of thermal barrier coating for gas turbine airfoil in engine test", Proceedings of the International Gas Turbine Congress, Gas Turbine Society of Japan, pp. 737-741, 1983: Tokyo.

TABLE 1 Test programme overview

- TBC COMBINATIONS : (1) $\text{ZrO}_2/\text{MgO} + \text{Ni-5 \% Al}$
(2) $\text{ZrO}_2/\text{MgO} + \text{NiCoCrAlY}$
(3) $\text{ZrO}_2/\text{Y}_2\text{O}_3 + \text{NiCoCrAlY}$
- METALLIC SUBSTRATES : (1) Hastelloy X nickel-base superalloy
(2) Haynes alloy HS 188 cobalt-base superalloy
- SPECIMENS : (1) Cylindrical tube
(2) Flat strip
- TYPES OF TEST : (1) Thermal shock
(2) Long term oxidation
- TESTING CONDITIONS : Burner rig flight-by-flight simulation

TEST MATRIX

TYPES OF TEST	TBC COMBINATIONS	SUBSTRATES	SPECIMEN CONFIGURATIONS*
THERMAL SHOCK	$\text{ZrO}_2/\text{MgO} + \text{Ni-5 \% Al}$ $\text{ZrO}_2/\text{Y}_2\text{O}_3 + \text{NiCoCrAlY}$	Hastelloy X	
	$\text{ZrO}_2/\text{MgO} + \text{Ni-5 \% Al}$ $\text{ZrO}_2/\text{Y}_2\text{O}_3 + \text{NiCoCrAlY}$	HS 188	
LONG TERM OXIDATION	$\text{ZrO}_2/\text{MgO} + \text{Ni-5 \% Al}$ $\text{ZrO}_2/\text{MgO} + \text{NiCoCrAlY}$ $\text{ZrO}_2/\text{Y}_2\text{O}_3 + \text{NiCoCrAlY}$	HS 188	

* All dimensions in mm

TABLE 2 Chemical compositions of the metallic substrates (weight %)

SUBSTRATES		Ni	Cr	Co	Mo	W	Fe	Mn	Si	C	La
Hastelloy X	NOMINAL [2]	47.3	22.0	1.5	9.0	0.6	18.5	0.5	0.5	0.1	-
	EDX ANALYSIS	47.8	21.8	1.8	8.6	0.4	18.6	0.5	0.5	-	-
HS 188	NOMINAL [2]	22.0	22.0	39.2	-	14.0	1.5	0.75	0.4	0.1	0.08
	EDX ANALYSIS	22.0	22.5	37.2	-	16.2	1.4	0.71	0.0	-	-

TABLE 3 Chemical compositions (weight %) and thicknesses of the thermal barrier coatings

TBC COMBINATIONS	COMPOSITIONS (EDX ANALYSIS)									COATING THICKNESS (μm)	
	BOND COAT					TOP COAT				BOND COAT	TOP COAT
	Ni	Co	Cr	Al	Y	MgO	Y_2O_3	ZrO_2			
$\text{ZrO}_2/\text{MgO} + \text{Ni-5 \% Al}$	95.5	-	-	4.5	-	17.5	-	82.5		40 - 100	170 - 250
$\text{ZrO}_2/\text{MgO} + \text{NiCoCrAlY}$	73.1	2.7	19.1	5.0	0.1	17.5	-	82.5		70 - 90	200 - 250
$\text{ZrO}_2/\text{Y}_2\text{O}_3 + \text{NiCoCrAlY}$	70.8	2.9	18.9	7.2	0.2	-	8.2	91.8		50 - 100	50 - 130

TABLE 4 Beacon burner rig technical specifications

● COMPRESSOR	: 127 kW
● MASS FLOW	
● Hot section at 1000 °C	: ± 0.4 kg/s
● Cold section	: ± 0.8 kg/s
● TOTAL AIR PRESSURE	: 1.45 bar
● MACH NUMBER	: 0.2 - 0.7
● GAS TEMPERATURE	: 500 °C - 1650 °C
● SPECIMEN TEMPERATURE VARIATION AT 1000 °C	: ± 5 °C
● PRESSURE VARIATION ACROSS NOZZLE	: ± 0.5 %
● RESPONSE TIME 1000 °C - 300 °C	: 10s
● SPECIMEN TEST AREA	: 50 mm diameter
● POLLUTANT INJECTION	: SO ₂ , NaCl, etc; erosive particles

TABLE 5 Applied test sequences

TYPES OF TEST	TBC COMBINATIONS	SUBSTRATES	SPECIMEN CODES	NUMBER OF LOW-HIGH-LOW THERMAL CYCLES	TEST DURATIONS (HOURS)
THERMAL SHOCK	ZrO ₂ /MgO + Ni-5 % Al	Hastelloy X	HX 1	496	16
			HX 2	496	16
			HX 3	248	8
			HX 4	744	24
	ZrO ₂ /Y ₂ O ₃ + NiCoCrAlY	Hastelloy X	HX 5	1736	56
			HX 6	496	16
			HX 7	1240	40
			HX 8	496	16
LONG TERM OXIDATION	ZrO ₂ /MgO + Ni-5 % Al	HS 188	HS 9	496	16
			HS 10	1240	40
			HS 11	1240	40
			HS 12	992	32
	ZrO ₂ /Y ₂ O ₃ + NiCoCrAlY	HS 188	HS 13	744	24
			HS 14	496	16
			HS 15	992	32
			HS 16	1240	40
	ZrO ₂ /MgO + Ni-5 % Al	HS 188	1	100	100
			2	100	100
			3	100	100
			4	100	100
	ZrO ₂ /MgO + NiCoCrAlY	HS 188	11	100	100
			12	200	200
			13	100	100
	ZrO ₂ /Y ₂ O ₃ + NiCoCrAlY	HS 188	6	200	200
			7	100	100
			8	100	100
			10	200	200

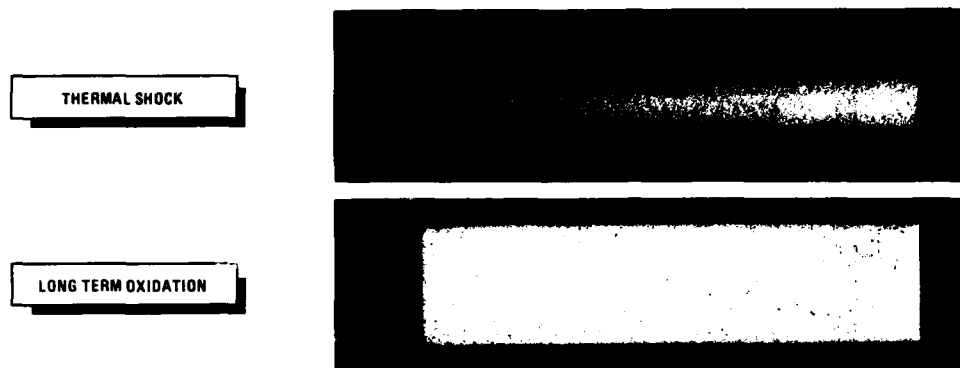


Fig. 1 Examples of TBC coated specimens before testing

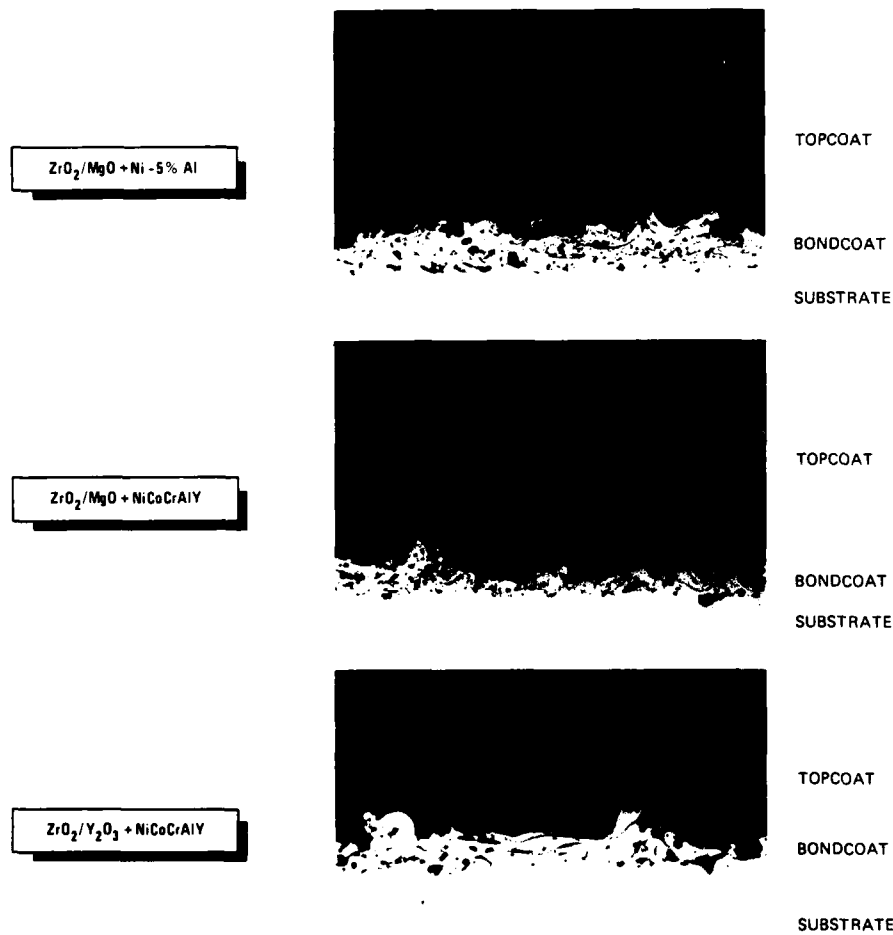


Fig. 2 Cross-sections of the TBCs before testing (X100)

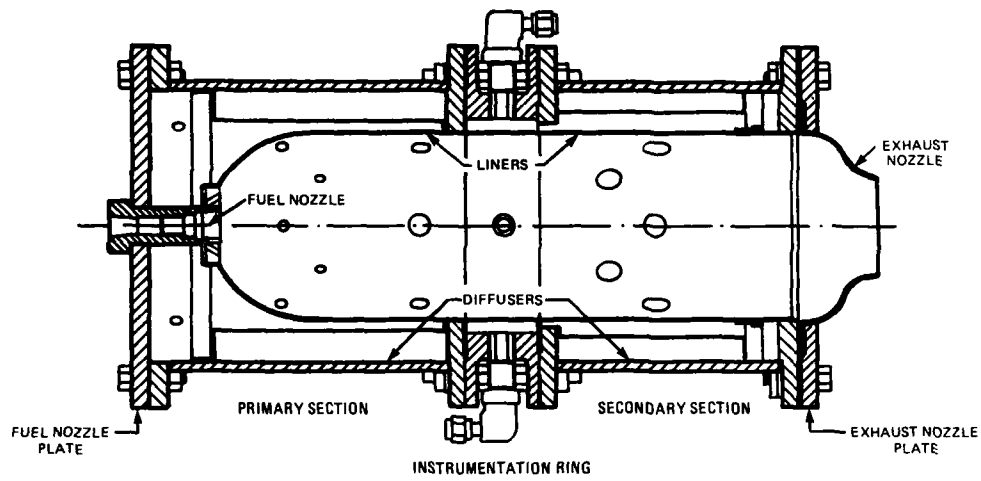


Fig. 3 Schematic of the BECON rig combustor

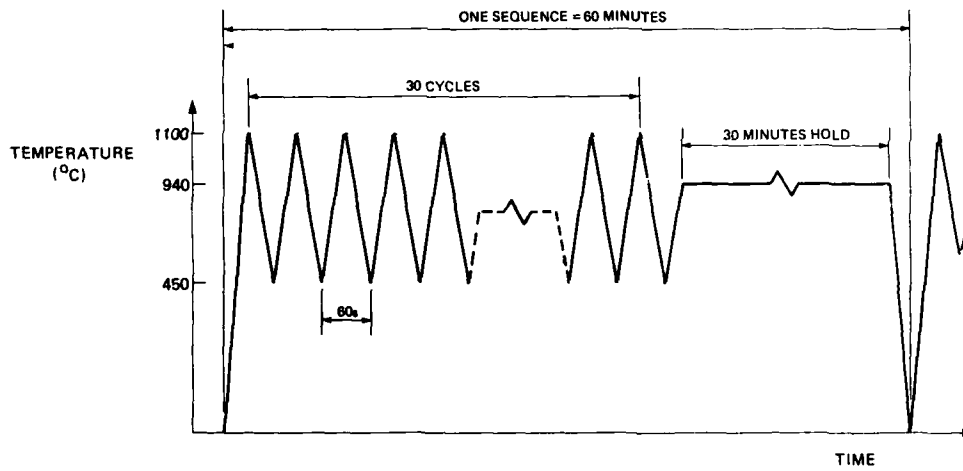


Fig. 4 Temperature - time sequence for thermal shock tests (schematic)

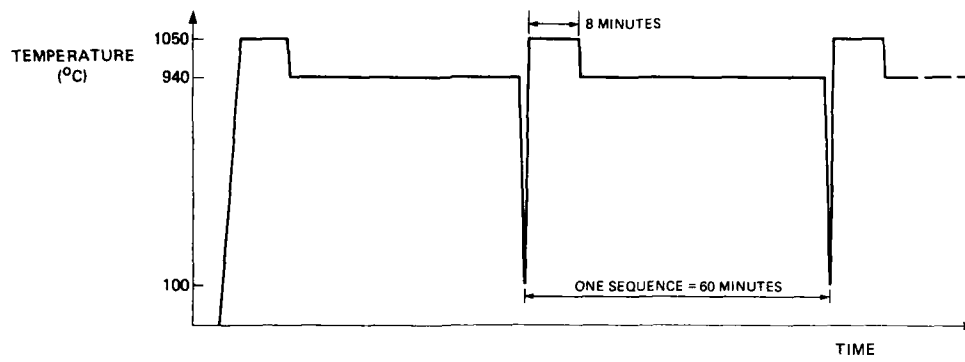


Fig. 5 Temperature - time sequences for long term oxidation tests (schematic)

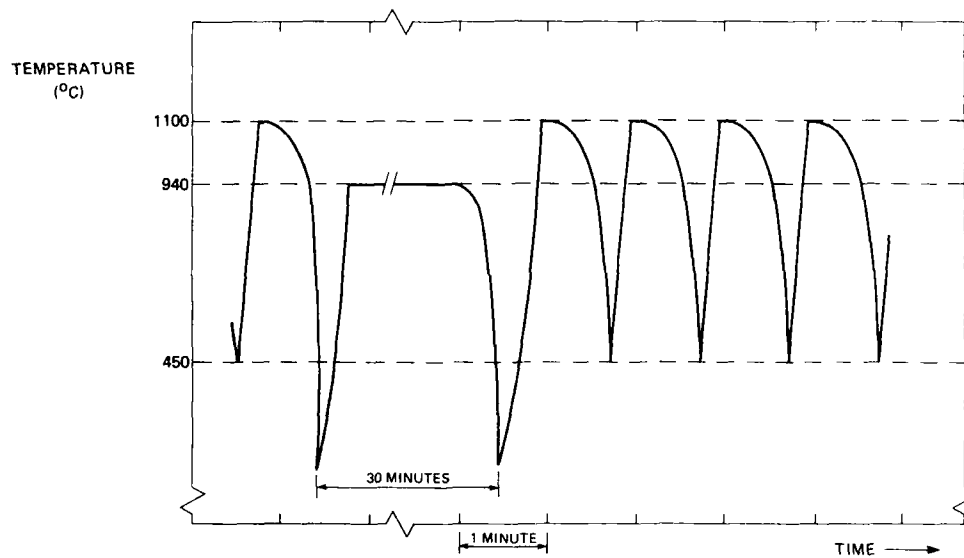


Fig. 6 Measured temperature - time profiles for part of a thermal shock test

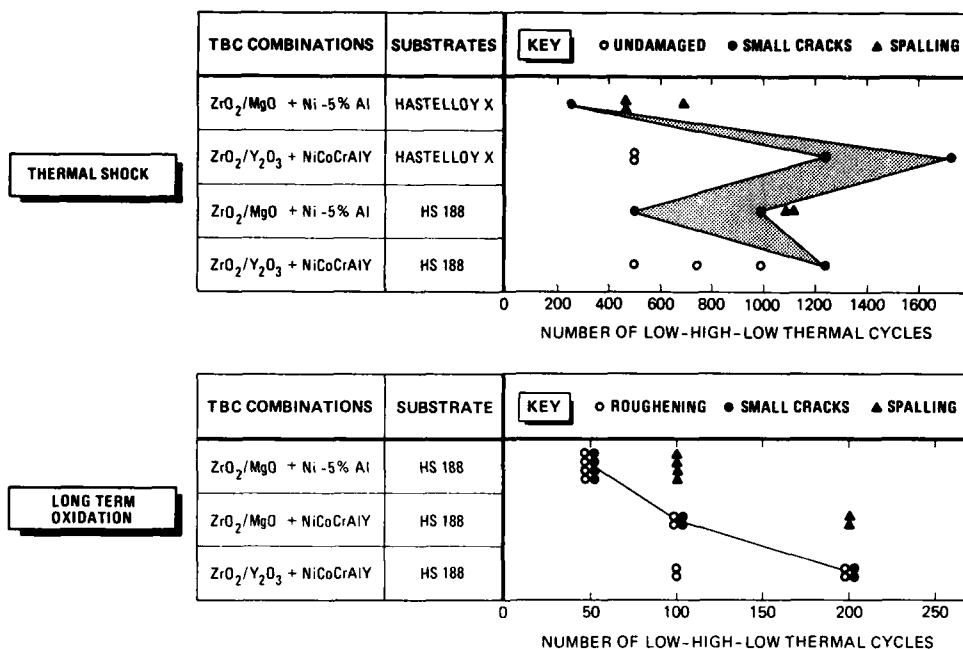


Fig. 7 Macroscopic assessment of TBC damage

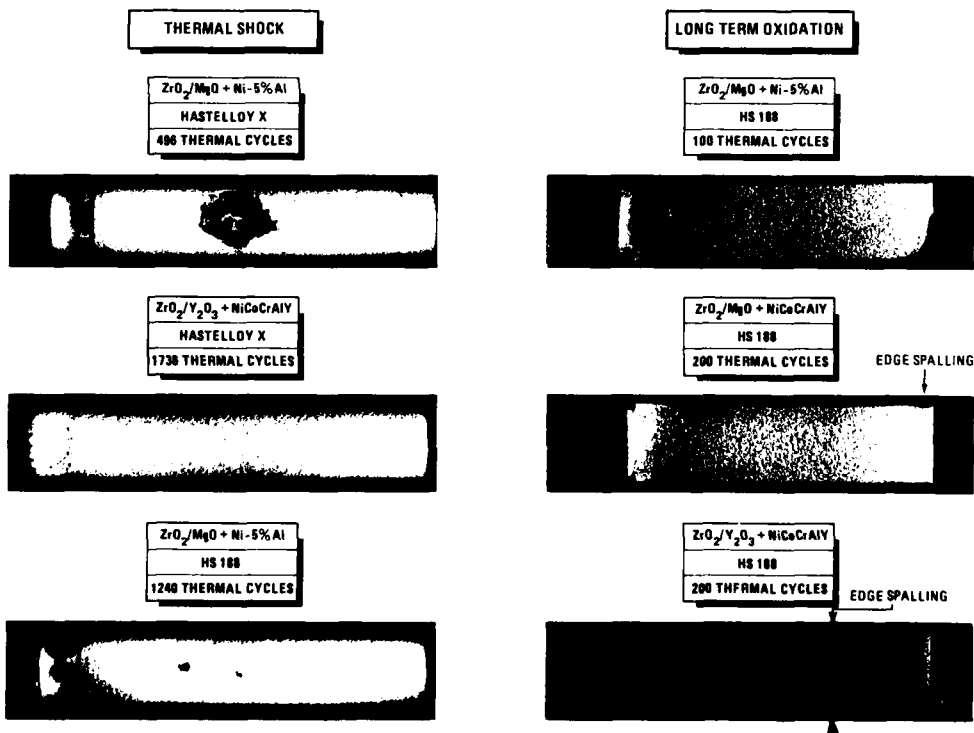


Fig. 8 Representative examples of the macroscopic appearances of TBCs after testing

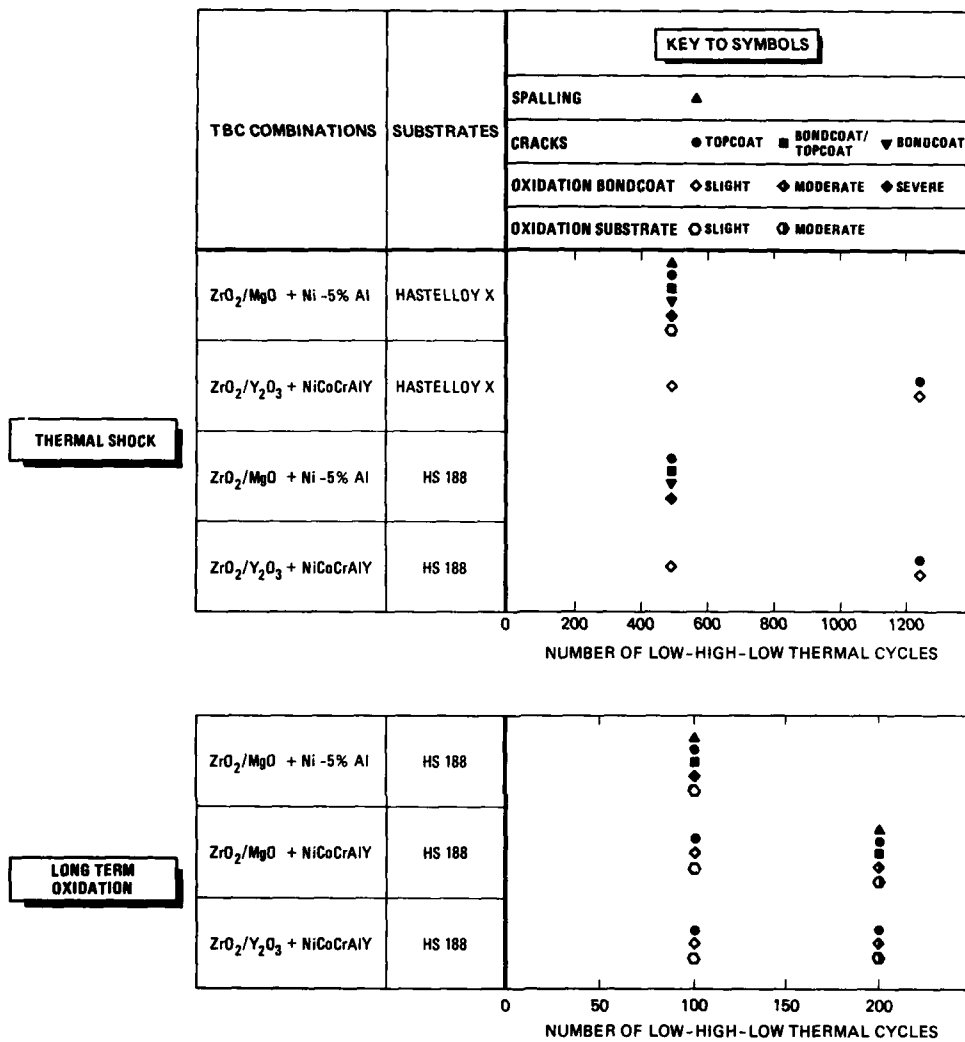


Fig. 9 Optical metallographic assessment of TBC damage

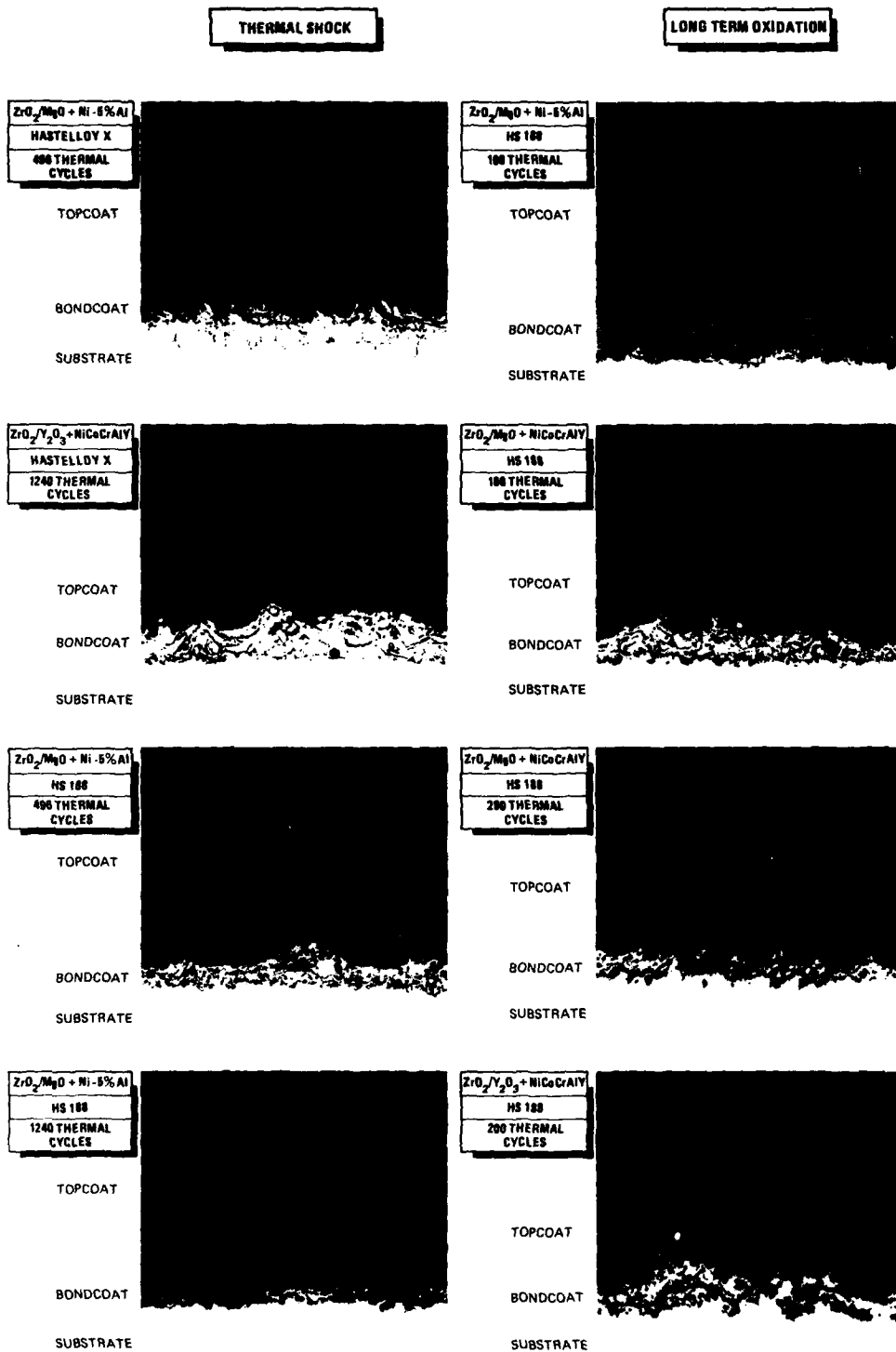
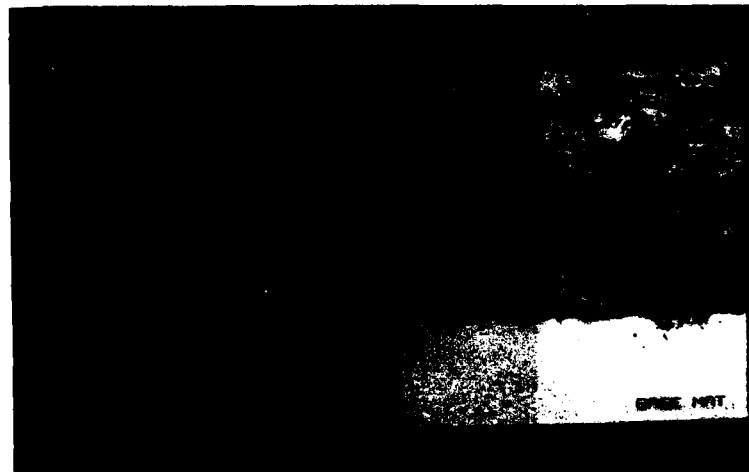


Fig. 10 Representative examples of metallographic cross-section of TBCs after testing (x 100)

$\text{ZrO}_2/\text{MgO} + \text{Ni} - 5\% \text{ Al}$
HS 100
UNTESTED



$\text{ZrO}_2/\text{MgO} + \text{Ni} - 5\% \text{ Al}$
HS 100
THERMAL SHOCK 1240 CYCLES



$\text{ZrO}_2/\text{MgO} + \text{Ni} - 5\% \text{ Al}$
HS 100
LONG TERM OXIDATION 100 CYCLES

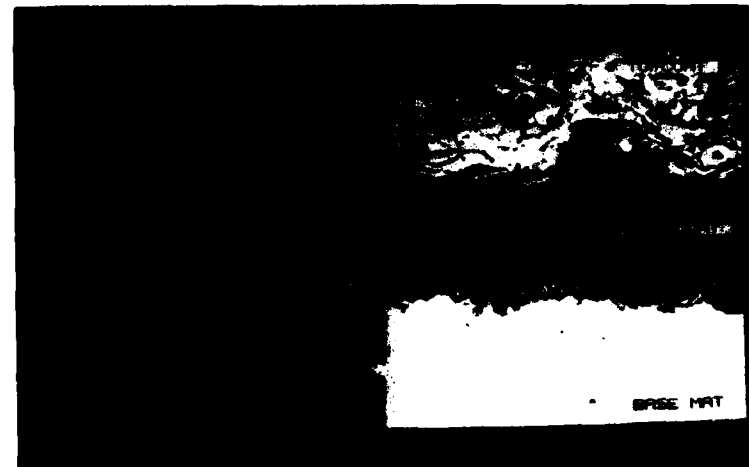


Fig. 11 Elemental X-ray maps and video images of untested and tested $\text{ZrO}_2/\text{MgO} + \text{Ni} - 5\% \text{ Al}$ thermal barrier coating

$\text{ZrO}_2/\text{MgO} + \text{NiCoCrAlY}$
HS 188
UNTESTED

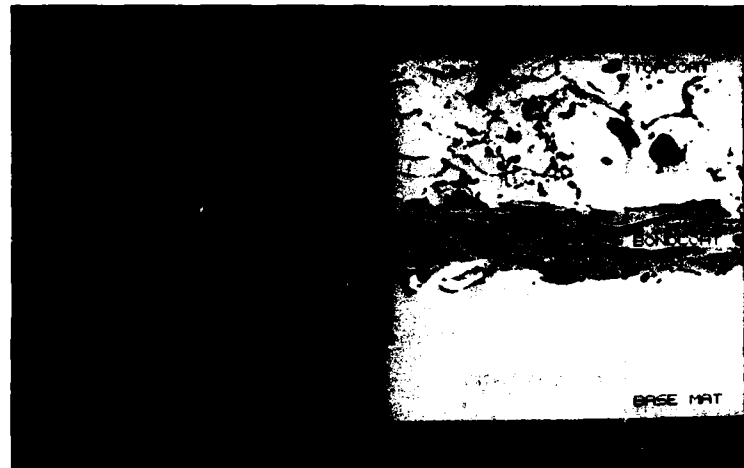


$\text{ZrO}_2/\text{MgO} + \text{NiCoCrAlY}$
HS 188
LONG TERM OXIDATION 200 CYCLES

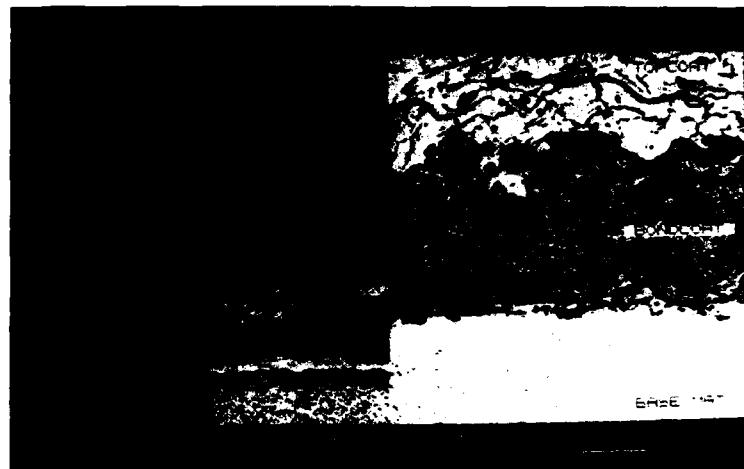


Fig. 12 Elemental X-ray maps and video images of untested and tested $\text{ZrO}_2/\text{MgO} + \text{NiCoCrAlY}$ thermal barrier coating

$\text{ZrO}_2/\text{Y}_2\text{O}_3 + \text{NiCoCrAlY}$
HS 188
UNTESTED



$\text{ZrO}_2/\text{Y}_2\text{O}_3 + \text{NiCoCrAlY}$
HS 188
THERMAL SHOCK 1240 CYCLES



$\text{ZrO}_2/\text{Y}_2\text{O}_3 + \text{NiCoCrAlY}$
HS 188
LONG TERM OXIDATION 200 CYCLES

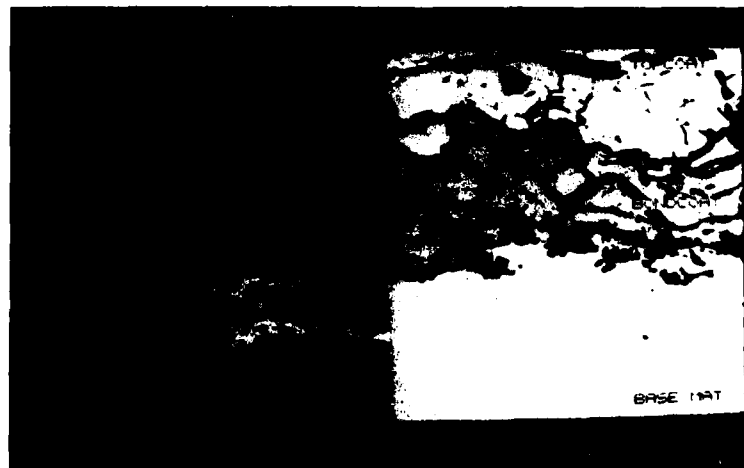


Fig. 13 Elemental X-ray maps and video images of untested and tested $\text{ZrO}_2/\text{Y}_2\text{O}_3 + \text{NiCoCrAlY}$ thermal barrier coating

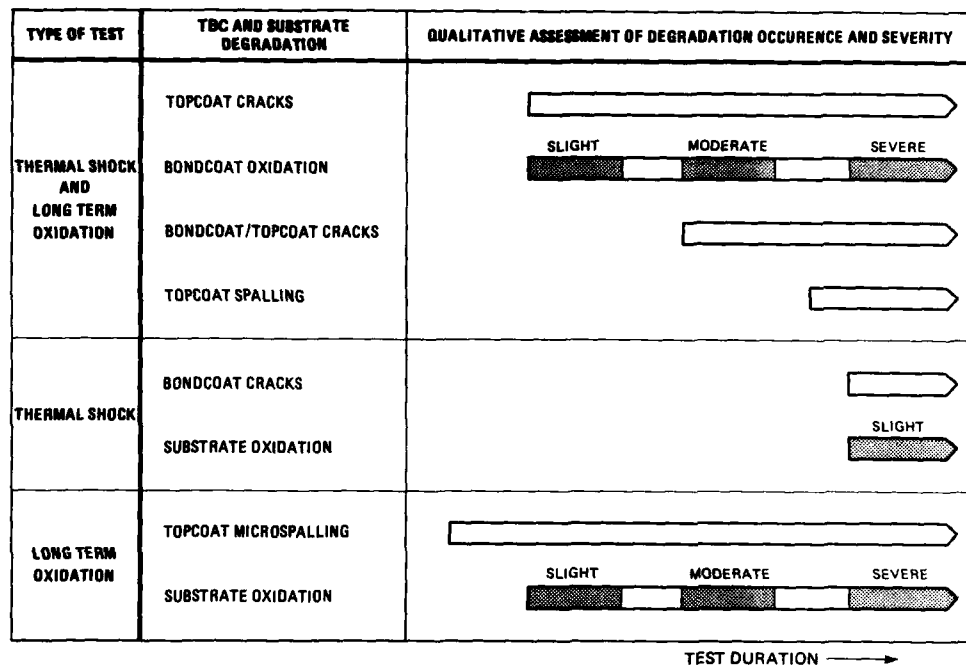


Fig. 14 Schematic of TBC and substrate degradation mechanisms according to test type and duration

EVALUATION OF HIGH TEMPERATURE PROTECTIVE COATINGS FOR GAS TURBINE ENGINES UNDER SIMULATED SERVICE CONDITIONS

A.K. Gupta*, T. Terada*, P.C. Patnaik** and J.-P. Immrigeon*

*National Aeronautical Establishment
National Research Council Canada
Ottawa, Ontario, Canada, K1A 0R6

**Orinda Division, Hawker Siddeley Canada Ltd.
Toronto, Ontario, Canada, L5P 1B3

SUMMARY:

The surface degradation of turbine hot section components, due to oxidation, hot corrosion, erosion and thermal fatigue, is discussed. The mechanisms of each mode of attack are summarized and the state-of-the-art in protective coatings for gas path components is reviewed. Durability evaluations of coatings under simulated service conditions are discussed, including evaluations conducted in high velocity burner rigs. Inconsistencies in the ranking of coatings in rigs is attributed to laboratory-to-laboratory variations in test procedures and/or test conditions. Finally, the important parameters for durability testing in rigs are discussed in terms of the environmental and operational factors that control hot gas chemistry and the extent of surface damage of hot parts. A description of commonly used burner rigs and test procedures employed is also provided to complete the paper.

1.0 INTRODUCTION

Performance of the gas turbine engine has increased considerably in terms of thrust to weight ratio, fuel consumption and reliability ever since the first experimental Whittle engine was built in the late thirties. This progress was achieved by approximately doubling the turbine inlet entry temperature to ~1775 K, and was made possible by the introduction of materials capable of withstanding increasingly higher inlet temperatures and by the introduction of internal cooling technology for hot parts. Austenitic steel turbine blades were first replaced by the stronger Ni-20% Cr alloys and the latter were subsequently replaced by even stronger γ' strengthened Ni based superalloys. Several forms of these alloys such as IN738LC, MM200, DS MM200+HF, DS René 80, PWA 1480, MA6000, René 80 etc. are now in use in gas turbines including cast, wrought and powder processed versions of the alloys.

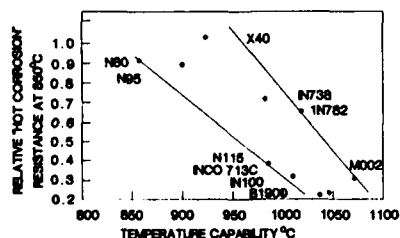


Figure 1: Relationship between hot corrosion resistance and temperature capability of nickel based superalloys. Creep rupture in 100 h, stress level 108 MN/m² (3).

Materials research is still motivated by the demand for materials with improved high temperature capability, creep and fatigue resistance as well as strength coupled with toughness and long term microstructural stability. Traditionally, improvements in these properties for nickel based superalloys have been sought by additional strengthening from the γ' phase. This is achieved by increasing the aluminum and titanium contents while decreasing chromium content (1,2). Although such developments have allowed higher service temperatures, the higher strength alloys are inherently less resistant than their predecessors to environmental attack, including hot corrosion. The reduction in hot corrosion resistance that accompanies increasing temperature capabilities of nickel based superalloys is illustrated in Fig. 1 (3). Such shortcomings have often caused premature rejection of expensive to replace turbine hardware (4). This review is concerned with laboratory evaluations of these high strength alloys and the coatings employed to mitigate surface degradation.

Surface degradation due to oxidation and hot corrosion of nickel based superalloys has already been extensively studied. Both modes of attack are relatively well understood and several reviews have been published on the subject that provide an insight into the reaction mechanisms involved and the role of alloying elements (5-21). Similarly, protective coatings for these materials have been thoroughly investigated in the past although their response to environmental attack is not well understood.

It is shown that modes of service degradation of hot part are many, and that protective coatings are an essential element of hot section material developments if further enhancements in engine efficiency or performance and/or component longevity are to be obtained. It is also shown that coating selection is often complicated by conflicting laboratory results on their relative durabilities and that this complication is due primarily to the absence of standard test methods and procedures employed in evaluating coatings.

Of the numerous laboratory techniques for ranking high temperature materials and coatings in terms of their relative resistance to environmental attack, exposures to simulated service conditions in burner rigs are by far the most powerful ones. However, burner rig tests can be quite complex to perform and interpretation of the results can be quite delicate. This interpretation requires not only a clear understanding of modes of degradation of materials and coatings in turbines, but also of the factors that control the gaseous environment responsible for environmental attack. In this paper, the primary modes of attack responsible for surface degradation are first described. The state-of-the-art in protective coatings is then reviewed. Environmental and operational factors that are believed to influence hot section environment in terms of contaminant chemistries, combustion reactions, formation and deposition of corrosive species and their interactions with hot parts are discussed in detail. Finally state-of-the-art burner rigs are described and current test procedures outlined. Emphasis throughout the paper is placed on hot salt corrosion evaluations since hot corrosion is the most complex mode of degradation that can affect hot section components and the most difficult to simulate in the laboratory.

2.0 MODES OF SERVICE DEGRADATION:

Service-induced damage of hot section components in the gas turbine is a complex problem. The damage can take many forms depending on component type and operating environment. For gas path components, both internal and surface damage may occur. The internal damage is related to microstructural changes which occur slowly in service as a result of long term exposures to high temperatures and stresses. The surface damage is related to oxidation, hot corrosion or erosion, acting singly or in combination, and to thermal fatigue cracking. Both forms of damage can lead to loss of load bearing capacity in blades and vanes and ultimately to component rejection if costly in-service failures are to be avoided. A brief description of the mechanisms associated with each mode of surface degradation is presented below.

2.1 Oxidation:

At high temperatures, elements such as Al, Cr or Si in nickel based superalloys react with oxygen present in combustion gases to form surface oxides. The oxide layers of Al_2O_3 , Cr_2O_3 , and SiO_2 that form provide protection against further oxidation by providing a diffusion barrier between the alloy and the gaseous environment. In practice, a reservoir of the oxide forming elements is supplied by coating components (singly or in combination) with Al, Cr or Si to ensure long term, trouble free, service in the aggressive environment of the turbine hot section. Of the Al_2O_3 , Cr_2O_3 , or SiO_2 scales that form, the first two are known to provide better protection against oxidation. At temperatures in the range of 1175 to 1475 K an Al_2O_3 scale provides better protection than a Cr_2O_3 scale, because of its slower growth rate. Protective properties of a Cr_2O_3 scale are also limited above 1225 K in oxidizing environments due to the formation of volatile CrO_3 . Therefore, above 1225 K, oxidation resistance of an alloy or a coating is generally provided by Al_2O_3 scales. SiO_2 has occasionally been used as a protective oxide scale but transformation of SiO_2 to less durable SiO in reducing atmospheres at higher temperatures greatly limits its application. Also, there is some evidence that SiO_2 can react with other metallic ions to form complex and undesirable oxides (17).

Protective properties of scales are normally reduced with time. Several factors may be responsible for this degradation. Most of these are associated with mechanically, thermally and/or oxide growth induced stresses which can cause cracking of the oxide scales. The degradation of oxide scales can be further enhanced by the presence of water vapour and/or compounds containing chlorides such as NaCl or HCl. For example, Cr_2O_3 transforms to volatile $Cr(OH)_3$ in the presence of water vapour at or above 1225 K and when compounds containing chlorine are present, volatile metal chlorides and oxychlorides can also form (22).

During service, cracked oxide scales tend to spall and are replaced by new protective scales resulting from oxidation of the exposed substrate. Volatilization and spalling leads to gradual depletion of oxide forming elements below the surface and formation of less stable oxides such as NiO or CoO. In the end, the substrate is attacked by internal oxidation which can lead ultimately to loss of component load bearing capability. An example of oxidation damage at the tip of a DS René 80H high pressure turbine (HPT) blade that probably resulted from the above scenario is shown in Fig. 2 (23).



Figure 2: Localized oxidation damage at a thermal fatigue crack at the tip of a HPT René 80H blade (23).

2.2 Hot Corrosion:

Hot corrosion is the degradation of materials caused by the presence of corrosive salt deposit or ash on hot parts in the temperature range between 875 and 1225 K. This form of damage is encountered primarily in engines that are operated in marine environments when sodium chloride, ingested as sea salt, reacts with sulphur impurities from the fuel in combustion gases to form corrosive sulphates. The sulphates produced by this reaction may be deposited onto the surface of hot parts where they can flux the protective oxide scales, resulting in accelerated metal loss. This degradation mode occurs usually in two steps, one an incubation and the other a propagation step. The former corresponds to the formation of a sulphate deposit and its reaction via either acidic or basic fluxing with the protective oxide scale, while the latter is characterized by a rapid increase in the corrosion rate associated with changes in the morphology of the corrosion layers. Pettit and Goward have reported that the incubation time is controlled by many factors including alloy composition, gas composition and velocity, salt deposition rate and temperature (14). The time associated with the propagation stage is comparatively small and therefore the incubation time is normally considered as a criterion in determining the relative hot corrosion resistance of materials.

Two forms of hot corrosion are possible, one prevailing at an intermediate temperature of ~975 K and another that dominates around 1125 K. This is indicated by a maximum in corrosion rates at these two temperatures as shown schematically in Fig. 3 (22). The first maximum situated around 975 K corresponds to a low temperature form of hot corrosion known as LTHC, or Type II corrosion, which involves the formation of a complex sulphate deposit often containing cobalt in addition to sodium. The second maximum, at about 1125 K, corresponds to a high temperature form of hot corrosion known as HTHC, or type I corrosion, which appears to involve fluxing by Na_2SO_4 , perhaps in combination with MgSO_4 and CaSO_4 , with the latter serving only to depress the melting point of Na_2SO_4 . The condensed salt deposits, totally or partially molten, dissolve the protective oxides by acidic or basic fluxing depending upon the alloy composition and the environmental parameters. Type I hot corrosion (HTHC) develops a broad front of corrosion products containing chromium sulphides and a layer, within the alloy, depleted in more reactive elements. In contrast, in type II corrosion (LTHC), eutectic sulphate mixtures are formed giving rise to pitting attack with pits filled with a mixture of aluminum and chromium oxides with little or no sulphides and minimum alloy depletion (22).

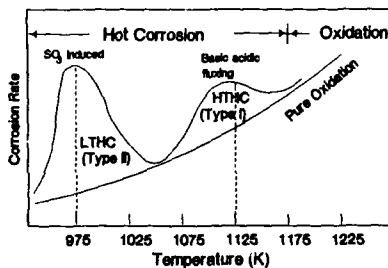


Figure 3: Schematic diagram of corrosion rate versus temperature depicting occurrence of type I and type II hot corrosion at approximately 1125 and 975 K respectively (22).

Gas turbines blades and vanes in aircraft engines are subjected to complex thermal, mechanical and chemical loads (14). These components are exposed to a chemically aggressive environment, and depending on service conditions, either form of hot corrosion may occur. As a result, their dimensions can be altered which can in turn have negative impact upon their structural integrity or aerodynamic properties. An example of type I hot corrosion at the trailing edge of an IN713 blade retrieved from a T56 engine is shown in Fig. 4a. The innermost layer contains chromium sulphides (Cr_2S_3) in the form of globules. No such sulphides form in type II hot corrosion as shown in Fig. 4b for a CoCrAlY coated alloy of similar composition. Both type I and type II hot corrosion may occur on the same component as a result of thermal gradients present on component surfaces during engine operation.



Figure 4: Characteristic appearance of type I and II hot corrosion (a) type I, IN713; (b) type II, CoCrAlY coating ((b) Courtesy G.W. Goward of Turbine Components Corporation).

2.3 Erosion:

Erosion of gas path components is caused by sand ingested during take off or landing, or during cruising at altitudes up to 10,000 meters over some areas. The particles of sand in the gas stream may strike gas path components and destroy the reaction product barrier that normally provides resistance against oxidation and hot corrosion. Leading edge surface morphology of a HPT blade damaged by erosion is shown in Fig. 5a,b. Pyrolytic carbon produced due to poor combustion conditions or unevaporated sea salt particles in the combustion gases can also cause erosion of hot parts (24-32). The former can accelerate the hot corrosion damage by creating locally reducing conditions or high sulphur potentials at the component surface (27). Erosion or combined erosion - hot corrosion processes can lead to catastrophic failure of hot parts. The extent of damage depends upon size, amount and impact energy of the particles. Galsworthy et al. (26) and Sorell (31) have reviewed erosion - hot corrosion interactions in detail and the reader is referred to these reviews for more information.



Figure 5: Characteristic appearance of an eroded surface at the leading edge of a turbine blade (a) general view, (b) magnified image of encircled area shown in (a).

2.4 Thermal Fatigue:

By definition, thermal fatigue is the gradual deterioration and eventual cracking of a material under thermal strains resulting from rapid temperature changes in high temperature environments and during which free thermal expansion is partially or completely constrained (33). In this respect, thinner sections of gas turbine blades at the leading and trailing edges heat up and cool down faster than the bulk of the component during service (34). The temperature transients at various points in time in the flight cycle give rise to large cyclic thermal strains at these locations, which can result in cracking due to thermal fatigue damage accumulation. In addition, coatings and substrates are sometimes mechanically incompatible in terms of their thermal expansion and therefore significant strain mismatch can also develop in a coating/alloy system during service. The resulting tensile or compressive thermal expansion mismatch strains can either increase or decrease the overall cyclic thermal strains within the coating, depending on materials properties and operating conditions. When cyclic strains are relatively severe, the protective barrier provided by coatings may crack prematurely. Cracks in the coating provide an easy path for contaminant to reach the substrate, leading to preferential attack of the substrate. An example of such localized attack along the trailing edge of an IN713 C nozzle guide vane is shown in Fig. 6. Such localized attacks can lead to a loss of load bearing capacity and ultimately to overload failure of the component.

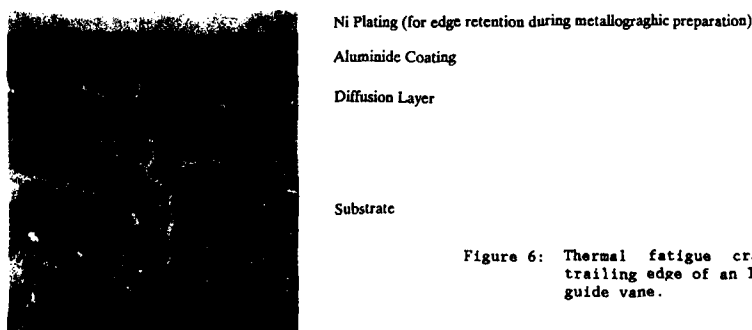


Figure 6: Thermal fatigue crack at the trailing edge of an IN713C nozzle guide vane.

The overall factors contributing to the degradation of hot section components in gas turbines are summarized in Table 1, which compares operating environments, forms of damage and expected life times for hot parts in aeronautical, industrial and marine engines. Irrespective of the type of engine, environmental attack due to oxidation, hot corrosion or erosion can be life limiting depending upon the operating conditions.

Table 1: Main Factors Contributing to the Degradation of Components in Hot Sections of Gas Turbines.

Factors Type of turbine	Environment				Nature of Damage		
	Temperature*, K	Thermal Cycles	Contaminant level		Mechanically Induced	Environmentally Induced	Expected Life h
			Fuel %	Air, ppm			
Military Aircraft	> 1175	•Several (function of missions)	•Aviation Fuel Containing S < 0.3%	•Salt-0.1ppm •Sand from runway	•Thermal Fatigue •Creep	•Oxidation •Type I hot corrosion	1,000 to 5,000
Civil Aircraft	> 1075	•Several (function of flight schedules)		(Contaminants in air is a function of flying locations)		•Erosion if air contains sand particles	> 10,000
Industrial and Utility	1125-1175	•Variable, short cycles (top up machines) •Stable (power generation)	•Gas oil, Crude oil containing S > 0.3% along with (Na + V) and K	•Depends on location of machine	•Thermal fatigue (if short cycles) •High cycle fatigue (large machines)	•Severe type I hot corrosion •Type II hot corrosion (some times) •Erosion if air contains particles	30,000 to 100,000
Marine	< 1025 (often) 1125 (occasionally)		•Marine Diesel containing S-0.3-1.6 % along with Na, V	•Sea salt from marine aerosols	•High cycle fatigue (large machines)	•Severe type II hot corrosion •Some cases of type I hot corrosion •Erosion if air contains particles	> 10,000

*Metal surface temperature of 1st stage turbine blade.

3.0 MATERIALS AND PROTECTIVE COATINGS:

Many techniques can be used to minimize environmental attack on hot parts (35-38). In practice one usually relies on a combination of them. For instance, air filters can be used to screen off contaminants from the intake air, while undesirable fuel elements such as Na, V, S can be minimized by using high quality cleaner fuels. Also special materials that combines high strength and corrosion resistance can be used. However, in the end one generally relies upon coatings to provide the necessary protection against high temperature environmental attack within the hot end of turbines.

3.1 Materials for Gas Turbine Blades and Vanes:

Alloys able to withstand oxidation in combination with both type I and type II corrosion in aggressive turbine environments are difficult to make and/or expensive to produce while maintaining an optimum compromise with mechanical properties. In practice, Co and Ni based superalloys are used for hot parts, with Co base alloys providing better resistance to type I hot corrosion and thermal fatigue than nickel based alloys. The latter, however, have better oxidation resistance and superior mechanical properties overall, for most applications. Hot corrosion resistance of nickel based superalloys can be improved by increasing chromium content. However, as the chromium content is increased the relative concentration of γ' precipitate forming elements (Al + Ti) is lowered at the expense of strength and oxidation resistance. Furthermore, increasing chromium content is no guarantee that an alloy will not corrode, as materials that show good resistance to one type of corrosion are not necessarily resistant to the other. This is the case of IN939 with good type I hot corrosion resistance but poorer properties under conditions conducive to type II corrosion than the lower chromium alloy IN738 (38-40).

3.2 Protective Coatings:

Protection against environmental attack is provided by coatings applied on the external as well as internal surfaces of internally cooled components. Coatings have been shown to extend usable lives of components by delaying the threshold beyond which damage becomes excessive, as shown in Fig. 7 (41). There are two main groups of coatings for high temperature components, namely the metallic and the ceramic-based thermal barrier coatings. Their characteristics are summarized below and the reader is referred to other work for more details (42-46).

3.2.1 Metallic coatings:

Metallic coatings protect structural components from environmental attack by acting as a barrier to minimize chemical interactions between the substrate and the environment. Depending on the service conditions and the nature of the gaseous environment, coating composition is selected to minimize oxidation and/or hot corrosion. Aluminum rich coatings are used for protection against oxidation while chromium rich coatings are used for protection against type I hot corrosion. The incorporation of Si to aluminum based coatings usually provides resistance to type II hot corrosion. Protective coatings are applied by two methods, one where the surface of the component is enriched by diffusion and the other where an alloy of desired composition is deposited directly onto the surface of the part by one of many techniques. The former method gives rise to so called diffusion coatings and the latter to overlay coatings.

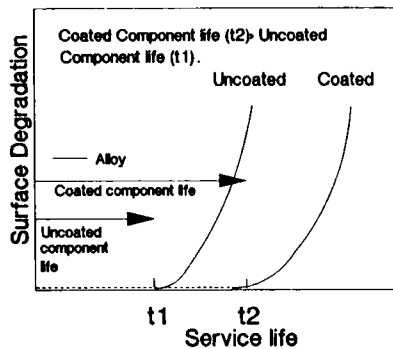


Figure 7: Schematic diagram illustrating that one primary function of a protective coating is to delay the initiation of surface degradation (41).

3.2.1.1 Diffusion coatings

Diffusion coatings in which aluminum is diffused into the substrate are generally aluminides obtained by pack cementation, slurry fusion, or chemical vapour deposition (CVD). Pack cementation is used predominantly because of its low cost and simplicity (47-48). The component to be coated is placed in a retort with an aluminum source and a halide activator (NH_4Cl). The assembly is sealed in an inert gas environment and held at an elevated temperature for sufficient time to allow build up of a $\sim 30\text{--}70\ \mu\text{m}$ thick coating. The coating usually consists of an outer layer of one or more aluminides, and an inner diffusion layer containing substitutional alloying elements, carbide and chromium rich sigma phases.

Diffusion aluminide coatings can either be of the 'inward' or 'outward' type depending upon the activity of the aluminum in the powder pack. Low activity aluminide coatings are formed by outward diffusion of nickel (or cobalt) from the base metal, while high activity aluminide coatings (e.g. Alpak) result from inward diffusion of the aluminum during subsequent heat treatment. Normally, high activity processing is preferred; this produces a coating with good oxidation resistance but poor hot corrosion performance. The hot corrosion resistance (type I) is improved by addition of elements such as chromium, platinum and rhodium. A typical microstructure of a low temperature high activity aluminide coating is shown in Fig. 8.



Ni Plating
B NiAl Carbides
B NiAl Solid Solution
Carbides +
Sigma Phase
Substrate

Figure 8: Typical microstructure of a low temperature high activity aluminide coating on an IN713C blade.

The first commercial Pt-modified coating, LDC-2, was produced by electrodepositing a platinum layer less than $\sim 10\ \mu\text{m}$ thick onto a component and subsequently aluminizing for several hours at 1325°K . A modified version of LDC-2 known as RT22, is widely used today to protect hot section components in industrial gas turbines. While coatings of this type have good resistance to type I hot corrosion, their performance against type II hot corrosion has however been questioned (59).

3.2.1.2 Overlay coatings:

Overlay coatings can be applied by several techniques including electron beam physical vapour deposition (EBPVD), sputtering, plasma spraying and cladding. They are typified by the so called MCrAlY coatings where M can be either Co, Ni or Fe. The interaction of the deposited $150\text{--}300\ \mu\text{m}$ thick coating with the substrate during deposition is usually negligible. Consequently, they offer tailored solutions for protection in specific environments due to flexibility in the design of coating compositions, as the applied coating is independent of the substrate composition. A good compromise of oxidation resistance, hot corrosion resistance and mechanical properties can be achieved with such coatings by suitably choosing the coating elements. Early interest in overlay coatings was focused on several cobalt based CoCrAlY's with composition in the range of 20-40% Cr, 12-20% Al and 0.5% yttrium, the latter to improve oxide adhesion. Since then, several overlay coatings have been introduced commercially. A comprehensive listing of these products can be found elsewhere (45).

The advantages and disadvantages of diffusion and overlay coatings and processes employed for their application are presented in Table 2 (22).

Table 2: The main advantages and disadvantages of various types of metallic coatings and coating processes (22).

DIFFUSION ALUMINIDE COATINGS						OVERLAY COATINGS			
	C.V.D. type method		Sprayed	Pt. modified	Cr. modified	Electron beam physical vapour deposition (EBPVD)	Plasma spraying under argon shield or low temperature.		
	High activity	Low Activity							
Composition	Much dependant on alloy composition			Dependant on alloy composition.		Large variety except alloys containing Ta.	Any powder composition commercially available.		
Ductility	Low, improved by: •Increase in thickness of coating •Appropriate heat treatments except for Pt modified aluminides					Good (depends on composition Al content). Sprayed coatings are more ductile than evaporated coatings of equivalent compositions			
Compatibility with alloy heat treatments	Good	Low except vapour phase treatments.	Good	Low except high activity aluminizing or vapour phase aluminizing.		No problems			
Thickness	Regular	Limited	Irregular	Regular	Limited	No limitation			
Adherence	Very good					Diffusion heat treatment compatible with the alloy heat treatment is required			
Reproducibility	Very good		Function of know how	Depends on Pt deposit quality	Good	Good if deposition parameters are closely controlled			
Masking	Possible	Difficult except for vapour phase treatments.	Easy	Difficult	Difficult except for vapour phase treatments.	Very easy			
Post Treatments	Eventual wet grit blasting.					Shot peening	Appropriate finishing treatments, shot peening.		
Coating internal Cooling passages	Possible but easier with vapour phase processes.		No	No	Possible if vapour phase aluminizing.	No			
Coating complex shaped components	Yes		Difficult	Yes		No			

3.2.2 Thermal barrier coatings:

Thermal barrier coatings (TBC), often applied by plasma spraying, are multilayer coating systems consisting of a ceramic insulating layer (top coat) and a metallic inner layer (bond coat) between the ceramic and the substrate, Fig. 9. Zirconia (ZrO_2) is normally used as a base material for the insulating layer due to its extremely low thermal conductivity. Yttria, magnesia or calcium oxide is also added to prevent transformation of cubic ZrO_2 during thermal cycling (60). The bond coat usually consists of a MCrAlY layer. Yttria stabilized zirconia is considered to have good oxidation and hot corrosion resistance which may be further enhanced by the addition of a MCrAlY layer on top of the TBC.

TBC's reduce the heat flux to the cooled metal surface. These types of coatings provide an opportunity to increase gas turbine efficiency by allowing higher gas inlet temperatures or by reducing cooling air requirements in airfoils (43). Alternatively, these coatings can be used to extend component life through lowering metal temperature and/or reducing the thermal strains induced during engine transients. The potential for increasing operating temperature by as much as 140 K makes them exceptionally attractive.

TBC's have been used for extending usable lives of burner and after burner liners and air cooled components in gas turbines and other heat engines (14,6). However, current usage is limited due to problems associated with high surface roughness, excessive porosity, slag inclusions, microcracking and poor adhesion. These limitations lead to premature degradation and failure by internal sulphidation, spallation, reduced resistance to thermo-mechanical strains, pitting corrosion, condensed salt penetration and oxygen penetration at high temperatures. However, research efforts are still continuing to overcome these limitations. Currently, use of these coatings is limited to non critical stationary parts.



Figure 9: Typical microstructure of a thermal barrier coating consisting of 8% Y_2O_3 stabilized ZrO_2 ceramic insulating layer (top coat) and CoNiCrAlY metallic inner layer (bond coat) on IN738 LC alloy.

4.0 SELECTION OF PROTECTIVE COATINGS:

Hot section coatings should provide protection against environmental attack to an extent which gives component life times compatible with the structural potential of the substrate. The main role of coatings is to minimize surface degradation so that structural integrity and aerodynamic characteristics of components are preserved. Rhy-Jones has tabulated the properties required by a coating system and these are presented in Table 3 (62).

Before selecting a coating for a particular component, the designer should ideally have insight information on the severity of the corrosive environment and the level of the thermal and mechanical loads likely to be experienced by the component in service. The coating must have adequate resistance to hot corrosion and a sufficiently high ductility so that cracks do not initiate too readily during thermal cycling (63). In addition, it is important to account for the possible interactions with the base material during coating application as well as during service, as these interactions can influence mechanical properties of the substrate (55,63-64). Coatings are normally applied at temperatures where

Table 3: Properties required by a coating/substrate system for turbine blades and vanes application (62).

Property	Requirements	Property	Requirements
Corrosion and oxidation resistance	Initial rapid formation of thin, uniform adherent and continuous protective oxide film. Slow subsequent rate of scale growth. Highly stable and adherent oxide scale. High concentrations of oxide forming elements in the coating.	Coating adhesion	Matched/similar coating and substrate properties e.g. thermal expansion. Clean alloy/coating interface. Ability to withstand all strain-temperature cycles encountered by the component.
Erosion resistance	Acceptable rate of oxidation/corrosion.	Mechanical properties	Appropriate coating ductility. Little or no effect on substrate properties. Surface finish close to cast airfoil.
Coating and interface stability	Ductile and adherent oxide scale. Moderate coating ductility. Low rates of diffusion across interface. Minimum compositional changes, particularly with reference to brittle phases.	Aerodynamic properties	Acceptable thickness and uniformity on airfoil. Minimum loss of surface smoothness during service.
		Coating process	Optimized for composition, structure, thickness and thickness distribution. Ability to coat complex geometries e.g. aerofoils. Cost effectiveness.

the substrate microstructure may be altered. In practice, processing conditions as well as post coating thermal treatments are adjusted to optimize substrate properties for the application at hand (63,65). During service, alloying elements from the coating also diffuse into the substrate and vice versa, with the result that embrittling phases such as sigma can form at the coating substrate interface. The nature of these interactions and their influence on mechanical properties are summarized in Fig. 10 for both diffusion and overlay coatings (65).

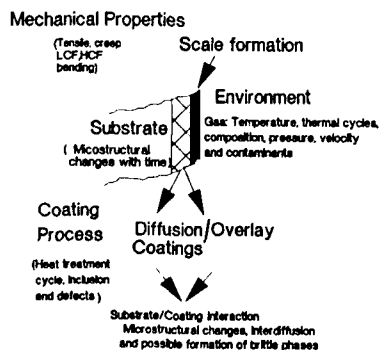


Figure 10: Interaction between the coating, the substrate and the environment (65).

In order to meet the needs of specific environments, while taking into consideration increasingly demanding mechanical property requirements, more and more effective coatings have been developed. The final selection of a coating from commercial products and processing technology for a particular component is a complex process. This complexity is due to the fact that the lives of identical materials in hot sections of nominally identical gas turbines can differ substantially depending on engine application (66), fuel quality (67), mission type and severity (68-69) and engine maintenance procedures (70). Despite considerable progress in coating technology, a sufficient understanding of the mechanistic details associated with coating/substrate degradation, to provide predictive capability of coating lives in specific environments, does not yet exist. This is further complicated by disagreement on the applicability of laboratory test methods and procedures used for the ranking of coatings as discussed below (71).

5.0 TESTING METHODS AND EVALUATION PROCEDURES:

There are several testing procedures available to assess the resistance of coatings to environmental degradation. They range from simple laboratory tests to the more complex combustor rig tests, which closely simulate hot section component environments, and finally to field tests. Each test has its own merits and limitations and these are compiled in Table 4 (22). The different test procedures often produce conflicting results due to differences in test conditions, as discussed by Just (72), where the author points out that it is not unusual to find for every detailed result based upon a single specific test, another test with the opposite result.

Table 4: Different Corrosion Test Methods, Their Advantages and Disadvantages

Tests	Laboratory				Burner rig			Field
	Salt Immersion		Furnace		Low velocity low pressure	High velocity Low pressure	High Velocity High pressure	
	Crucible	Electrochemical Measurements	Salt spray	Dean Test	P = 1atm Vg = 20m/s	P = 1atm Vg > 100m/s	P > 1atm Vg > 100m/s	
Operating Conditions	Total or partial immersion in a fused salt bath of known composition in a controlled atmosphere (air, SO ₃ /SO ₂)		Depositing salt on the specimen at low temperature (475K) followed by reaction at the test temperature with or without renewal of salt	Continuous deposition of salt to specimen at the test temperature in a controlled atmosphere (air, SO ₃ /SO ₂)	•Combustion of petroleum derived products in oxidizing environment •Controlled addition of SO ₃ and V in fuel and salt or synthetic sea salt in air. •Possibility of thermal cycling.			Testing in engines with severe operating conditions
Advantages	•Very simple •Easy to perform tests •Low cost	•Corrosion rate can be continuously monitored	•Simple •Realistic contaminant flux rate •Easily adaptable	•Realistic mass flow rate •Continuous salt deposition	•Continuous contamination •Realistic deposition rate •Easy to modify contaminant composition •Very Flexible		•Best Simulation	•Most Reliable test
Drawbacks	•Thickness of salt layer too high •Oxygen partial pressure at sample surface high	•Corrosion rate too high •Unrealistic corrosion morphologies	•Interrupted contamination	•Difficulties in carrying out thermal cycles and to modify contaminant composition	•High Maintenance cost •No simulation of gas velocity (high residence times)	•High cost and maintenance	•High maintenance cost (about 10% of field costs)	•No exploitable results before 2 years of accumulated test time •High cost

In laboratory tests, such as furnace and crucible tests, or electrochemical measurements in fused salt baths, test parameters are well defined and can be well monitored. Also, the test results are reproducible but are not necessarily realistic. In this respect, the procedures suffer from two major drawbacks. Firstly, and with the exception of the so called Dean test (c.f. Table 4), the procedures involve one time applications of Na₂SO₄, whereas continuous or near continuous deposition of Na₂SO₄ occurs during service. Secondly, under actual service conditions, material surfaces are exposed to temperatures, pressures, velocities or gas compositions which vary significantly and rapidly with time, which cannot be easily considered simultaneously in furnace or crucible tests (73-74). As a result of these drawbacks, surface degradation may differ substantially from that experienced in service.

Ultimately there is no substitute for tests in an engine that operate at significantly high pressures and mass flows of combustion gases. However, the high cost and time required to rank materials and coating in this way can be prohibitive. Also, the results derived from one engine may not be applicable to other engines.

Combustor rig tests, under simulated service conditions, provide a compromise between laboratory and field tests. Testing in rigs can be tailored to simulate unique aspects of service environments which can not be taken into consideration in simple laboratory tests. In particular, the combined effects of erosion, oxidation, corrosion and thermal cycling can be easily studied. Furthermore, high velocity gases of composition representative of gas streams in turbines can be easily obtained in rigs while at the same time the influence of aerodynamic loads can be taken into consideration. In this way, rig tests can be used to induce modes of service degradation and coating/substrate responses that closely approximate service behaviour. Therefore, rig tests are well suited to coating evaluation studies (75-85). There are, however, difficulties in analyzing rig results as explained below.

In 1970, the ASTM gas turbine panel hot corrosion task force sponsored (78) a round robin test programme in which six superalloys were evaluated by 15 participants in combustor rigs under the conditions given in Table 5 (85). The results of this programme are compared in Table 6 in terms of ranking of alloys. Rig results showed good reproducibility within a given laboratory but laboratory-to-laboratory correlation was inconsistent in terms of degree of attack and relative ranking of the same materials. Dapkunas (86) pointed out that poor correlation from one rig to the next was not entirely unexpected as various rigs were designed to simulate different types of engine environments and the tests were therefore not conducted under identical conditions. In particular, because of differences in combustor design, the gas dynamic conditions established in the different rigs were not identical (87). Also, Deadmore et al. (88) pointed out that ranking differences would be expected when comparing results obtained with high velocity rigs operated at gas velocities of 200-800 m/s (Mach 0.3-Mach 1.0) with those

Table 5: Test Conditions used by Participants of ASTM Round Robin Test Programme

Participant	Salt concentration, ppm	Fuel	Sulphur content in fuel wt.-%	Temperature K	Fuel/Air ratio	Pressure, atm	Gas velocity, ms ⁻¹	Cycling	Time, h
A	5	JP-4R	0.20	1175	0.033	1	215	Yes	100
B	5	JP-5	*	1175	0.033	1	*	No	100
C	5	Jet A	0.40	1175	*	1	215	Yes	100
D	5	JP-4	0.16	1175	0.012	1	60	Yes	100
E	**	Natural gas	*	1255	*	1	*	Yes	104
F	5	Kerosene	0.95	1145	*	1	*	No	100
G	***	1175	***	1	...	No	100
H	1	JP-5	0.04	1375	0.016 to 0.010	15	50 - 85	Yes	44
I	100	Diesel	0.86	1175	.033	1	4.45 SCFM	No	100
J	5	JP-4R	*	1175	**	1	*	No	100
K	****	1200	****
L	100	*	*	1175	0.033	1	*	No	100
M	100	2 Diesel	0.15	1175	0.059	1	6.71 SCFM	Yes	100
N	5	JP-5	*	1175	**	1	Mach 1	Yes	100
O	5	JP-4R	0.16	1175	0.033	1	215	Yes	100

*Not Known

** Salt solution (1% sulphate ion, water solution) sprayed on specimens during cooling cycle.

*** Static rig specimens coated with Na₂SO₄-NaCl(50/50) mixture exposed to 0.15% SO₂-2.25% CO₂ air and water vapour mixture.**** Crucible tests, 90% Na₂SO₄-10% NaCl at 1200°C

Table 6: Results of ASTM round Robin Test Programme.

Alloy	Ranking of alloy by participant															Average Rank	Order of alloys by average rank	No. of participants ranking alloy					
	A	B	C	D	E	F	G	H	I	J	K	L	M	N	O			1	2	3	4	5	6
U-500	1	2	2	2	1	3	1	1	3	3	3	3	1	3	1	2.00	1	6	3	6	0	0	0
IN-738	2	1	1	3	3	2	3	2	2	2	1	2	3	1	2	2.00	1	4	7	4	0	0	0
MM-421	3	3	3	4	4	1	2	4	1	5	2	1	2	2	3	2.67	3	3	4	4	3	1	0
U-700	4	4	4	1	2	4	4	3	4	1	4	4	4	4	4	3.40	4	2	1	1	11	0	0
IN-713C	5	6	5	5	6	5	5	5	5	6	6	5	5	5	5	5.27	5	0	0	0	0	11	4
IN-100	6	5	6	6	5	6	6	6	6	4	5	6	6	6	6	5.67	6	0	0	0	1	3	11

in a low velocity rig where gas velocity is only of the order of 6-30 m/s or when comparing results from rigs operating at high pressures to those obtainable at atmospheric pressure (88). Meaningful comparison of results from different laboratories requires that the test conditions employed be the same. Meaningful rig testing also requires that the test be conducted under conditions representative of service environments, such that results can be extrapolated to predict service behaviour (37). In this respect, it is important to ensure as a minimum requirement that damage morphologies normally incurred in service are consistently reproduced during rig testing. It should also be shown that the corrosive species formed during testing are chemically identical to those formed in service on engine components. Finally, ranking of materials should be established at comparable deposition rates of the contaminant species, since deposition rate is one of the factors controlling hot corrosion (89). In most investigations, composition and amounts of salt deposits are rarely documented (89). Also many other variables associated with combustor flame tube design and gas stream dynamics are rarely identified as other key variables. A survey of the literature reveals that there are in fact no standard test procedures for assessing materials durabilities in rigs.

Of the many variables that can be expected to influence surface degradation downstream of combustors, many are either directly or indirectly influenced by the type and design of combustor. Dils has made significant contributions in defining all the meaningful variables associated with combustors and has been able to design a rig for testing materials under a variety of well controlled conditions (73,90-91).

Identifying factors which contribute towards environmental degradation is a precursor to both the understanding of corrosion mechanisms and the selection of simulation criteria required to develop realistic testing procedures. In this respect, it is important to understand the basics of combustion in gas turbine engines and the following section summarizes briefly the principles of operation of a turbine combustor. The environment downstream of combustors and the factors that influence component degradation are then discussed in details. Finally, several types of laboratory combustors including that developed by Dils are illustrated.

6.0 TURBINE ENGINE COMBUSTORS - DESIGN AND OPERATION:

There are several types of gas turbine engines designed for different applications in mind. Their principles of operation are however basically the same (92). Air compressed by a radial or axial compressor is mixed with fuel and the mixture is ignited in a combustor. The expanding gases produced by combustion drive a single or multistage turbine which in turn drives the compressor and produces thrust either directly or through a gear box via a propeller. A cutaway view of an Allison T56 engine used to power Canadian forces Hercules transport aircraft is shown in Fig. 11 which identifies the compressor, combustor and turbine sections of this turboprop engine.

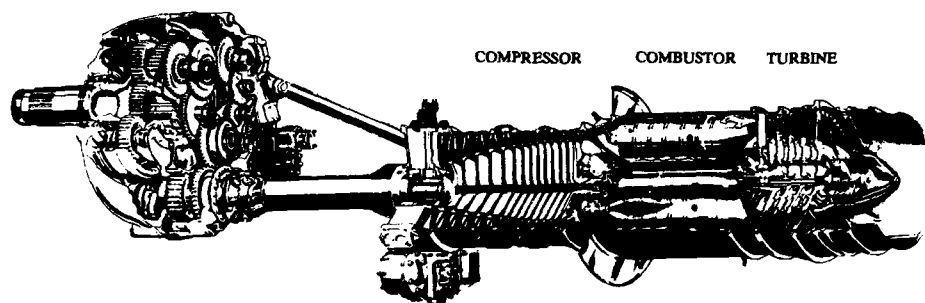


Figure 11: Cutaway view of an Allison T56 engine (Courtesy Allison Gas Turbine Div. of General Motors).

There are three basic designs of combustion chamber for turbines, the multiple chamber, the tuboannular chamber and the annular chamber. Cross-section of each type are shown in Fig. 12. The multiple chamber design, such as used in the T56 engine, consists of a series of individual combustor cans (usually 6 to 14, 6 in the T56 engine) arranged circumferentially around the main rotor shaft, Fig. 12 a. Each can consists of an outer casing and a perforated inner liner or flame tube as shown schematically in Fig. 13 (93). The cans are interconnected by means of a tube to allow them to operate at the same pressure and to ensure uniform combustion. The interconnection also allows the flame to travel between cans during ignition, since in normal installations only two cans are equipped with spark plug ignitors.

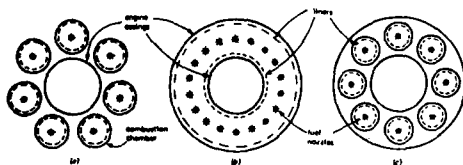
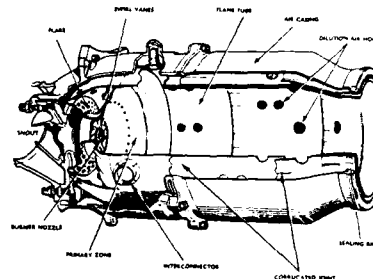


Figure 12: Cross-sections through the three basic types of axial flow combustion systems (a) Tubular; (b) Annular and (c) Tuboannular or Cannular.

Figure 13: Schematic cutaway view of a typical tubular combustor can (after the Jet Engine, Rolls Royce, 1973) (93).



The tuboannular type of combustor also consists of an individual combustor but in this case the outer casing is shared by all the flame tubes, Fig. 12 c. Finally, the annular type of chamber consists of a singular annular flame tube contained within an annular outer casing, Fig. 12 b. While the three designs are obviously quite different, their principles of operation in relation to the air flow distribution used to achieve and maintain combustion are the same. In all cases, the incoming air is slowed down and a stable flow pattern is generated within the primary zone, Fig. 13, to provide adequate residence time for efficient combustion before the outflow is mixed with dilution air and accelerated towards the turbine (92).

The hydrocarbon liquid fuels used in gas turbines have a stoichiometric fuel to air ratio of about 0.06 (15:1 air to fuel ratio) for complete combustion. Gas turbine engines cannot be operated with overall mixture ratios which even approach the stoichiometric value, because such ratios produce exhaust gas temperatures of about 2475 K which is far in excess of the temperatures that structural components can withstand. A large amount of excess air is therefore required to reduce the temperature of gases leaving the combustion chamber to acceptable levels. This usually means a decrease in the overall fuel to air ratio to levels ranging from 0.02 to 0.008, depending on operation of the engine (93). These fuel to air ratios are, of course, too lean for burning, hence combustor designs provide a method of by passing about 60 to 75% of the air around the actual combustion zone. The by passed air is known as secondary air because it does not participate in the combustion process, whereas the remainder of the air which actually takes part in the combustion is known as primary air (92).

In order to achieve the correct fuel to air mixture for stoichiometric combustion, the fuel nozzle must produce a fuel spray which consists of very fine droplets or mists, such that fuel can readily evaporate and quickly combine with air, while avoiding liquid droplets from being carried down the flame tube with consequent incomplete combustion. For the combustion process to be continuous, the temperature of the reactants is kept above the ignition temperature, and turbulence is maintained in the gas stream for sufficient time to allow fuel to burn completely before leaving the primary zone.

7.0 FACTORS INFLUENCING HOT SECTION COMPONENTS ENVIRONMENT:

Surface degradation of turbine hot parts is a direct consequence of their operating environment. This environment is the end product of a chain of events which begins from environmental conditions ahead of the compressor and terminates at the component, as summarized schematically in Fig. 14 (94). The factors which contribute to this environment can be separated in two main groups (29,35,89,94-104):

- (i) external factors that influence the environment ahead of the combustor and
- (ii) internal factors that influence the environment within the combustion chamber itself as well as downstream of the combustor.

The former are associated with intake contaminants including airborne and fuel contaminants, as well as with the load condition of the compressor. The latter are associated with combustor design and its influence on the characteristics of the gas flow dynamics, as well as with operating temperatures and geometries of the components. The internal factors dictate the state of chemical species in the gas stream i.e. whether the species are present in the gaseous, liquid or solid states, along with their thermodynamic activities, concentrations and residence times within the combustor, or as deposits on the components. The internal factors also control the rate of reactions taking place within the gas phase or at the surface of hot parts.

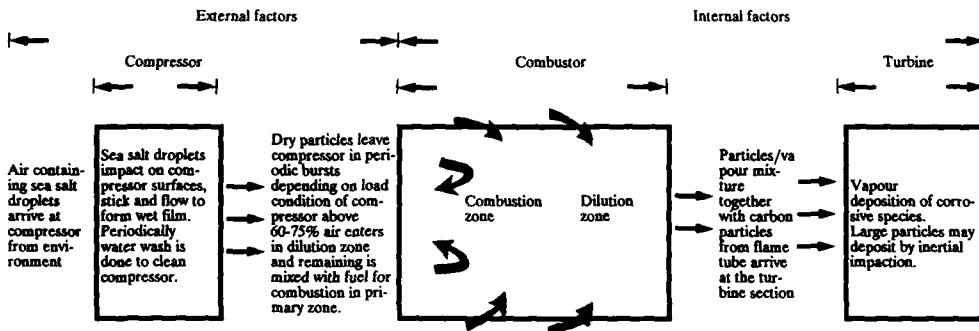


Figure 14: Factors contributing to the hot section environment (22).

7.1 External Factors:

Contaminants from the intake air or the fuel, either singly or in combination after reaction in the hot gases can cause extensive damage to gas path components. The form and extent of damage ultimately depends on air and fuel purities both of which are dictated by the type of engine and its application, Table 1. Highly rated aero engines use relatively pure fuel, and generally the air purity is good unless there are frequent flights at low altitudes in dusty or polluted regions or near marine environments. The marine engines use lower grades of fuels, and even though great care is taken to filter air intakes, the compressor air quality is generally poor. In the case of industrial turbines, gas-oil fuels of varying purities are employed and their quality depends to a great extent on engine location. While it may be unwise to generalize, there is much evidence to show that contaminant levels are usually the highest in the case of industrial turbines, particularly when they are run on inexpensive fuel and in marine or polluted industrial environments (88).

7.1.1 Air quality:

The quality of air is particularly important due to the small fuel to air ratios involved, typically in the range from 0.02 to 0.008 (92). For aero engines, airborne contaminants enter the engine either as sea-salt aerosols, runway dust, sand or ash. The concentration of these contaminants determines ultimately the form and severity of attack by dictating the possible forms of aggressive species in combustor gases.

Sodium chloride is usually ingested especially over seawater from marine aerosols. The amount of airborne NaCl in marine aerosols depends upon wind speed, ship's or aircraft's speed, air temperature, sea state, relative wind speed, relative wind direction, relative humidity and atmospheric pressure as shown in Fig. 15 (41,105-106). Most of these parameters are weather dependent, while some are influenced by the type of engine and its mission (which will affect aircraft's and ship's speed, and if helicopter operations are a significant factor, relative wind speed and direction). On the basis of several studies, the National Gas Turbine Establishment (NGTE) has published standards for marine aerosols which correlate

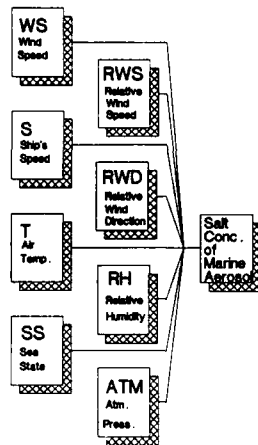


Figure 15: Environmental and operational factors influencing marine aerosols (106).

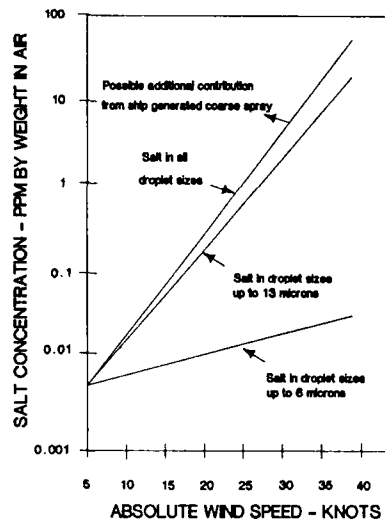


Figure 16: Variation in sea salt concentration as a function of wind speed (after NGTE standard marine aerosols).

airborne NaCl concentration levels for several ranges of particle sizes as a function of wind velocity for gas turbines operating in a marine environment (105-112). It is evident from Fig. 16, that the total concentration of NaCl in droplets less than 13 μm in diameter in marine atmosphere does not exceed 0.2 ppm by weight in air. When diameters above 13 μm are included the total is still less than 1 ppm by weight in air for wind speeds up to 20 knots (1 knot = 1.85 km/h). It has been argued that NGTE standard test data shown in Fig. 16 give an overestimate of NaCl concentration, as no humidity, air temperature, air pressure or sea state data are contained in the descriptions (106). They serve as a severe testing standards for designing air filters for offshore installations. Meanwhile, Rolls-Royce has set an upper limit of 0.01 ppm NaCl in air for filter design purposes, based on tests on Proteus and Tyne engines (107-108).

Compressors of gas turbine engines that operate in marine environment are periodically cleaned so that accumulated contaminants are removed from the engine. This can be done by water wash while the engine is mechanically cranked. Solutions after washing contain mostly sulphate anions and little, if any, chloride anions which are the main anions in ingested sea salt. It indicates that sulphates adhere preferentially to compressor parts while ingested chlorides make their way with air to the combustor during service (113). Therefore, with or without regular washing, NaCl ultimately reaches the combustor with the compressed air.

Ingestion of desert sand by gas turbine engines can cause extensive erosion damage to both compressor and turbine blades and vanes. On occasion, deposits of ultra fine sand (5-10 μm) have been found to accumulate on compressor gas path components. This can provide indirect protection to turbine blades and vanes as the fine particles are filtered out from the gas stream. A compressor can thus act as a massive filter, a condition which normally prevails under constant load operation (35). However, during acceleration, shedding of the accumulated sand (or other form of deposits including those of dried salt) is possible, such that concentrations considerably higher than the mean can be produced over a short period of time (35). In other cases, ingestion of fine sand, 5-10 μm in size, has been found to prevent solid contaminants from building up on compressor blades and vanes by continued erosive action, hence preventing entrainment of deposits and downstream impaction on turbine blades (102-103).

Not all airborne contaminants entering the engine are exposed to the elevated temperatures that are necessary for the formation of corrosive species. This is due to the fact that not all the compressor intake is directed through the combustor. Depending on the engine and its operation, approximately 10% of compressor discharge is typically bled off for general purpose cooling and this portion usually remains at temperatures less than 650°C. Of the remaining compressor discharge, 20-30% is used for combustion (primary zone) and the remaining 70-80% is introduced downstream of stoichiometric combustion as secondary cooling air as explained earlier (114).

7.1.2 Fuel quality:

There are a wide variety of fuels used in gas turbine, depending upon the type of turbine and the application. All of them are composed of carbon and hydrogen and may contain sulphur, as well as small amounts of sodium, vanadium lead and chlorine (115). Salt from ingested air can react with the trace amounts of sulphur and vanadium in the fuel to form corrosive deposits on hot parts. The nature and extent of the reactions, as well as the rate at which they proceed, are controlled to a great extent by the physical characteristics of the hot gas stream which is in turn influenced by many factors as explained below.

7.2 Internal Factors:

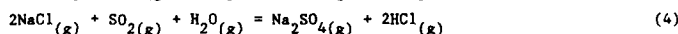
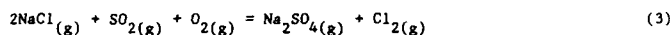
In order to understand the process of hot corrosion and develop models to predict its progression, it is important to understand:

- what happens to ingested contaminants in terms of physico-chemical reactions within the combustion gases and also
- what potential interactions the products from such reactions can have with hot parts downstream of combustors.

It is generally agreed that the presence of Na_2SO_4 is a pre-requisite for hot corrosion to occur. The principal source of Na is ingested sea salt. Sodium chloride is the main constituent of sea salt along with a minor quantity (typically 10%) of Na_2SO_4 and some other impurities. Sodium sulphate (Na_2SO_4) is not a naturally occurring impurity in fuels, nor a major constituent of the particulate matter normally ingested into gas turbines. Sodium sulphate for hot corrosion results from sulphidation of ingested NaCl with oxides of sulphur in combustion gases. These oxides (SO_2 and SO_3) are combustion products resulting from dissociation of sulphur containing compounds (thiophene, alkyl disulphide and alkylthiols) from the fuel and subsequent oxidation of sulphur. The equilibrium reaction that prevails in combustion gases is (116)



The conversion of NaCl to Na_2SO_4 during combustion at elevated temperatures involves the following evaporation and condensation reactions (116-123).



The possibility that reactions (1) to (5) will proceed to any significant extent to form Na_2SO_4 depends on many factors and is dictated by thermodynamic and kinetic considerations.

7.2.1 Thermodynamic considerations:

Johann (116) has calculated the mole ratio of SO_2 and SO_3 in combustion gases according to reaction (1) as a function of temperature. The results shown in Fig. 17 show that SO_3 should prevail at low temperatures during idling whereas SO_2 should dominate at high temperatures during take-off. Meanwhile partial pressures of oxygen (P_{O_2}) and sulphur oxides ($\text{P}_{\text{SO}_2} + \text{P}_{\text{SO}_3}$) in the combustion gases are of the order of 1 atm and 5×10^{-4} atm respectively (124). At low to moderate salt levels and moderate pressure of SO_3 , most of the ingested sodium chloride should be sulphidated within the hot gas stream, Eqs. (2 to 5) (121). It has also been reported that over the operating range of an engine combustor, the equilibrium flame temperature, T, for fuel to air ratios, ϕ , up to 0.04, is related to the equivalence fuel to air ratio (ϕ) and inlet air temperature (T_0) by the following relation (116):

$$T(\text{K}) = 2180 (\phi)^{0.835} + 0.75 T_0 + 68 \quad (6)$$

where $\phi \equiv \epsilon/\epsilon_{\text{stoichio}}$. The equilibrium flame temperature computed using the above equation is shown in Fig. 18 for several values of inlet air temperatures. For an inlet air temperature of 811 K, the flame temperature at the turbine entry varies over the range of 1075 K to 1800 K under normal operating conditions and approaches peak at ~ 2600 K for the stoichiometric ratio (Fig. 18). Johann (116) and later Kohl and co-workers (121,123) have computed equilibrium gas compositions for jet fuel containing two different levels of S (0.5 and 0.3% s respectively) and 5 ppm NaCl in inlet air. The results of both computations were similar and the data of Kohl and co-workers (121,123) are reproduced in Fig. 19. From these data, one can see that the equilibrium gases contain N_2 , O_2 , CO_2 , H_2O , Ar, NO, OH and CO along with minor quantities of CHNO species. Chlorine appears mainly as HCl while sodium is distributed in a complex pattern between $\text{Na}_2\text{SO}_4(\text{c or g})$, $\text{NaCl}(\text{g})$, $\text{NaOH}(\text{g})$, $\text{Na}(\text{g})$, $\text{NaO}(\text{g})$ and $\text{NaH}(\text{g})$. In the range of fuel to air ratios at which modern aircraft engine operate, sodium is tied up mostly as Na_2SO_4 along with an increasing proportion of NaCl as the fuel to air ratio (i.e. combustion temperature) increases, Fig. 19. It has been reported that the amounts of Na_2SO_4 and the distribution of Na among other species in the flame is strongly dependent on the amount of ingested sea salt and to a lesser extent on sulphur content in fuel along with the fuel to air ratio. The sodium from all the compounds irrespective of its chemical form can ultimately interact with hot parts to cause hot corrosion.

7.2.2 Kinetic considerations:

It has been suggested that in real engines kinetic conditions may not be favorable to achieve equilibrium conditions (124). For example, engine tests performed by Pratt and Whitney Aircraft show the SO_2/SO_3 ratio in hot gases to be several orders of magnitude lower than that corresponding to equilibrium at the exhaust temperatures (116). This can be rationalized on the basis of residence time, which is defined as the time interval between introduction of airborne salt into the combustor and the arrival of the salt or reaction products downstream at the hot section components. The residence time of the hot gases in an engine is considerably lower than that required to achieve equilibrium conditions for reactions (1) to (5) (124).

*c represents a condensed phase, either solid or liquid.

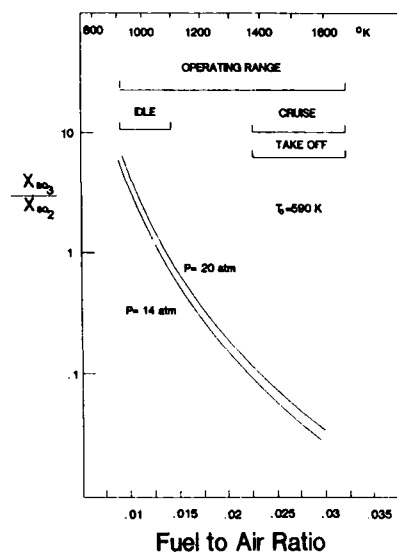


Figure 17: Variation in the equilibrium mole ratio, X_{SO_3}/X_{SO_2} , as a function of fuel to air ratio, ϵ , in the operating range of an aero engine (Fuel: 0.5 wt% S; Air: 5 ppm NaCl) (116).

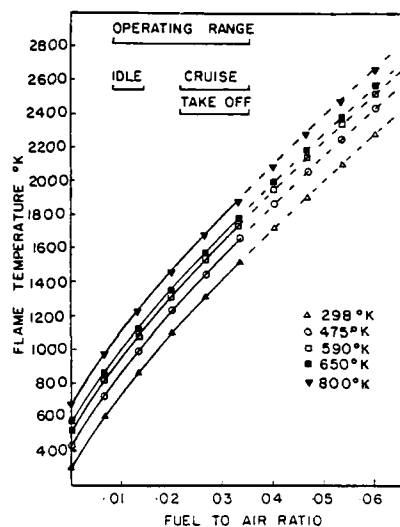


Figure 18: Variation in combustion flame temperature as a function of fuel to air ratio, ϵ , for different inlet temperatures (T_0) (116).

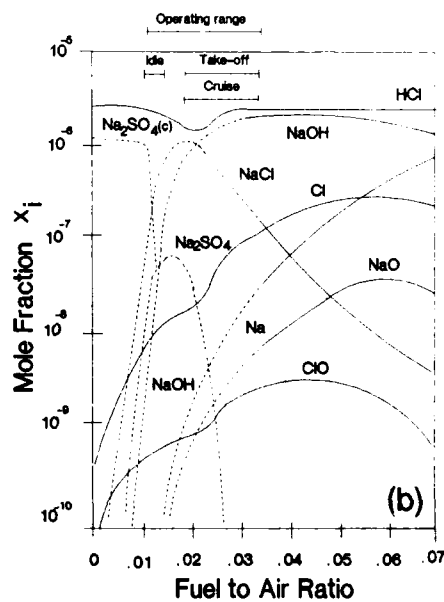
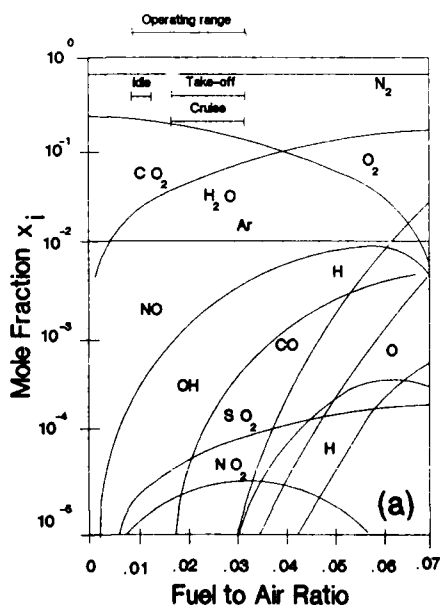


Figure 19: Variation in equilibrium chemical composition of combustion flame as a function of fuel to air, ϵ , at $P = 22.1$ atm. and inlet temperature $T_0 = 811$ K (Fuel: Jet A + 0.3 wt% S; Air: 5 ppm sea salt (123) (a) major products (b) sodium and chlorine containing species.

Residence time is largely controlled by the flame tube design (73,94,100). In this respect, flow distribution in terms of primary and secondary air within the combustor is an important feature of flame tube design which together with fuel flow rate governs the gas temperature and gas pressure distributions within and downstream of the combustor in addition to residence time. This in turn dictates, gas composition and the state of the contaminant species for any given amount of S in fuel or ingested NaCl.

The aerodynamic flow field within the primary, intermediate and dilution zones of a representative combustor is shown schematically in Fig. 20. Sea salt particles or droplets arriving from the compressor can enter the combustor through the swirler-vaporizer, secondary or dilution ports. Ingested particles entering through swirlers can evaporate due to recirculation and the high temperatures within the primary zone. The extent of this evaporation depends upon particle size and residence time within this zone (94,100).

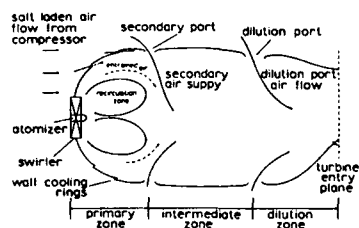


Figure 20: Schematic diagram describing the flow of air and combustion gas within a gas turbine flame tube (35).

The residence time available to the contaminants depends upon the strength of the recirculation within the primary zone which in turn depends on the swirler number (type) and the size, number and spacing of ports supplying air to this zone. Relative to the primary zone, temperature and residence time of the particulate laden air is significantly reduced through the transition and dilution zones. As a result, while solid sea salt particles entering the primary zone through the swirler can undergo significant evaporation, those entering through secondary or dilution port have neither the residence time nor a high enough temperature to evaporate to any significant extent (125). Consequently, they remain virtually intact until they reach nozzle guide vanes downstream of the combustor where they can strike gas path components. This also means that the salt present in secondary air i.e., the larger portion of compressor discharge is mostly unchanged in form when it reaches first stage hot section vanes and blades. Particle histories during transit through the combustor tubes of two different engines are described schematically in Fig. 21 (125). It can be seen that particles of a size typically below $6 \mu\text{m}$, undergo significant evaporation in both engines.

The mass percentage of particles which evaporate (Fig. 2) is available immediately for conversion of its chloride content into sulphates. However, gases have only a few milliseconds to mix within a combustor and therefore there may not be sufficient time for the gaseous reactions (Eqs. 3 to 5) to proceed to any extent. For that reason, it has been argued that evaporation and sulphidation reactions may not occur in the hot gas stream within or downstream of the combustor but may instead proceed at the surface of the hot parts themselves (117).

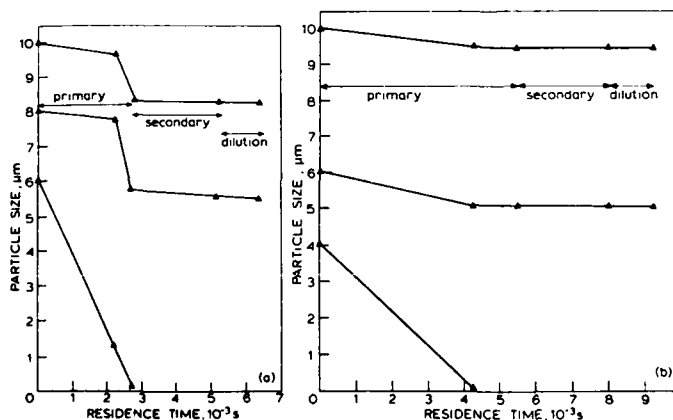


Figure 21: Histories of sea salt particle sizes in flame tubes for cruise conditions in (a) Tyne RM1A and (b) Olympus B engines (35).

Hanby (117) has studied the effects of the quantity of salt ingested and the influence of sulphur level in the fuel on the rate of conversion of NaCl into Na_2SO_4 during combustion in marine gas turbines. Results of this work indicated that there is no conversion for residence times below 8 ms and that less than 10% of NaCl is converted after 16 ms. Also, the level of sulphur in the fuel, over the range of 0.1 to 1.0% was found to have little influence on the rate of conversion. Other studies have shown that complete conversion of NaCl to Na_2SO_4 in an atmosphere containing 0.2% SO_2 takes place in 60 s at 923 K to 1023 K and in 30 s at 1123 K (126). Considering that residence time in combustors is typically in the range from 5 to 10 ms and that time to convert NaCl to Na_2SO_4 is of the order of seconds, it has been argued by some investigators that the conversion to corrosive Na_2SO_4 occurs primarily after deposition of NaCl on hot parts (116, 117, 126-128). In contrast, others have shown that the complete conversion of NaCl to Na_2SO_4 in a burner rig takes place in less than 2.2 ms, which is somewhat less than the residence time in modern aircraft combustor and have argued on that basis that NaCl is not likely to be deposited on hot parts (129-131). Wortman et al. (132) have confirmed this view on the basis of the following argument that, owing to the relatively slow velocity of a moderate size NaCl particle in combustion gases, impaction on vanes and blades would be expected to occur primarily on the convex surface of airfoils, whereas engine components show less intense attack of this side as compared to their concave side. In this respect, Kohl and co-workers (121) have reported that the activation energy for sulphidation of NaCl is only ~ 12 kcal/mole, which is so low that the conversion of NaCl to Na_2SO_4 should occur instantly in combustion gases even at low temperatures, further supporting the view that NaCl is not likely to be deposited directly on hot parts. Meanwhile, conflicting results have been reported by McKee et al. (120, 133) on the stability of NaCl in NaCl - Na_2SO_4 mixtures. These authors have reported NaCl to be stable for 6 h at temperatures between 1023 K to 1123 K in $\text{O}_2 + \text{SO}_2$ atmosphere on the basis of crucible test results (120). The same authors have also reached entirely different conclusions on the basis of accelerated oxidation tests where NaCl in deposit was rapidly sulphidated in an $\text{O}_2 + \text{SO}_2$ atmosphere with no influence on the hot corrosion behaviour of IN738 at 1023°C. These results were explained on the basis of differences in local environment.

Meanwhile, some investigators (94, 121) have taken a middle ground view, suggesting that while some sodium chloride particles may convert into sodium sulphate via evaporation and sulphidation reactions (Eqs. 2 to 5) within the combustion gases, particularly at high operating temperatures, some may survive to be deposited on hot parts. These particles are however likely to evaporate almost instantly because of the high vapour pressure of sodium chloride at turbine operating temperatures (121). The same authors suggest that the extent of sodium chloride deposition and residence time on the surface of hot parts would increase as operating temperature is decreased, although there is no direct experimental evidence to support this view.

A schematic representation of what might happen to ingested sodium chloride from sea salt aerosols according to Kohl and co-workers of NASA Lewis is presented in Fig. 22 (121). The possible paths from ingestion to interaction with hot parts are numerous and the reactions occurring in each case are complex, involving either gas/solid, liquid/solid, solid/solid or gas/liquid reactions. Some of the sodium chloride may vaporize while some may remain as particles in the gas stream depending upon particle size, residence time within the combustor and temperature. Sodium chloride in either solid or gaseous forms can lead to sodium sulphate formation by several possible routes or it can contribute to hot corrosion

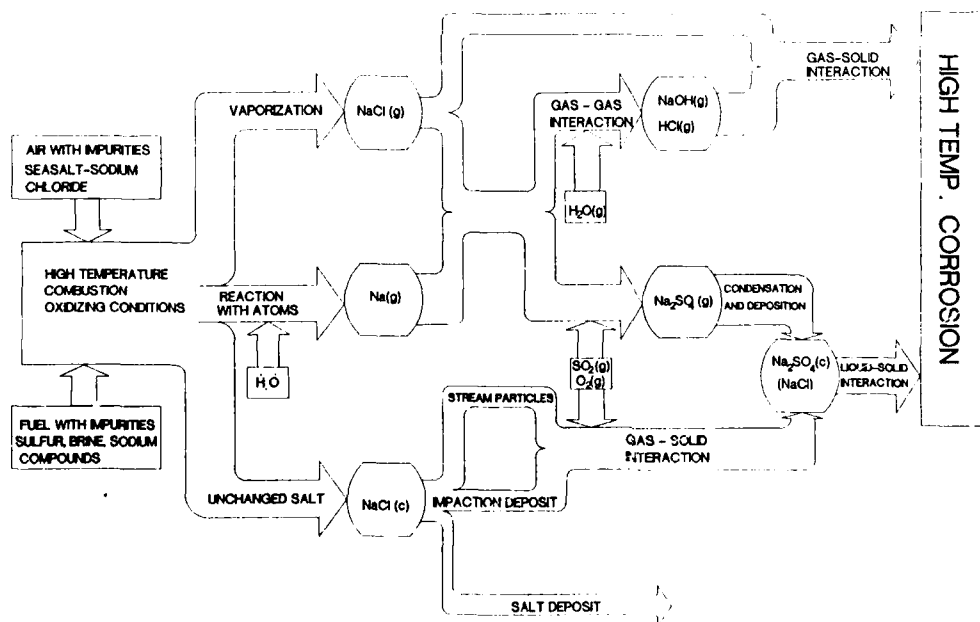


Figure 22: Possible reaction scenarios for ingested sodium chloride in the hot section environment of a turbine engine (121).

directly (Fig. 22) (121). There is also some evidence that large particles of sea salt can be stable for appreciable times in combustion gases, certainly long enough to be deposited on the blades and to remain there for times which will depend upon particle size, component surface temperature, deposition rate and gas velocity. Because of the low activation energy associated with the conversion of $\text{NaCl}_{(c)}$ into Na_2SO_4 in oxidizing atmospheres containing SO_2 via evaporation and sulphidation reactions (eq. (2) to (5)) any deposited $\text{NaCl}_{(c)}$ that does not evaporate should transform readily into corrosive Na_2SO_4 (121). Kohl and coworkers have also suggested that reactions between $\text{NaCl}_{(c)}$ and atomic H_2 and O_2 , early in the combustion process, can release $\text{Na}(s)$, thereby releasing Na atoms which can ultimately form corrosive species in SO_2 containing atmospheres without the need for NaCl vaporization (121).

7.2.3 Influence of chlorides:

Whatever the fate of Na containing contaminants entering the engine might be, it is ultimately Na in the form of Na_2SO_4 which is generally believed to provide the primary driving force for accelerated and catastrophic hot corrosion. However, it is also believed that all forms of chlorides including HCl and NaCl enhance corrosion attack by destroying the integrity of protective oxide scales or by impairing their repair capability (134-150). Smeggil and Bronstein (143-144) have shown that $\text{NaCl}_{(g)}$ is effective in reducing the oxide forming elements (i.e. Al and Cr) contents just below the surface of the protective oxide layers which in turn leads to progressive weakening of the scale-substrate bonds and rupture of the protective oxide scales. Ultimately, because of the decrease in Al and Cr contents, the propensity for reforming protective oxides of these elements is decreased and this effect is further reduced as the temperature is lowered.

Mixtures of $\text{Na}_2\text{SO}_4_{(c)}$ and $\text{NaCl}_{(c)}/\text{HCl}_{(g)}$ are believed to be much more aggressive in inducing very high rates of hot corrosion (68,114,120,145-150). Fryxell and Bessen (68) have reported that a mixture of Na_2SO_4 and HCl is possibly even more aggressive than Na_2SO_4 and NaCl mixtures if spalling characteristics are considered. Presence of chlorides can also reduce the melting point of salt deposits, and possibly enhance the solubility of some of the oxides present as scales on hot parts (151). They are also believed to increase wetting action by molten salts (151).

It has been suggested that NaCl whether it is derived from fuel, air or sea salt, may contribute differently to hot corrosion of components although this effect has not been well studied (72). However, according to Stevens and Tidy (152), the form of the Na in the fuel does not affect the deposition of Na_2SO_4 on the surface of hot parts.

8.0 CONDENSATION AND DEPOSITION OF CORROSIVE SPECIES:

As pointed out earlier on, thermodynamic calculations predict that Na_2SO_4 is the only species expected to condense to any extent onto the component under normal operating conditions. The only other phase which could also form from a thermodynamic view point is Na_2CO_3 (121). The NaCl and HCl which are highly stable in gaseous environments are unstable in a condensed state. Therefore, NaCl and HCl are not likely to be present onto the surface of hot parts.

8.1 Condensation:

The condensation of $\text{Na}_2\text{SO}_4_{(g)}$ can take place within combustion gases in an aero engine during idling and low power end of the take off and cruise ranges. This is clearly indicated in Fig. 19 which maps out concentrations of major contaminant species present in combustion gases against fuel to air ratio (and therefore combustion gas temperature) for the expected range of operating conditions.

At low values of fuel to air ratios the Na is tied up mostly as $\text{Na}_2\text{SO}_4_{(c)}$ up to a sharp cut off point beyond which this compound begins to evaporate. At this point, the partial pressure of $\text{Na}_2\text{SO}_4_{(g)}$ becomes equal to its equilibrium value, which defines the transition point for evaporation/condensation reactions (123). Cutler (124) has also shown that if the concentration of Na in fuel is greater than 1 ppm or 0.02 mg/m³ in combustion gases, the equilibrium concentration of $\text{Na}_2\text{SO}_4_{(g)}$ will exceed its saturation vapour pressure at normal operating metal temperatures (1000-1200 K) for first stage turbine blades. Under such circumstances, condensation and deposition of $\text{Na}_2\text{SO}_4_{(c)}$ onto these components can take place which will be molten at the highest metal temperatures.

The condensation temperature of $\text{Na}_2\text{SO}_4_{(g)}$ is influenced by the fraction of sulphur in the fuel, concentration of sea salt in air, fuel to air ratio, temperature and pressure. Several investigators have calculated the condensation temperatures under a variety of conditions using an equilibrium thermodynamic method (115,116,123,153,154). The results of calculations performed at NASA Lewis are shown in Fig. 23 for various salt concentrations as a function of weight fraction of S multiplied by the fuel to air ratio (F) (123). The parameter F is used in order to fully characterize the combustion system so that the total amount of S in fuel with NaCl in air is taken into consideration for any specified fuel to air ratio. It can be seen that for a given amount of NaCl and up to $F \approx 0.4$, the condensation temperature of $\text{Na}_2\text{SO}_4_{(g)}$ can vary by up to 140 K, while, changes in F above 3.4 have no effect on the condensation temperature. The condensation temperature is also expected to vary with an increase in the sea salt content of inlet air from 0.1 ppm to 20 ppm by 200 K at any given value on the parameter F, Fig. 23.

The fraction of Na_2SO_4 condensed is shown in Fig. 24 as a function of flame temperature. The intersections on the abscissa correspond with the temperatures of saturation with $\text{Na}_2\text{SO}_4_{(g)}$ at a given concentration of NaCl in inlet air (123). It can be seen that condensation of Na_2SO_4 goes to completion within a narrow range of temperatures.

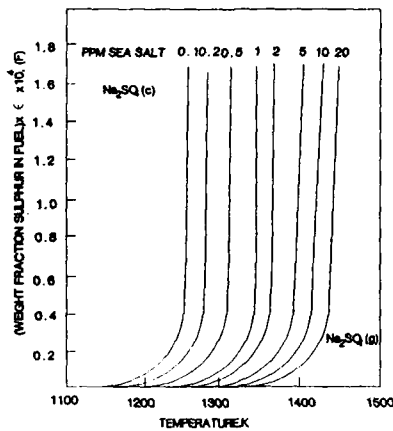


Figure 23: Variation in condensation temperature of Na_2SO_4 as a function of parameter 'F' for different seasalt concentrations in inlet air at $T_0 = 811$ K and $P = 22.1$ atm (123).

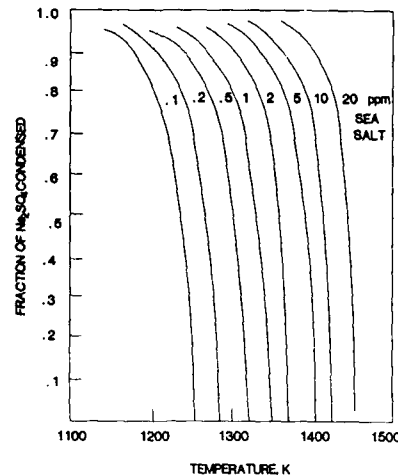


Figure 24: Fraction of Na_2SO_4 condensed as a function of temperature and sea salt concentration. Test conditions: $\epsilon = 0.020$, $T_0 = 811$ K and $P = 22.1$ atm (123).

8.2 Deposition:

The deposition mechanisms of Na containing species onto the surface of hot parts have not been extensively studied. However, it is generally believed that mass transfer of Na onto the surface of hot parts may occur through:

- deposition of either partly or wholly unevaporated Na containing solid species (e.g. solid sea salt particles),
- deposition of $\text{Na}_2\text{SO}_4(c)$ from combustion gases and
- vapour diffusion of Na salts (Na_2SO_4 , NaCl , NaOH etc.)

Stearns et al. (155) have identified three modes of deposition based on characteristics of deposition for a wide spectrum of particle sizes (between 0.1 and 10^5 nm, Table 7). The modes are vapour diffusion, particle diffusion and inertial impaction. The vapour diffusion mode represents one extreme in the deposition behaviour of particles in the ranges from 0.1-1 nm. At the opposite extreme, deposition occurs by inertial impaction of macroscopic particles (10^3 - 10^5 nm) which are too heavy to follow the combustion gas stream. Between these two extremes there is a wide range of particle sizes where processes such as Brownian diffusion, eddy diffusion and thermophoresis (thermal diffusion of heavy molecular size particles across a temperature gradient) dominate the deposition process. In practice, these three modes of deposition are not entirely independent of each other. For example, the gas stream may consist of vapours of condensable Na-species and unevaporated sea salt particles and/or condensed Na_2SO_4 , such that deposition may result from the combination of vapour diffusion and eddy impaction. However, it is also possible that one particular mode of deposition may dominate over the other (156).

Table 7: Characteristics of Deposition for Spectrum of Particle Sizes(157)

Size Range ^a nm	Mass Transport Mode	Deposition Species	Transport Mechanism
0.1-1	Vapour Diffusion	Atoms and molecules	Fick, Soret and eddy diffusion
1- 10^3	Vapour Diffusion Transition	Heavy molecules (condensate aerosols, clusters, and submicroscopic particles)	Brownian and eddy diffusion and thermophoresis
10^3 - 10^5	Inertial	Macroscopic particles	Inertial and eddy impaction

^aMode of deposition is not fixed by particle size alone.

Most of the deposition studies performed in service engines or under simulated service in rigs seems to favour the mechanism of deposition by vapour diffusion of Na_2SO_4 or NaOH across a boundary layer at the component surface (197,152,156-159). Support for this view comes from the appearance of crystalline needles composed of mainly Na and S (a characteristic of Na_2SO_4 in EDS analysis) protruding from deposits on platinum collector pins in burner rig tests as reported by Santoro and co-workers (156). According to these authors, these protrusions must form spontaneously from the vapour phase. Stevens and Tidy (97,152) using a rig simulating an industrial turbine have also concluded that the deposition of Na species occurs by vapour diffusion of Na_2SO_4 , NaOH and NaCl species across the boundary layer. In their opinion, conversion of NaOH and NaCl to Na_2SO_4 vapours takes place within this boundary layer. The Na_2SO_4 then condenses as its near-surface concentration reaches levels where the saturation vapour pressure is exceeded. Stevens and Tidy have also reported that a threshold concentration of Na in combustion gases is exceeded.

required for deposition to occur (97,152). Their threshold concentrations compared well with the values obtained from industrial turbines only when other elements such as Ca, Mg, or K were present in the fuels which were used in the rig. Beyond this threshold, the weight of Na deposited per unit area has been reported to increase linearly with time.

Researchers at the NASA Lewis Research Centre have developed a model which predicts deposition rates using a chemically frozen boundary layer (CFBL) theory of vapour diffusion (156). They have claimed that the CFBL theory is capable of handling both vapour and heavy molecule deposition modes (up to 10^3 nm particle sizes, 1st two rows in Table 7). The CFBL theory assumes that all the Na added to the combustion gases is available for transport to the deposition site via vapour species (of NaCl, NaOH, Na and Na_2SO_4) and that a local thermodynamic equilibrium exists at the outer and inner edges of the concentration boundary layer around the deposition surface. The boundary layer is chemically frozen in the sense that no homogeneous chemical reactions occur within it. The NaCl, NaOH and Na species convert to Na_2SO_4 in the presence of excess oxygen and S containing vapours at the gas/boundary layer interface. The CFBL theory (156) also includes a contribution to the total deposition by large Na_2SO_4 droplets which survive their residence times within the combustor prior to their deposition by inertial impaction. Claims have been made that predictions based on this theory compare well with experimental results observed in burner rigs. This is demonstrated in Fig. 25 which also reveals that the deposition rates of Na_2SO_4 is independent of collector surface temperature up to the melting point of Na_2SO_4 (156). However, the deposition rates of

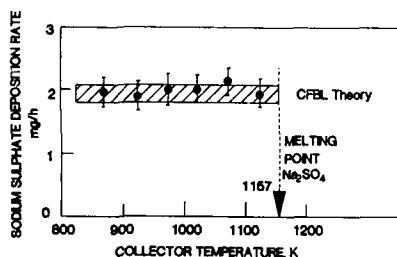


Figure 25: Comparison of predictions of CFBL theory with experimental deposition rates (\dot{m}) of Na_2SO_4 . \square CFBL theory, \bullet experimental data points. Test conditions: $V_g = \text{Mach } 0.3$, $Re = 1.83 \times 10^4$, Fuel = Jet A + 0.3 wt% S, air = 5 ppm NaCl, Gas temperature = 1673 K (157).

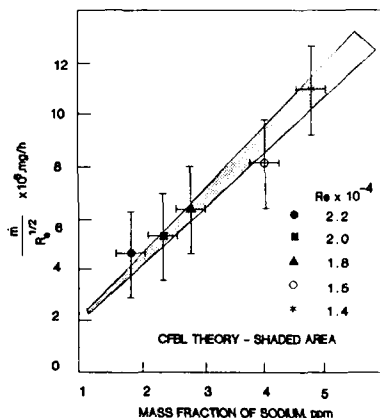


Figure 26: Variation of predicted and experimental deposition rates (\dot{m}) as a function of sodium concentration in combustion gases and mass flow rate (Reynolds number). Test conditions: Gas temperature = 1673 K, $V_g = \text{Mach } 0.3$, Collector temperature = 1023 K and $\epsilon = 0.034$. (157).

Na_2SO_4 , above its melting point are lower than predicted by theory and appear to reach a terminal value. This has been attributed to the removal of molten deposit beyond this value by aerodynamic shearing of the deposit (101). The deposition studies performed by Misra support this claim (74). The CFBL theory also predicts that deposition rates are directly proportional to the Na concentration in combustion gases and the square root of the Reynolds number, as verified by experimental results, Fig. 27 (157). The shaded region corresponds to theoretical predictions based on the CFBL theory. The scatter in experimental results arises apparently from the stray deposition on the inner wall of the burner liner. NASA researchers, in developing the CFBL theory, have conducted extensive testing and reported that changes in test parameters such as salt solution concentration, atomizing air pressure, salt pump speed, liner to liner variation can alter the mode of deposition (156). Their observations are entirely consistent with the CFBL theory, since these parameters can be expected to influence either directly or indirectly sodium concentration or gas velocity and therefore the Reynolds number.

9.0 DEPOSITS AND SURFACE INTERACTIONS:

Once corrosive species are deposited from combustion gases onto hot parts, complex interactions may occur between the gaseous surrounding, the liquid and/or solid deposit and the solid substrate. A detailed discussion of these interactions is outside the scope of this paper, and the reader is referred to several comprehensive reviews on the subject for more information (124).

It is known that the extent of hot corrosion and morphology of the corrosion products largely depend upon the amount of deposit and the substrate composition. In previous sections, thermodynamic and kinetic considerations under engine operating conditions were discussed. It was realized that for a given amount of salt in inlet air and S in fuel, the deposition rate of corrosive species depends on several inter-related factors which are summarized in Fig. 27. Any change in these factors can alter the chemical dynamics of combustion gases and the subsequent rates of deposition of corrosive species and hot corrosion damage. For example, changes in SO_3/SO_2 ratio of the combustion gases can not only influence the deposition rate but also the composition of the deposit (124). Similarly, changes in residence time can influence deposition rate and the possible role of NaCl in the hot corrosion process. It should be noted from Fig. 27 that the deposition rate is also dependent upon the component's propensity in collecting corrosive species from the gas stream. This propensity depends in turn upon inertial parameters and the Reynolds number as well as upon the geometry and surface smoothness of the component and the temperature gradients across its surface.

The aerodynamic flow distribution around and within internally cooled components is largely responsible for large thermal gradients over their surface. These gradients influence the rates of chemical reactions between deposit and substrate as well as the rate of flow of any molten material over the surface of the component. At high temperatures, deposits may disappear by rapid evaporation or migrate to cooler regions as a result of increased fluidity under the influence of centrifugal and aerodynamic forces (69,97). Consequently, deposits can be found in varying amounts across, around, up and down an airfoil surface. A typical distribution of temperatures across airfoils of a nozzle guide vane is represented schematically, in Fig. 28 (29) which identifies areas where deposits are likely to be formed and cause either Type I (LTHC) or Type II (HTHC) hot corrosion depending upon local conditions.

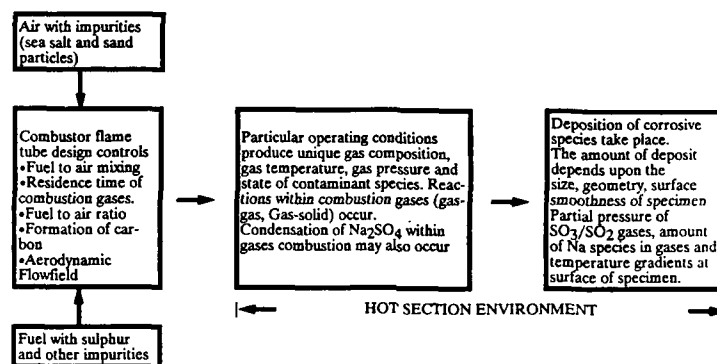


Figure 27: Factors influencing the deposition rates of Na_2SO_4 onto hot section components.

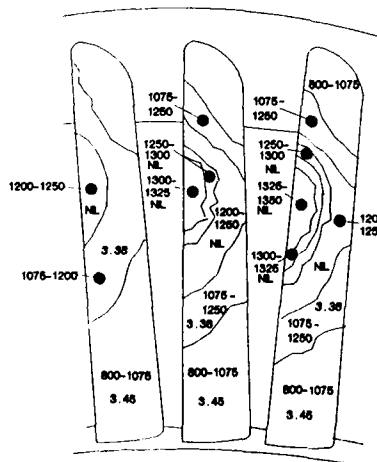


Figure 28: Typical distribution of temperatures (K) and Na_2SO_4 deposition rates ($\times 10^4 \text{ g/cm}^2/\text{s}$) on suction surfaces of high pressure nozzle guide vanes in an engine (126).

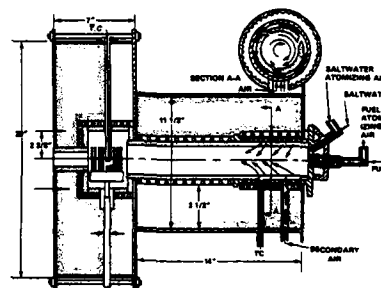


Figure 29: Cross-section of low velocity-low pressure burner rig (77).

10.0 LABORATORY COMBUSTOR RIGS:

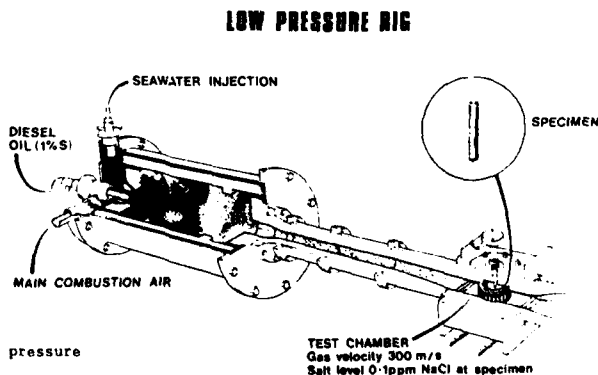
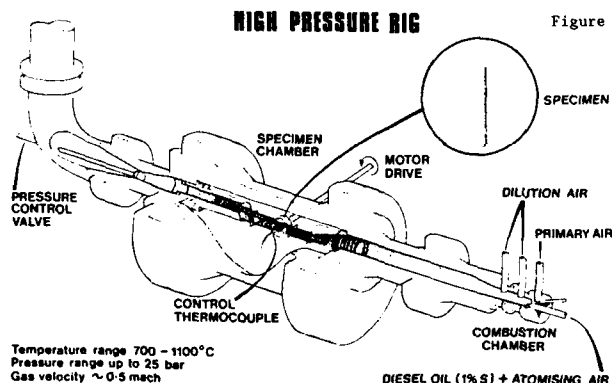
For materials testing under simulated service conditions in a laboratory combustor rig, the most important features of the combustion process should be realistically reproduced. In particular, a rig should be designed to reproduce similar temperature fluctuations in combustion gases and combustion products to those prevailing in engines, as well as rates of deposition and deposit morphologies and chemistries representative of service conditions. In order to meet these requirements, a large number of test parameters must normally be controlled including those influencing contaminant concentrations in both combustion air and fuel and those pertaining to the combustion process itself. Among the latter parameters, the most important ones are the fuel to air ratio, the ratio of primary to secondary air mass flow, which ultimately controls gas temperature and gas velocity downstream of the combustion, the type of liner, the nozzle and test chamber geometries, the specimen geometry and smoothness and specimen rotational speed within the hot gas stream. Specimens are normally rotated in rig tests in front of the burner nozzle to minimize any non-uniformity of attack that might arise as a result of temperature and contaminant concentrations gradients across the gas stream.

10.1 Types of Rigs:

There are several types of combustor rigs that can provide close simulations of the dynamic environment prevailing in gas turbine engines. Their characteristics and the conditions under which they are used in various laboratories have been compiled by Booth and Clarke (85). Rigs can be classified as:

- (a) low velocity - low pressure rigs,
- (b) high velocity - high pressure rigs, and
- (c) high velocity - low pressure rigs.

The low velocity - low pressure rigs are closely related to laboratory furnaces in that they rely on resistance heating to maintain uniform gas stream temperature, Fig. 29 (77). With such rigs, large amounts of salt are injected into the low velocity combustion stream and test parameters can be adjusted to induce various damage morphologies. However, relating results to practice has proven difficult primarily because combustion dynamics are not reproduced. Also, this type of rig is not particularly effective in demonstrating the good performance of Pt modified aluminide coatings in spite of favourable reports from engine tests (73,160,161).



High velocity - high pressure rigs are by implication considerably more complex pieces of apparatus, but they can closely duplicate engine environment and are capable of producing realistic heating and cooling rates. The number of such rigs is however limited due to high installation and maintenance costs. A cut-away view of the Admiralty Research Establishment (ARE) high pressure rig is shown in Fig. 30 (161).

High velocity - low pressure rigs (Fig. 31) are a good compromise between the other types of rig (94). They are capable of producing surface damage due to environmental attack similar to that found in engines at realistic salt-in-air levels of ~ 1 ppm. Also, the loss of information associated with using an atmospheric rather than a high pressure rig has been claimed to be minimal on the grounds that gas dynamics can be adjusted to compensate for lower heat transfer coefficients. The rig designed by Dils, belongs to this category and is described in detail in a later section.

10.2 Characteristics of High Velocity - Low Pressure Rigs:

High velocity - low pressure rigs are entirely capable of simulating the relationships between exhaust gas temperatures and fuel to air ratios, Fig. 18, and therefore are expected from equilibrium thermodynamics to produce chemistries of combustion gases, similar to those expected for engines, Fig. 32 (123). By comparing the data from this figure with that contained in Fig. 19, it can be seen that the gaseous products of adiabatic combustion predicted for rigs are similar for all practical purposes to those predicted for engines, and that this is so in spite of the difference in operating pressure of close to 21 atmospheres between atmospheric pressure rigs and engines. There are however some differences, in that the range of temperatures over which gaseous species are expected are shifted to higher temperatures (by ~ 100 K) in the case of rigs. Also in rigs, the range of temperature over which Na_2SO_4 is expected to condense, as the concentration of sea salt is varied, Fig. 33, is reduced down from 140 to ~ 110 K, as a result of differences in partial pressures of NaCl , HCl , SO_2 , and other gaseous species. It has been shown that in order to obtain the same contaminant partial pressures in rigs as in engines, and therefore the same deposition rates, the contaminant level in rigs must be raised relative to the engine contaminant level by some factor (115). This factor depends on the difference in operating pressure and the contaminant level, and has been reported to be as high as 100 times in some studies (123).

10.3 Test Procedures:

There appears to be no unique salt level at which rig tests are conducted in different laboratories and there are wide variations in salt levels used, Table 5. In simulation tests, 1 ppm salt is considered to be a realistic level, and 10 ppm is often used for accelerated tests (162). Ishida and coworkers (163) have reported an overall increase in corrosion rate with an increase in salt levels from 0 to 10 ppm. Varying salt level from 10 ppm to 50 ppm in air has been reported to have little effect on LTHC behaviour (149).

Several specimens are usually mounted on a carousel and tested together with the hot gas stream impinging upon the specimens at right angles to their longitudinal axis. In unducted rigs, specimens are directly exposed to the hot gases arriving from the combustor. Under such conditions only type I hot corrosion damage can be obtained. Furthermore, the extent of damage may differ substantially from that obtained with ducted rigs. It is not possible to obtain type II hot corrosion damage because of dilution of the hot gas stream by surrounding ambient air, which makes it impossible to maintain the critical partial pressures of SO_2/SO_3 for type II hot corrosion to proceed (85). Dilution also affects chemistry and temperature of combustion gases which adds to uncertainties in test results.

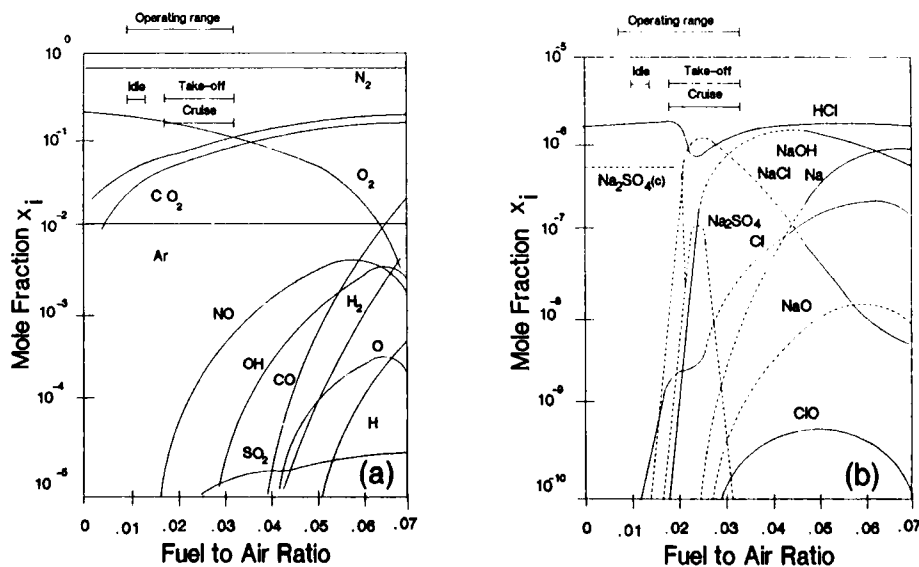


Figure 32: Variation in equilibrium chemical composition of combustion flame as a function of fuel to air ratio ϕ at $P = 1$ atm and $T_0 = 298$ K (Fuel: Jet A + 0.3 wt% S; Air = 5 ppm salt) (123), (a) major products and (b) sodium and chlorine containing species.

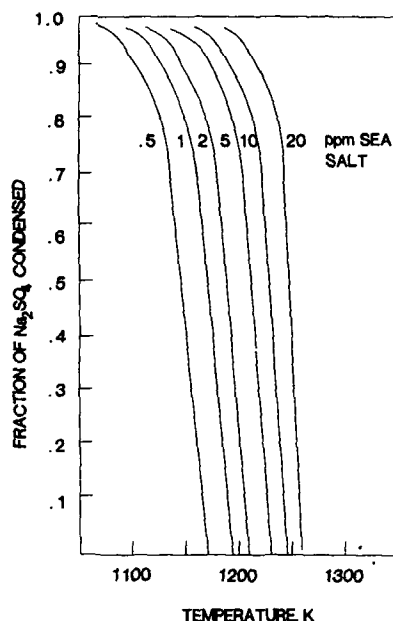


Figure 33: Fraction of Na_2SO_4 condensed as a function of temperature for several seasalt concentrations in inlet air. Test conditions: $\epsilon = 0.020$, $T_0 = 811 \text{ K}$ and $P = 1 \text{ atm}$ (123).

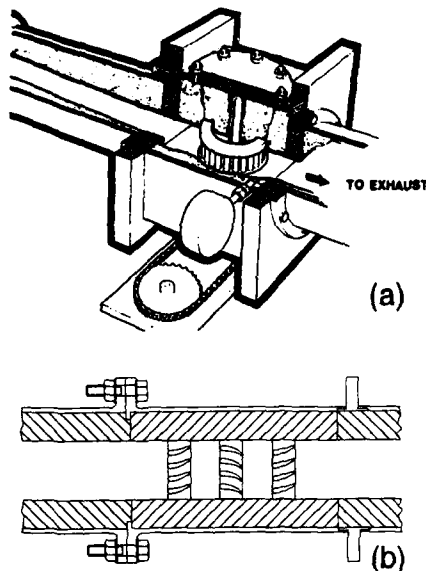


Figure 34: Typical designs of test chambers for (a) rod shaped specimens and (b) aerofoil specimens (81).

Ducted rigs are used to gain better control on the test environment. In ducted rig specimens are exposed in a test chamber attached to the combustor downstream of the nozzle. The dimensions of the duct work influence the aerodynamic flow and heat transfer characteristics around the test specimens (164). It has been reported that the combination of duct configuration, specimen design and gas flow characteristics can alter the boundary layer at the specimen surface sufficiently to give variations in deposition rates. For rig to rig comparisons, it is therefore important that deposition rates be documented. This is normally done by measurements on a platinum reference specimen of similar shape and dimensions as the specimens being tested.

The flow and heat transfer characteristics around a cylindrical specimen are well documented and can be readily reproduced from one laboratory to another. Therefore, cylindrical test specimens are normally used for rig testing. Pins with length to diameter ratio close to 8:1 are recommended but other dimension and complex shapes are also used (73). Typical examples of specimen chambers for cylindrical and aerofoil shaped specimens are shown in Fig. 34(a) and 34(b) respectively (81). In general specimens can be retracted and forced cooled outside test chambers to achieve thermal cycling. Also the specimen are usually rotated to keep all specimens at the same temperature and ensure uniform exposure to contaminants from the gas stream.

10.4 The NAE Rig and Programme:

The NAE rig designed by Dils and supplied by Bacon Inc. of South Windsor, Connecticut, USA, is based on a dynamic combustor similar to that used in modern gas turbines (Fig. 35) (73). It is capable of handling 200-400 scfm and 5-10 gal/h of a wide variety of fuels including aviation fuel (J-P4, J-P5 or Jet A for instance), with or without contaminants, over a wide range of fuel to air ratios. The mixing and flow in the combustor closely approximate those of many conventional combustor designs and the critical features of the combustor chemistry are reproducible. Briefly, the fuel is introduced at the front end of the combustor by a pressure atomizing fuel nozzle and the combustion is stabilized in the forward section of the combustor by developing a strong swirl stabilized recirculation zone. The hot combustion gases from the forward sections of the combustor are cooled by dilution or secondary air jets which are located at the back of the facility. A wide variety of exhaust nozzles can be used to vary the cross-sectional geometry of the gas jet. By independently adjusting the primary and secondary air flow and the exit nozzle geometry, the velocity and temperature variations of combustion gases can be altered to match the combustion characteristics of a particular gas turbine. Also, by selecting the proper liners and changing the mass flows of air and fuel, the gas velocities can be varied from Mach 0.2 to Mach 0.8 and the gas temperature from 775 to 1875 K.

The NAE rig is shown in Fig. 36 along with the remotely controlled specimen stand to manipulate test specimens in and out of the hot gas stream for thermal fatigue or cyclic oxidation studies. A salt solution injection system for cyclic hot corrosion work and a solid particulate injection system for erosion studies are also available at NAE which allow the conduct of combined erosion, hot corrosion and

thermal fatigue studies. The NAE rig has been commissioned only recently to support research activities on high temperature materials and coatings of particular interest to aero engine operational groups of the Department of National Defence of Canada. On-going projects are concerned with the development of life extension techniques and residual life prediction models for turbine blades and vanes. Support is also being provided to an industrial partner for the development of new high performance coatings produced by chemical vapour deposition. Both coupon and component level testing are involved in this work.

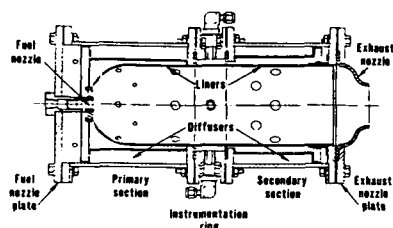


Figure 35: A schematic diagram showing the flame tube of the NAE combustor rig.

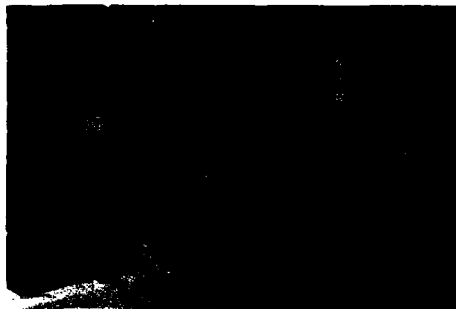


Figure 36. NAE Laboratory combustor rig (Beacon Inc. Model LCS 4B).

The NAE also intends to participate in a project of the Versailles Agreement on Advanced Materials and Standards (VAMAS) concerned with hot salt corrosion testing. To date, the lack of a reliable procedure for evaluating hot salt corrosion resistance of high temperature materials has been a major obstacle in evaluating the prospects of new materials and coatings for high temperature applications. A systematic attempt to correct this problem is being pursued by several VAMAS participants who have proposed another round robin test programme to evaluate the reliability and reproducibility of burner rig test data. Several laboratories from Canada, Japan, the United Kingdom and the United States have planned to participate in this programme under which rig data obtained under nominally identical test conditions will be compared and analyzed with a view to developing a standard test procedure for durability testing in rigs. It is beyond the scope of the present paper to discuss the details of the proposed programme. This is left to other contributors from the Specialists meeting, several of whom have been involved in the VAMAS programme definition from its inception.

11.0 CONCLUDING REMARKS:

This review has clearly shown that resistance to environmental attack and surface degradation of hot gas path components in gas turbines is strongly influenced by service conditions. Depending on the component and the operating environment, the surface degradation can be quite severe and can lead to loss of structural integrity and premature failures of components in engines.

Improving the resistance of gas path components to environmental attack is achieved by proper selection of alloys and proper use of protective coatings. The choice of an alloy or coating for a given application is a delicate task because of uncertainties associated with their long term stabilities and actual service conditions. This choice is further complicated by the absence of reliable standard test methods for evaluating materials in the laboratory. In addition, laboratory test results do not in general correlate well with actual service conditions, often leading to damage morphologies that differ substantially from those experienced in engines. Of all the laboratory test methods that might be considered, rig testing under simulated service conditions is probably the most powerful technique available. However, rig testing conditions unless properly controlled can also lead to unreliable results, as noted during the 1970 ASTM round-robin test programme.

Understanding the factors that control the hot section environment, along with reactions responsible for corrosive species in combustion gases, and their interactions with components downstream of combustor is an essential precursor to the development of realistic test methods for durability analysis of high temperature materials. The factors are many and their interactions are complex. Many pertain to the combustion process itself, and therefore, it is important that the operating environment of gas path components is reproduced as closely as possible in the laboratory in terms of the dynamics of gas flow for testing purposes.

ACKNOWLEDGEMENTS:

The authors are grateful to Messrs. D. Morphy and D. Chow of the Structures and Materials Laboratory of NAE for their timely preparations of all illustration material used in this review. The authors would also like to thank the Chief of Research and Development of the Department of National Defence of Canada for financial support and permission to publish the review. One of the authors (A.K. Gupta) would also like to thank the Natural Sciences and Engineering Research Council for the award of a fellowship and Dr. W. Wallace, Laboratory Head of the Structures and Materials Laboratory of the National Aeronautical Establishment (NAE) for providing him an opportunity to hold this fellowship at NAE.

REFERENCES

1. R.W. Fawley, The Superalloys, C.T. Sims and W.C. Hagel (eds.), John Wiley and Sons, Chapter I, 1972, 3.
2. G.W. Meetham, Met. Mat. Technol., 1976, 11, 589.
3. G.W. Meetham, J. Vac. Sci. Tech., 1985, A 3(6), 2509.
4. W.T. Reid, External Corrosion and Deposits in Boilers and Gas Turbines, Elsevier, NY, 1971, 115.
5. J. Stringer, Hot Corrosion in Gas Turbines, 1972, MCIC Report No. 72-08.
6. J.A. Goebel, F.S. Pettit and G.W. Goward, Met. Trans., 1973, 4, 261.
7. J.F. Stringer, AGARDograph-200, Advisory Group for Aerospace Research and Development, Paris (France), 1975.
8. J. Stringer, Ann. Rev. Mat. Sci., 1976, 7, 477.
9. J. Stringer, Proc. of the Symposium on the Properties of High Temperature Alloys (Z. Foroulis and F.S. Pettit, eds), Electrochemical Society, NJ, 1976, 513.
10. D.A. Shores and K.L. Luthra, Proc. of the Conf. on the Corrosion-Erosion Behaviour of Materials, St. Louis, MO, 17-18 Oct. 1978, 86.
11. J.F.G. Conde and C.G. McCreath, SAE Australia, 1980, 40(6) 265.
12. D.A. Shores, High Temperature Corrosion, R.A. Rapp (ed.) International Conference series, NACF-6, San Diego, CA, 1983, 493.
13. J.F.G. Conde, E. Erdoes and A. Rahmel, High Temperature Alloys for Gas Turbines, Brunetaud et al., (eds.), Proc. Conf., Liege, Belgium, D. Reidel Pub. Comp., 1982, 99.
14. F.S. Pettit and G.W. Goward, Coatings for High Temperature Applications, F. Lang, (ed.), App. Sci. Pub., Chapter I, 1983, 1.
15. F.S. Pettit and G.W. Goward, Superalloys Source Book, ASM, Metal Park, OH, 1984, 170.
16. S.R.J. Saunders, Met. Tech., 1984, 465.
17. P.C. Patnaik, High Temperature Oxidation and Corrosion of Nickel and Cobalt Based Superalloys, National Research Council of Canada, 1985, NAE-AN-33 (NRC No. 25075).
18. J. Stringer, High Temperature Corrosion in Energy Systems, M.F. Rothman, (ed.), The Met. Soc. of AIME, PA, 1985, 3.
19. G.H. Meier and F.S. Pettit, High Temperature Corrosion in Energy Systems, M.F. Rothman, (ed.), The Met. Soc. of AIME, PA, 1985, 161.
20. F.S. Pettit and C.G. Giggins, Superalloys II, C.T. Sims, N. Stoloff and W. Hagel, (ed.), J. Wiley & Sons, NY, Chapter 12, 1987, 327.
21. J. Stringer, Mat. Sci. Tech., 1987, 3, 482.
22. C. Durat-Thual, R. Morbioli and P. Steinmetz, A Guide to the Control of High Temperature Corrosion and Protection of Gas Turbine Materials, O. Morocutti, (ed.), Published by Commission of European Communities, Luxembourg, 1986.
23. P.C. Patnaik, J.E. Elder and R. Thamburaj, Superalloys 88, Proc. of the 6th International Symposium on Superalloys, sponsored by High Temperature Alloys committee of the Met. Soc. of AIME, PA, Sept. 18-22, 1988, 815.
24. D.W. McKee and G. Romeo, Met. Trans., 1973, 4, 1877.
25. D.W. McKee and G. Romeo, Proc. of 1974 Conf. on Gas Turbine Materials in a Marine Environment, J.W. Fairbanks and I. Machlin (eds.), Castaine, Maine, 1975, MCIC-Report No. 75-27, 183.
26. J.E. Restall, Proc. of 1974 Conf. on Gas Turbine Materials in a Marine Environment, J.W. Fairbanks and I. Machlin (eds.), Castaine, Maine, 1975, MCIC Report No. 75-27, 195.
27. J.E. Restall, Inst. Metallurgists, 1980, Series 3, 13(1), 4/13-4/26.
28. J.C. Galsworthy, J.E. Restall and G.C. Booth, High Temperature Alloys for Gas Turbines, Brunetaud et al., (eds.), Proc. Conf., Liege, Belgium, D. Reidel Pub. Comp., 1982, 207.
29. C.G. McCreath, Corr. Sci., 1983, 23(9), 1017.
30. H.J. Kolkman, Proc. of Sixth International Conf. on Corrosion by Liquid and Solid Impact, UK, 4-8 Sept. 1983.

31. G. Sorell, Proc. of Conf. on Corrosion-Erosion-Wear of Materials at Elevated Temperatures, Berkeley, CA, 27-29 Jan. 1986, NACE, 204.
32. F.C. Toriz, J. Wolverson and S. Gupta, Proc. of Conf. on Gas Turbines, Houston, TX, 18-21 March, 1985, 85-GT-94.
33. D.A. Spera, Thermal Fatigue of Materials and Components, ASTM-STP-612, (D.A. Spera and D.F. Mowbray eds.), ASTM publication, 1976, 3.
34. D.A. Woodford and D.F. Mowbray, Mat. Sci. Eng., 1974, 16, 5.
35. C.G. McCreath, Mat. Sci. Tech., 1987, 3, 494.
36. M. Van De Voorde, Mat. Sci. and Eng., 1987, 88, 341.
37. P. Hancock, Mat. Sci. and Eng., 1987, 88, 303.
38. H. Von E. Doering, High Temperature Corrosion in Energy Systems, M.F. Rothman, (ed.), The Met. Soc. of AIME, PA, 1985, 77.
39. A.J.A. Mom and H.J. Kolkman, Proc. Conference on Gas Turbines, Amsterdam, 1984, ASME, 84-G-256.
40. J.F.G. Conde, G.C. Booth and A.F. Taylor, Mat. Sci. Tech., 1986, 2, 314.
41. L.L. Hsu, Surf. and Coat. Tech., 1987, 32(1-4), 1.
42. G.W. Goward, Mat. Sci. Tech., 1986, 2, 194.
43. G.W. Goward, High Temperature Corrosion, R.A. Rapp (ed.), International Conf. Series, NACE-6, San Diego, CA, 1983, 553.
44. C. Duret, A. Davin, G. Marijnissen and R. Pichoir, High Temperature Alloys for Gas Turbines, R. Brunetaud et al., (eds.), Proc. Conf., Liege, Belgium, D. Reidel Pub. Comp., 1982, 53.
45. P.C. Patnaik and J.-P. Immarigeon, "High Temperature Protective Coating for Aero Engine Gas Turbine Components, National Research Council of Canada, NAE-AN-42, NRC No. 26475, 1986; See also J. Adv. Mat. Manf. Proc., 1989, 4(2), (in press).
46. J.H. Wood and E. Goldman, Superalloys II, C.T. Sims, N. Stoloff and W. Hagel, (eds.), John Wiley and Sons, NY, Chapter 13, 1987, 359.
47. R. Mevrel, C. Duret and R. Pichoir, Mat. Sci. Tech., 1986, 2, 201.
48. G.W. Goward and L.W. Cannon, J. Eng. Gas Turb. Pow., 1988, 110, 150.
49. G. Lehnert, British Patent, 121006, 1970.
50. G. Lehnert and H. Meinhard, Electrodep. Surf. Treat., 1972-73, 189.
51. M.R. Jackson and J.R. Rairden, Met. Trans. A, 1977, 8, 1697.
52. J.A. Goebel, R.H. Barkalow and F.S. Pettit, Tri-Service Conf. on Corrosion, 1978, MCIC Rept. No. 79-40, 165.
53. R.P. Seeling and R.J. Stuber, High Temp. High Press., 1978, 10, 207.
54. R.G. Wing and R.I. McGill, Plat. Met. Rev., 1981, 25, 94.
55. R.L. Clarke, David Taylor Naval Scientific Research and Development Centre, Annapolis, MD, 1981, DTNS RDC Rept. No. SME-81/60.
56. R. Streiff and D.H. Boone, International Metallic Cong. on Corrosion, Toronto, 1984, 3, 489.
57. G.J. Tatlock and T.J. Hurd, Oxid. Met., 1984, (5-6), 22.
58. J.W. Fairbanks and R.J. Hecht, Mat. Sci. & Engg., 1987, 88, 321.
59. F.D. Lordi, A.D. Foster and W.D. Schilling, Mod. Pow. Sys., 1983, 3, 37.
60. S. Stecura, Effects of Compositional Changes on the Performance of a TBC System, 1978, NASA-TM-78976.
61. J.R. Nicholls and P. Hancock, Ind. Corr. 1987, 5(4), 8.
62. T.N. Rhy-Jones, Mat. Sci. Tech., 1988, 4, 421.
63. N. Czech, W. Epeer and F. Schmitz, Mat. Sci. Tech., 1986, 2, 244.
64. A. Strang and E. Lang, High Temperature Alloys for Gas Turbines, R. Brunetaud et al., (eds.), Proc. Conf. Liege, Belgium, Reidel Pub. Comp., 1982, 469.
65. A.R. Nicholls, Coatings for High Temperature Applications, E. Lang (ed.), App. Sci. Pub., Chapter 9, 1983, 269.

66. J.E. Restall, Environmental Degradation of High Temperature Materials, vol. 1, Spring Residential Conf. Series, 3, 13, Inst. Met., London, 1980, 4/13-4/26.
67. D.W. McKee, R. McCarron, D. Chatterji and H.S. Spacil, 3rd UK/US Navy Conf. on Gas Turbine Materials in a Marine Environment, University of Bath, Bath (UK), 1976.
68. R.E. Fryxell and I.I. Bessen, Proc. of 1974 Naval Conf. on Gas Turbine Materials in a Marine Environment, J.W. Fairbanks and I. Machlin (eds.), Castaine, Maine, 1975, MCIC Rept. No. 75-27, 259.
69. P.F. Hawkins, 4th US/UK Navy Conf. on Gas Turbine Materials in a Marine Environment, vol. II, U.S. Naval Sea Command, Annapolis, MD, 1979, 49.
70. F.J.D. Tasker, C.W. Harris and N.S. Musgrave, Deposition and Corrosion in Gas Turbines, A.B. Hart and A.J.E. Cutler (eds.), A Halsted Press Book, 1973, 385.
71. H. Gilder and R. Mirobioli, High Temperature Alloys for Gas Turbines, D. Coutsouradis et al., (eds.), App. Sci. Pub., London, 1978, 125.
72. Ch. Just, High Temperature Alloys for Gas Turbines, Coutsouradis et al., (eds.), Proc. Conf. Liege, Belgium, App. Sci. Pub., London, 1978, 147.
73. R.R. Dils and F.S. Follansbee, Corrosion, NACE, 1977, 33(11), 385
74. A.K. Misra, Corrosion, NACE, 1987, 43(7), 440.
75. B.O. Buckland, A.D. Foster and J.J. Treanor, The Life of Gas Turbine Parts as Limited by Elevated Temperature Corrosion, Presented at the NACE Annual Meeting, Miami, FA, April 21, 1966.
76. W.A. Rentz, W.R. Freeman, Jr., and J.J. Walters, J. Mat., 1969, 4(3), 520.
77. H. Von E. Doering and P. Bergman, Mat. Res. Stand. 1969, 9(2), 35.
78. Hot Corrosion in Gas Turbines: Mechanisms, Alloy and Coating Development, Environmental Effects and Evaluations, NMAB-260, National Materials Advisory Board, Washington, DC, 1970.
79. S.Y. Lee, S.M. DeCorso and W.E. Young, J. Eng. Power, 1971, 93(3), 313.
80. K. Page and R.J. Taylor, Deposition and Corrosion in Gas Turbines, A.B. Hart and A.J.E. Cutler, (eds.), A Halsted Press Book, 1973, 350.
81. J.F.G. Conde and G.C. Booth, Deposition and Corrosion in Gas Turbines, A.B. Hart and A.J.E. Cutler, (eds.), A Halsted Press Book, 1973, 278.
82. P.C. Felix, Deposition and Corrosion in Gas Turbines, A.B. Hart and A.J.E. Cutler, (eds.), A Halsted Press Book, 1973, 331.
83. J.W. Schultz and W.R. Hulsizer, Met. Engg., Quart., 1976, 16(3), 15.
84. A.D. Foster, H. Von E. Doering and J.W. Hickley, Fuel Flexibility in GE Gas Turbines, GER-2222L, General Electric, 1977.
85. G.C. Booth and R.L. Clarke, Mat. Sci. Tech., 1986, 2, 272.
86. S.J. Dapkunas, Conf. Proc., 1972 Gas Turbine Materials, Naval Ship Engineering Centre, Naval Air System Command, Washington, DC, 1972, 151.
87. J.A. Goebel, F.J. Felton and F.S. Pettit, Proc. of 1974 Conf. on Gas Turbine Materials in a Marine Environment, J.W. Fairbanks and I. Machlin (eds.), Castaine, Maine, 1975, MCIC Rept. No. 75-27, 93.
88. D.L. Deadmore, C.E. Lowell and F.J. Kohl, Corr. Sci. 1979, 19, 371.
89. P. Hancock, Corr. Sci., 1982, 22(1), 51.
90. R.R. Dils, "A New Material Test Combustor", Presented at the 5th Annual AIME Spring Meeting, Philadelphia, PA, May 29-June 1, 1973.
91. R.R. Dils, "Dynamic Gas Temperature Measurements in a Gas Turbine Transition Duct Exit, 1972, ASME-GT-73-67-7.
92. Jet Propulsion for Space Applications, W.J. Heise and N.V.S. Munford, Jr. (eds.), Pitman Pub. Corp., NY, 1964, 209.
93. The Jet Engine, Rolls Royce Ltd. Derby, UK, Pub #T.S.D., 1302, 3rd revised edition, 1973.
94. J.F.G. Conde and C.G. McCreath, J. Nav. Sci., 1981, 7(2) 124.
95. H. Von E. Doering, Conf. Proc. 1972 on Gas Turbine Materials, Naval Ship Engineering Centre, Naval Air System Command, Washington, DC, 1972, 143.
96. A.F. Taylor, B.A. Wareham, G.C. Booth and J.F.G. Conde, 3rd UK/US Navy Conf. on Gas Turbine Materials in a Marine Environment, University of Bath, Bath, 1976, Session III, Paper III.

97. A.B. Hart, J.W. Laxton, C.G. Stevens and D. Tidy, High Temperature Alloys for Gas Turbines, Coutsouradis et al., (eds.), Proc. Conf. Liege, Belgium, App. Sci. Pub., London, 1978, 816.
98. R. Huber, High Temperature Alloys for Gas Turbines, Coutsouradis et al., (eds.), Proc. Conf. Liege, Belgium, App. Sci. Pub., London, 1978, 251.
99. P. Hancock, 4th US/UK Navy Conf. on Gas Turbine Materials in a Marine Environment, Vol. II, U.S. Naval Sea Command, Annapolis, MD, 1979, 465.
100. J.F.G. Conde and C.G. McCreath, J. Nav. Sci., 1981, 7(3), 184.
101. S.R.J. Saunders, M.K. Hossain and J.M. Ferguson, High Temperature Alloys for Gas Turbines, W. Weltz et al., (eds.), Proc. Conf., Liege, Belgium, D. Reidel Pub. Comp., London, 1982, 177.
102. S.R.J. Saunders, Surf. Eng., 1985, 1(3), 179.
103. S.R.J. Saunders, Mat. Sci. Tech. 1986, 2, 28.
104. W.L. Fielder, C.A. Stearns and F.J. Kohl, Reactions of NaCl with Gaseous SO₂, SO₃ and O₂, 1983, NASA-TM-83423.
105. L.V. Shelton and R.S. Carlton, J. Eng. Gas Turbine Power (Trans ASME), 1984, 106, 819.
106. J.S. Hobday and J.S. Havill, J. Eng. Gas Turb. Power (Trans. ASME), 1988, 110, 321.
107. A.J. Clarke, "Endurance Testing of a Rolls Royce Tyne Engine in a Marine Environment", Naval Wing Note #7167, NGTE, Pyestock, Hants, UK.
108. L.J. Young, "A Report of the Salt in Air Sampling Trials Carried out in HDMS Pedar Skram", Oct/Nov. 1966, Naval Marine Wing Noted NT/648, NGTE, Pyestock, Hants, UK.
109. R.E. Kaufman and R.J. Pollini, Proc. Conf. on Gas Turbines, Houston, Texas, 1967, ASME Paper, 67-GT-44.
110. 'Code of Practice for Gas Turbine Intake and Exhaust, D.G. Ships /522,03/25/215, Rept. No. JB/JLN/RM, NGTE, National Gas Turbine Establishment, Naval Marine Wing, Pyestock, Hants, UK, 1973.
111. A. Meszaros, R.K. Jack and H.E. Gerber, Progress Report on Sea Salt Measurements, NRL Memo Report 3270, American National Research Laboratory, Washington, DC, 1976.
112. C. Frazier, R. Ruskin, L. Radke, E. Mihalek, K. Phillips, H. Ozarko and D. Taylor, 3rd UK/US Navy Conf. on Gas Turbine Materials in a Marine Environment, University of Bath, Bath, UK, 1976, paper III, Session II.
113. N.S. Bronstein, M.A. DeCrescente and M.A. Roth, Proc. of 1974 Gas Turbine Materials in a Marine Environment, J.W. Fairbanks and I. Machlin (eds.), Castaine, Maine, 1975, MCIC Report #75-27, 115.
114. P. Carter, 4th US/UK Conf. on Gas Turbine Materials in a Marine Environment, Vol. I, U.S. Naval Sea Command, Annapolis, MD, 1979, 1.
115. W.D. Halstead, Deposition and Corrosion in Gas Turbines, A.B. Hart and A.J.E. Cutler, (eds.), A Halsted Press Book, 1973, 23.
116. J.G. Tschinkel, Corrosion NACE, 1972, 28(5), 161.
117. V.I. Hanby, J. Eng. Power (Trans. ASME), 1974, 86, 129.
118. P.M. Johnson, D.P. Whittle and J. Stringer, Corr. Sci., 1975, 15, 721.
119. Y. Bourdis and C. St. John, Oxid. Met., 1975, 9, 507.
120. D.W. McKee, D.A. Shores and K.L. Luthra, J. Electrochem. Soc., 1978, 125, 411.
121. F.J. Kohl, C.A. Stearns and G.C. Fryburg, 4th US/UK Navy Conf. on Gas Turbine Materials in a Marine Environment, Vol. II, U.S. Naval Sea Command Annapolis, MD, 1979, 565.
122. T.I. Barry and A.T. Disdale, Mat. Sci. Tech., 1987, 3, 501.
123. F.J. Kohl, C.A. Stearns and G.C. Fryburg, Sodium Sulphate: Vaporization Thermodynamics and Reactions in Corrosive Flames, NASA-TM-X-71641.
124. A.J.B. Cutler, Mat. Sci. Tech., 1987, 3, 512.
125. C.G. McCreath, 4th US/UK Navy Conf. on Gas Turbine Materials in a Marine Environment, Vol. II, US Naval Sea Command, Annapolis, MD, 1979, 126, 339.
126. J.F.G. Conde, N. Birks, M.G. Hocking and V. Vasantsree, 4th US/UK Navy Conf. on Gas Turbine Materials in a Marine Environment, Vol. II, US Naval Sea Command, Annapolis, MD, 1979, 385.
127. P. Hancock, J. Electrochem. Soc., 1978, 78(1), 645.

128. P. Hancock, Proc. of 1974 Conf. on Gas Turbine Materials in a Marine Environment, J.W. Fairbanks and I. Machlin (eds.), Castaine, Maine, 1975, MCIC Rept. No. 75-27, 225.
129. C.A. Stearns, R.A. Miller, F.J. Kohl and G.C. Fryburg, Gaseous Na_2SO_4 Formation in Flames and Flowing Gas Environment, 1977, NASA-TM-73600.
130. C.A. Stearns, R.A. Miller, F.J. Kohl and G.C. Fryburg, J. Electrochem. Soc., 1977, 124, 1145.
131. F.J. Kohl, G.J. Santoro, C.A. Stearns and G.C. Fryburg, J. Electrochem. Soc., 1979, 126, 1054.
132. D.J. Wortman, R.E. Fryxell and I.I. Bessen, 3rd US/UK Navy Conf. on Gas Turbine Materials in a Marine Environment, the University of Bath, Bath, UK, 1976, Paper II, Session V.
133. D.A. Shores, K.L. Luthra and D.W. McKee, High Temperature Metal Halide Chemistry, D.L. Hildenbrand and D.D. Cubicciotti (eds.), The Electrochemical Society Inc., P.O. Box 2071, Princeton, NJ, 1978, 538.
134. W.D. Halstead and A.B. Hart, "The Role of Chlorides in Corrosion by Flue Gas Deposit," CGEB RD/L/M-272.
135. H. Boettger and F. Umland, Untersuchungen Zur Hochtemperaturkorrosion durch chloride, Werkstoffe und Korrosion, 1974, Heft II.
136. E.J. Felton and F.S. Pettit, "Pratt and Whitney Quarterly report," 1 March 1976 - 31 May, 1976., NRL Contract # N00173-76-C-0146.
137. T.J. Radzavich and F.S. Pettit, "Pratt and Whitney Quarterly report," 1 June 1976 - Aug. 1976, NRL Contract # N00173-76-C-0146.
138. R.L. Jones and S.T. Gadomski, J. Electrochem. Soc., 1977, 124, 1641.
139. C.A. Stearns, F.J. Kohl, G.C. Fryburg and R.A. Miller, High Temperature Metal Halide Chemistry, D.L. Hildenbrand and D.D. Cubicciotti (eds.), The Electrochemical Society, P.O. Box 2071, Princeton, NJ, 1978, 555; NASA-TM73796.
140. V. Patarini, N.S. Bronstein and M.A. DeCrescente, Hot Corrosion of Gas Turbine Components, ASME paper No. 78-GT-82.
141. M.K. Hussain, J.E. Rhoades and S.R.J. Saunders, Proc. Conf. on Behaviour of High Temperature Alloys in Aggressive Environments, Petten (NH), The Netherlands, The Metal Society for the Commission of the European Communities, 1979, 483.
142. P. Hancock, Mat. Sci. Tech., 1987, 3, 536.
143. J.G. Smeggil and N.S. Bronstein, Study of the Effects of Gaseous Environments on Sulphidation Attack of Superalloys, 1977, NASA-CR-135348.
144. J.G. Smeggil, N.S. Bronstein and M.A. DeCrescente, "Ash-Deposits and Corrosion due to Impurities in Combustion Gases," R.W. Bryers, (ed.), Hemisphere Pub. Corp., Washington, DC, 1978, 271.
145. C.A.C. Sequeira and M.H. Hocking, J. App. Electrochem., 1978, 8, 179.
146. F. Mansfield, N.E. Paton and W.M. Robertson, Met. Trans. 1973, 4, 321.
147. R.H. Barkalow and F.S. Pettit, Degradation of Coating Alloys in Simulated Marine Environments, NRL contract # N00173-76-C-0146, Final Report, June 15, 1978.
148. R.L. Jones and J.W. Fairbanks, Proc. of 1974 Conf. on Gas Turbine Materials in a Marine Environment, J.W. Fairbanks and I. Machlin (eds.), Castaine, Maine, 1975, MCIC Report #75-27, 219.
149. D.J. Wortman, R.E. Fryxell, K.L. Luthra and P. Bergman, 4th US/UK Navy Conf. on Gas Turbine Materials in a Marine Environment, Vol. I, US Naval Sea Command, Annapolis, MD, 1979, 317.
150. P. Hancock, High Temperature Metal Halide Chemistry, D.L. Hildenbrand and D.D. Cubicciotti, (eds.), The Electrochemical Society, P.O. Box 2071, Princeton, NJ, 1978, 645.
151. J.F.G. Conde and B.A. Wareham, Proc. of 1974 Gas Turbine Materials in a Marine Environment, J.W. Fairbanks and I. Machlin, (eds.), Naval Ship Engineering Centre, Naval Air System Command, Castaine, Maine, 1975, MCIC Report No. 75-27, 73.
152. C.G. Stevens and D. Tidy, J. Inst. Energy, 1981, 3, 2.
153. M.A. DeCrescente and N.S. Bronstein, Corrosion, 1968, 24, 127.
154. J.F.G. Conde, High Temperature Corrosion in Aerospace Alloys, AGARD-CP-120, 1972, 203.
155. C.A. Stearns, F.J. Kohl and D.E. Rosner, High Temperature Corrosion, R.A. Rapp, (ed.), International Conference Series, NACE-6, San Diego, CA, 1983, 441.
156. G.J. Santoro, F.J. Kohl, C.A. Stearns, S.A. Gokuglu and D.E. Rosner, "Experimental and Theoretical Deposition Rates from Salt Seeded Combustion Gases of Mach 0.3 Burner Rig, 1984, NASA-TM-2225.

157. S.A. Gokuglu and G.J. Santoro, Experimental Verification of Corrosive Vapour Deposition Theory in High Velocity Burner Rigs, 1986, NASA-TM-87287.
158. G. Vermes, J. Eng. Power, 1979, 101, 542.
159. P.J. Jackson, Ash Deposits and Corrosion Due to Impurities in Combustion Gases, R.W. Bryers, (ed.), Hemisphere Pub., Washington DC, 1978, 147.
160. G.C. Booth and J.F.G. Conde, 4th US/UK Navy Conference on Gas Turbine Materials in a Marine Environment, Vol. I, US Naval Sea Command, Annapolis, MD, 1979, 253.
161. G.C. Booth, J.C. Galsworthy and A.F. Taylor, 4th US/UK Navy Conference on Gas Turbine Materials in a Marine Environment, Vol. I, US Naval Sea Command, Annapolis, MD, 1979, 259.
162. R.M. Shirmer and H.T. Quigg, Phillips Petroleum Corp., Research and Development Report 4370-66R, 1966.
163. A. Ishida, I. Tomizuka, K. Ogawa, Y. Sato and M. Yamazaki, Trans. Nat. Res. Inst. Met., 1988, 30(1), 15.
164. M.J. Moore and R.I. Crane, Deposition and Corrosion in Gas Turbines, A.B. Hart and A.J.E. Cutler, (eds.), A Halsted Press Book, 1973, 35.

SURFACE PROPERTY IMPROVEMENT IN TITANIUM ALLOY GAS TURBINE COMPONENTS THROUGH ION IMPLANTATION

by

J.E. Elder, M.R. Pishva, N.C. Bellinger, P.C. Patnaik and R. Thamburaj

Research and Technology Development Group
Orenda Division
Hawker Siddeley Canada Inc.
3160 Derry Road East
Mississauga, Ontario
Canada, L4T 1A9

ABSTRACT

The feasibility of applying ion implantation to produce substantial improvement in the wear/fretting fatigue resistance of titanium alloys used as gas turbine fan and compressor blade material has been studied. Detailed microscopy and mechanical test results have been used to analyze the various mechanisms contributing to wear and fretting fatigue damage in titanium alloys at room and elevated temperatures. The manner in which ion implantation might modify the normal wear/fretting fatigue response of these alloys is discussed in detail, along with the factors to be considered in choosing optimum ion implantation parameters.

1. INTRODUCTION

The beneficial effects of ion implantation in improving a wide variety of surface mechanical and chemical properties of metals and alloys are well established (1,2). In a gas turbine engine where titanium alloys used in the rotating components degrade due to wear, fatigue and fretting fatigue, improvement in the component lives may be achieved by ion implantation, leading to a reduction in expensive component replacement costs as well as increasing flight safety.

Fretting is a type of surface degradation which results from oscillating slip between two surfaces in contact under a normal load as shown in Figure 1. In situations where fretting occurs in the presence of cyclic stress or relative motion between the two contacting surfaces, the surface degradation which occurs is termed fretting fatigue.

Every surface, no matter how polished, has a degree of micro-roughness associated with it. The so called "hills" which comprise this micro-roughness are termed asperities. When two surfaces are placed together, they are only in contact at the asperities. In the initial stages of fretting, when a normal load is applied to the two surfaces in contact and relative movement is occurring as a result of a cyclic load, debris is generated due to the adhesion of the asperity tips on the two surfaces and

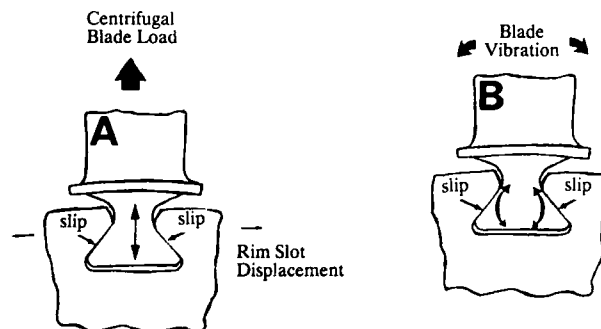


Fig. 1 Fan blade dovetail displacements which cause fretting as a result of (a) alternating centrifugal forces and (b) natural blade vibration.

subsequently breaking off of these tips. Once generated, this debris may either re-adhere after only causing a small amount of abrasive damage or it may oxidize and subsequently cause considerable abrasive damage, (Figure 2). In fretting, both situations occur. As the number of fretting cycles increase, the amount of oxidized debris increases which causes severe abrasion of the surface to begin.

In the intermediate stages of fretting, the severe abrasion caused by the debris results in the development of rough trench like marks (known as scoring) and the formation of deep pits. Pits are formed in areas where debris has built up and the debris abrasively digs into the material during the relative movement of the two surfaces. It is in these region of the pits where cracks are most likely to initiate and then propagate to failure as a result of the cyclic loading. This premature fatigue crack initiation has a significant effect on the life of rotating components, since for alloys such as titanium, the largest part of the fatigue life is taken up in the crack initiation stage. This effect is illustrated schematically in the S/N curves in Figure 3.

In the present work, the fretting fatigue properties of titanium alloys at elevated temperatures are reviewed. Results from in-service exposure of Ti-6Al-4V alloy fan and compressor blades from a gas turbine engine with respect to their degradation in the dovetail are analyzed and the modes established. Types of ions and the optimum conditions of their implantation into Ti-6Al-4V, in order to improve the blade lives are presented. Transmission electron microscopy (TEM) results on ion implanted Ti-6Al-4V are presented and discussed.

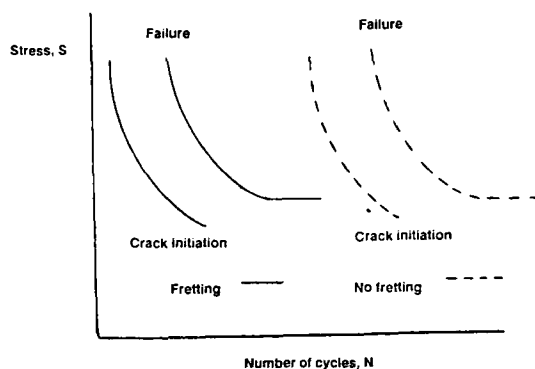


Fig. 3 Effect of fretting on fatigue life.

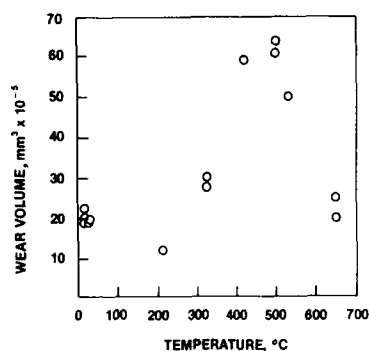


Fig. 4 Fretting wear volume as a function of fretting temperature for pure titanium (Ref. 5).

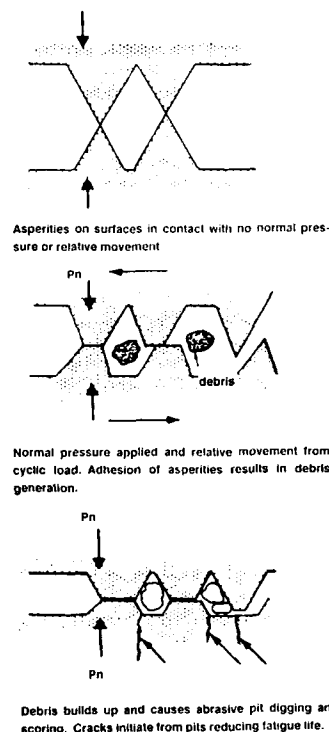


Fig. 2 Schematic of fretting fatigue mechanism.

2. FRETTING FATIGUE OF TITANIUM ALLOYS AT ELEVATED TEMPERATURES

Fretting wear is quite different from other modes of wear and occurs principally in oxidizing environments. The principal characteristics of fretting are that it is caused by a combination of adhesion, abrasion and oxidation. In fretting fatigue, cracks are initiated within the abraded pits on the fretted surface.

Oxidation complicates the fretting process by making it very sensitive to environmental factors such as temperature and reactivity. In strongly oxidizing atmospheres, fretting wear or fretting fatigue is greatly accelerated and are therefore often termed fretting corrosion. It is possible that oxidation could enhance material loss through the cyclic removal of an oxide film that forms on the contact surface during the interval between fretting strokes.

The effect an oxide film has on fretting depends on the oxidation kinetics of the contacting materials and therefore also on the temperature. For instance, transition from slow logarithmic oxidation to parabolic oxidation occurs at approximately 550°C for the case of titanium. As illustrated in Figure 4, this also corresponds to a sudden reduction in the fretting wear rate⁽³⁾. Inspection of titanium surfaces fretted above 650°C revealed a relatively damage free surface, whereas surfaces fretted below 500°C revealed evidence of oxide film disruption accompanied by loose debris and pitting of the metal surface. For a given metal and temperature, the oxide film will be beneficial in fretting wear only if a critical thickness is maintained, provided the adhesion to the base metal is sufficient. It would appear that for the case of Ti, this critical oxide film thickness is only attained during parabolic oxidation, i.e. at temperatures > 550°C.

On the other hand, at room temperature, most alloy systems, including titanium, are unable to maintain this critical oxide thickness and one of two situations will prevail. In locations on the fretting surfaces where the contact is metal to metal, strain hardening strengthens the surfaces preventing or slowing down the formation of wear particles. In addition, since the sliding distance is so small in fretting, wear particles can become trapped and subsequently re-adhere to the bare metal resulting in less net material loss. Alternatively, if wear particles become oxidized, or if oxide is disrupted from the fretting surfaces forming debris, an abrasive mode of wear can prevail.

Broszeit et al⁽⁴⁾ found that the fretting fatigue strength of Ti-6Al-4V was dependent upon the testing environment. Fretting fatigue tests at room temperature in dry air and nitrogen reported approximately the same results. For the fretting damage and resultant fatigue strength reduction to be the same in both these atmospheres, this alloy must wear predominantly by a mechanism of adhesion during fretting, even in an oxidizing atmosphere. Titanium does not form a thick adherent protective oxide film during fretting at low temperatures (< 500°C) and the debris and pits which form on surfaces of titanium fretted in air at room temperature are indicative of adhesion⁽³⁾. It is likely that abrasion by oxidized debris and particle generation via

delamination also occur but are outweighed by particle generation through the mechanism of adhesion. Results of Hamdy and Waterhouse⁽⁵⁾ support this hypothesis where their studies indicate that adhesion is the dominant mode of fretting in Ti-6Al-4V for temperatures below 400°C. It is likely that in the more advanced stages of fretting, abrasion by oxide debris may become more predominant. It should be noted that for temperatures >400°C, the results shown in Figure 4 clearly indicate that oxidation must play a large role in the mechanism of fretting of Ti. In addition to the deleterious effect on fretting fatigue of Ti alloys which may be expected from oxidation, oxygen diffusion may also serve to reduce the fretting fatigue strength according to an entirely different mechanism. It has been found that in the case of $\alpha+\beta$ titanium alloys, oxygen diffuses relatively deep into the material along the α/β phase interfaces under the combined effect of temperature (>400°C) and stress. This may cause cracking of the interfaces leading to a reduction in the fatigue or fretting fatigue strength.

3. CHARACTERIZATION OF SURFACE DAMAGE IN PREMATURELY RETIRED FAN AND COMPRESSOR BLADES

3.1 EXPERIMENTAL MATERIALS AND METHODS

Retired first and second stage fan blades as well as third stage compressor blades from an advanced turbofan engine were examined to determine the type of service damage experienced by the dovetail region. All the blades are manufactured from Ti-6Al-4V alloy and coated with a thermally sprayed Cu-Ni-In coating on the pressure surfaces of the dovetail. In addition, a solid film lubricant coating, MoS₂ is used on top of the Cu-Ni-In coating in order to protect it during assembly. Various analytical techniques such as optical and scanning electron microscopy and energy dispersive X-ray analysis (EDAX) were used to analyze the service damage.

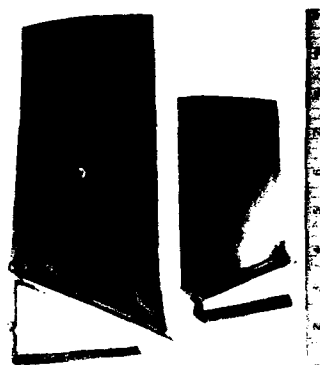


Fig. 5 First and second stage fan blades of an advanced aeroengine, respectively.

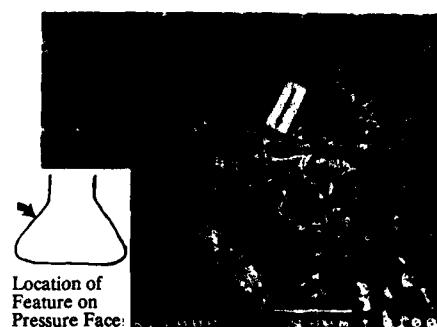


Fig. 6 Crack like defect present on fan blade dovetail pressure surface.

3.2 IN SERVICE DAMAGE TO RETIRED STAGE 1 AND 2 FAN BLADE DOVETAIL PRESSURE FACES

Moderate to severe fretting wear were observed on the dovetail pressure surfaces of several first and second stage fan blades (Figure 5). Small crack-like defects as shown in Figure 6, were found on the pressure faces extending into the parent material. The fretting damage has been associated with service induced slip at the interface between the dovetail pressure surface and the fan disc rim slot.

Typical dovetail pressure surface damage experienced by the first and second stage blades are shown in Figure 7a and 7b, respectively. It was observed that in both blades, wear scars were formed in a direction parallel to the longitudinal axis of the blade. Based on an optical examination of a number of retired stage 1 and 2 blades, it was quite apparent that the dovetail pressure surfaces of the second stage blades were subjected to a more severe fretting wear. The difference in the fretting damage between the two blades is perhaps associated with an increased freedom to vibrate since the stage 2 blades do not have the mid span dampers which the first stage blades have.



Fig. 7 Typical fretting on the dovetail pressure surface of (a) first stage fan blade and (b) second stage fan blade.



Fig. 8 Typical delamination of MoS₂ coating on fan blade.

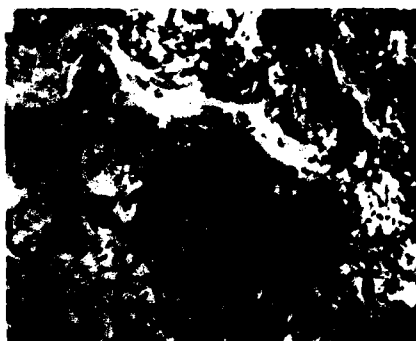


Fig. 9 Typical appearance of fretting wear damage on Cu-Ni-In coating for a stage 2 fan blade.

The molybdenum disulfide (MoS₂) solid lubricant coating was present only in limited quantities on the pressure surfaces of the first and second stage blades. The exception to this was found only in a few low time stage 1 blades where up to approximately one third of the pressure surface area still contained the MoS₂ coating. The failure mechanism for the MoS₂ coating was found to be delamination at the MoS₂/Cu-Ni-In interface (Figure 8).

The fretting action on the Cu-Ni-In coating was found to result in a material removal process consisting of a crumbling phenomenon which involved delamination to a lesser extent (Figure 9). In this coating, delamination typical of plasma sprayed coatings was found to occur along the plasma sprayed layers rather than at the Cu-Ni-In/Ti-6Al-4V interface (Figure 10). Therefore, it was concluded that the Cu-Ni-In coating had good adherence to the Ti-6Al-4V substrate. The surface crumbling process is believed to occur as either failure at the discontinuities within the coating (as shown by arrows in Figure 10) or by surface embrittlement due to oxidation. It should be pointed out that Cu-Ni-In is a soft coating and serves to inhibit fretting of the Ti-6Al-4V by reducing the shear loads which are transmitted to the surface of the Ti-6Al-4V by the fretting motion. Examination of several service exposed blade pressure surfaces by SEM indicated that very little of the Ti-6Al-4V substrate was directly attacked by the fretting action.



Fig. 10 Discontinuities within the plasma sprayed Cu-Ni-In coating on the first stage fan blade dovetail.

3.3 IN SERVICE DAMAGE TO THIRD STAGE COMPRESSOR BLADE DOVETAIL PRESSURE SURFACES

In contrast to the fan blades, the service exposed third stage compressor blades showed severe signs of wear, fretting, Cu-Ni-In coating delamination, oxidation and pitting on the dovetail pressure surfaces. The substrate Ti-6Al-4V was attacked and cracking was observed. The fretting damage observed on the pressure surface can be categorized as follows:

Mode 1: This type of damage is associated with the formation of wear or score marks and pits on the dovetail pressure face, an illustration of which is presented in Figure 11.

Mode 2: This type of damage is associated with the deformation of the pressure face base which can result in the formation of cracks. This deformation is associated with unusually high loading conditions imposed upon the blade during service which results in the extrusion of the Cu-Ni-In coating, Figure 12. The effectiveness of this coating can drastically be reduced due to this reduction in thickness and further contribute towards the initiation of a number of fine cracks, Figure 13. The deformation of the coating by extrusion has been commonly observed at the corner regions of the pressure face. This extruded coating tends to oxidize readily at the dovetail temperature, Figure 14. The coating is degraded even further when the debris chips generated from the oxidized coating is trapped between the dovetail and disc surface.

Mode 3: This type of damage is associated with the formation of localized pits and the premature initiation of cracks in the coating as well as in the substrate which is the most severe of all the damage that has been observed on the pressure face, Figure 15. All cracks found on the dovetail region of the blade which were present in both the coating and base material initiated on the pressure surface as shown in Figure 16. It was found that all these cracks had initiated in an area of the pressure surface where the coating had either been totally removed or significantly decreased in thickness. The cracks subsequently grew at an angle of approximately 45° to the pressure face. There was also evidence that the crack grew under a combination of HCF/LCF loading conditions due to the presence of striations on the fracture surfaces examined.

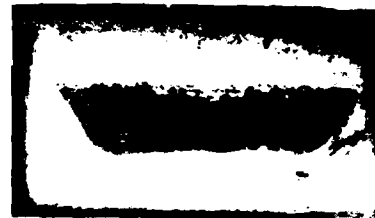
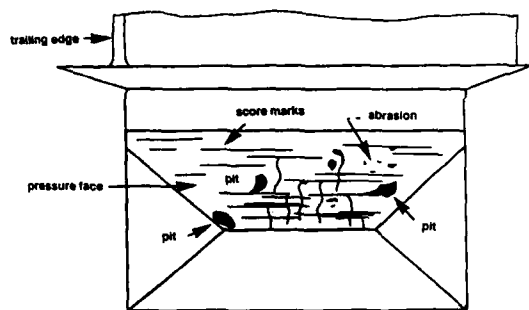


Fig. 11 Mode 1 damage showing scoring of dovetail pressure surface.

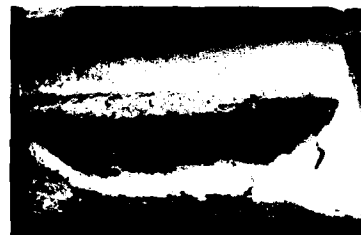
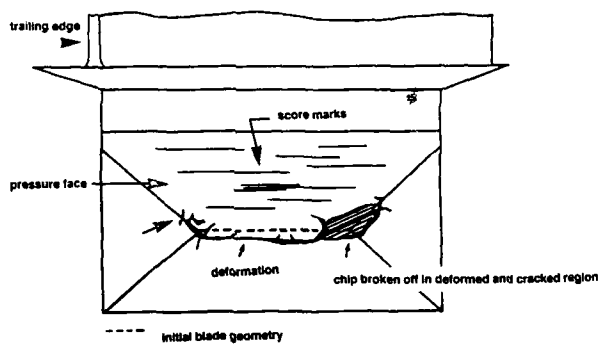


Fig. 12 Mode 2 damage showing extrusion of Cu-Ni-In coating.

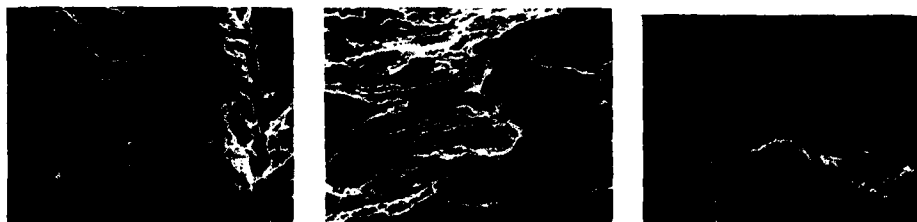


Fig. 13 Micrograph showing cracks present in the Cu-Ni-In coating.

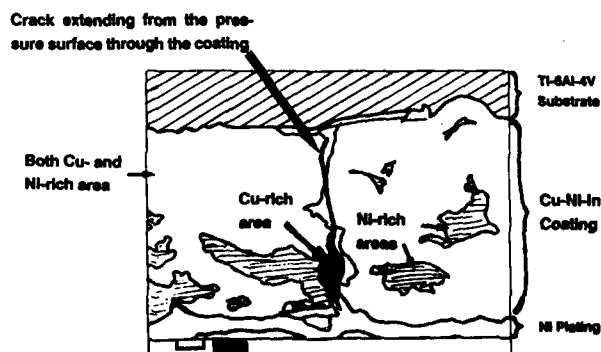


Fig. 14 Back scattered electron image (above) and schematic of a third stage compressor dovetail showing enriched Cu and Ni regions (left).

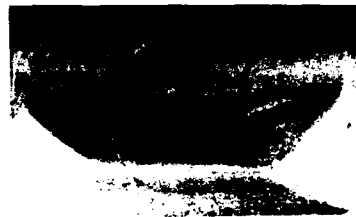
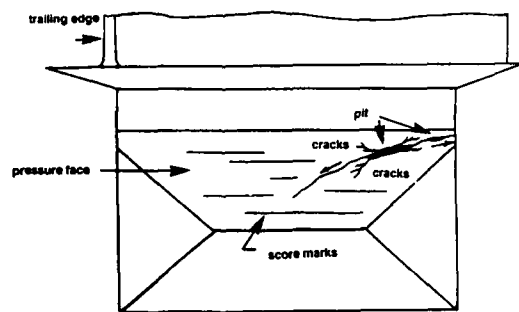


Fig. 15 Mode 3 damage showing cracks in the Cu-Ni-In coating which extend into the Ti-6Al-4V substrate.



Fig. 16 Scanning electron micrograph showing (a) crack initiation site and (b) striations present on the fracture surface.

3.4 EFFECT OF TEMPERATURE ON THE MODE OF FRETTING DAMAGE

Where fretting fatigue of Ti alloy gas turbine engine components is concerned, the effect of temperature on the fretting process can be quite significant. It is likely that the mechanism of fretting in fan blades which operate at ambient temperatures would be quite different than compressor blades which operate at temperatures ranging from 400-600°C. In fact, the lower temperature fan blade has been observed to fret by a mechanism of adhesion and abrasion by oxide debris. As the operating temperature increases, the abrasion by oxide debris becomes the more predominant and severe mechanism as observed in the compressor blades. According to the results of Bill⁽⁴⁾ (Figure 4), the most severe fretting may be expected at 500-550°C for the alloy Ti-6Al-4V, right at the point where the oxidation kinetics change from logarithmic to parabolic. These results also suggest that compressor blades are more susceptible to fretting than fan blades as has been observed in the present investigation.

4. ION IMPLANTATION OF Ti-6Al-4V FAN AND COMPRESSOR BLADES

Ion implantation is a viable technique for improving the properties of Ti-6Al-4V fan and compressor blades as it has been found to be successful for improving the wear, fatigue, oxidation and fretting properties of Ti-6Al-4V in past studies, a detailed review of which has been published recently⁽⁶⁾. As fan and compressor blades likely fret by different mechanisms, the same implantation parameters (ion species, dose and energy) may not be optimum for both. Therefore, it is necessary to evaluate the optimum implantation conditions for the fan and compressor blades independently based on what is known of the mechanism of fretting.

The factors to consider when developing the optimum ion implantation conditions for improving the fretting fatigue properties of Ti-6Al-4V are:

- (i) Previous results of the effect of ion implantation on the wear properties of Ti-6Al-4V. These results are useful as the mechanisms of wear and fretting (adhesion, abrasion, oxidation and delamination) are essentially the same.
- (ii) Previous results of the effect of ion implantation on the high cycle fatigue strength of Ti-6Al-4V. These results are useful as the main component of fatigue of the fan and compressor blades is high cycle fatigue (HCF).
- (iii) Previous results of the effect of ion implantation on the oxidation resistance of Ti-6Al-4V. These results may be particularly useful where compressor blades are concerned.

It should be noted that only limited work has been done on the effect of ion implantation on the fretting fatigue properties of Ti-6Al-4V.

4.1 THE EFFECT OF ION IMPLANTATION ON THE WEAR PROPERTIES OF Ti-6Al-4V

Several previous investigations have been carried out on the effect of ion implantation on the wear properties of Ti-6Al-4V. The main thrust of this work has been focused on either nitrogen or carbon ion implantation. It is clear that for each particular ion species a certain microstructure must be developed in the implanted layer for wear improvement to occur.

(i) Nitrogen Ion Implantation

Figure 17 summarizes the results of previous investigations into the effect of N^+ implantation on the wear properties of Ti-6Al-4V as a function of peak ion concentration in the implanted layer and the occurrence of nitride precipitates in the implanted layer⁽⁷⁻¹⁷⁾. The peak ion concentrations (atoms/cm³) given in this figure were obtained using a TRIM computer program⁽¹⁸⁾ to generate implant profiles using the particular dose and energy conditions specified in each investigation as input data. Investigations numbered 1 through 4 resulted in no wear improvement. Only three of these investigations analyzed the implanted material to determine if second phase precipitates were present in the implanted layer. In each of these three cases, including the investigation where the implantation was carried out at 300°C or 400°C, no TiN was detected. The investigations numbered 5 through 11 all resulted in wear improvement and in all cases where implanted layer characterization was carried out, TiN precipitates were found. Note that in investigation number 8 the implantation was done at either 500°C or 600°C.

With the exception of investigations 5, 6 and 8, all of the investigations which resulted in wear improvement had a peak ion concentration much larger than the concentrations in the investigations which resulted in no wear improvement. More specifically, it would appear that a peak implanted ion concentration of at least $48 \times 10^{21} \text{ N/cm}^3$ is required in order to achieve improved wear properties, as indicated by the dashed line in Figure 17. Since the presence of TiN precipitates in the implanted layer appears to be required for wear improvement and wear improvement has been shown to occur only for peak ion concentrations greater than $48 \times 10^{21} \text{ N/cm}^3$, then a peak N^+ ion concentration of at least $48 \times 10^{21} \text{ N/cm}^3$ is required to obtain the required volume fraction of TiN precipitates in the implanted layer.

Yet, a question arises with regards to the presence of nitride precipitates found in investigation 8 where the peak N^+ concentration was less than $48 \times 10^{21} \text{ N/cm}^3$ but led to wear improvement as outlined in investigations 5, 6 and 8. With regard to investigation number 8, the presence of TiN at a peak concentration of $35 \times 10^{21} \text{ N/cm}^3$ may be explained by the fact that the implantation was done at either 500°C or 600°C . It has been found that a temperature of at least 500°C is required to cause a measurable change in TiN particle size and volume fraction in N^+ implanted Ti-6Al-4V(2). Therefore it may be expected that for a high temperature implant such as this, TiN precipitates may form for peak ion concentrations less than $48 \times 10^{21} \text{ N/cm}^3$ and accordingly, improved wear properties would result. With regard to investigations 5 and 6, according to the results presented so far, TiN precipitates would not be expected to be present in the implanted layers under the conditions used in these analyses. The improvement which resulted in these cases however was improved corrosive wear properties rather than improved wear properties. Because these two situations differ so dramatically with regard to the mechanism of surface degradation, they really cannot be compared.

In order to further substantiate the fact that a peak N^+ ion concentration of at least $48 \times 10^{21} \text{ N/cm}^3$ would be required for TiN precipitation to occur, investigations 12 through 14 have been included in Figure 17. These investigations involved only microstructural characterization of N^+ implanted titanium, no wear tests were carried out. In each investigation the peak N^+ ion concentration was at least $48 \times 10^{21} \text{ N/cm}^3$ and presence of TiN precipitates in the implanted layer was confirmed. Interestingly, in investigation 14 where a peak concentration of $107 \times 10^{21} \text{ N/cm}^3$ was used, the implanted layer was found to be fully transformed to TiN.

(ii) Carbon Ion Implantation

Unfortunately, less work has been done on the effect of carbon implantation on the wear properties of Ti-6Al-4V than for nitrogen. However, the results which are available in the literature are summarized in Table 1(11,13,19,20). In each of the four investigations reported in Table 1, C^+ implantation resulted in improved wear properties of Ti-6Al-4V. The work done by Vardiman (1982)(20) however provides the largest amount of information available for determining the optimum implant conditions for improving wear of Ti-6Al-4V by C^+ implantation.

Vardiman(20) found the largest improvement in wear properties to occur after implanting carbon ions to a concentration of $15.7 \times 10^{21} \text{ C/cm}^3$ followed by a second anneal at 400°C . After annealing at 500°C a much smaller improvement resulted. The reduction of the improvement which occurred in going from the 400°C anneal to the 500°C anneal was attributed to an overgrowth of TiC precipitate size which suggests that an optimum TiC size exists for maximizing wear property improvement. Microstructural characterization of the 400°C annealed material revealed the carbide particle size to be roughly 60 nm with a few particles $10\text{-}20 \text{ nm}$ in size. It is not clear what peak C^+ concentration is required to obtain the optimum carbide size without following the implantation by a post implant anneal. It may be noted that Vardiman(19) has also done a study into the effect of C^+ implantation on the fretting fatigue properties of Ti-6Al-4V and found an improvement for a concentration of $15.7 \times 10^{21} \text{ C/cm}^3$ with no post implant anneal.

Table 1: Results of carbon implantation studies of Ti-6Al-4V.

Paper	Peak Conc. $\times 10^{21} \text{ ions/cm}^2$	Wear Improvement
Vardiman (1982)	15.7 (anneal at 300°C , 400°C and 500°C)	Largest improvement after 400°C anneal TiC observed in each case
Vardiman (1982)	15.7	Improved fretting fatigue life
Sioshansi (1985)	26.7	Wear against UHMWPE improved
Oliver (1984)	45	Slight improvement

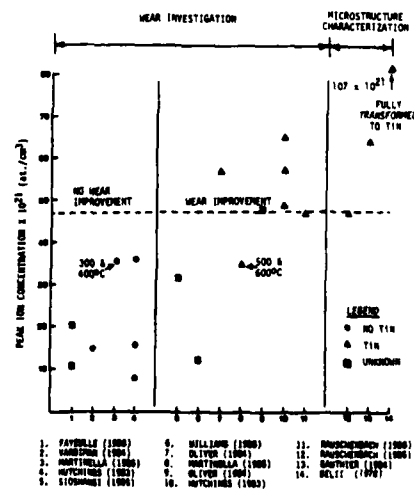


Fig. 17 Summary of the investigations which have been carried out on nitrogen implanted Ti-6Al-4V.

4.2 EFFECT OF ION IMPLANTATION ON THE HIGH CYCLE FATIGUE STRENGTH OF Ti-6Al-4V

Ion implantation results in a surface layer with restricted dislocation movement which in turn means an increased surface hardness. This situation can serve to delay fatigue crack initiation. Damage induced dislocation loops can increase fatigue life by reducing the slip distance, and, provided the strength of these barriers is sufficient, by enhancing the amount of reversible slip. In addition to this, because the stress levels in HCF are usually much lower than yield stress, the surface residual compressive stresses created in an implanted layer may provide one mechanism by which ion implantation can increase the fatigue life. The damage induced by the ion beam is sufficient to develop dislocation tangles and residual stresses which contribute to the surface hardening. In this respect, the size of the implanted ion can be quite important where ions larger than the matrix create a compressive stress and ions smaller than the matrix create a tensile stress. Compressive residual stresses can increase the fatigue life as they reduce the damaging tensile component of the cyclic stress.

Because surface hardening should theoretically increase the fatigue life, nitrogen and carbon ions which are effective in improving wear according to this mechanism should also be effective in increasing the fatigue crack initiation life.

Presently, the only extensive investigation into the effect of ion implantation on the HCF life of Ti-6Al-4V has been done by Vardiman and Kant⁽¹⁹⁾. In that work, nitrogen was implanted into samples to a dose of 2×10^{17} atoms cm^{-2} at an energy of 75 keV per atom to give a peak concentration of 18×10^{21} atoms cm^{-3} . Some of the samples received a 500°C post-implant anneal for 4h. Carbon was implanted into samples at the same energy and dose giving a peak concentration of 15.7×10^{21} atoms cm^{-3} . The effect of heat treatment on carbon implanted samples was investigated by carrying out a 400°C post-implant anneal for 1h and the effect of dose was tested by implanting samples with carbon doses, greater than and less than 2×10^{17} atoms cm^{-2} . The results of rotating beam fatigue tests rotated at 1600 rev min^{-1} are illustrated in Figures 18 and 19. The unimplanted endurance limit of 73 ksi (500 MPa) is increased approximately 10% by N^+ implantation and 20% by C^+ . For high stress amplitudes (> 100 ksi; 690 MPa) the effect of nitrogen implantation disappeared while carbon implantation increased the life by a factor of 4 to 5. Results of the heat treated samples are not shown as they resulted in no significant additional improvement for either nitrogen or carbon implantation. According to Figure 19, a dose of only 1×10^{17} C^+ cm^{-2} (7.9×10^{21} C^+ cm^{-3} peak concentration) is required to obtain full fatigue life improvement at 98 ksi (676 MPa) with higher doses providing no increased benefit.

Transmission electron microscope analysis published to date revealed the presence of second phase precipitates in both the C^+ and N^+ implanted Ti-6Al-4V. The nitride precipitates found were TiN, 10-20 nm in size, incoherent with the α -Ti matrix. After the post-implant anneal, a small size increase of TiN precipitates occurred to a maximum of about 30 nm. Much larger increases in precipitate size occurred after annealing the carbon implanted samples. With regard to the C^+ implantation, the main implication of these results is that the size of the precipitates is not as significant a factor for increasing fatigue life as for improving wear. This conclusion is based on the fact that after the 400°C anneal, during which precipitate growth occurred, no further HCF life increase was observed. Because for both the C^+ and N^+ implanted samples, heat treatment would cause the number of precipitates to increase, and yet no further increase in the fatigue life was observed, it would appear that second phase precipitation is not the dominant mechanism responsible for the observed increased fatigue life.

The presence of a compressive residual stress in the ion implanted layer, which results from expansion of the lattice during implantation, may also explain some of the improvement in fatigue life observed after nitrogen or carbon implantation of Ti-6Al-4V.

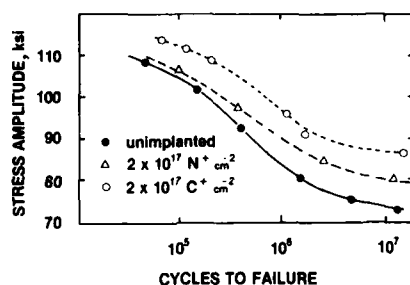


Fig. 18 Cycles to failure vs. maximum stress for C^+ and N^+ implanted Ti-6Al-4V (Ref. 19): 1 ksi = 6.9 MPa.

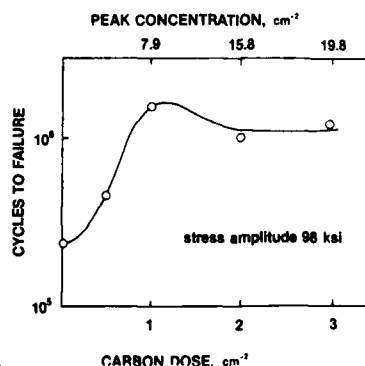


Fig. 19 Cycles to failure vs. C^+ dose for Ti-6Al-4V, 98 ksi maximum stress (Ref. 19): 98 ksi = 676 MPa.

Because the presence of a large density of second phase precipitates is not a necessity for increasing the fatigue life, then solid solution hardening must be the dominant mechanism responsible for the increase in the fatigue life of Ti-6Al-4V with the presence of a compressive residual stress resulting in an uncertain amount of the improvement. This would also explain the difference in the effects of C^+ and N^+ . Carbon may segregate to dislocations more readily than nitrogen owing to its lower solubility and greater mobility in α -Ti, and thus it may be more efficient in the pinning of dislocations.

Although the effect of ion implantation on fatigue life is not as dramatic as on wear, it can provide a measurable improvement. The optimum implant conditions include a smaller dose than is required for wear as the dominant mechanism causing the improvement in solid solution strengthening rather than precipitation hardening as would appear to be the case for wear. In addition to this, no post-implant heat treatment is required for either carbon or nitrogen implantation as precipitate number and size would appear to be insignificant.

4.3 EFFECT OF ION IMPLANTATION ON THE OXIDATION PROPERTIES OF Ti-6Al-4V

Oxidation of Ti-6Al-4V is inhibited by barium ions which diffuse towards the dislocations and block the inward diffusion of oxygen. This can be beneficial in situations where oxide is prone to flaking and delamination, i.e. fretting wear. Ba⁺ implantation can also lead to hardening whereby after diffusing to dislocations the ions can react with oxygen to form BaTiO precipitates which can pin the dislocation movement(2).

4.4 EFFECT OF ION IMPLANTATION ON THE FRETTING FATIGUE PROPERTIES OF Ti-6Al-4V

One study by Vardiman and Kant(19) involved fretting fatigue testing of C⁺ implanted Ti-6Al-4V (at 75keV to a dose of 2×10^{17} C⁺ cm⁻²). The results, illustrated in Figure 20, indicate that a significant increase in the fretting fatigue strength can be gained via C⁺ ion implantation. Because no difference was seen between the fretting and fracture surfaces of the implanted and unimplanted material it would appear that the improvement may be ascribed to a slowing of debris formation and damage on the hardened layer, i.e. improved fretting wear resistance. The mechanism of fretting is apparently not affected by the implantation.

In an investigation by Dearnaley(2), it was found that Ba⁺ ions implanted into Ti-6Al-4V improved fretting fatigue by 50%. As mentioned above, barium inhibits oxidation of Ti-6Al-4V. If an increase in the room temperature fretting fatigue strength of Ti-6Al-4V was achieved by Ba⁺ implantation then the hypothesis that the low temperature (<400°C) fretting of titanium in air occurs predominantly by adhesion, would appear to be incorrect. It is possible that the effect barium ion implantation has on the oxidation of Ti may be very useful in reducing fretting at temperatures between 500 and 600°C. Note that the improvement in the fretting fatigue of Ba⁺ implanted Ti-6Al-4V as described above may also have resulted from a hardening effect caused by the presence of BaTiO precipitates.

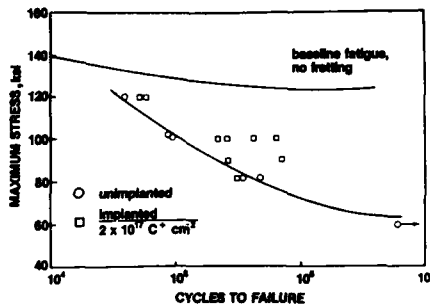


Fig. 20 Cycles to failure vs. maximum fatigue stress for carbon implanted and unimplanted Ti-6Al-4V; normal stress 3 ksi (Ref. 20): 3 ksi = 21 MPa.

Table 2: Selection of optimum ion implantation conditions for minimizing fretting fatigue in Ti-6Al-4V at temperatures <400°C

Ion Species	Approximate dose, 10^{17} atoms cm ⁻² *	Peak concentration, 10^{21} atoms cm ⁻³	Comments
N ⁺	>5	>48	Must suffice for a large density of second phase precipitates
C ⁺	>3	>16	Optimize number and size of precipitates (low temperature heat treatment)
Ba ⁺	Optimum dose not established

* Depends on the energy

4.5 OPTIMUM IMPLANT SPECIES AND CONDITIONS FOR REDUCING FRETTING FATIGUE OF Ti-6Al-4V FAN AND COMPRESSOR BLADES

In light of the difference in operating temperature between fan and compressor blades and the resultant difference in the mechanism of fretting to be expected, the development of the optimum implant conditions for the two cases must be treated separately.

(i) Low Temperature Fretting Fatigue (<400°C)

Fan blades and stage 1 or stage 2 compressor blades would be expected to fret in this temperature regime. It has already been established that fretting of Ti at temperatures <400°C likely occurs predominantly by a mechanism of adhesion. In addition to this, the main fatigue component where fretting fatigue of fan and compressor blades is concerned, is that of high cycle fatigue. Therefore, in determining the optimum ion implantation conditions for improving the fretting fatigue resistance of Ti-6Al-4V fan and compressor blades in this temperature regime, the results on the effect of ion implantation on the wear, high cycle fatigue, and fretting resistance of Ti-6Al-4V may be consulted. Note that although unidirectional and fretting wear differ in many respects, it is clear that the fundamental modes of wear including adhesion, abrasion, and delamination are characteristic of both. It is therefore possible that those ion species which improve unidirectional wear will also improve fretting wear.

Ion implantation has resulted in a more dramatic improvement in the wear resistance of Ti-6Al-4V than that in the high cycle fatigue strength(6). It would seem logical, therefore, that in order to maximize the increase in the fretting fatigue strength of the alloy by ion implantation, implant conditions for maximizing the wear resistance must be selected. Significantly, most of the ions which result in improved high cycle fatigue strength of Ti-6Al-4V have also been shown to result in improved wear resistance.

Based on this reasoning, certain implant conditions which might hold the highest potential for improving fretting fatigue of Ti-6Al-4V have been summarized in Table 2. N⁺ and C⁺ implantation are the obvious selections as they have both resulted in improved wear and fatigue of Ti-6Al-4V. If an increase in wear resistance is to provide the best results second phase precipitation is a necessity meaning that a high dose is required. This is especially true for the case of N⁺ unless a post-implant

heat treatment is considered. Results by Dearnaley for Ba⁺ implantation⁽²⁾ are also encouraging and are worth considering for further work. Ba⁺ implantation would be especially interesting as the results would likely clarify some of the uncertainties regarding the role of oxide in fretting in this temperature regime.

(ii) High Temperature Fretting Fatigue (>400°C)

Unfortunately, there has been no published work on the effect of ion implantation on the wear, high cycle fatigue and fretting fatigue of Ti-6Al-4V in this temperature regime. However, it is likely that those optimum implant conditions (N⁺ and C⁺ implantation) selected for the low temperature regime (<400°C) would also result in improved fretting fatigue properties of Ti-6Al-4V in the high temperature regime (>400°C). However, of particular interest for fretting fatigue at temperatures >400°C is Ba⁺ ion implantation.

Barium ion implantation has been found to inhibit oxidation of Ti-6Al-4V by blocking the inward diffusion of oxygen⁽²⁾. This phenomena may be particularly useful for increasing the fretting fatigue resistance of Ti-6Al-4V at temperatures >400°C in accordance with the following three mechanisms:

- By slowing down the oxidation kinetics of Ti-6Al-4V so that fretting occurs predominantly by adhesion rather than oxidation i.e. see Figure 4.
- By blocking the inward diffusion of oxygen premature fatigue crack initiation along α/β phase boundaries may be prevented.
- By providing additional hardness due to the formation of BaTiO precipitates.

5. TRANSMISSION ELECTRON MICROSCOPY OF ION IMPLANTED Ti-6Al-4V

5.1 IMPLANTATION CONDITIONS

Five implantation conditions were selected for the fretting fatigue study as summarized in Table 3. For the nitrogen or carbon implantation both a single energy implantation and a triple energy implantation were considered. The triple energy implants result in flatter concentration profiles compared with the approximately gaussian profiles which would be obtained from the single energy implants. It is uncertain what effect the flatter profiles may have on the fretting fatigue properties of Ti-6Al-4V compared with the gaussian profiles. In addition to nitrogen or carbon implantation, a dual species implant (N⁺ plus C⁺) was considered. Prior to carrying out fretting fatigue tests on Ti-6Al-4V implanted with each of these conditions, a TEM investigation was conducted so that a microstructural characterization of each of these implanted layers could be made.

Table 3: Ion implantation conditions selected for the fretting fatigue study

Ion Species	Condition
N ⁺	- Dose and energy selected to give a peak concentration greater than 48×10^{21} N/cm ³ . - Will consider both a single energy implant and a triple energy implant.
C ⁺	- Dose and energy selected to give a peak concentration large enough to obtain a larger density of carbide precipitates. (Peak concentration selected is greater than 15.7×10^{21} N/cm ³) - Will consider both a single energy implant and a triple energy implant
C ⁺ and N ⁺	- Dual implant



Fig. 21 Electron diffraction pattern of (a) C⁺ implanted <011> cubic pattern and (b) N⁺ implanted <001> cubic pattern.



Fig. 22 TEM micrograph of N⁺ implanted Ti-6Al-4V.

5.2 TEM SAMPLE PREPARATION

Disks of Ti-6Al-4V alloy, 3 mm in diameter, were mechanically polished to a 1 μ m finish prior to ion implantation. After implanting the disks on one side, they were thinned by standard jet polishing technique. In order to preserve the ion implanted layer for electron microscopy, the foils were back thinned to perforation by masking the ion implanted surface with a thin glass plate. The polishing solution used was 94% acetic acid plus 6% perchloric acid by volume. Nitrogen and carbon implanted foils were analyzed together with foils which received a dual implant of both carbon and nitrogen ions.

5.3 TEM RESULTS

With the exception of the foils which received the dual N⁺ plus C⁺ implant, both cubic Ti(C,N) and hexagonal close packed (α -Ti) diffraction patterns were observed. Examples are given in Figures 21 a and b for the case of a single energy carbon and nitrogen implant respectively. Only cubic diffraction patterns were obtained from the foils which received the dual C⁺ plus N⁺ implantation. Note that these foils received the highest dose of all the samples examined. Many of the cubic crystal patterns were sharp (Figure 21a), while other patterns showed clear evidence of twinning (Figure 21b). On examination by imaging techniques some grains appeared twinned while others were free of twins. Figure 22 illustrates a micrograph of a grain in a N⁺ (single energy) implanted foil where indications of twinning is clearly evident. Note that similar results were obtained for the single and triple energy carbon and nitrogen implanted foils.

These results suggest, but do not prove, that if twinning is associated with relief of the transformation strains for Ti to Ti(C,N) the accommodation of the strains is dependent on the original crystallographic orientation of the grains at the surface. The exact nature of the strains would depend on the crystallographic orientation between the TiN(C) and Ti which has not been established yet for these ion implanted samples.

6. SUMMARY AND CONCLUSIONS

1. Ion implantation has been identified as being a viable technique for improving the fretting fatigue damage which occurs on the dovetail surface of Ti-6Al-4V aircraft gas turbine fan and compressor blades.
2. The results of studies on the effects of ion implantation on the wear properties of Ti-6Al-4V may be used as a starting point for establishing the implantation conditions which hold the optimum potential for improving the fretting fatigue properties of the alloy.
3. It appears that second phase precipitates must be present in the implanted layer for both nitrogen or carbon implantation of Ti-6Al-4V if wear improvement is to occur.
4. The effect a particular set of ion implantation conditions has on the fretting fatigue properties of fan and compressor blades may differ as a result of the difference in operating temperatures. The severity of damage and likely the mechanism of fretting is generally much worse in compressor blades as compared to fan blades.

7. ACKNOWLEDGEMENTS

The authors would like to acknowledge the financial support provided by the Department of National Defence Canada. Thanks should be given to Dr. G. Weatherly of the Department of Metallurgical Engineering and Material Science at the University of Toronto for his expert assistance in the TEM work and Mr. Wayne Doswell of the Department of Mechanical and Aeronautical Engineering of Carleton University for his assistance with the technical work.

8. REFERENCES

1. G. Dearnaley, Mater. Eng. Appl., Sept 1978, 1, 28-41.
2. G. Dearnaley, IEEE Trans. Nucl. Sci., 1981, NS-28, (2), 1806-1810.
3. R.C. Bill, "Materials evaluation under fretting conditions", STP 780, 165-182, 1982, Philadelphia, PA., American Society for Testing and Materials.
4. E. Broszeit, K.H. Kloos and B. Schweighofer, "Titanium science and technology", (ed. G. Lutjering et al.), Vol. 4, 2171-2186, 1985, Oberursel, Deutsche Gesellschaft für Metallkunde.
5. M.M. Hamdy and R.B. Waterhouse, Key Eng. Mater., 1985, 47, 1-16.
6. J.E. Elder, R. Thamburaj, P.C. Patnaik, International Material Reviews, 1988, Vol. 33, No. 6, 289-313.
7. S. Fayeulle, Wear, 107, 1986, 61-70.
8. R.G. Vardiman, Res. Soc. Stmp. Proc., Vol. 27, 1984, Elsevier Science Publ. Inc.
9. R. Martinella, S. Giovanardi, G. Chevallard, M. Villani, A. Molinari and C. Tosello, Mat. Sci. Eng., 69, 1985, 247-252.
10. R. Hutchings and W.C. Oliver, Met. Sci. Technol. A, Vol. 3, No. 6, Nov/Dec 1985.
11. P. Sioshansi and R.W. Oliver, Met. Sci. Technol. A, Vol. 3, No. 6, Nov/Dec 1985.
12. J.M. Williams, Nucl. Instru. And Methods in Phys. Research B10/11, 1985, 539-544.
13. W.C. Oliver, R. Hutchings, J.B. Pethica, E.L. Paradis and A.J. Shuskus, Mat. Res. Soc. Symp. Proc., Vol. 27, (1984), Elsevier Science Publ. Inc., Milan, Italy.
14. B. Rauschenbach, Formation of Compounds by High Flux Nitrogen On Implantation in Titanium, Chapman and Hall Ltd., 1986.
15. B. Rauschenbach and K. Hohmuth, Phys. Status Solidi (a), 94, 833, 1986.
16. P. Gauthier, D. Pleche, J. Pivot and J.A. Roger, Vacuum, Vol. 34, No. 10, 1013, 1984.
17. I.M. Belii, F.F. Komarov, V.S. Tishkov and V.M. Yankovskii, Phys. Status Solidi (a), 45, 343, 1978.
18. D. Thompson, private communication, McMaster University, Hamilton, Ontario, Sept. 1986.
19. R.G. Vardiman and R.A. Kant, J. Appl. Phys., 53 (1), Jan. 1982.
20. R.G. Vardiman, D. Creighton, G. Salivar, A. Effatian and B.B. Rath, Materials Evaluation Under Fretting Conditions, ASTM STP 780, American Society for Testing and Materials, 1982, pp 138-149.

OVERVIEW ON HOT GAS TESTS AND MOLTEN SALT CORROSION EXPERIMENTS AT THE DLR

by

H.-J. Rätzer-Scheibe
German Aerospace Research Establishment (DLR)
Institute for Materials Research
D-5000 Köln 90
Federal Republic of Germany

INTRODUCTION

The use of more corrosive low-grade fuels in combination with increasing combustion gas temperatures are major challenges in the present and future operation of heat engines. Improved thermal efficiency under practical operating conditions can only be accomplished by improved materials and/or coatings. This development motivated us, in 1982, to procure a high-velocity burner rig for our institute to simulate the operation of gas turbines under service conditions. As an aircraft R&D establishment, we have been mainly interested in corrosion and oxidation of aircraft gas turbines. Working in this new field of research yielded a review on hot corrosion in aircraft engines [1].

For an overview of our work, to date, in the field of hot corrosion and high temperature oxidation some topics are selected. We started burner rig tests with investigations on the hot corrosion resistance of protective coating systems to evaluate coating alloys for use in highly contaminated combustion gases. Thermocyclic oxidation tests of coated aircraft turbine blade materials in hot gases of JP4 up to temperatures of 1100 °C, followed later.

Since "hot corrosion" is induced by molten salts or low-melting oxides deposited from the hot gas on the material surface we saw the necessity for fundamental investigations of molten salt corrosion. Therefore a device was developed for electrochemical experiments in molten salts. Another motivation for developing molten salt experimentation was to have an alternative test procedure to the high-cost burner rig tests.

HOT GAS TESTS

High-Velocity Burner Rig at DLR

The burner rig at DLR (Figure 1) permits materials testing at high gas temperatures and velocities. Hence, ignoring the pressure conditions of the gas stream, processes in gas turbines, particularly in aircraft gas turbines, can be simulated sufficiently.

The equipment (LCS-3BR Laboratory Combustor System) was supplied from Becon Inc., South Windsor, Connecticut 06074, USA. The system can be applied to oxidation or corrosion under isothermal as well as cyclic conditions. Additional components are necessary to perform hot particulate erosion experiments.

Diesel and aircraft fuel can be used with the standard nozzle system. Heavy distillates of oil or gaseous fuel would require special fuel nozzle systems. For testing of hot corrosion, salt solution can be injected into the combustion chamber. To accelerate corrosive attack contaminations such as S, V, Na, and Cl can be also added to the fuel as soluble compounds.

Cylindrical bars (length: 120-140 mm, diameter: 7-12 mm) are usually used as test specimens. Eight specimens are uniformly spaced in the holder around a 1.8 inch (45.72 mm) diameter circle centered on the axis of rotation (180 up to 1800 rpm) and are exposed to the hot gas stream. Normally one space on the holder has to be reserved for a dummy specimen to measure the test temperature by Ni/NiCr

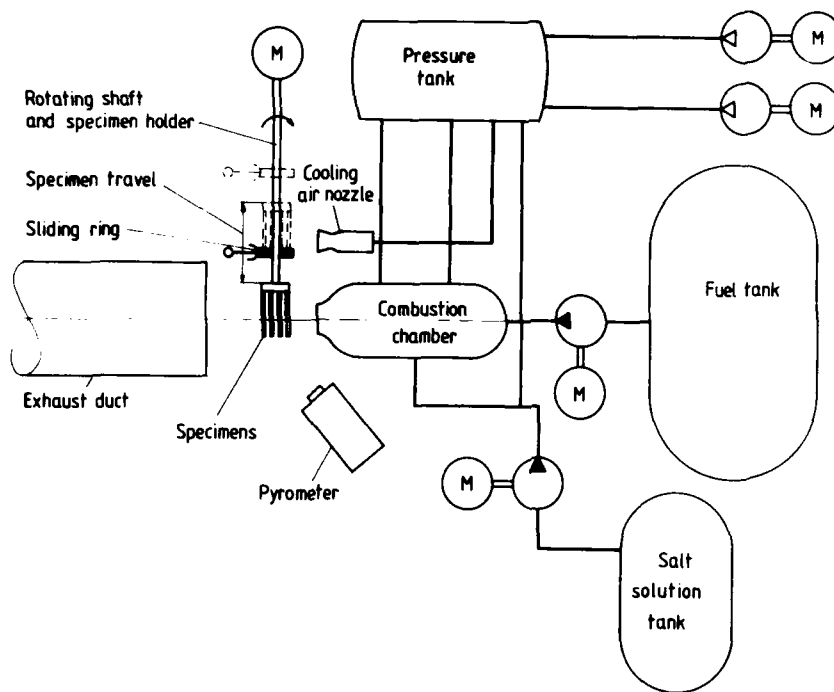


Figure 1. Schematic view of burner rig at DLR.

thermocouples embedded in its metallic interior. The thermoelectric voltages are conducted by a sliding ring system. In addition, specimen temperatures can be detected with an optical pyrometer.

The gas temperature can be varied between 550 °C and 1650 °C, and the gas velocity will reach values between Mach 0.3 and 0.8. For thermocyclic tests the specimens are held at constant temperature during a heating period and are cooled in a Mach 0.1 air stream to ambient temperature (Figure 2).

Hot Corrosion Studies of EB-PVD and Plasma Sprayed Coatings in Combustion Gases of Low-Grade Fuel

This work resulted from a German/Norwegian cooperative study [2], [3], [4]. Waspaloy, a typical material for heat engines, were selected as substrate due to its high strength at high temperatures (1000 h creep rupture strength at 900 °C: 80 MPa). The low oxidation and hot corrosion resistance of this material necessitates a surface protection. So far, overlay coatings have proved most effective against severe hot corrosion attack. Therefore various coatings produced by electron beam physical vapour deposition (EB-PVD), air plasma spraying (APS), and

low pressure plasma spraying (LPPS) were evaluated and utilized in this programme (Table 1 and Table 2). As is shown in Table 2, the intended coating thickness of approx. 300 μm was only partially achieved.

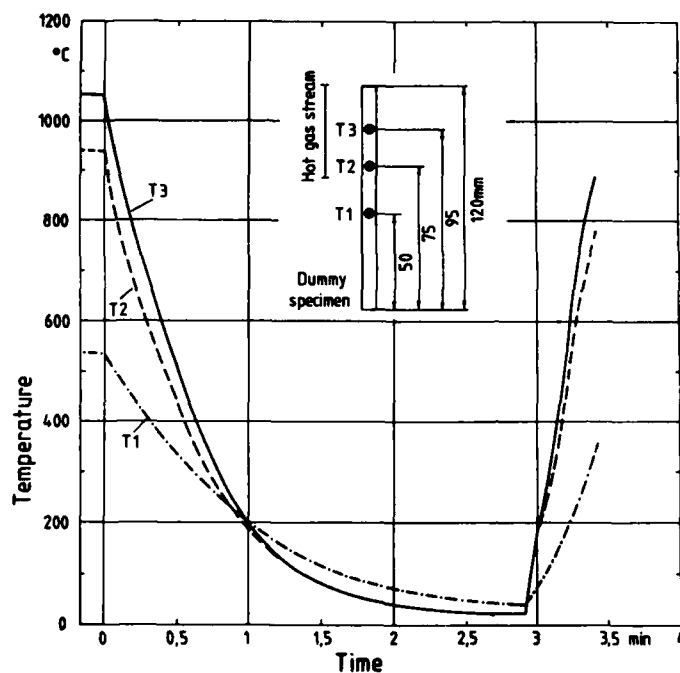


Figure 2. Cooling and reheating curves for the specimens during a thermocyclic test (57 min. at temperature, 3-min. cool to ambient temperature).

Substrate	Waspaloy						
Coating	NiCoCrAlY			NiCrAlY			FeCrAlY
Technique	PVD ¹	APS ²	LPPS ³	PVD ¹	APS ²	LPPS ³	APS ²

¹DLR, Köln (F.R.G.)

²DLR, Stuttgart (F.R.G.)

³SI, Oslo (N)

Table 1. Coating/substrate combinations.

Isothermal and cyclic hot gas tests were carried out in a combustion gas of diesel fuel at gas velocities of Mach 0.3-0.4. The fuel was contaminated with 3 % sulphur, 200 ppm vanadium, and 100 ppm sodium. A temperature cycle consisted of a period of 57 min. at constant temperature and subsequent cooling in a Mach 0.1 air stream for 3 min. to reach ambient temperature (see Figure 2). Specimens were tested at peak temperatures of 650, 700, 800, and 950 °C. The tests were

scheduled for 250 h but had to be reduced to 80 or 50 h due to unexpected severe corrosion attack on the burner.

Alloy	Ni	Cr	Co	Al	Y	Others	d in μm
Waspaloy	bal.	20.0	13.5	1.4	-	3Ti, 4.3Mo	-
NiCoCrAlY(PVD)	bal.	20.0	24.0	12.5	0.4	-	175
NiCoCrAlY(APS)	bal.	16.0	20.0	10.0	0.6	9 MO	500
NiCoCrAlY(LPPS)	bal.	21.0	22.0	13.0	0.3	n.d.	130
NiCrAlY(PVD)	bal.	15.9	-	8.3	0.5	-	350
NiCrAlY(APS)	bal.	19.0	-	6.0	0.2	12 MO	500
NiCrAlY(LPPS)	bal.	21.7	-	9.8	0.8	n.d.	400
FeCrAlY(APS)	0.1	21.0	-	2.0	0.1	bal. Fe	500

n.d.: not determined

MO: metal oxides

Table 2. Composition (wt. %) of Waspaloy and the coatings; d indicates the averaged thickness of coatings.

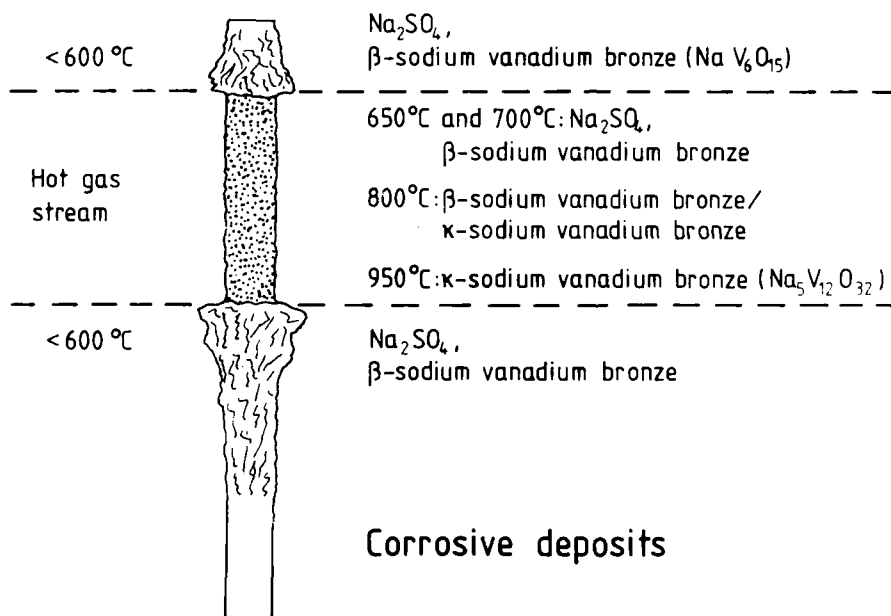


Figure 3. Composition of corrosive deposits on specimens which were exposed combustion gas of diesel fuel contaminated with sulfur, vanadium and sodium (schematic).

Heavy deposits were formed on the areas of the specimens which were only marginally exposed to the gas stream thereby reaching temperatures lower than approx. 600 °C (Figure 3). These areas shift outwards to cooler regions of the

specimens when the test temperature was increased. The heavy deposits consisted mainly of sodium sulphate (Na_2SO_4) and β -sodium vanadium bronze ($\text{NaV}_8\text{O}_{15}$) [2].

Deposits condensed on the hot zone of the specimens, where the temperature exceeded approximately 600 °C, were mostly molten. Fast velocities of the gas stream allowed formation of only thin deposits ($\leq 500 \mu\text{m}$). The deposits formed at 650 and 700 °C consisted of sodium sulphate and β -sodium vanadium bronze. Mixed β - and κ -sodium vanadium bronze were formed at 800 °C while deposits formed at 950 °C only contained κ -sodium vanadium bronze ($\text{Na}_5\text{V}_{12}\text{O}_{32}$) [2]. The deposited molten layers initiate the successive hot corrosion process of the metallic materials.

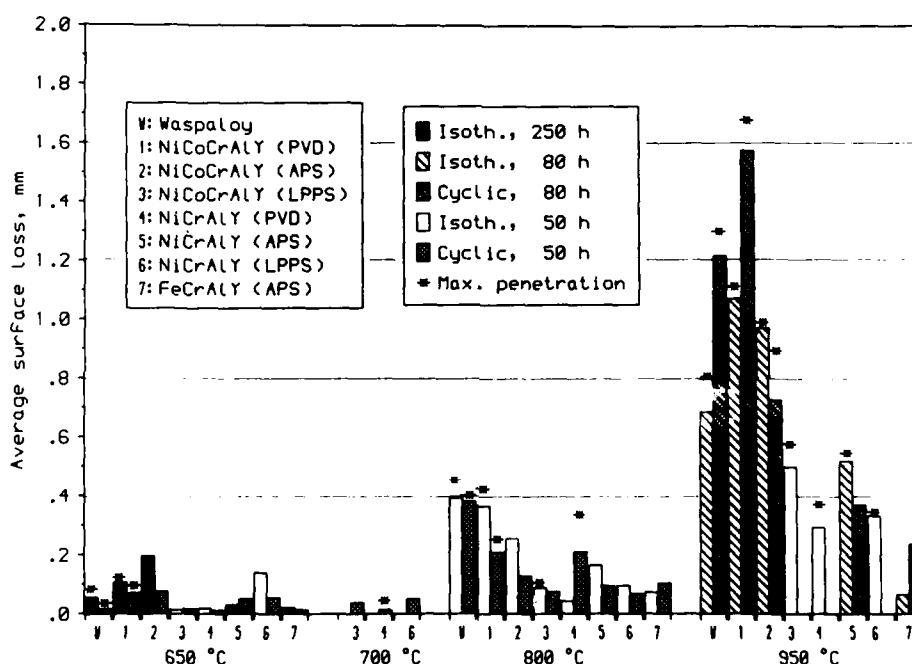


Figure 4. Corrosion attack data for Waspaloy and coating alloys exposed to high velocity gas stream at 650, 700, 800, and 950 °C.

The corrosion attack of coated and uncoated Waspaloy measured as surface loss from central sections of the test bars is summarized in Figure 4. The corrosive degradation generally increased with temperature at equal exposure time. Especially at the higher test temperatures, many coatings were corroded completely or at least in patches, thus corrosion could spread to the substrate. The extent of consumption depended on the type of coating as well as the original coating thickness (see Table 2). In contrast to the corrosion of the coating alloys, essentially induced by vanadates, Waspaloy was additionally susceptible to internal

sulphidation and oxidation (Figure 5). The maximum penetration of this kind of internal corrosion is specially marked in Figure 4.

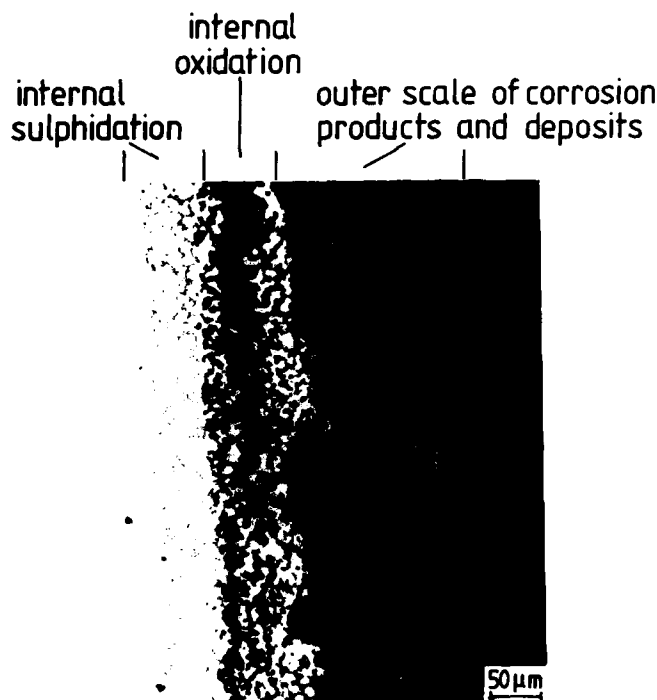


Figure 5. Cross section (backscattered electron imaging) of the corrosion products formed on Waspaloy at 950 °C (cyclic) after 80 h.

In general, unprotected Waspaloy has the highest corrosion rate. All APS- and LPPS-coatings tested at temperatures up to 800 °C reduce the corrosion rate during the tests, which last 50 h. When the original thickness of PVD-coatings was sufficient (approx. 300 μm), then these coatings were even superior to the plasma sprayed coatings as is shown by those NiCrAlY(PVD)-coated specimens isothermally and cyclically tested at 650 °C and isothermally tested at 800 °C. Considering all test temperatures, FeCrAlY(APS) coatings generally were the most corrosion-resistant. This is clearly shown by tests at 950 °C, where FeCrAlY(APS) was the only coating which was not completely corroded.

Typical microstructures of the scales formed on Ni-base and FeCrAlY coatings are illustrated in Figure 6 and Figure 7, respectively. The scales consist of a thin oxide layer adjacent to the metal and a thick outer layer composed of deposits and corrosion products. The matrix phase of the outer layer (medium grey on Ni-base coatings, dark gray on FeCrAlY coating) represents the vanadium containing deposits mentioned above. The main corrosion product on Ni-base coatings is

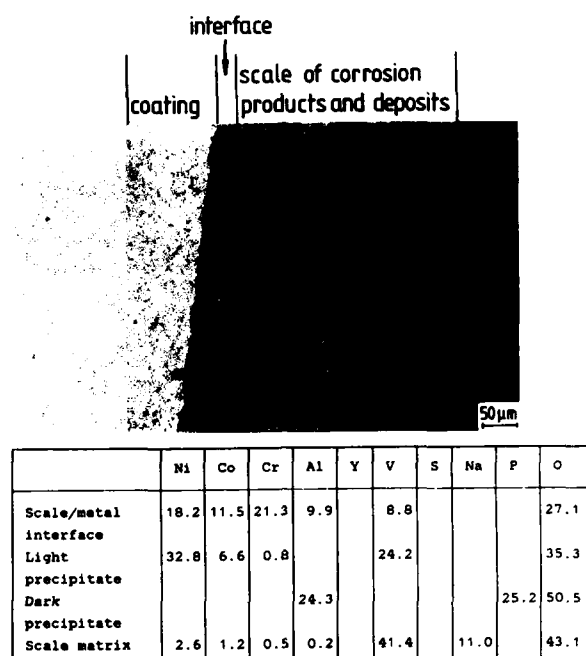


Figure 6. Cross section (backscattered electron imaging) of the scale formed on NiCoCrAlY(APS) at 800 °C (isothermal) after 50 h and results of microprobe analysis (wt. %).

nickel orthovanadate ($Ni_2(VO_4)_2$) precipitated from the molten vanadate matrix on cooling. The corresponding precipitates on NiCoCrAlY coatings contain additional cobalt in solid solution and may be described as $(Ni,Co)_2(VO_4)_2$ (light grey in Figure 6). The dark phase in the outer layer is shown by microprobe analysis to be $AlPO_4$, probably originating from phosphorus in the diesel fuel. The thin interface oxide layer consists of various oxides of the coating elements which mainly have spinel phases. Sharp-cornered precipitates in the scales on FeCrAlY-coatings (light grey in Figure 7) are probably $(Ni,Fe)(Cr,Fe)_2O_4$ spinels. The oxide layer (medium grey) adjacent to the metal consists of various iron and chromium oxides. These oxides seem to be less soluble in molten vanadate than nickel and cobalt oxides. This may explain the better corrosion behaviour of FeCrAlY coatings, especially at 950 °C, compared with Ni-base coatings. The respective mechanisms were detailed by Seiersten and Kofstad [5].

When comparing isothermal tests with cyclic tests, no clear effect of these test conditions on surface loss can be observed. So, temperature cycles were by no means detrimental. Only FeCrAlY coatings corroded faster on cycling.

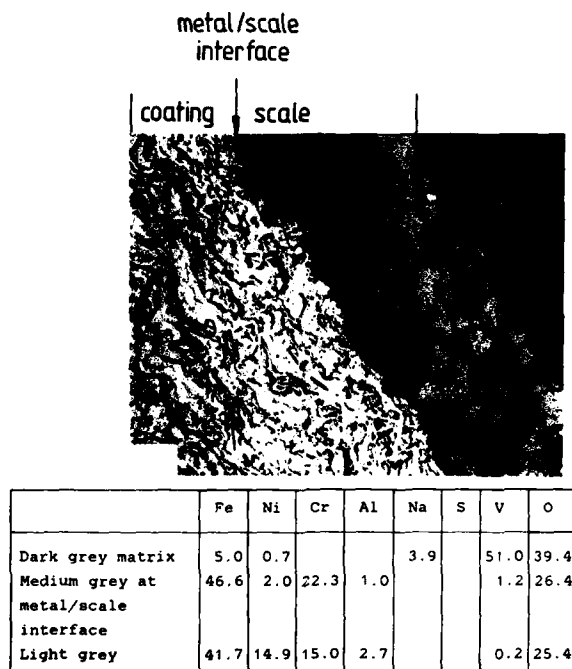


Figure 7. Cross section (backscattered electron imaging) of the scale formed on FeCrAlY(APS) at 950 °C (isothermal) after 80 h and results of microprobe analysis (wt. %).

The High Temperature Oxidation Behaviour of the Single Crystal Ni-Base Alloy M002 mod. with and without Protective Coatings

These investigations were accomplished in cooperation with the MTU, München [6]. Turbine blades for advanced aero engines have been produced from Ni-base alloys in single crystal form. In comparison to polycrystalline blades, their improved creep strength allows a higher operating temperature. The surface temperature of turbine blades at the leading and trailing edge is sometimes in the range of 1050 to 1100 °C. Under these conditions, the surface attack by oxidation cannot be neglected, and protection by a suitable coating has to be provided.

The single crystal alloy M002 mod. (composition (wt. %): Ni, 8.5Cr, 5Co, 5.5Al, 2.2Ti, 9.5W, 2.8Ta) which is identical with the alloy SRR99 were used as substrate material. Cylindrical bars of this alloy, uncoated as well as coated with Al (Codep), PtAl (RT22), and LPPS-MCrAlY (LCO22; composition (wt. %): Co, 31Ni, 21Cr, 8Al, 0.5Y), were used for testing by the high-velocity burner rig (see Figure 1) under service-like conditions. The specimens were cyclically tested at 1050 °C for 400, 600, and 1000 h and at 1100 °C for 200 and 400 h.

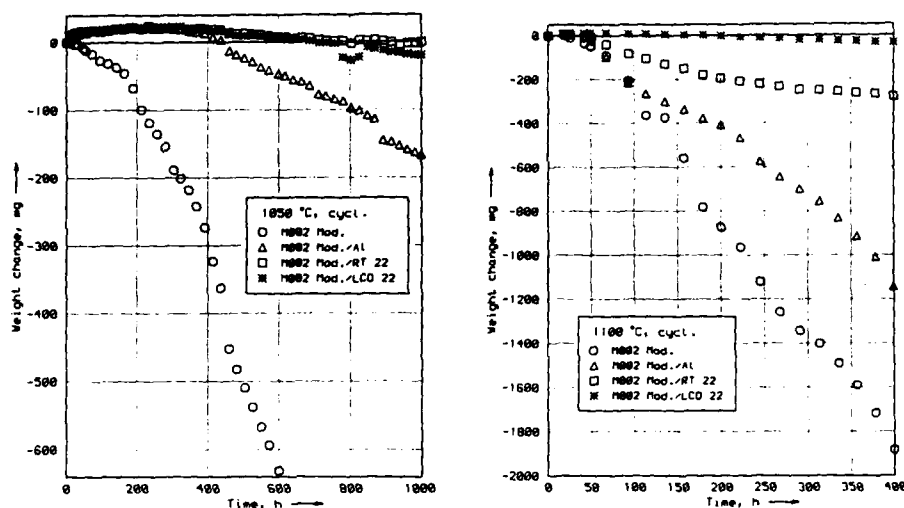


Figure 8. Weight change vs. time of coated and uncoated M002 mod. obtained during cyclic testing in a hot gas stream of Mach 0.3 at 1050 °C and 1100 °C.

Figure 8 shows weight change vs. time data measured at test temperatures of 1050 and 1100 °C. At 1050 °C the oxidation resistance of the substrate is markedly improved by the coatings, with RT22 and LCO22 being more resistant to degradation than Codep. At 1100 °C Codep and RT22 coatings show a significant loss of material within about 50 h, whereas LCO22 proved stable over several hundred hours. These weight measurements are roughly confirmed by determining the average surface loss of the specimens at the zone of maximum temperature (Figure 9).

For the Codep and RT22 coatings whose oxidation resistance is based on a high aluminium concentration resolved Al-rich phases can be taken as a measure of coating consumption. Figure 10 shows patches of the β -NiAl phase (grey) for a Codep coating tested at 1050 °C for 400 h. The fraction of the Al-rich phase determined by relating the area of the β -NiAl phase to the corresponding area of the initial state represents the consumption of the coatings (Figure 11). At 1050 °C the Codep coating is almost completely consumed after 400 h, whereas the RT22 coating still has, even after 1000 h, a residual thickness of about 40 % of its original value. At 1100 °C, Codep and RT22 coatings are already consumed after less than 200 h.

The LCO22 coating shows hardly any reduction in thickness by oxidation at 1050 °C (see Figure 9). Also, aluminide phases could not be detected in this plasma sprayed coating even after the shortest testing time of 400 h. LCO22 is not significantly oxidized at 1100 °C after 400 h, too. On the other hand, voids were formed in the LCO22 coatings, especially close to the original coating-substrate interface (Figure 12). The void density increases and the size of voids grows with longer testing times and higher temperatures.

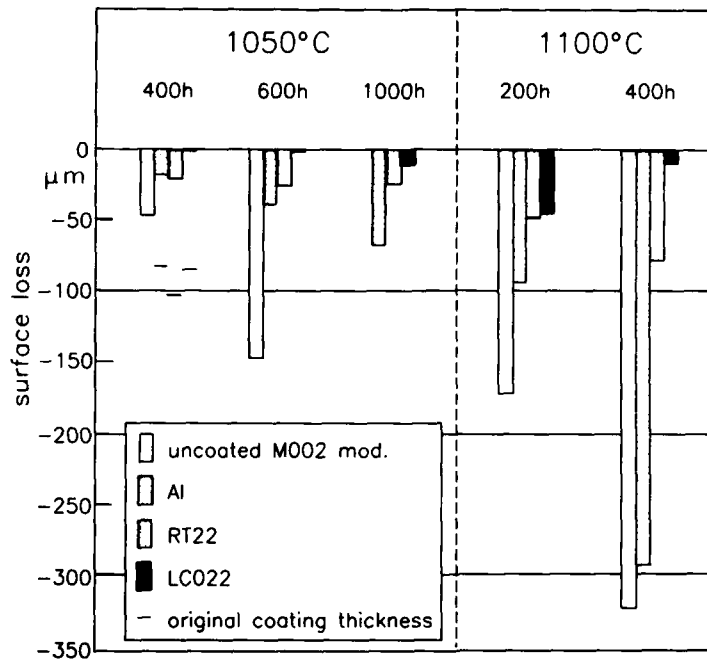


Figure 9. Average surface loss for M002 mod. and coatings as a function of testing time and temperature.

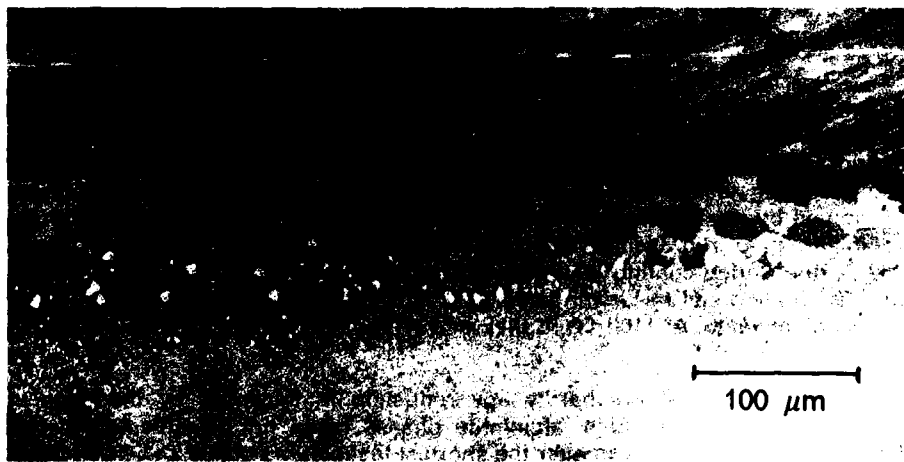


Figure 10. Al (Codep) coating tested at 1050 °C for 400 h (optical micrograph from a cross section).

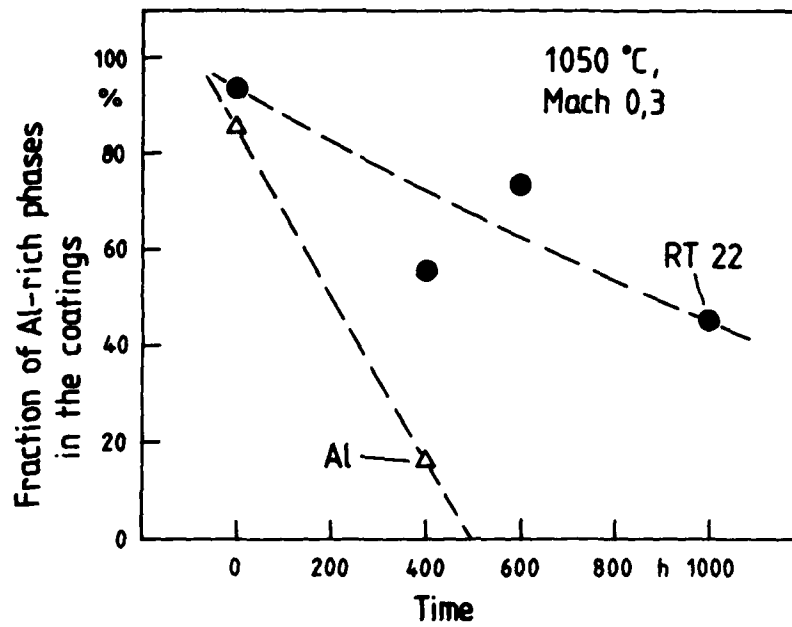


Figure 11. Consumption of Al (Codep) and RT22 coatings as a function of time at 1050 °C.

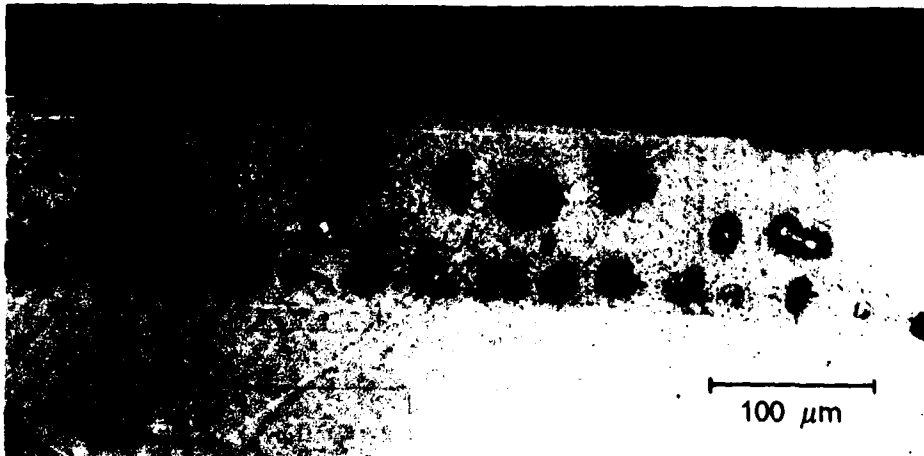


Figure 12. Formation of voids in the LCO22 coating tested at 1100 °C for 400 h (optical micrograph from a cross section).

In general, tests have demonstrated that the oxidation resistance of the M002 mod. coating systems increases in the sequence: uncoated - Al(Codep) - PtAl(RT22) - MCrAlY(LCO22).

MOLTEN SALT CORROSION

Figure 13 shows the electrochemical cell which is used for experiments in molten salts. The arrangement, especially the electrodes, was essentially developed on the model of an apparatus that had existed at Sulzer Bros. Ltd., Winterthur, Switzerland [7], [8].

A grounded gastight Inconel-601 insert placed between the furnace windings and the cell serves as electrical shielding and protection against corrosion. The alumina crucible, which contains the salt melt, is put on the bottom inside this insert. For experiments under a controlled atmosphere gas can flow through a alumina tube and bubble through the melt. Passing along a coil of platinum wire, gas reactions can be catalysed.

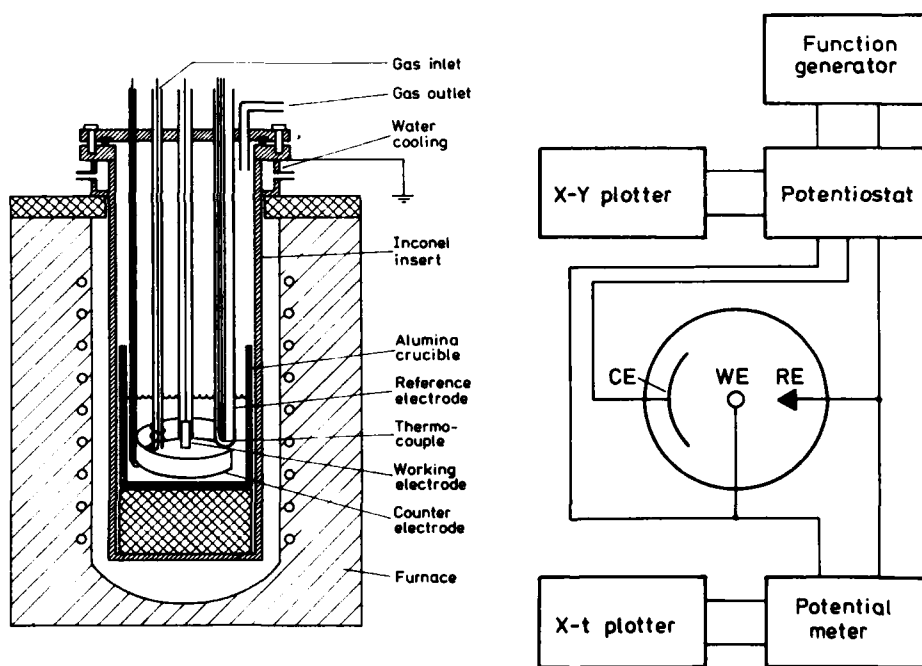


Figure 13. Schematic assembly for electrochemical studies.

For electrochemical measurements a three-electrode arrangement including counter, working, and reference electrode is used. The working electrode is constructed by sealing a metal rod with ceramic cement into one end of an alumina tube. The platinum lead wire contacting with the specimen is thus isolated from the melt. A platinum foil cylindrically bent is utilized as counter electrode and surrounds the working electrode. The $\text{Pt}(\text{O}_2)/\text{ZrO}_2(\text{Y}_2\text{O}_3)$ -electrode, really an indicator electrode for oxygen, was propagated by Erdős et.al. [7] as appropriate reference electrode in sulfate melts. A Pt/PtRh-thermocouple inserted into the $\text{ZrO}_2(\text{Y}_2\text{O}_3)$ tube of this electrode measures the temperatures of the melt. For comparative measurements the platinum coil in the gas inlet tube contacting with a lead wire can additionally be used as reference electrode. If the three electrodes are connected with a potentiostat, polarization measurements can be employed to determine current-potential curves. Potential-time curves can be measured by a potentiometer which is joined to the working and reference electrode.

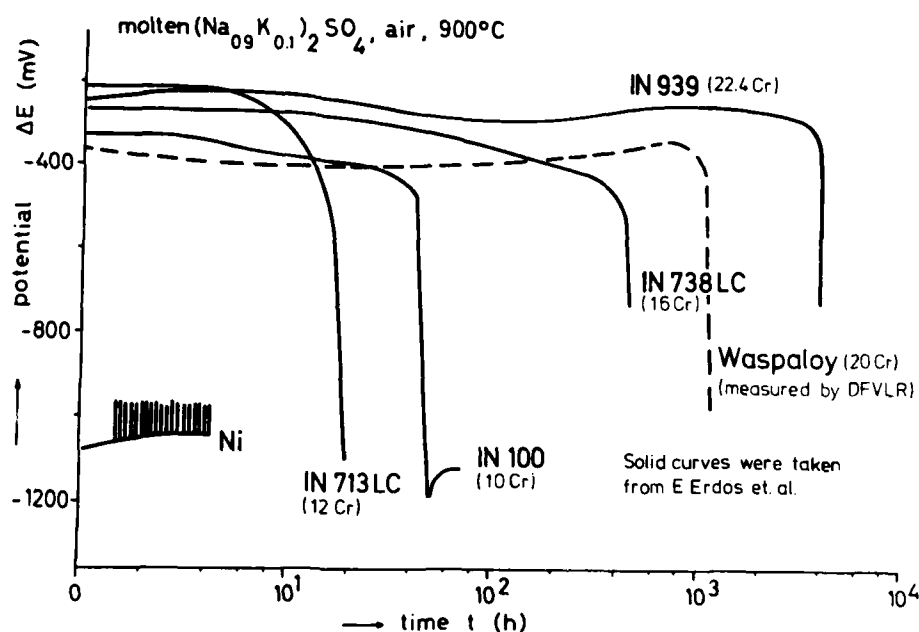


Figure 14. Potential vs. time of nickel and Ni-base alloys in a sulfate melt under air atmosphere at 900 °C (potential measurement with a $\text{Pt}(\text{O}_2)/\text{ZrO}_2(\text{Y}_2\text{O}_3)$ -electrode).

The diagram of Figure 14 shows the time-dependent variation of the potential for Waspaloy in molten $(\text{Na}_{0.9}\text{K}_{0.1})_2\text{SO}_4$ under air atmosphere at 900 °C in comparison with corresponding measurements of Erdős et.al. [8] for nickel and some Ni-base superalloys. The range of curves with an approximate constant potential represents the incubation period where the nickel alloys are protected by a closed oxide

layer. The potential drop is caused by breaking down of this layer because fresh metal surface comes in contact with the molten salt. Corrosion can now attack the Ni-base alloys at unprotected points. In the case of sulfate melts, sulphidation is usually involved in the corrosion process.

The onset of the potential drop depends on the chromium concentration of the nickel alloys. This result confirms the increase in corrosion resistance with increasing fraction of chromia in the surface oxide layer.

The potential of unalloyed nickel is at all times more negative than that of the nickel alloys. Since the oxide layer formed on nickel contains no chromia, resistance against hot corrosion is reduced.

REFERENCES

- [1] H.-J. Rätzer-Scheibe: "Heißgaskorrosion in Flugtriebwerken", DFVLR-Mitt. 84-04 (1984); Engl. transl.: "Hot corrosion in aircraft engines", ESA-TT-887 (1985).
- [2] M. Seiersten, H.-J. Rätzer-Scheibe, K. Fritscher: Final Report, SI Oslo and DLR Köln, June 1986.
- [3] M. Seiersten, H.-J. Rätzer-Scheibe, P. Kofstad: Werkstoffe u. Korrosion 38 (1987) 532-540.
- [4] H.-J. Rätzer-Scheibe, K. Fritscher, M. Seiersten: Proc. 1st Int. Conf. on Plasma Surface Engineering (Eds. E. Broszeit et.al., DGM Informationsges. mbH, Oberursel, FRG, 1989), Garmisch-Partenkirchen, FRG, Sept. 19-23, 1988, Vol. 2, pp. 1141-1148.
- [5] M. Seiersten, P. Kofstad: Mat. Sci. Techn. 3 (1987) 576-583.
- [6] L. Peichl, J. Wortmann, H.-J. Rätzer-Scheibe: Proc. Petten Int. Conf. "High temperature alloys: their exploitable potential" (Eds. J.B. Marriott et.al., Elsevier Applied Science, London and New York, 1988), JRC Petten Establishment, Petten, Netherlands, Oct. 15-17, 1985, pp. 363-373.
- [7] E. Erdős, H. Altörfer: Electrochim. Acta 20 (1975) 937-944.
- [8] E. Erdős, H. Altörfer, E. Denzler: Werkstoffe u. Korrosion 33 (1982) 373-385.

AGARD-NATO-SMP

Specialists' Meeting on "HIGH TEMPERATURE SURFACE INTERACTIONS" of the Corrosion Subcommittee

J. J. DeLuccia, Subcommittee and Meeting Chairman

SESSION V, Discussion/Workshop

26 April, 0900-1200

Recorders:	T. A. Kircher and	P. C. Patniak
	Naval Air	Orenda Division
	Development Center	Hawker Siddeley Canada
	Warminster, PA	Inc., Toronto, Ontario,
	USA	Canada

A paper was presented by Mr. Garrett Browne of the U. S. Navy which covered various fleet problems in the area of high temperature oxidation and hot corrosion. This is a summary of the responses to this presentation.

The discussion which followed Mr. Browne's presentation can be grouped into the following primary topic areas:

- I. Water washing of aircraft engines
 - A. Comments on the efficacy in reducing or preventing hot corrosion problems by washing away salt deposits.
 - B. Comments on the drawbacks of water washing, including introduction of additional corrosion problems.
 - C. Comments on the implementation of water washing, including the use of inhibitors.
- II. User's view of high temperature corrosion problem.
 - A. RAF (UK)
 1. T-56 engine
 2. Pegasus engine
 3. RV-199 (Tornado) engine
 4. Spey 750 (Nimrod AEW) engine
 - B. Canadian laboratories (CA)
 1. F404 engine
- III. Selection and evaluation of coatings
 - A. Standardization of testing
 1. Difficulties of standardization, technical and administrative.
 2. Methods of coating characterization.
 - B. Choosing coatings
 1. Coatings for hot corrosion.
 2. Difficulties of making general rules for coating selection.
 3. Need for independent data base.

At the conclusion of the discussion two topics for future AGARD Workshops were suggested. One topic was in the area of engine testing for hot corrosion. This was a primary concern of engine users who questioned the adequacy or sufficiency of existing engine testing requirements for high temperature corrosion. The second topic was in the area of repairability of engine components with regard to high temperature corrosion and coatings. This was suggested as a relevant area since hot corrosion problems often appear in local regions of a component such as the leading edge, trailing edge, tip, etc.

The following is a summary of the individual questions and comments which comprised the discussion session. The comments written here are not verbatim but rather paraphrased and condensed. Every attempt has been made to preserve the accuracy of the technical content of each response.

R-2

M. DeCrescente (US): Commercial engines don't show as much of a hot corrosion problem as military engines. We spent a lot of time in years past looking at sulfidation in industrial turbines and turbines on container ships, and much of my personal experience is based on these investigations.

The following comprises my understanding of the naval aircraft gas turbine engine hot corrosion problem:

The primary source of the problem occurs when the aircraft is on the deck of an aircraft carrier or on an airfield, engines idling. At this point ingestion of salt-laden air occurs. This salt can deposit onto the compressor or pass into the turbine and deposit on relatively cool parts. The aircraft then takes off and once above approximately fifty feet there is no further ingestion of salt. Therefore the damaging salt is ingested at ground level.

The greatest period of concern for hot corrosion is when the engine is at full thrust and the metal parts are at their highest temperatures. Two possibilities for the salt/metal interaction are as follows:

(a) The salt can evaporate from the hot part before the incubation period expires. This is why that incubation period is so important and why we are trying to extend the incubation period.

(b) The salt can spall from the compressor parts. In this case you have pieces of salt passing through the combustor rather than vapor. These then splash onto the hot metal parts, typically the leading edges. This results in extensive sulfidation.

In the industrial turbine work we realized the importance of the start-up period. The turbines which underwent "hot starts" experienced extensive sulfidation problems. We also found that water washing was effective in the industrial turbine area.

The use of new parts is highly recommended for a water wash study, since the residual sulfur left in refurbished parts can by itself cause the re-appearance of sulfidation.

UTRC considered using inhibitors for preventing hot corrosion in our turbines. We decided against it because of expense, logistics, and environmental concerns. The use of an addition to a water wash which would remain behind to act as an inhibitor during the start-up period might be effective.

Finally, I think that future technological advances such as better materials and hotter engines should reduce the hot corrosion problem, providing compressor shedding is avoided.

J. DeLuccia (US): The presence of chlorides above fifty feet has been observed and documented.

G. Browne (US): A USAF study determined that NaCl can be found at altitudes up to 30,000 feet above the ocean. Additionally, during Indian Ocean deployments at monsoon season heavy concentrations of sand and salt particulates are found at altitudes up to 2500 feet.

M. DeCrescente (US): What were the relative concentrations of salts at sea level and 30,000 feet?

G. Browne (US): Much lower at 30,000 feet, but they are there. The U. S. Air Force has started rinsing its aircraft. The result is that \$1.00 was saved in maintenance costs for each \$0.02 spent on washing.

A. Gupta (CA): Has the water wash effluent been analyzed coming out of the compressor? I have a study which shows that NaCl is not a primary contaminant, so I assume that it makes its way further into the combustor.

Also, the concentration of NaCl in the air is dependant on many variables such as temperature, sea state, ship speed, etc.

J. DeLuccia (US): All environments are not the same. The carrier deck is an extreme. We were surprised at the severity of our Indian Ocean deployments, which we find are twice as severe as other deployments. We have a lot of work to do.

J-F. Immarigeon (CA): I would like to dampen the enthusiasm concerning water washing and its potential benefits. The critical area for hot corrosion is near the cooling holes in the turbine blades. Here you find a temperature gradient and a lack of protective coating both of which favor hot corrosion attack. This localized attack

leads to swelling of the metal and blockage of the cooling holes and further damage due to oxidation as the metal temperature increases. Because of the need for cooling passages and therefore the presence of such temperature gradients higher engine temperatures will not necessarily diminish the problem. There will still be a region on the blade which will be susceptible to hot corrosion.

Furthermore, concerning the question of incubation times for hot corrosion and water washing. If the incubation times are on the order of hours, and washes are performed on the order of tens or hundreds of hours, will the wash be effective if corrosion has already started?

M. DeCrescente (US): Have you tried water washing to solve your problem?

J-P. Immarigeon (CA): The problem will exist under any condition since it is highly localized. The location of the problem will simply shift. The real solution to the high temperature corrosion problem lies in controlling the high temperature surface reactions by use of coatings and alloying.

J. DeLuccia (US): On the subject of incubation time, Dr. Bornstein clarified this the other day. The incubation times given were for accelerated laboratory tests, not from actual engine operating time.

It is clear that the solution to this problem does not lie with water washing alone. It is only a "band-aid", not a permanent solution. We have to approach the problem on many fronts.

G. Browne (US): Concerning the implementation of water washing- normally we run the engine for five minutes after the fresh water rinse. This procedure thoroughly dries the engine.

A. LeBlanc (CA): I have a question for the U. S. Navy concerning their experience with the IPS (inlet particle separator) on the T-700 engine. Has the use of the IPS had an impact on the engine wash cycle?

G. Browne (US): We have had no problems with the IPS. The particle separator seems to help. Concerning water washing- the problem we have with the helicopter engine is during the close hover to the water. The rotor wash can result in a continuous salt laden mist. Our documentation shows that the engine that is washed last longer. But you have to get the contaminants out after washing, by flushing the engine thoroughly with pure water. You also must dry it out by running the engine.

M. Cannon (UK): I would like to give, from a user's viewpoint, the RAF's experience with corrosion problems in some of their engines. These comments were collected through informal discussions with the various program offices responsible for these engines.

First, regarding the T-56 Hercules. With the LPI rotor blade we see sulfidation, oxidation of the internal cooling passages, and premature stress-rupture failure. Some solutions are as follows:

1. Reduce the cruise TIT from 985 to 932 °C. This is a possible short term solution.
2. Perform a half-life turbine overhaul. This is a more likely solution. The Royal New Zealand Air Force is looking at this also.
3. Change the blade material from IN738 to MM246. This is the manufacturer's recommendation.
4. Internal treatment of the cooling holes. This is the best long term solution but development of a process is needed.

Concerning the Pegasus engine, used in the RAF Harrier and the Royal Navy Sea Harrier. I have a question for the U. S. Navy: This engine operates using a water injection system. Is this a possible source for the problems the U. S. Navy is experiencing?

G. Browne (US): I really can't answer that. But I do know that this aircraft is used by the Marines under very harsh environments including sand ingestion. There is no question that the problem is not just the engine design or fabrication but also the environment which the engine is used. The environment is part of the problem.

M. Cannon (UK): The Pegasus engine is designed for a 400 hour life for the combustor/turbine. We are considering using a TBC on the NGV and a single crystal blade material.

R-4

Concerning the RV199 engine used in the Tornado aircraft - currently the HP turbine uses an IN100 blade and we are experiencing tip plug loss. This is basically corrosion under the plug which forces the plug out, followed by a loss of blade cooling. One possible cause which has been suggested is "gunfiring" and re-ingestion of gaseous propellant. One solution may be to close the tip by welding or protecting the part with a ceramic material.

Concerning the Spey 250 engine used in the Nimrod AEW aircraft - here we see a high cost of spare parts due to loss of engine parts to corrosion. One solution may be double aluminizing or the use of a cermet sacrificial coating on the blades and disks.

Concerning the RAF and compressor washing - the RAF has blown hot and cold on this issue over the years. It is currently out of vogue, but is being reviewed again for possible implementation.

The IPS for helicopter engines is being reviewed with interest for use in dusty environments.

R. Thamburaj (CA): Some comments for the Canadian laboratories on the F404 HPT. The blades shown by Mr. Browne had a TMF count of 15,700 cycles, or about one-half their expected life. The material used is a DS Rene 80, and we are observing tip damage. The exact mechanism is unknown but it is tip oxidation and not tip erosion. No sulfur compounds are observed in the hardware. The Australians also have a problem with tip oxidation in the HPT and we would like to know if the U. S. Navy also sees this problem.

The outside damage is only half the story. Internal damage of the blade is also important. As a solution we are looking at improving the tip oxidation resistance. The Australians are developing their own coating for this blade.

P. Patniak (CA): We see the same problem with both the GE and PWA blade at one-half FTC, about 15,000 cycles. We see tip oxidation due to plugged cooling holes. There are twenty-two cooling holes in the tip region of these blades. We have examined fifty to sixty blades and most had blockages in at least sixteen of these cooling holes. GE has issued an Engineering Change Proposal to introduce two new cooling holes into the trailing edge near the tip. This will not be sufficient as a solution since the problem is so extensive.

A cause of tip cracking in these blades may be loss of the aluminide coating caused when the tip rubs the outer seal. Remember that Rene 80 is a relatively poor alloy for oxidation resistance, but good in hot corrosion.

I have a concern for coating technology. We have seen component technology grow from polycrystal to DS to single crystal. Is aluminide coating technology and coating technology in general keeping pace?

J-F Immarigeon (CA): I'd like to expand a bit on surface degradation and internal cooling holes of blades in the F404 and the T-56. The U.K. is having problems with the T-56. The problem has grown in size over the last few years. We are seeing damage of this type in Canadian engines, although I don't know of any premature stress-rupture failures at this time. We are looking at coating the internal cooling passages. Let me note that an industrial version of this engine has had internal cooling passages coated by the manufacturer and has done very well. We are looking at this from a metallurgical viewpoint, but we would like to try it in Canadian engines. There would be no need for blade re-design.

M. Doruk (TU): The question I have regards the replacement of a polycrystal component with a DS component. What effect can I expect on the oxidation and hot corrosion behavior?

P. Patniak (CA): I can comment on the fact that such a change can affect the creep behavior of the blade. For example, Codep-coated DS Rene 80 will have reduced creep properties and improved TMF characteristics relative to Codep-coated polycrystal Rene 80.

I am also interested in hearing more about the role of active elements such as yttrium and hafnium in the substrate and the relation to oxidation resistance.

M. DeCrescente (US): I can comment on the so-called active element effects. Our research shows quite conclusively that active elements prevent sulfur from diffusing to the coated surface thereby enhancing oxide scale adherence.

A. Gupta (CA): I would like to broaden the horizon somewhat and ask the question - there are so many coatings. Which coating do we select? What about standard testing

procedures, such as VAMAS? We should be talking about developing some standard testing procedures.

J. DeLuccia (US): Perhaps Dr. Gibbons can give us a few words on that topic.

T. Gibbons (UK): I can comment on the topic of standardization and VAMAS as an example. Here is a case where the research institute can help the user community. But the problem is also the perception of corrosion as a "low tech" problem. Topics such as MMC's, high strength polymers, and RST are popular. Hot salt corrosion just isn't perceived as such an important technology by the funding sources.

As far as standardization, we must become more quantitative in our research. There just isn't a "magic solution" to the high temperature corrosion problem. What we need is the ability to make discrete and finely judged differences between one material and another and one coating and another. For this we need to be able to make quantitative measurements and reliably perform standard procedures.

What we also must do as a body of researchers is to be more public about our difficulties and the need for corrosion research. In particular this publicity needs to reach the funding sources.

J. DeLuccia (US): I can comment about the difficulties in developing standard test procedures from my experience in the area of corrosion fatigue. Twelve years ago we started an eight nation round-robin testing program. It took six years to finish the core program. We had to write our own test manual which each participating laboratory had to use. It took another six years to complete a follow-on program. So you are talking about a long-term investment of time to develop standardization procedures. That is a good question - should a hot corrosion round-robin be initiated within AGARD?

A. Gupta (CA): This still does not answer the question as to what coating should I be using. What is the basis for selecting a coating? We should start some activity on the testing side.

R. Rapp (US): I can comment on the aspect of what kind of coating would do any good as far as hot corrosion is concerned.

The following points are important regarding the nature of the hot corrosion process:

1. Hot corrosion occurs immediately when molten sodium sulfate contacts the metal substrate. Metals are not thermodynamically stable in the presence of molten salts. Therefore an oxide barrier is necessary.
2. The two most important oxides are Cr_2O_3 and Al_2O_3 . The reason is because gas turbines produce an acidic molten salt and these are the two most stable oxides under acidic conditions.
3. Al_2O_3 films grow slowly. This is why long-term oxidation behavior depends on Al_2O_3 formation. But increasing the chromium content in the coating will help by promoting a rapidly-forming chromia as a transient oxide which will initially protect the metal from the molten salt.
4. Finally, one wants to keep the salt acid, and keep the substrate beneath an acid stable oxide such as Al_2O_3 or Cr_2O_3 . Then continuous dissolution and reprecipitation can be avoided.

As far as water washing is concerned, I think it is a fine idea. I could see washing with a hot water solution and finishing with a solution containing an aqueous chromate inhibitor. And as far as the type of coating one wants, aluminide coatings form an Al_2O_3 film which grows too slow. I think a coating such as the chromized-aluminized pack coating we have developed would be best. Our problem with this coating has been the "NIH" factor, or the "not-invented-here" factor. There can be a problem in transitioning university research to a coating manufacturer.

R. Mevrel (FR): Some comments on how to choose a coating - I think there are four primary factors which must be considered. First, the environment - the temperature, the cycle shape, the atmosphere. Secondly, the substrate, and its compatibility with the coating. Here we mean chemical compatibility (limited interdiffusion) and mechanical compatibility. Thirdly, the application process must be considered. Each process has advantages and disadvantages. For internal cooling passages some type of CVD or modified pack process must be considered. Plasma spray is restricted to simpler component geometries. Finally, the users requirements come in. Most users do not want a coating which has only one source. There can be patent problems. And the cost is often not the least important factor. For these reasons it is difficult to design general rules for coating selection.

A. Gupta (CA): My question perhaps was misunderstood. I don't mean coating development. What I mean to ask is that there are so many coatings available. I know my need, but there is no data for selecting from available coatings based upon my need. For example, we would like an ASTM source book which would tell me that for TMF improvement, select this, for hot corrosion improvement, select this.

I also have difficulty with the definitions for hot corrosion, sulfidation, sulfation, etc.

M. DeCrescente (US): There is a need for standardization as far as the manufacturers are concerned. At PWA there is a push to minimize the number of coatings in their inventories. In terms of coating selection, cost is often the driver. Diffusion coatings are better than the overlays in this regard. Furthermore, diffusion coatings are better in TMF than the overlays. We are trying to improve the oxidation resistance of diffusion coatings to match that of the overlay coatings.

R. Waterhouse (UK): We have submitted a proposal for an independent (unprejudiced) information center on coatings and surface treatments to be set up at Nottingham, but the proposal was not funded. There is a national center for information on tribological coatings.

R. Rapp (US): Characterization of coatings is a difficult task. At the minimum one needs the following:

1. a good photomicrograph
2. compositional analysis
3. phase identification
4. thickness on substrate
5. performance in a specific type of test

So some degree of sophistication is necessary for an "expert system" on coatings.

A. LeBlanc (CA): From a user's view, I don't care about coatings. I am concerned only with engine performance. I would like to know if the newer engines, the ones of the past 5-10 years, show a hot corrosion problem.

G. Browne (US): The Naval Air Propulsion Center, Trenton, NJ will have that information for the U. S. Navy.

A. LeBlanc (CA): As far as testing of engines concerned, will engines which pass specifications still have a basic coating problem?

J. DeLuccia (US): Yes.

G. Browne (US): The problem goes across the spectrum of manufacturers. The basic cause is the deterioration of the blades, and it is a universal problem.

J. DeLuccia (US): Oxidation and hot corrosion problems will not disappear. It is more a question of keeping them tractable. The problems we have discussed here today show a great deal of commonality, and the solutions will in most cases share a great deal of commonality. We are looking for new directions for research, and for new directions for maintenance.

Some of the ideas we have discussed are

1. water washing - the U. S. Navy has a severe enough problem that water washing is necessary.
2. research approaches and the need for a central repository for information.

I'm not sure how AGARD figures into this at this time. Any other comments?

J-F Immarigeon (CA): I would like to emphasize the need for a data base. I believe the national laboratories are the place for this effort. And we need more than just burner rig data. We also need quantification of interactions between the coating and substrate, etc. What we really need is a standard procedure for coating evaluation.

P. Patniak (CA): I see three types of coatings in the field today - diffusion, overlay and TBC. I would like to see a thrust in AGARD concerning the repairability of

diffusion coatings. This is especially important since 80-90% of the problems with oxidation and hot corrosion are discovered after the fact, that is, after the engine is designed and qualified.

Since many of the problems are localized to certain regions of the blades, such as leading edge, trailing edge, and tip, I believe that a workshop on local repair techniques for coatings would be highly received and worthwhile.

J. DeLuccia (US): Perhaps we should consider an AGARD Workshop on repairability of engine components with regard to high temperature corrosion and coatings.

T. Gibbons (UK): I would like to offer a comment in support of Dr. Immarigeon. If standardization is needed, don't think that it will just happen by itself. And, don't underestimate the power of a group such as ourselves, the user group, to influence the engine community.

A. LeBlanc (CA): My observations are from the perspective of the user, someone who buys engines. My question is still the same - are the requirements for engine hot corrosion testing sufficient?

J. DeLuccia (US): Unfortunately that question falls outside the scope of the present Workshop. We could consider an AGARD Workshop on engine testing requirements. An AGARD Workshop on repairability could also be considered.

f-8

REPORT DOCUMENTATION PAGE			
1. Recipient's Reference	2. Originator's Reference	3. Further Reference	4. Security Classification of Document
	AGARD-CP-461	ISBN 92-835-0533-6	UNCLASSIFIED
5. Originator	Advisory Group for Aerospace Research and Development North Atlantic Treaty Organization 7 rue Ancelle, 92200 Neuilly sur Seine, France		
6. Title	HIGH TEMPERATURE SURFACE INTERACTIONS		
7. Presented at	the 68th Meeting of the Structures and Materials Panel of AGARD in Ottawa, Canada, 23-28 April 1989.		
8. Author(s)/Editor(s)	Various		9. Date November 1989
10. Author's/Editor's Address	Various		11. Pages 242
12. Distribution Statement	This document is distributed in accordance with AGARD policies and regulations, which are outlined on the Outside Back Covers of all AGARD publications.		
13. Keywords/Descriptors	<p> <i>Terminal shock;</i> Aircraft engines Corrosion prevention Corrosion environments Military aircraft Erosion corrosion <i>Supersonic</i> <i>Gas turbines</i> <i>Protective coatings</i> <i>Sliding/Friction</i> <i>Titanium alloys</i> <i>Corrosion mechanisms</i> Degradation Surface chemistry Surface temperature <i>Hot corrosion</i> <i>Hot salt corrosion</i> <i>Aluminum base materials</i> <i>Wear</i> <i>Erosion</i> <i>High-temperature</i> <i>(EDC) 4</i> </p>		
14. Abstract	<p> In today's climate of life extension for military aircraft, the topic of corrosion control assumes a role of greater importance. At its sixty-eighth meeting, the Structures and Materials Panel held a conference of Specialists, focussed on controlling the degradative effects of flight environments on aircraft engine materials. </p> <p> The meeting reviewed the chemical and mechanical mechanisms involved in degradative processes and considered some state-of-the-art solutions. Emphasis in discussions centred on hot-salt corrosion topics but wear and erosion problems were also considered. </p> <p> Papers presented at the 68th Meeting of the Structures and Materials Panel of AGARD held in Ottawa, Canada, 23-28 April 1989. </p>		

AGARD Conference Proceedings No.461 Advisory Group for Aerospace Research and Development, NATO HIGH TEMPERATURE SURFACE INTERACTIONS Published November 1989 242 pages In today's climate of life extension for military aircraft, the topic of corrosion control assumes a role of greater importance. At its sixty-eighth meeting, the Structures and Materials Panel held a conference of Specialists, focussed on controlling the degradative effects of flight environments on aircraft engine materials. The meeting reviewed the chemical and mechanical mechanisms involved in degradative processes and P.T.O.	AGARD-CP-461 Aircraft engines Corrosion prevention Military aircraft Erosion corrosion Corrosion mechanisms Degradation Surface chemistry Surface temperature	AGARD Conference Proceedings No.461 Advisory Group for Aerospace Research and Development, NATO HIGH TEMPERATURE SURFACE INTERACTIONS Published November 1989 242 pages In today's climate of life extension for military aircraft, the topic of corrosion control assumes a role of greater importance. At its sixty-eighth meeting, the Structures and Materials Panel held a conference of Specialists, focussed on controlling the degradative effects of flight environments on aircraft engine materials. The meeting reviewed the chemical and mechanical mechanisms involved in degradative processes and P.T.O.	AGARD-CP-461 Aircraft engines Corrosion prevention Military aircraft Erosion corrosion Corrosion mechanisms Degradation Surface chemistry Surface temperature
AGARD Conference Proceedings No.461 Advisory Group for Aerospace Research and Development, NATO HIGH TEMPERATURE SURFACE INTERACTIONS Published November 1989 242 pages In today's climate of life extension for military aircraft, the topic of corrosion control assumes a role of greater importance. At its sixty-eighth meeting, the Structures and Materials Panel held a conference of Specialists, focussed on controlling the degradative effects of flight environments on aircraft engine materials. The meeting reviewed the chemical and mechanical mechanisms involved in degradative processes and P.T.O.	AGARD-CP-461 Aircraft engines Corrosion prevention Military aircraft Erosion corrosion Corrosion mechanisms Degradation Surface chemistry Surface temperature	AGARD Conference Proceedings No.461 Advisory Group for Aerospace Research and Development, NATO HIGH TEMPERATURE SURFACE INTERACTIONS Published November 1989 242 pages In today's climate of life extension for military aircraft, the topic of corrosion control assumes a role of greater importance. At its sixty-eighth meeting, the Structures and Materials Panel held a conference of Specialists, focussed on controlling the degradative effects of flight environments on aircraft engine materials. The meeting reviewed the chemical and mechanical mechanisms involved in degradative processes and P.T.O.	AGARD-CP-461 Aircraft engines Corrosion prevention Military aircraft Erosion corrosion Corrosion mechanisms Degradation Surface chemistry Surface temperature

<p>considered some state-of-the-art solutions. Emphasis in discussions centred on hot-salt corrosion topics but wear and erosion problems were also considered.</p> <p>Papers presented at the 68th Meeting of the Structures and Materials Panel of AGARD held in Ottawa, Canada, 23—28 April 1989.</p> <p>ISBN 92-835-0533-6</p>	<p>considered some state-of-the-art solutions. Emphasis in discussions centred on hot-salt corrosion topics but wear and erosion problems were also considered.</p> <p>Papers presented at the 68th Meeting of the Structures and Materials Panel of AGARD held in Ottawa, Canada, 23—28 April 1989.</p> <p>ISBN 92-835-0533-6</p>
<p>considered some state-of-the-art solutions. Emphasis in discussions centred on hot-salt corrosion topics but wear and erosion problems were also considered.</p> <p>Papers presented at the 68th Meeting of the Structures and Materials Panel of AGARD held in Ottawa, Canada, 23—28 April 1989.</p> <p>ISBN 92-835-0533-6</p>	<p>considered some state-of-the-art solutions. Emphasis in discussions centred on hot-salt corrosion topics but wear and erosion problems were also considered.</p> <p>Papers presented at the 68th Meeting of the Structures and Materials Panel of AGARD held in Ottawa, Canada, 23—28 April 1989.</p> <p>ISBN 92-835-0533-6</p>

ISBN 92-835-0533-6